Pixel Detector Studies for the ATLAS ITk Upgrade for the HL-LHC

Dissertation

for the award of the degree
“Doctor rerum naturalium” (Dr. rer. nat.)
Division of Mathematics and Natural Sciences
of the Georg-August-Universität Göttingen

within the Physics doctoral programme
of the Georg-August University School of Science (GAUSS)

submitted by

Silke Möbius

from Heidelberg, Germany

Göttingen, 2022

Thesis Committee:

Prof. Dr. Arnulf Quadt
II. Institute of Physics, Georg-August-Universität Göttingen

Prof. Dr. Stan Lai
II. Institute of Physics, Georg-August-Universität Göttingen

Prof. Dr. Steffen Schumann
Institute for Theoretical Physics, Georg-August-Universität Göttingen

Members of the Examination Board:

Reviewer:	Prof. Dr. Arnulf Quadt II. Institute of Physics, Georg-August-Universität Göttingen
Second Reviewer:	Dr. habil. Susanne Kühn CERN

Further members of the Examination Board:

Prof. Dr. Steffen Schumann
Institute for Theoretical Physics, Georg-August-Universität Göttingen

Prof. Dr. Stefan Dreizler
Institute for Astrophysics, Georg-August-Universität Göttingen

Dr. habil. Markus Keil
CERN

Prof. Dr. Ulrich Husemann
Institute of Experimental Particle Physics, Karlsruhe Institute of Technology

Date of the oral examination: 2 December 2022

Reference: II.Physik-UniGö-Diss-2022/03

Pixel Detector Studies for the ATLAS ITk Upgrade for the HL-LHC

Abstract

The integrated luminosity of the Large Hadron Collider (LHC), which is proportional to the number of particles colliding and thus data being collected, is planned to be increased by a factor of 5-7.5 compared to the design luminosity of the LHC by the end of the 2020s. This step is motivated by the potential to measure Standard Model physics processes especially in the top quark and Higgs sector with high precision and discover new physics.

However, this upgrade to the High Luminosity-LHC will result in an increased particle density in the experiments, causing a higher hit occupancy in the detectors and an increased radiation damage. In order to tackle this problem, the current tracking detectors of the LHC experiments ATLAS and CMS need to be replaced by radiation harder, faster detectors of higher granularity. The inner tracking detector of the ATLAS Experiment will be upgraded to an all silicon detector by the end of 2028. There will be a new strip detector with planar sensors and a hybrid pixel detector which features inner layers with 3D sensors and outer layers with planar sensors.

The following work is focused on the outer layers of the PIXEL Detector and the different steps towards the upgrade. First, suitable sensors need to be decided on based on laboratory and test beam measurements. A second step is the PIXEL Detector module building with a newly developed tool and electrical and mechanical testing of the modules themselves. Validation measurements of the tool in addition to a well-defined assembly process are crucial for a successful production. Eventually, the performance of several modules together needs to be investigated, which is done by integrating them in a larger prototype structure built at CERN.

Results from all these steps are presented within the scope of this thesis.

Was man tief in seinem Herzen besitzt,
kann man nicht durch den Tod verlieren.

(Johann Wolfgang von Goethe)

Ein Jahr mit seinen Höhen und Tiefen

In memory of my father

Contents

Acknowledgements

A thesis might be written by one person but most certainly not without support and encouragement from others.

While my path into particle physics was not as straight as it could have been, coming from optics over theoretical physics to hardware, I want to thank my supervisor Arnulf Quadt for believing in me and convincing me to join his working group. Thank you for inspiring me and pushing me to my limits, especially when I was losing trust in my work.

A big thank you goes also to Steffen Schumann, my former master thesis supervisor and thesis committee member, who reminded me to focus – although I cannot say that this always worked exactly as planned…

Thank you, Stan Lai, also from my thesis advisory committee, for finding motivating and friendly words whenever we met.

On a day-to-day basis I am grateful for my colleagues, brightening up the darkest day. Special thanks to my hardware and workshop men in Göttingen, who made Covid pandemics working style bearable. I want to specifically mention Jörn Lange and Jörn Große-Knetter, for me known as Jörn^2, and Hua Ye for answering my endless stream of questions and discussing with me when needed. I appreciate your will to help and also your trust in me and my suggestions. Also, Peter Arnsberger, Sascha Böhlken, Tim Kanngießer, Uwe Ronsöhr and Rüdiger Widera, thanks for your openness and will to find solutions to all our lab and not lab related problems.

When my biggest wish came true and I went to CERN for more than a year, there was everything closed down. Thanks to all the people at CERN and especially Susanne Kühn and Benedikt Vormwald for making me feel welcome, giving me advice, opportunities and an open ear when I started working there. I am grateful for your openness and helpful communication, in whatever situations I needed them.

Not to forget all of my old and new friends, in Göttingen, at CERN and at home for being there, spending endless nights talking and letting me inspire you to do all different kinds of crazy things. This goes especially to my CERN friends and all our crazy almost physics related tours in the mountains.

I would also like to thank the Konrad-Adenauer-Foundation for their scholarship that supported me with my research. Some of the measurements leading to these results have been performed at the Test Beam Facility at DESY Hamburg (Germany), a member of the

Helmholtz Association (HGF).

Thank you Ali, Benedikt, Brendan, Florian, Hans, Hua, Jörn^2, Knut, Moritz, my mum Imke, Sebastian and Tobias for proofreading chapters of this thesis and giving advice. Special thanks to Knut for talking me through this thesis and providing help with LaTeX.

When life takes an unexpected turn, support is most valuable. For all those giving me support when needed mostly I am very grateful.

Physics has always been a part of me, starting with the dinner table discussions with my parents. Thank you for pushing me and reminding me why I am doing what I am doing, even in times of deepest doubt in the usefulness of what I do. A big hug goes to my mother for supporting me even when she was needing support herself and my dad for inspiring me beyond death and somehow making me feel the urge to continue.

Contributions by the author

The experiments at the LHC, such as the ATLAS Detector, are developed and operated by a collaboration of thousands of physicists. All papers are published in the name of the entire collaboration and not attributed to individuals as different contributions such as detector development and operation play an equally important role as the data analysis.

A short summary of the topics to which the author has contributed to in the first three years of the work for this thesis are published in Ref. [1].

The following is a (non-exhaustive) list of the author's contributions to these studies.

The author has worked with the physics modelling group on the improvement of the implementation of physics parameters in several event generators.

Towards the production of ITk pixel modules the author made important contributions to the measurements of planar silicon pixel sensors in a so-called market survey, as described in Chapter 6. For measurements and analysis in Göttingen, already existing software from Jörn Große-Knetter was used and altered to the author's needs. Within the supervision of a bachelor student sensor analysis programmes were developed [2]. During test beams the author was co-responsible for the setup and the data taking while focusing on preparing the samples for the measurements by tuning. The analysis was split and cross checked by all members of the ITk test beam analysis team. Results from this effort are hence published in the doctoral theses [3, 4]. Based on the measurements and comparisons of the data, a decision on the vendor for the ITk sensors was made.

In terms of module building, the performance of the module building tooling developed and constructed in the institute workshop of the II. Institute of Physics and the Central Workshop of the University of Göttingen, needed to be validated. The author of this thesis developed a validation procedure in collaboration with the workshop team and Jörn Lange to perform the desired measurements as described in Section 7.1. Based on these findings an improved version of the tooling could be designed.

With this module building tooling, the author glued several modules and performed measurements and developed an analysis. Based on this, Göttingen was qualified as module assembly site. After first experiences, the module building and measuring was transferred to the technical personnel and the author's focus was on the analysis of the measurements. Based on experience with the tooling, the module assembly manual was reworked and complemented to serve as guidelines for all module building institutes.

Starting from a module testing setup as described in [5], a new testing environment was installed by the author. The main component, a cooling box, was assembled, commissioned and extensively tested. Two modules were characterised and tested in the context of the testing site qualification by the author before leaving to CERN. Together with final tests done by Jörn Große-Knetter, Baida Achkar and Rafael Gonçalves-Gama, this served as qualification for Göttingen as quad module testing site.

At CERN, the author was part of a constantly evolving small team repeating and finalising the measurements on the FE-I4 demonstrator and involved in the recommissioning of the system, the measurements themselves and part of the analysis of the data. For the analysis collaborative code from Stefano Zambito and Quentin Buat was adopted and utilised. The preparation of the RD53A demonstrator was in parts also task of the author. Especially the interlock and measurements for the recommissioning of the CO_2 system are to be named here. Making of cables, testing of them, commissioning power supplies and performing connection tests were also part of the author's contribution.

In order to do efficient tests on modules for the RD53A demonstrator, several testing setups were commissioned at CERN, where parts were done in collaboration with other people of the module measuring team. These setups were then extensively used for measurements by all members. The analysis of the data is done with a software the author is developing based on a script [6] initiated by the summer student Tsz Hong Kwok co-supervised by the author and Benedikt Vormwald in 2021, as shown in Chapter 9.

Towards the first readout chain of the RD53A demonstrator, the author has contributed with several testbench measurements and data analysis.

CHAPTER 1

Introduction

“What are we made of?” Summer students at the European Organization for Nuclear Research (CERN- (Conseil Européen pour la Recherche Nucléaire)) asked themselves this question and printed it on their group shirts. More than 200 years before, Goethes famous Faust [7] (V. 382f) was contemplating

> “So that I may perceive whatever holds.
> The world together in its inmost folds.”

Uncountable theories have been evoked by questions about the structure of matter as well as that of the universe. But – however fascinating a theory may be – without experimental evidence it stays a fantasy. Particle physics, together with cosmology, is at the root of these questions about the universe. The so-called Standard Model of particle physics (SM) is as of today one of the most successful theories in science. It shows unprecedented experimental agreement regarding the elementary particle parameters and their interactions.

The search for the smallest particles described by the SM has required tremendous effort. Experiments of unprecedented scale, where particles are accelerated to higher and higher energies and subsequently collided, have been built in the past century to search for new particles, compatible with the SM. In 1954 CERN was founded to provide a particle physics research infrastructure on European ground, peacefully uniting countries formerly at war. Since its foundation it has hosted many different accelerators and experiments, run by international collaborations and resulting in important discoveries. At the four experiments at the Large Hadron Collider (LHC) the SM is to date tested with proton-proton collisions at unprecedented precision. With the discovery of the Higgs boson [8, 9] in the two multi-purpose LHC experiments ATLAS (A Toroidal LHC ApparatuS) [10] and CMS (Compact Muon Solenoid) [11] in 2012, more than 10 years ago by now, the last non-discovered particle described by the SM was found, demonstrating its power to describe the experimental findings well. However, not all experimental findings agree with the SM which has led to theories beyond the Standard Model (BSM) which motivate further investigation on a larger data set. For example, only 5% of visible matter make up the universe, the rest, so-called dark matter and dark energy, are still to be understood. With the LHC it would, however, take decades to collect the data necessary for the analyses.

Towards maintaining its world-class high-tech environment for fundamental research at the frontier of knowledge, a vast number of engineering and technical tasks need to be solved at CERN. The LHC has therefore recently been upgraded to higher energies and will be upgraded further to the High Luminosity-LHC (HL-LHC) by the end of the 2020s, which will provide higher instantaneous luminosity and thus larger amounts of collision data for precision studies of the SM. In Chapter 2, the Standard Model with a few historical highlights and possible additions is explained to motivate the planned upgrades of the LHC and its experiments to enhance the physics reach.

In order to be able to reconstruct interesting physics events and eliminate background in ATLAS physics data, fast, highly granular and radiation hard detectors are needed for energy, trajectory and momentum measurements, especially for the upgraded HL-LHC. Amongst other detector components, the current innermost part of ATLAS, the PIXEL Detector, will therefore be exchanged with the highly radiation tolerant Inner Tracking Detector (ITk), an all-silicon detector with strip and pixel modules, to cope with the harsher environment, as explained in Chapter 3 with an overview of the LHC, ATLAS and the anticipated upgrades. The particle detection mechanisms which are exploited in silicon detectors such as the ITk are explained in Chapter 4.

The new tracking detector ITk consists of more than ten thousand pixel modules with silicon sensors, as explained in Section 5. The sensors need to be of high quality, so the sensor quality was tested in a so-called sensor market survey which qualified pixel sensors on wafer and sensor level. Chapter 6 describes these mechanical, electrical and test beam market survey sensor tests, executed within the scope of this thesis before and after irradiation.

Moreover, common procedures are defined to control the quality and assure high standards when it comes to module assembly and testing by a collaboration as large as the ATLAS collaboration. The studies on a dedicated tooling designed for the assembly of modules and testing measurements at various stages are presented in Chapter 7 and have contributed largely to the formulation of a common procedure. Electrical module tests, which comprise test setup commissioning, actual measurements, their analysis and interpretation, are a key component in quality control for production of the detector and are shown in Chapter 7.

A method was developed to easily compare module properties after different stages of assembly and amongst modules, which is exploited to get a sufficient number of modules for system tests on a prototype system of the new PIXEL Detector, which is called a demonstrator. The purpose of a demonstrator is to test design and integration aspects of modules in a larger system to estimate the possible effects. Prototype modules from the current PIXEL Detector were used in the first version of the demonstrator, while the latest version uses prototype ITk modules. The preparation and commissioning of the latest setup and the final tests on the previous setup are subject of Chapter 8. Furthermore, the demonstrator programmes with their results and the status of the measurements are explained. Chapter 9 finally gives details on the module related results of the demonstrator which build on the comparison method of modules.

CHAPTER 2

The Standard Model of Particle Physics

The Standard Model describes the elementary particles and their interactions by employing quantum field theories [12–22]. It was formulated in the 1970s based on a long history of discoveries and theoretical developments.

2.1. The Beginning of Particle Physics

The first particle discovery happened more than hundred years ago, when in 1897 the electron was discovered by J. J. Thomson [23]. This was the beginning of a new era of physics, leading to the theories of particles we know today. Although not an elementary particle, the discovery of a nucleus by Rutherford [24] and Chadwick's discovery of the neutron [25] initiated the understanding of matter as made from particles as later postulated by Bohr with the model of the atom [26–28]. Experimental findings like the photoelectric effect [29] by Einstein and Planck's black-body radiation spectra and the quantisation of energy [30] heralded theoretical considerations which culminated in the formulation of quantum physics, which is the fundamental base for particle physics theories today.

Amongst the theorists were Einstein, with his well known formula postulating the mass-energy equivalence and special relativity [31–33], Heisenberg and Born with their matrix mechanics [34–36], Schrödinger with his wave formulation of quantum mechanics [37] and Dirac with the relativistic wave equation [38, 39] giving a relativistically consistent description of spin-$\frac{1}{2}$ particles by postulating negative energy states.

But not only theories were evolving drastically, also the experiments. The cloud chamber of C. T. R. Wilson [40] was one of the first particle detectors and with it the anti-particle of the electron, the positron, was discovered by Anderson in 1933 [41]. This is one of the negative energy states postulated by Dirac which were reinterpreted as anti-particles by Stückelberg [42] and Feynman [43]. With the experimental evidence this finally led to quantum electrodynamics [44–51], one part of the SM.

Based on the stability of the nuclei a strong force was postulated. In the following years a number of particles were discovered, which could only be ordered by the postulation of the existence of quarks and gluons, which was proposed by Gell-Mann [52]. The existence of quarks was confirmed by deep-inelastic scattering experiments at the linear collider at SLAC [53], which showed that hadrons are constituted of smaller particles. At DESY at the DORIS and PETRA colliders, experimental evidence for gluons was found [54, 55]. Following this, the quarks were discovered at different experiments, leading to further theories concerning their interaction, finally formulating the weak interaction, the last piece of the SM.

In the following section the aforementioned particles and their role in the SM are discussed.

2.2. Particles of the Standard Model

Commonly, the particles taking part in the SM are summarised as can be seen in Figure 2.1.

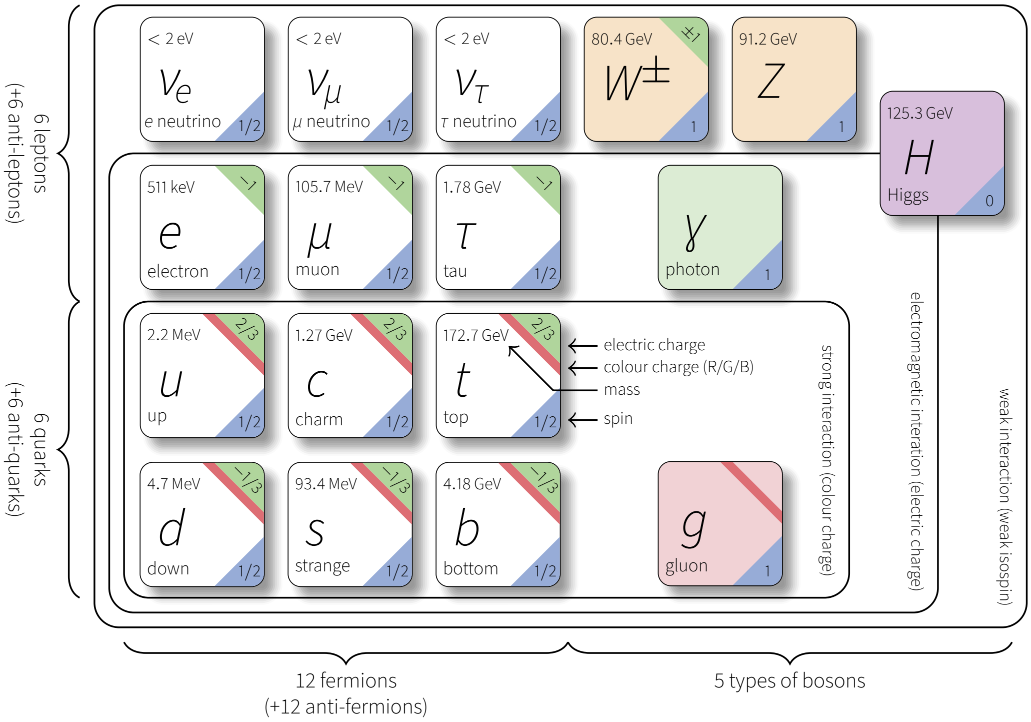

Figure 2.1: The Standard Model relies on the elementary particles: quarks, leptons and bosons. The twelve fermions are shown on the left, grouped into leptons in the two upper rows and quarks in the two lower rows. The gauge bosons and the Higgs boson are represented by the coloured boxes on the right. The quoted mass values are according to Ref. [56].

Both, quarks and leptons, are fermions, spin-$\frac{1}{2}$ particles of which there are twelve in the SM. The leptons include the electron (e), the muon (μ) and the tau (τ) with their respective weak isospin partners, the neutrinos (ν_e, ν_μ and ν_τ). The charged leptons and neutrinos are grouped into three generations consisting of isospin doublets, a quantity which transforms like spin in quantum mechanics. Of the first three leptons the electric charge is $-e$, where e is the elementary charge. The neutrinos are uncharged. Quarks belong either to the up-type quarks: up (u), charm (c) and top quark (t) or the down-type quarks: down (d), strange

(s) and bottom quark (b). Up-type quarks have an electric charge of $+\frac{2}{3}e$ and down-type quarks an electric charge of $-\frac{1}{3}e$. Quarks also have a colour charge and thus carry one of the three colours (red, green or blue). All fermions have an antiparticle of same mass but opposite quantum numbers, such as electric charge or colour.

Depending on their mass, these particles can be ordered into three families, also called generations, where the neutrinos are assumed to be massless but nonetheless unambiguously associated with their respective partner.

Ordinary matter is made up of the first generation particles, which are the lightest and therefore cannot decay. The other generations are heavier, which makes them unstable. Quarks hadronise before decaying, which means that they form hadrons made up of quarks. Due to its huge mass of $(172.69 \pm 0.30)\,\mathrm{GeV/c^2}$ [56], the top quark has a very short lifetime and is thus not able to hadronise before it decays, which means that its quantum numbers are passed on to its decay products and can be observed without dilution from chromodynamic interactions. It is the heaviest elementary particle of the SM and was discovered by the CDF and DØ collaborations at the Tevatron collider at Fermilab in Chicago in 1995 [57, 58].

Three interactions between these fundamental particles are mediated via spin-1 gauge bosons. These interactions are described theoretically by expressing the dynamics via Lorentz invariant Lagrange densities of local quantum fields. The Lagrange densities are called Lagrangians. Gravitation is not yet understood on the scale of elementary particles as its interaction is in practice negligible compared to the strong and electroweak interactions [59].

The quantum field theory describing the Standard Model has a local symmetry:

$$SU(3)_c \times SU(2)_L \times U(1)_Y \, .$$

Quantum Electrodynamics (QED) describes the electromagnetic interactions. It is based on the requirement of local gauge invariance of the Lagrangian under phase transformations. The gauge group is the unitary group $U(1)$, which is Abelian. In order to describe the physics, the fields need to be quantised, representing the particles observed. The photon (γ) is the gauge boson and couples to electric charge, which is hence the coupling quantum number for QED.

Quantum Chromodynamics (QCD), the theory describing the interactions of quarks and gluons, is described by a non-Abelian gauge theory. In the $SU(3)$ non-Abelian gauge theory two kinds of particles are involved, the colour charge carriers (quarks and gluons) and the mediators (gluons). As the eight massless and colour-charged gluons (g) are also charge carriers they undergo self-interactions. These self interactions govern the coupling behaviour of QCD.

The remaining interaction is the weak interaction. The W and Z bosons conduct the weak force and couple to all fermions. There are also triple gauge boson couplings possible, i.e. WWZ. Depending on the charge and the weak isospin of the particle it interacts with, the coupling boson is an electrically charged $W^{\pm}$ or an electrically uncharged Z^0 boson. The bosons have a mass of about 80 and $92\,\mathrm{GeV/c^2}$. The exact group structure of the SM is $SU(2)_L \times U(1)_Y$, with the weak isospin and its third component (T, T_3) and the weak hypercharge (Y) as quantum numbers, respectively. The weak isospin describes left-handed or right-handed coupling behaviour, where right-handed particles have no isospin. For left-handed particles, the spin and the momentum are anti-aligned, while they are aligned for right-handed particles. The weak force is anti-symmetric with respect to chiralities. Hence, as only left-handed states transform as a doublet under $SU(2)$, the subscript L is given. This distinct behaviour of the charged-current weak interaction violates parity maximally. Parity violation exists also in Z boson couplings but is less strong. In order to understand this fact better or to maybe find evidence for BSM physics, precision measurements of the weak interactions are of great interest. As of now, with the so-called electroweak unification the electromagnetic and the weak interaction can be described consistently [12, 15, 16].

The origin of the mass of fermions and bosons can be described with the Brout-Englert-Higgs mechanism [60–63]. In a "spontaneous symmetry breaking" of the electroweak theory the particles and massive gauge bosons are given their mass through coupling to the Higgs field. Distinct is that the Higgs field has a non-zero expectation value. The corresponding quantum or excitation of the Higgs field, the Higgs boson, was discovered by the ATLAS and CMS collaborations in 2012 [8, 9].

One of the greatest achievements of the SM is its predictive power, as can be seen in Figure 2.2 where SM theoretical expectations are compared to cross section measurements by the ATLAS Collaboration, which are corrected for branching fractions. The cross section is a measure for the strength of an interaction to take place. With the differential cross section $\mathrm{d}\sigma/\mathrm{d}\Omega$ the particle and energy dependent scattering rate in the solid angle $\mathrm{d}\Omega$ per unit particle flux is given. By integrating over the full phase space the total cross section is obtained.

2.3. Limitations of the Standard Model

While the SM has large predictive power regarding the particles of the universe and their interactions, there exist insufficiencies which have been discovered in experiments. With BSM theories these deficiencies are tried to be solved.

One prominent example is the predicted vanishing mass of neutrinos in the SM. With a neutrino being massless it is impossible for a neutrino to change flavour, which means that it oscillates into another neutrino. However, with the Homestake experiment the electron neutrino flux from the sun was measured in the 1960s and only a fraction of the expected rate was measured [65]. An oscillation between different flavours could explain this apparent loss of neutrinos. In 1998 the Super-Kamiokande experiment then measured atmospheric neutrinos and detected a deficit of electron neutrinos while observing muon neutrinos [66]. In 2002 the Sudbury neutrino Observatory (SNO) investigated the flux of electron neutrinos and the total flux, which was as expected, and found direct evidence for flavour oscillations [67]. A non-zero neutrino mass was proposed to explain that neutrinos can oscillate between different flavours. To include neutrino masses, the SM can be extended with an additional mixing matrix.

Dark matter is another problem of the SM. With dark matter a stable form of matter is described that does not interact electromagnetically, so that it cannot be observed with astronomical instruments. Searches for dark matter are ongoing, but up to now no particle

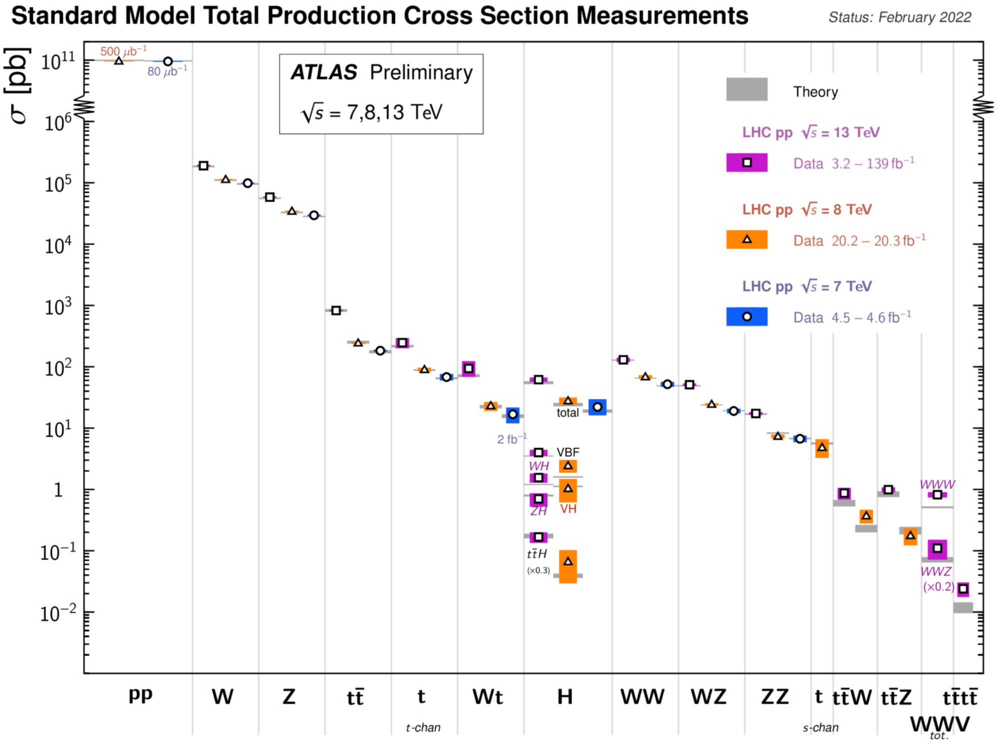

Figure 2.2: Theoretical expectations of Standard Model cross sections compared to ATLAS cross section measurements corrected for branching fractions [64].

candidate was found that could make up for the assumed 26% of dark matter in the universe [68]. The existence of dark matter was demonstrated by observing the rotation speed of galaxies and the collision of the Bullet Cluster, which cannot be explained by the visible matter of the galaxy and therefore are in need of another source of mass [69–71].

Another notion which should be mentioned here is baryogenesis in early stages of the universe [72] which describes the antimatter-matter asymmetry in the universe. A long time assumption was that there exist symmetries of charge (C – exchanging a particle with its anti-particle) and parity (P – inverting particle chirality). Violating the CP-symmetry creates an imbalance of matter to anti-matter. While CP-violation was observed in the SM, it does not occur nearly at the scale needed to explain the asymmetry observed in the universe. Also, there has no CP-violation in the strong interaction been found [73].

Other shortcomings are that the SM does not explain the origin of the mass difference between the different generations and gravitation. Super-symmetry (SUSY) is one possible theory which postulates new particles, the super partners for the SM particles, where fermions are partners for bosons and vice-versa. These are supposed to solve the problem of gravitation and mass and unify all the interactions. As no such particles have been found yet, these particles must be very heavy. A candidate for dark matter would need to be stable, which means that only the lightest of these SUSY particles would be an option.

In order to set new theories under test, with the limit that the current measurements at the LHC have not shown any evidence of the existence of these particles yet, higher energies or more data at higher energies are needed. At higher energies more massive particles can be produced. More data is produced with longer run times or higher luminosity, simultaneously increasing the mass reach, which is why the HL-LHC is being built. See Chapter 3 for a description of the LHC and the ATLAS Detector and Section 3.4.1 for a discussion of the planned upgrades. In Section 3.2.2 the physics interest and possible measurements are discussed.

CHAPTER 3

The Large Hadron Collider and the ATLAS Experiment

3.1. The Accelerator Complex at CERN

Particle colliders have been used over the past decades, in order to find the particles postulated by the Standard Model. The LHC is the world's largest and most powerful particle collider with a circumference of about 27 km, located at CERN in the Geneva area around 100 m underground and spanning under the Franco-Swiss border.

Data taking started in 2010 with a center-of-mass energy of $\sqrt{s} = 7\,\text{TeV}$ and was resumed in 2012 with an increased energy of $\sqrt{s} = 8\,\text{TeV}$. After a first long shutdown for repairs and upgrades, the LHC was restarted in 2015 with 13 TeV and the goal to reach the design instantaneous luminosity of $L = 10^{34}\,\text{cm}^{-2}\,\text{s}^{-1}$ [74].

Inside the LHC two beams circulate in separate beam pipes in opposite directions. About 1200 superconducting dipole magnets with a field strength of 8.33 TeV bend the particle beams in the LHC on a circular trajectory. Nb-Ti alloy superconducting magnets are used which operate at 1.9 K, thus requiring cooling with superfluid helium and making the LHC one of the coldest places on earth. The LHC does not operate with continuous beams but with up to 2808 proton bunches of about 10^{11} protons, colliding them in so-called bunch crossing intervals. In order to focus the beam and bring them into collision with the highest focus at the four collision points, quadrupole magnets are used.

After the first shutdown, the LHC in the so-called Run 2 has operated with a bunch spacing of 25 ns, resulting in collision rates of up to 40 MHz and eventually reaching a peak luminosity twice as high as the design luminosity. The design center-of-mass energy is 14 TeV with a peak luminosity of $2 \times 10^{34}\,\text{cm}^{-2}\,\text{s}^{-1}$. This energy was planned for Run 3 which started in summer 2022 after the second long shutdown [74]. However, the Run 3 energy was decided to be 13.6 TeV due to technical difficulties.

The instantaneous luminosity L is a measure for the rate of collisions and thus related to the event rate $\mathrm{d}N_p/\mathrm{d}t$ and the corresponding cross section σ of any process p

$$\frac{\mathrm{d}N_p}{\mathrm{d}t} = L \cdot \sigma_p \,.$$

It is only dependent on the accelerator parameters and can be expressed as the number of potential collisions per unit area per second [75]:

$$L = \gamma \frac{n_b N^2 f_{\mathrm{rev}}}{4\pi\beta^* \epsilon_{\mathrm{n}}} R \tag{3.1}$$

with the relativistic gamma factor γ, the number of bunches per beam n_b, the revolution frequency f_{rev}, the number of protons per bunch N, the beam beta function at the collision point β^*, which is related to the transverse beam size and has a local minimum at the collision point, the transverse normalised emittance ϵ_{n} and the luminosity geometrical reduction factor R.

The reduction factor is dependent on the beam crossing angle Θ_{c} between colliding beams, the RMS of the longitudinal bunch length σ_z and the RMS of the transverse beam size σ^* as

$$R = \frac{1}{\sqrt{1 + \frac{\Theta_{\mathrm{c}}\sigma_z}{\sigma^*}}} \,.$$

Apart from the proton-proton collisions, heavy-ions can also be used in either ion-ion or ion-proton collisions. The particles are accelerated in several steps, starting with a linear accelerator, where one is exclusively used for the heavy-ions and the other one for protons. Radiofrequency (RF) cavities generate particle bunches. Protons are created by accelerating hydrogen anions which are freed of their electrons by passing a stripping foil. They are inserted into the linear accelerator LINAC4 and reaching energies of 160 MeV [76–78]. After being pre-accelerated in LINAC4, the protons enter the BOOSTER, where they reach 1.4 GeV. Ions are accelerated in the LINAC3 and then enter the Low Energy Ion Ring (LEIR). Both particle types enter the proton synchrotron (PS) [79], first operated in 1959. They are forwarded with 25 GeV to the super proton synchrotron (SPS), first used in 1976 [80], before entering the LHC with 450 GeV. At this stage the proton beam is split in two and injected in the LHC from two different points in opposite directions. The LHC is built in the tunnel which was used by the Large Electron Positron Collier (LEP) [81, 82] from 1989 until 2000.

The beams from the pre-accelerators are also extracted to test beam areas and other experiments. The accelerator complex is shown in Figure 3.1. Before LEP was built, the SPS was used as proton-antiproton collider and called SP$\bar{\mathrm{P}}$S, and delivered the beams for the discovery of the W and Z bosons.

Along the LHC tunnel, the four experiments ALICE (A Large Ion Collider Experiment) [83], LHCb (Large Hadron Collider beauty) [84] and the already mentioned experiments CMS and ATLAS are set up. While ATLAS and CMS are multipurpose detectors and used for a wide range of searches for new physics and for precision measurements at the highest possible energies, ALICE is designed for heavy-ion collisions and studies of the quark-gluon

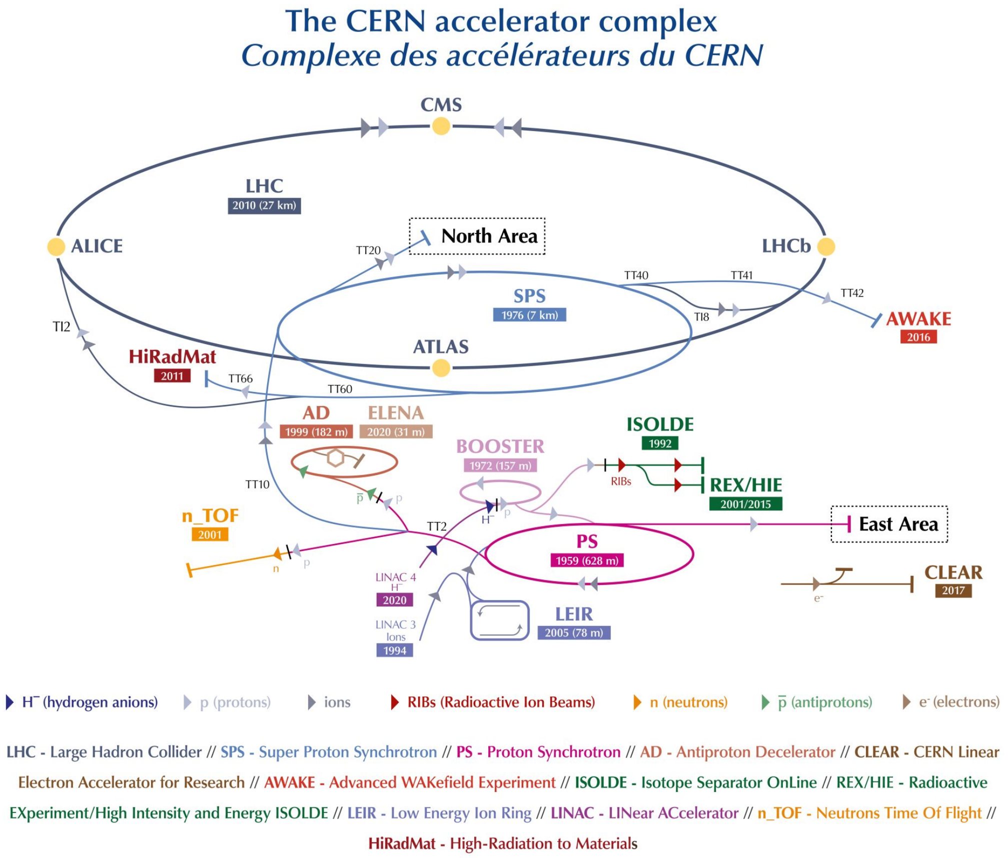

Figure 3.1: CERN accelerator complex with the pre-accelerator stages of the LHC. Proton-proton collisions start in LINAC4, go to the BOOSTER, the PS and the SPS. They are injected into the LHC from two directions and brought to collision at four intersection points. ATLAS Experiment © 2021 CERN modified.

plasma and LHCb for specific measurements on the decay of B-mesons.

The integrated luminosity, a measure for the total number of collisions is defined as

$$\mathcal{L} = \int_{\Delta t} L \mathrm{d}t \,.$$

The number of events can also be written as $N = \sigma\mathcal{L}$ which implies that processes with a small cross section need high luminosities to collect enough data for analysis. About $5.5\,\mathrm{fb}^{-1}$ of data were collected in the first run and about $20\,\mathrm{fb}^{-1}$ integrated luminosity with the higher energy in 2012. In Run 2 a total luminosity of $156\,\mathrm{fb}^{-1}$ was delivered by the LHC, resulting for ATLAS in $139\,\mathrm{fb}^{-1}$ of data considered to be “good for physics” [85], which means that data taken when the detector was not fully functioning are discarded.

3.2. Physics at the LHC

There are many interesting physics measurements to be made at the LHC. All of them are based on the acquisition of trajectories of the collision products. However, as measurements are made in the reference frame of the observers in the laboratory, it must be taken into account that quantities are Lorentz boosted with respect to the beam axis, when performing calculations. This fact leads to a commonly used coordinate system which is introduced in the following.

3.2.1. Coordinate System and Particle Kinematics

For particle collider experiments, the beam axis defines the z-axis. The center of the detectors and thus the theoretical interaction point is the origin of the detector coordinate system. The x-axis points towards the centre of the LHC and the y-axis upwards.

Particles can be described via their 4-momentum $p^{\mu} = (E, \boldsymbol{p}) = (E, p_x, p_y, p_z)$ (energy and three-momentum). Commonly in high energy physics, the transverse momentum in the plane of the detector is used and defined as

$$p_{\mathrm{T}} \equiv \sqrt{p_x^2 + p_y^2}\,. \tag{3.2}$$

For a two particle event the invariant mass M is calculated with

$$M = \sqrt{(p_1^{\mu} + p_2^{\mu})^2} = \sqrt{E^2 - (\boldsymbol{p})^2}\,. \tag{3.3}$$

Instead of the x and y coordinates the azimuthal angle ϕ and the polar angle θ between the three-momentum of the particle and the positive direction of the beam axis can be used to describe the momentum components.

More commonly, the rapidity

$$y = \frac{1}{2} \ln \left(\frac{|\boldsymbol{p}| - p_z}{|\boldsymbol{p}| + p_z} \right)$$

is used instead of θ, where p_z is the longitudinal component of the particle momentum.

When particles collide, often the center-of-mass frame moves down the z-axis, leading to the observers being Lorentz boosted with respect to this frame.

The *difference* between the rapidities of two particles is invariant under Lorentz boosts along the beam axis, the rapidity however is not.

For highly relativistic particles it is hard to measure the rapidity, as the total momentum vector and the energy are needed. Therefore another quantity, the pseudorapidity, is defined by assuming that the mass can be neglected compared to the four momentum. Implementing this in the formula for the rapidity yields the pseudorapidity

$$\eta = -\ln \left[\tan \left(\frac{\theta}{2} \right) \right]\,. \tag{3.4}$$

For exactly vertically emitted particles the pseudorapidity equals zero, while it approaches $\pm\infty$ towards the beam axis. As for highly relativistic particles $y \approx \eta$, η is used in experiments, as it is more suitable from a detector point of view.

The three-momentum of the particle is hence described as:

$$p_x = p_\mathrm{T} \cos\phi, \tag{3.5}$$

$$p_y = p_\mathrm{T} \sin\phi, \tag{3.6}$$

$$p_z = p_\mathrm{T} \sinh\eta. \tag{3.7}$$

The angular separation ΔR of two particles can be specified with the differences in azimuthal angles and pseudorapidites

$$\Delta R = \sqrt{(\Delta\eta_{12})^2 + (\Delta\phi_{12})^2}\,.$$

The angular separation is also invariant under Lorentz boosts along the z-axis.

3.2.2. Physics Goals

At rates of 40 MHz, the proton-proton collisions at the LHC create plenty of particles that pass the detectors. Most of these events result in elastic scattering and are not of interest for particle physics. However, there are also hard-scattering interactions in each bunch crossing, which might contain the Higgs boson or other heavy SM particles such as the top quark and are of interest for precision measurements or when searching for BSM physics.

The majority of the particles created in hard-scattering events has large transverse momenta and decays on short timescales into lighter and more stable particles. Only stable particles can interact with the detectors and create electrical signals as they need to survive the distance from the interaction point up to the first detector layer. Particles which can actually be detected are the elementary particles electrons, muons and photons, but also pions, kaons, protons and neutrons, which are stable or have long enough lifetimes to be detected in the detector volume.

When searching for particles in the data taken in the experiments, the observables introduced in Section 3.2.1 are used. New, also called exotic, particles and heavy particles of the SM cannot be observed directly in the LHC detectors, but they can be reconstructed from their decay products. Once the decay products of a particle are identified, its invariant mass can be calculated. The invariant mass of the particle's decay products shows a resonance in its spectrum around the mass of the particle.

Light quarks from the first two generations and the b-quark hadronise. Pions, kaons, protons and neutrons are hence compounds of colour-charged particles as colour confinement forces them to form hadronic bound states. They produce jets, sprays of colour-neutral compound particles which can be detected, when interacting with the detector material. Bound states with b-quarks can be distinguished by reconstructing the tracks in the detector. They have a characteristic lifetime that is long enough to displace their decay vertex from the primary vertex, i.e., their decay leaves a characteristic signature of a secondary vertex in the inner detector layers. This is for example helpful when searching for Higgs bosons or top quarks, as for both the preferred decay channel involves b-quarks. For the top quark, this can be seen from the Wolfenstein parametrisation of the CKM matrix, where the element

$|V_{tb}| \approx 1$, which means that the top quark almost always decays to a bottom quark and a W boson [86].

The discovery of the Higgs boson was one of the primary goals of the LHC. Cross sections were measured by the CMS and the ATLAS collaborations in different decay channels and production modes, and its decay width was determined from the accessible probed decay channels. From now on the focus will lie on the ATLAS Experiment. Current analyses study the rarer decay modes, but also try to measure the Higgs boson couplings to fermions directly through associated production, e.g. in $t\bar{t}H$ final states. As described in Chapter 2, the Higgs couples to the fermions to give them their mass according to the SM.

With the goal in mind to set the SM under test and detect possible BSM physics, the LHC will be upgraded to deliver more data. With more data, rare processes will have higher statistics and the smaller coupling of the Higgs with the light quarks can be investigated. Should further investigations confirm that the Higgs gives all fermions their mass, this part of the SM would stay as is. If, however, the Higgs does not couple to these, BSM theories of different Higgs particles would become of interest. Apart from Higgs and fermion couplings, Higgs self couplings which affect the Higgs potential and couplings to other vector bosons are also of interest. A more detailed discussion of the Run 2 physics performance and the planned performance can be found in [87, 88].

All these measurements require, however, the particle detection and identification with respect to the current situation in the detectors along the LHC to be improved. First and foremost, the detectors need to be highly granular to be able to tell tracks of high energetic particles with larger transverse momentum apart, which might lie very close to each other. This helps to obtain high efficiencies in b-tagging, a procedure which identifies jets with b-quarks based on their secondary vertex, as mentioned above. Also, the algorithm can be extended to tag c-quarks as well, as secondary vertices are a crucial tool for particle identification. The high granularity also enables background rejection by reconstructing the vertices with high precision.

A detailed discussion of the upgrades to suite the physics requirements is given in Section 3.4.1 and 3.4.2. The current data taking conditions in the ATLAS Detector are explained in the next section.

3.3. The ATLAS Detector

Around the nominal collision point, the ATLAS Detector [10, 89] is set up in order to explore the high-energy and high-luminosity regime of the LHC. It is by volume the largest of the LHC experiments. The expected physics performance of ATLAS is stated in [90] and highlights the discovery potential for new physics regarding especially the Higgs sector or SUSY particles and precision measurements of heavy quarks and gauge bosons.

The ATLAS Detector has a total length of 44 m, a height and width of 25 m and weighs approximately 7000 t, which is about as much as the Eiffel Tower. Particles can be measured and identified via their interactions with matter, which differs for different particle types, as described in Section 4.1. The structure of the detector is hence chosen to be onion-like with multiple layers of different detectors and magnetic systems. It features three main detector

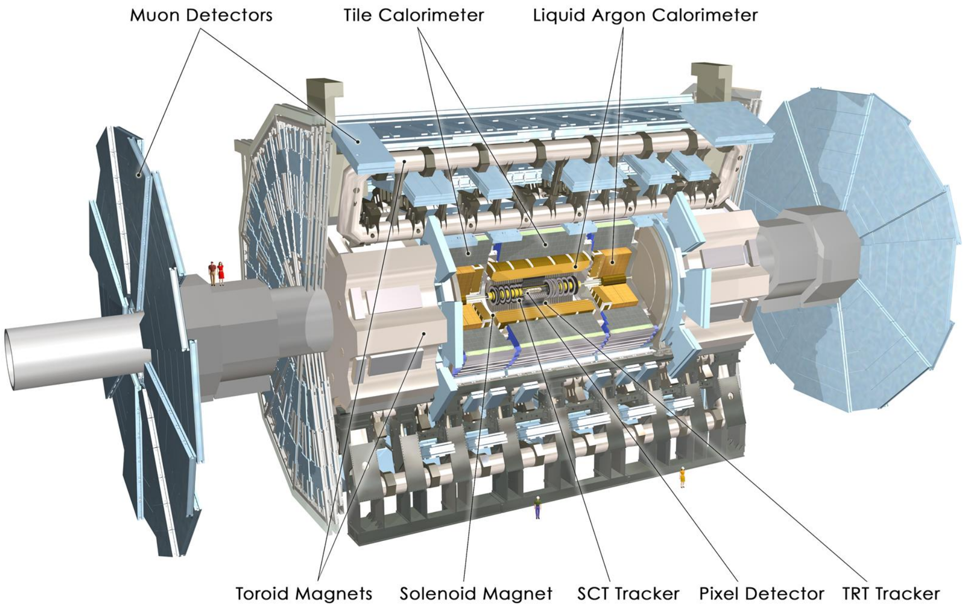

Figure 3.2: Schematics of the ATLAS Detector with humans shown for scale. ATLAS Experiment © 2021 CERN.

systems: the Inner Detector (ID) to obtain tracking information, the calorimeters for energy measurement and the muon system for muon tracking, as shown in Figure 3.2. All detector components aim for a large acceptance in pseudorapidity with almost full azimuthal angle coverage. Electrical signals returned from the recorded collisions in these detector systems are processed to reconstruct the physics objects passing the detector.

3.3.1. Tracking System

The purpose of the ID closest to the interaction point is efficient tracking and vertex detection for lepton-momentum measurements. It is 7 m long and 2.3 m wide and consists of three sub-systems, the semiconductor PIXEL Detector, the Semiconductor Tracker (SCT), which has several layers of silicon microstrip detectors and around these the Transition Radiation Tracker (TRT), a gaseous detector, for pattern recognition, momentum and vertex measurements. Figure 3.3 shows the layout of the ID.

The ID [91, 92] is enclosed in a longitudinal magnetic field of 2 T, provided by a superconducting solenoid [93], which bends the charged particles' trajectories and allows the determination of the sign of the electric charge of the particles. Apart from that, the transverse momentum of the particle is obtained from the radius of curvature r and the magnetic field strength $B(\mathrm{T})$ to be

$$p_{\mathrm{T}}(\mathrm{GeV}) = 0.3B(\mathrm{T})r(\mathrm{m})\,.$$

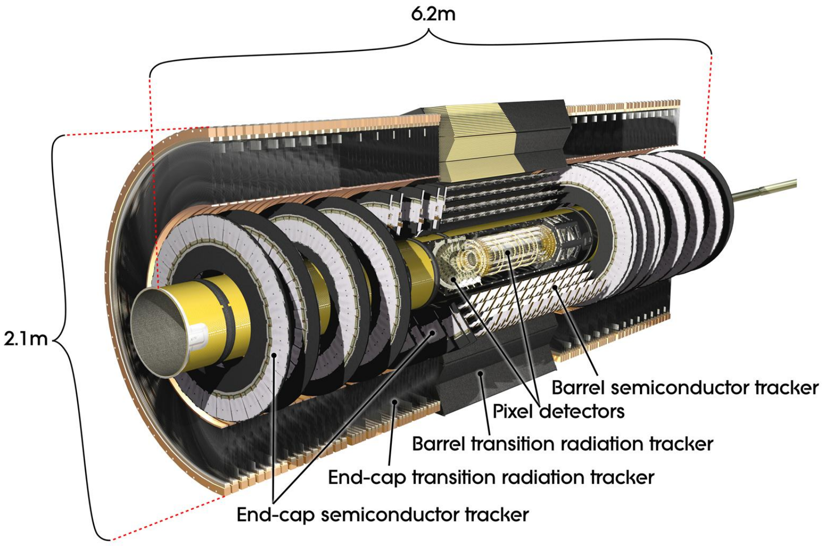

Figure 3.3: Schematics of the Inner Detector. ATLAS Experiment © 2021 CERN.

The resolution of the momentum is

$$\frac{\sigma_{p_\mathrm{T}}}{p_\mathrm{T}} \propto p_\mathrm{T}$$

and thus decreases with increasing transverse momentum p_T due to the smaller curvature of the trajectories [94].

Pixel Detector

The PIXEL Detector [95] was built in two stages. There were three layers of pixel modules in two different structures during Run 1. There are barrel shaped layers in the central section and three end-cap disks in the forward direction. The modules are hybrid pixel modules, which means that planar silicon sensors with 47232 pixels are bump bonded to sixteen readout chips with 2880 pixels each. The distances between the pixels, the pixel pitch of the sensor, is $(400 \times 50)\,\mu\mathrm{m}^2$ and the sensor thickness is $(256 \pm 3)\,\mu\mathrm{m}$ to offer high granularity for tracking and small material budget closest to the interaction point. n^+-in-n doped silicon is used as active detector material and FE-I3 readout chips, where FE stands for front-end. The p-n junction is on the backside of the sensor. This design is chosen to allow full depletion of the sensor even after type inversion of the n-bulk due to radiation damage. See Section 4.2 and 5.1.1 for details on concepts of silicon sensors and planar sensor technologies. A cooling system is used to minimise radiation damage effects on the detection capability, such as higher leakage current. For routing of the signals and powering the module, a Module Controller Chip (MCC) and a flexible printed circuit board (PCB) are used.

Figure 3.4 shows the three pixel layers in the middle of the ID and the three end-cap discs on both sides. The coverage of this detector is up to pseudorapidities of $|\eta| = 2.5$ in forward direction and the total active area is about $1.7\,\mathrm{m}^2$. With three hits in the pixel

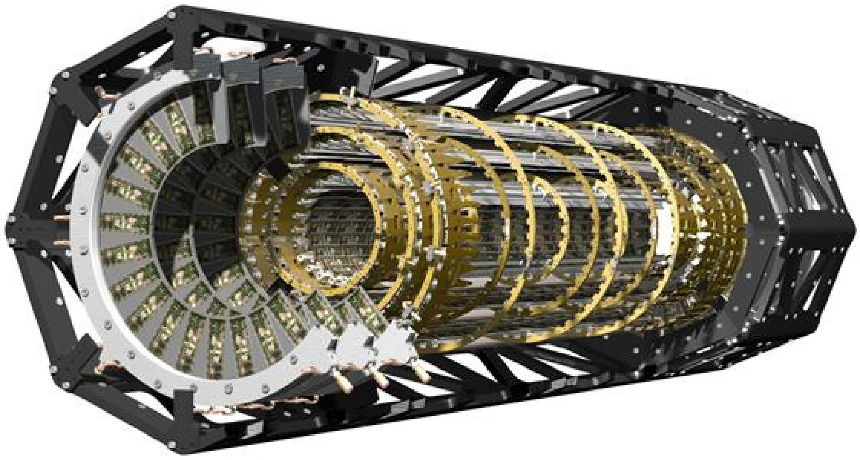

Figure 3.4: Schematics of the PIXEL Detector. Modules on the barrel staves and the end-cap discs are depicted. ATLAS Experiment © 2021 CERN.

layers the transverse momentum can be calculated.

In order to improve the tracking performance a new layer was inserted, the insertable B-Layer (IBL) [96]. It was added during the first long shutdown and the radius of the beam pipe had to be reduced to fit the further layer of pixel modules. Improvement of the tracking is achieved by this fourth additional measurement point and by compensating for modules, especially in the innermost layers, which are damaged by radiation or failing. Additionally the unexpectedly high particle rate of the overperforming LHC is putting pressure on the bandwidth of the PIXEL Detector. Given that the amount of radiation in each pseudorapidity-region is roughly the same but in the forward region the physical area is much smaller than in the barrel region, the forward detectors experience very high rates. The IBL reduced the bandwidth limitations by adding further channels due to its higher granularity.

Compared to the modules of the first three layers, new technologies are tried in the IBL. The readout chip is of a later generation called FE-I4 and has a smaller pixel pitch of $(250 \times 50)\,\mu\mathrm{m}^2$ and higher hit rate capability and radiation hardness [97]. In order to maximise the active sensor area, slim edge sensor technologies have been used, which reduce the inactive sensor edge from 1100 µm to 200 µm. The thickness of the sensors is also reduced to 200 µm for planar sensors with the same type as used in the other layers and to 230 µm for radiation harder sensors in 3D technology. Planar sensors are combined to dual chip modules with two readout chips and 3D sensors are used for 1-chip modules. See Section 5.1.2 for an explanation on 3D sensor technologies. These improvements are necessary due to the position closer to the interaction point and consequently higher radiation levels and space constraints. The radii for all four layers of the PIXEL Detector are 3.32 cm, 5.02 cm, 8.85 cm and 12.25 cm.

SCT and TRT

The SCT is built around the PIXEL Detector and has four layers of strip modules in the barrel region and nine end-cap disks on each side. A strip module is made up of two layers of active sensor area, thus providing eight hits per track. The strips of one module are rotated against each other in ϕ to improve the position resolution [91].

The gaseous TRT is made of approximately 372000 drift tubes, also called straws, with 4 mm diameter filled with 70% Xe, 27% CO_2 and 3% O_2 [10]. The readout is done via the electrode wire in the middle of the tube. In the barrel part, the tubes are placed in parallel to the beam pipe, while they are radially arranged in the end-caps. Transition radiation is produced by passing electrons at polypropylene fibres (barrel) or foils (end-cap) between the drift tubes and absorbed in the gas mixture. The hits due to this so-called transition radiation can be distinguished from normal tracking hits, making electron identification possible.

At least 36 measurement points are added by the up to 73 layers of straws in the barrel region of the TRT for a particle trajectory. An exception is the barrel-end-cap transition region, where at least 22 straws are crossed. For electrons with at least 2 GeV energy 7-10 transition radiation hits are expected.

3.3.2. Calorimeter System

The calorimeters measure the energy of the particles via absorption and support the tracking for high-p_{T} particles which have close to straight trajectories in the ID. Particle showers are created by the particles in the detector material and they gradually lose all their energy. Two different types of calorimeters are located outside of the solenoid, which allow accurate electron, photon, jet and missing transverse energy measurements [10, 98]. Figure 3.5 depicts the layout of the calorimeter system.

The innermost calorimeter is the so-called electromagnetic calorimeter (ECAL), which absorbs and measures the energy of electrons and photons with high granularity and is used as input for the trigger system [99]. Together with the ID, electron and photon identification is possible. It is a sampling calorimeter with materials to induce electromagnetic scattering, layers of lead absorber plates and liquid argon (LAr) as active material for detection. Both materials are stacked and shaped like an accordion and amount to a thickness of more than twenty radiation lengths. Ionisation of the lead atoms leads to electrons that trigger electrical signals in LAr. As the ID, the calorimeter is divided in barrel and end-cap calorimeter. An additional thin presampler corrects for energy loss upstream the calorimeter, covering the region $|\eta| < 1.8$. The pseudorapidity coverage for the full ECAL goes in forward direction up to $|\eta| < 3.2$.

The hadronic calorimeter (HCAL) is located around the electromagnetic calorimeter and mainly measures the energy of the hadrons. Ideally dense material maximises hard scattering so that all particles are stopped in the hadronic calorimeter except for the muons, thus limiting punch-through into the muon system to a minimum. It has three different parts, which provide good containment with a thickness of approximately ten interaction lengths.

The Tile Calorimeter [100] in the barrel region is a sampling calorimeter. It comprises

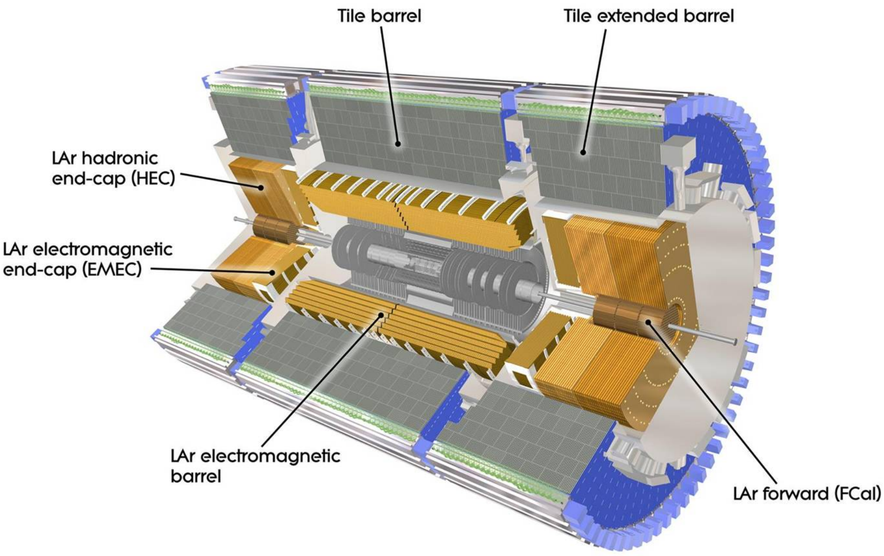

Figure 3.5: Schematics of the ATLAS calorimeters. ATLAS Experiment © 2021 CERN.

steel absorbers and scintillators whose light is collected with wavelength shifting fibres and recorded by photomultipliers. The scintillators give fast time information with moderate space information and the Tile Calorimeter is hence also used as trigger detector. The coverage is up to $|\eta| < 1.7$. There is also the Hadronic-Endcap-Calorimeter (HEC) with LAr and copper plates and a coverage of $1.5 < |\eta| < 3.2$ and the high density Forward Calorimeter (FCal) with LAr and copper and tungsten absorbers to optimise for electromagnetic and hadronic interactions, respectively, in the forward region covering $3.0 < |\eta| < 4.9$ [99].

3.3.3. Muon System

Around the calorimeters, the muon spectrometer [101] makes up for most of the volume of the detector to perform high-precision muon momentum measurements. With muons being minimum ionizing particles, they are not stopped in the calorimeter and need a large detector to get tracking information. The muon system consists of four different gas detectors, which give time and spatial information. Their working principle is very similar to silicon detectors with an ionising gas instead of doped semiconductors for signal creation. All muon detectors are enclosed in toroidal magnetic fields [102] created by eight large air-core toroidal magnets in the barrel region [103] and end-cap toroidal magnets in a cryogenic system on both sides [104]. The field strength is not constant, but at the order of 4 T. See Figure 3.6 for the schematics of the ATLAS muon system and the toroids.

Monitored Drift Tubes (MDTs) (and formerly also Cathode Strip Chambers (CSCs)) provide high-precision tracking information up to $|\eta| < 2.7$. The counting rate of the MDTs is only $250\,\mathrm{Hz\,cm^{-2}}$. With a higher counting rate of $1000\,\mathrm{Hz\,cm^{-2}}$ the CSCs were used in the inner layers up to the end of Run 2. The CSCs in the so-called Small Wheels, parts of the forward muon tracking system, have been replaced completely with the New Small Wheels [105] in the second long shutdown. Two technologies are used, small-strip Thin Gap

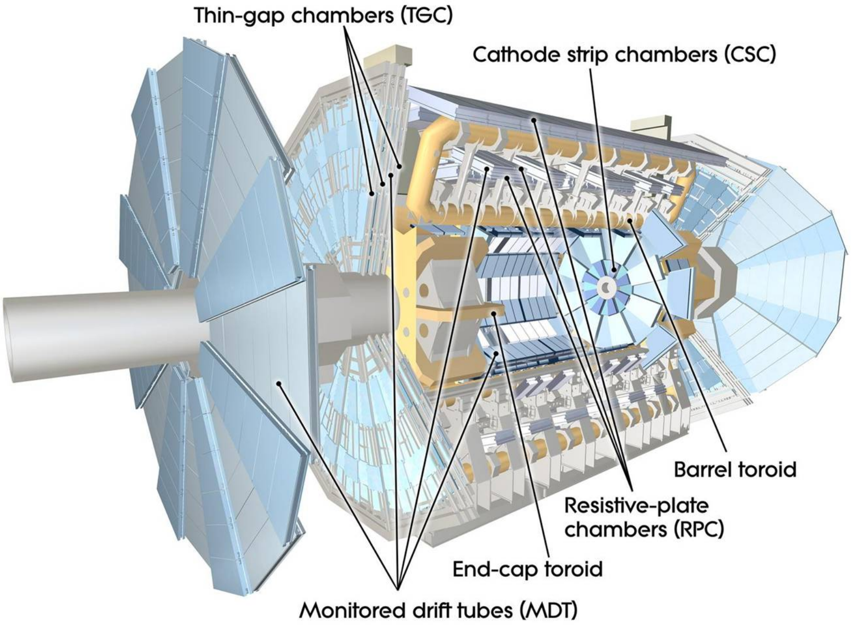

Figure 3.6: Schematics of the ATLAS muon detectors and the toroid magnets. ATLAS Experiment © 2021 CERN.

Chambers (sTGC) and Micromegas detectors (MM).

Two other types of detectors, Resistive Plate Chambers (RPCs) and Thin Gap Chambers (TGCs) with fast signal creation are used for fast trigger signals in the event selection. RPCs are used in the barrel region and TGCs in the end-caps, covering a pseudorapidity range up to $|\eta| < 2.4$.

3.3.4. Trigger and Data Acquisition System

This so-called TDAQ system is needed for event data acquisition from the separate detector systems. Triggers at different stages are needed that select events with interesting physics processes and reduce the rate of recorded events from the collision rate of 40 MHz to several hundred events per second, a rate at which data can be saved in permanent storage [10, 106]. Apart from the decision if an event should be stored or not, the dead time of the components also needs to be minimised by the trigger.

Two trigger levels reduce the event rate: L1 and HLT. The low-level trigger L1 is based on the aforementioned trigger detectors in the muon system and the calorimeter. Trigger criteria are for example high-p_{T} muons, electrons, photons, jets and large missing and total transverse energy, which can indicate interesting physics processes with e.g. Higgs bosons or top quarks. The rate is reduced to approximately 100 kHz and a Region of Interest (RoI) is defined in the pseudorapidity-azimuth $(\eta - \phi)$ plane with candidate events that have the aforementioned features. The RoI is $\approx 2\%$ of the total event data. In terms of data storage, the L1 accepted event is stored in a buffer system.

The high-level trigger HLT is software based and reduces the trigger rate to about 1 kHz by evaluating the detector data inside the RoI. For this purpose the full event data from all sub-detectors is taken and a trigger decision is made based on software decisions. Only after passing the HLT the events are stored permanently.

3.4. The LHC and ATLAS High Luminosity Upgrades

In order to increase the physics reach and tackle the open questions, both, the LHC and the ATLAS Detector undergo upgrades. The upgrades are performed in different steps and parts of the upgrades have already taken place in the past years during the periods of shutdown. The LHC operation can be divided in three different periods. There is the yearly shutdown from December till March where small issues can be solved, then a daily fill status of the machine, with approximately 20 h of beam and then every few years long shutdowns which make upgrades of the machine and the detectors possible.

In the first long shutdown, the energy as well as the luminosity of the LHC have been ramped up from 8 to 13 TeV and to the design luminosity of $1 \times 10^{34}\,\mathrm{cm}^{-2}\,\mathrm{s}^{-1}$, respectively. Accordingly, the ID was upgraded to withstand the new run conditions, as shown in Section 3.3.1.

The second long shutdown from December 2018 onwards ended in early 2022, initiating Run 3 with higher energy of 13.6 TeV. Several accelerator upgrades, including the replacement of the former proton linear accelerator LINAC2 with LINAC4, result in a twice as high beam brightness and intensity [76–78]. The brightness of a beam describes the phase space density of the protons in the beam and the intensity the number of protons or ions per bunch. During the current Run 3 the LHC is operated at twice the design luminosity.

Concerning ATLAS, the Small Wheels, parts of the forward muon tracking system, have been replaced with the New Small Wheels [105] as mentioned before. With higher luminosity improved tracking and trigger performance is needed to suppress background. The LAr calorimeter [107] and parts of the Tile Calorimeter were also upgraded to improve the L1 trigger, hence requiring an update of the trigger system [108].

3.4.1. The High Luminosity-LHC

With the High Luminosity-LHC a new era of particle physics is starting. The targets as specified in [75] are a peak luminosity of $5 \times 10^{34}\,\mathrm{cm}^{-2}\,\mathrm{s}^{-1}$, which is five times more than the original design luminosity and an integrated luminosity of $250\,\mathrm{fb}^{-1}$ per year, which adds up to a total of $3000\,\mathrm{fb}^{-1}$ over the runtime of the HL-LHC. However, by pushing the machine, a peak luminosity of $7.5 \times 10^{34}\,\mathrm{cm}^{-2}\,\mathrm{s}^{-1}$ and a total of $4000\,\mathrm{fb}^{-1}$ seem feasible.

The intensity and the brightness of the beam can only be controlled at the creation of the beam, as the phase space distribution function is conserved according to Liouville's theorem [109] and hence the protons in a bunch cannot change their density in phase space.

The luminosity is increased by means of the beam parameters in Eq. 3.1. Especially the number of protons per bunch N will be increased while keeping the transverse normalised emittance ϵ_n small [75]. By reducing the beam focus spot with stronger quadrupole magnets at the interaction point, the beam beta function β^* is also reduced. This requires, however, larger beam angles. Crab cavities which tilt the particle bunches at the interaction point make larger beam angles possible while keeping the two bunches geometrically

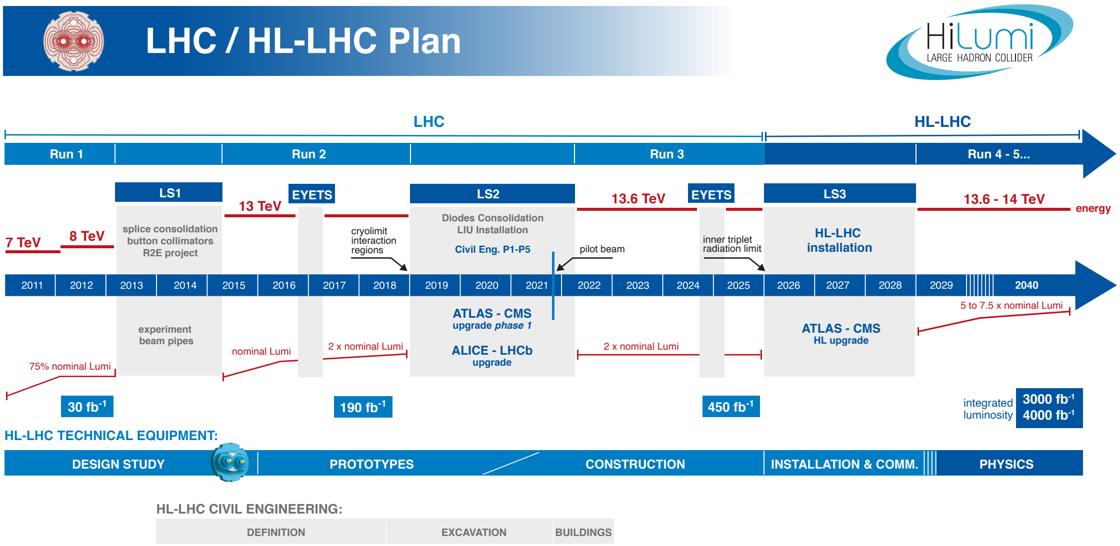

Figure 3.7: Schedule of the LHC and detector upgrades [111].

overlapping [75].

More interactions per bunch crossing and thus a much higher instantaneous luminosity of $5 - 7.5 \times 10^{34}\,\mathrm{cm}^{-2}\,\mathrm{s}^{-1}$ will deliver much more data but also create more challenging situations in the detectors. Especially pile-up, which describes the number of interactions per bunch crossing in the detector, will increase from $\langle\mu\rangle \approx 34$ in Run 2 to $\langle\mu\rangle \approx 200$.

By providing a lower instantaneous luminosity than the maximum at the start of a run, the pile-up can be reduced. As the interaction rate naturally decreases over time due to the interactions of the particles, a change of the beam parameters during the run can keep the instantaneous luminosity stable, resulting in the LHC delivering data at a controlled rate for a longer period of time. This is called luminosity levelling [110]. The integrated luminosity planned for the whole operation time of the HL-LHC is $4000\,\mathrm{fb}^{-1}$.

However, in order to be able to reconstruct events with high precision tracking performance and eliminate the background in the detector with a high track density and occupancy, fast, highly granular and radiation hard detectors are needed. The roadmap for the HL-LHC foresees the machine and detector upgrades to take place during long shutdown III [87], which is as of now foreseen from 2026 until the end of 2028 [111].

In order to withstand the new running conditions, the experiments have to undergo several upgrades. The main upgrades for the ATLAS Detector are the trigger and the ID upgrades as the ID will have reached its end of lifetime after Run 3. It will be exchanged with the highly radiation tolerant Inner Tracking Detector (ITk), an all-silicon detector with strip and pixel modules. The trigger architecture will also be renewed, profiting from the upgraded detector systems. In Figure 3.7, the schedule for the upgrades of the LHC and the detectors is shown.

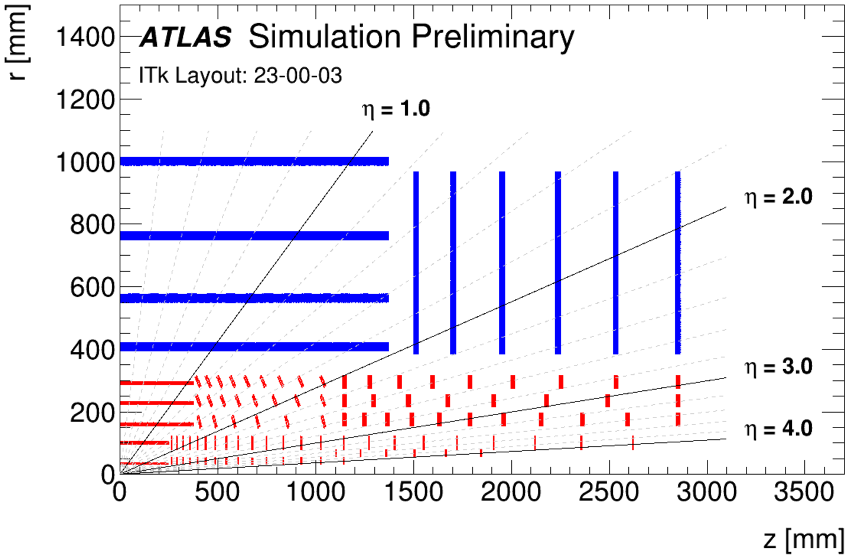

Figure 3.8: Schematics of the ITk layout for one quadrant, showing only the active detector elements, where the strip modules are depicted in blue and the pixel detector modules in red. The z-axis is oriented along the beam line, the origin of the coordinate system is the nominal interaction point and the r-axis is the radius measured from the interaction point [114].

3.4.2. The Inner Tracking Detector as part of the ATLAS Upgrade

As the radiation is the highest close to the interaction point, the innermost layers of the pixel detectors used in the large experiments to find the vertices and the trajectories of the particles need to be the radiation hardest and fastest. Hence, new pixel sensor technologies are needed to withstand these harsh environments and provide physics results.

The schematics of the ITk are shown in Figure 3.8. One quadrant and only active detector elements are shown. The layout differs compared to the original one as planned in the ATLAS ITk TDRs for the PIXEL Detector [112] and the strip detector [113].

The Strip Detector will have four layers of barrel modules and six end-cap petal-design disks on each side. With the PIXEL Detector being the subject of this thesis, the focus will be on this part of the ITk.

The ITk Pixel Detector

The PIXEL Detector will be separated from the Strip Detector by a Pixel Support Tube (PST) and consists of five layers of pixel modules and a forward region with different sensor technologies. Due to the high radiation in the innermost layers, the inner two layers are replaceable and housed in the Inner Support Tube (IST) for easier access. About 10000 modules will be implemented in the barrel layers and end-cap rings on each side to assure a coverage up to $|\eta| < 4$ [112].

The 1 MeV neutron equivalent fluences normalised to the integrated luminosity of 4000 fb^{-1} until the end of lifetime for an inelastic proton-proton cross section of 79.3 mb and a centre-

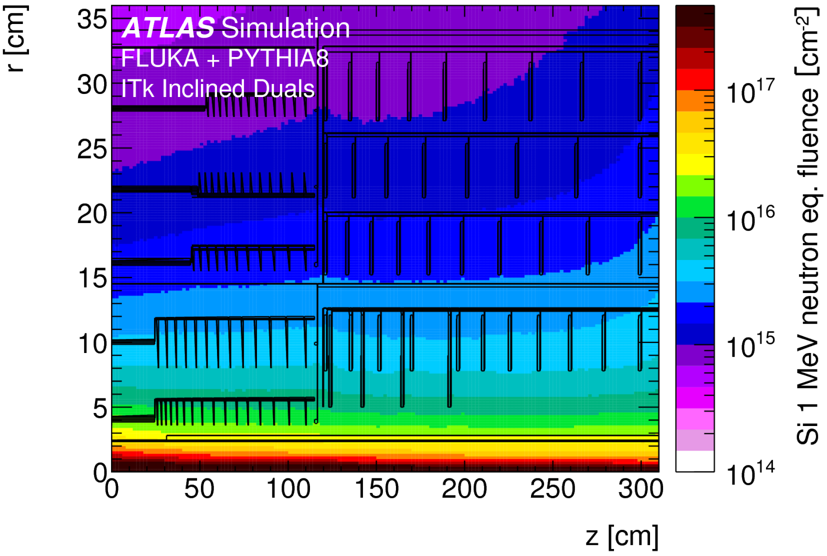

Figure 3.9: Simulated 1 MeV neutron equivalent fluence in the PIXEL Detector [112].

of-mass energy $\sqrt{s} = 14\,\text{TeV}$ are calculated with PYTHIA 8 [115] and FLUKA [116] and shown in Figure 3.9. The unit of the fluence is commonly written as $\mathrm{n_{eq}/cm^2}$. Compared to the ID the ATLAS ITk, with fluences of up to $1.3 \times 10^{16}\,\mathrm{n_{eq}/cm^2}$ [112], will receive radiation levels of roughly an order of magnitude more over its lifetime.

As stated above, the ITk needs to be fast, highly granular and radiation hard. With smaller pixel pitches of $(50 \times 50)\,\mu\text{m}^2$ or $(25 \times 100)\,\mu\text{m}^2$ compared to the ID $((400 \times 50)\,\mu\text{m}^2)$ the granularity is enlarged. This is needed to reduce pile-up and resolve tracks in boosted jets with narrow tracks and is from simulations expected to have 0.16 % channel occupancy at most in the innermost layer [112]. However, with more pixels, more channels need to be read out. As parallel powering is not feasible, the readout chips are powered in so-called serial power chains [117–119]. This saves space but also limits multiple scattering, see also Section 4.1.

For the readout new front-end pixel chips are jointly developed with CMS to accommodate for smaller pixels and higher bandwidth compared to the FE-I4 [120]. The joint development is known as RD53 collaboration and has produced the RD53A prototype readout chip for the ATLAS Experiment which has undergone some further development, known as RD53B or ITkPixV1. For extensive tests the RD53A prototype chip with $(50 \times 50)\,\mu\text{m}^2$ pitch and $\approx (1 \times 2)\,\text{cm}^2$ area is used [121]. Chapters 6, 7 and 9 present the results obtained within the scope of this thesis. The final chip ITkPix has an area of $\approx (2 \times 2)\,\text{cm}^2$ and four FEs are thus able to read out the full sensor with an area of $\approx (4 \times 4)\,\text{cm}^2$ and 307200 pixels. An improvement of the RD53A chip is its nominal bandwidth of 1.28 Gbit/s on up to four data outputs [121] compared to the rate capability of the FE-I4 chip of 160 Mbit/s [97].

Apart from that, it has a higher radiation tolerance of at least 500 Mrad = 5 MGy [112], where the requirement for the FE-I4 used in the IBL was 3.5 MGy.

The radiation also affects the sensors. Two different sensor types are used with 100 – 150 µm sensor thickness [112]. The 3D sensors with 15 µm thickness cover only layer 0. Pla-

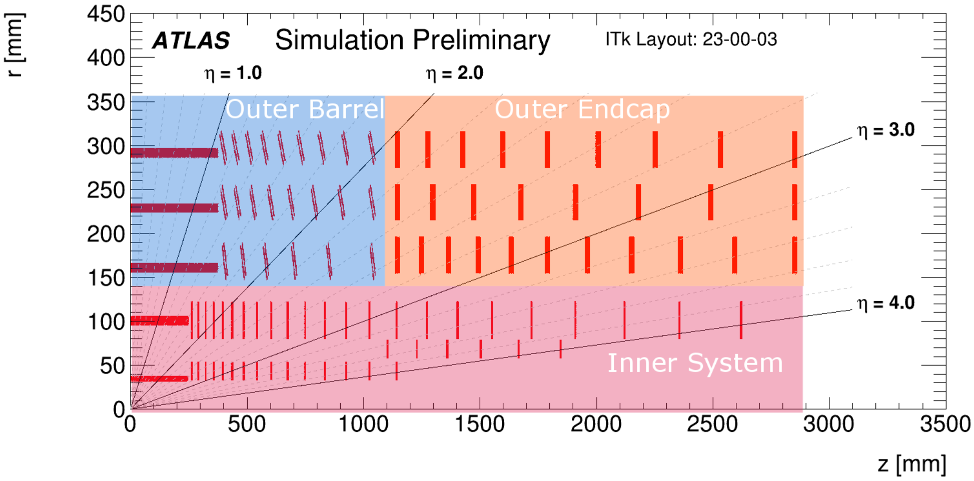

Figure 3.10: Different PIXEL Detector regions in the ITk, modified from [114].

nar sensors with 100 µm thickness are featured in layer 1. These two layers will be replaced after an integrated luminosity of 2000 fb^{-1}. The received fluence of $13 \times 10^{15}\,\mathrm{n_{eq}/cm^2}$ is so large that these sensors already reach their end of lifetime. In the outer layers, planar sensors with 150 µm thickness are used and no replacement is planned. Further details about these sensors can be found in Section 5.1. The PIXEL Detector is cooled with CO_2 to −10 °C at the module to minimise radiation effects. Also, the sensors are n-in-p sensors, i.e. different doping compared to the currently used n^+-in-n sensors in the ID. A p-bulk has the advantage that no type inversion takes place with radiation damage and it is a single sided process, which simplifies the product flow [112]. Section 4.2.3 discusses this in further detail.

In total, an area of 13 m^2 will be covered with pixel modules, where modules with one large sensor and four connected readout chips, so-called quad modules, and triplet modules with three sensors and three connected readout chips with similar sizes are used [114].

Demonstrator Projects

The PIXEL Detector consists of three different parts, the inner system, the outer barrel and the end-caps, as shown in Figure 3.10. In order to practise the production flow and set these sub systems under test, the so-called demonstrators are built for every system. Amongst other system aspects especially the serial powering functionality is validated.

The focus of this work are the outer barrel (OB) demonstrators. A first version with FE-I4 modules was used until mid-2021 for basic studies on a loaded stave [122]. The successful loading of a stave with modules, the first time powering of several module chains with common ground in serial powering mode, read out of many modules, cooling with CO_2 and steering with a Detector Control System (DCS) were the main achievements. The follow-up demonstrator with RD53A modules is still under test and closer to the final ITk design, with lessons learnt from the FE-I4 demonstrator already implemented.

Studies on the FE-I4 demonstrator have also been shown in the doctoral theses [5, 123] and in the not yet published thesis [124]. Final results from the FE-I4 demonstrator will be published in the near future. Several aspects are summarised in Section 8.3. In Section 8.4 first milestones of the RD53A demonstrator are presented.

CHAPTER 4

Semiconductor Pixel Detectors

The ATLAS inner tracker will be a semiconductor pixel detector with silicon as sensing material. Silicon is the current state of the art due to its high availability and excellent performance regarding spatial resolution, as discussed in Section 4.2.

A multi-purpose high energy physics detector is designed such that it is capable of measuring the particles that traverse it. Hence, in Section 4.1 the types of interactions of different particles with matter are discussed. Section 4.2 introduces the silicon pixel detector as an application of the interaction principles introduced before. As the interaction with matter is not necessarily non-destructive, the possible radiation damages are discussed in Section 4.2.3. For the ATLAS tracking detector, the pixel detector type of interest is the hybrid pixel detector, which is introduced in Section 5.

4.1. Interaction of Particles with Matter

The interaction processes differ for different particle types with different energies and depend on the detector material. Certain particles that can create a signal in semiconductors are discussed in the following: Light charged particles, such as electrons and positrons, photons, and heavy charged particles which include muons, protons and α-particles.

For charged particles electromagnetic interactions are dominant. Depending on the mass of the particle, they scatter with the electrons or the nucleus of the atoms in the matter via the Coulomb potential. The atoms on their turn get excited or ionised and the particle loses energy and gets deflected.

4.1.1. Heavy Charged Particles

While crossing matter, heavy charged particles, such as muons, protons or α-particles, mainly lose energy through interactions with the outer electrons of the atom, thereby ionising the atom. The electrons of the atom are considered free, as the energy and mass of the particle are much higher than the binding energy of the electron.

The Bethe-Bloch-Equation [125, 126] describes the average energy loss through ionisation per path length. This is also called the stopping power when normalised to the density. The formula as written in [56] with additional shell correction term is

$$-\left\langle \frac{\mathrm{d}E}{\mathrm{d}x} \right\rangle = 4\pi N_{\mathrm{A}} r_e^2 m_e c^2 \frac{Zz^2}{A\beta^2} \left[\frac{1}{2} \ln \left(\frac{2m_e c^2 \beta^2 \gamma^2 T_{\mathrm{max}}}{I^2} \right) - \beta^2 - \frac{\delta(\beta\gamma)}{2} - \frac{C}{Z} \right] , \qquad (4.1)$$

with $\beta = \frac{v}{c}$, the velocity v and the speed of light c, the charge z of the incident particle in electrons, the Avogadro number N_{A}, the atomic number Z of the absorbing material, A the atomic mass of absorbing material, m_e as electron mass, the classical electron radius r_e, C the shell correction and I, the mean excitation potential of the atoms. I is obtained with empirical formulas, dependent on the atomic number of the absorbing material Z:

$$I = 12Z + 7\,\mathrm{eV} \qquad Z < 13\,, \qquad (4.2)$$

$$I = 9.67Z + 58.8Z^{-0.19}\mathrm{eV} \qquad Z \geq 13\,. \qquad (4.3)$$

To correct for the polarisation of the atoms along the path, the density correction $\delta(\beta\gamma)$ is introduced. Electrons far away are shielded from the field of the particle due to the polarisation and interact less. The polarisation is proportional to the density of the material. Another addition to the original formula is the shell correction for the low energy regime where electron and particle have similar velocities and the electron cannot be approximated as free any more.

In a range from $0.1 \leq \beta\gamma \leq 1000$ the energy loss can be described with Eq. 4.1, while for higher $\beta\gamma$ radiative losses dominate. β^2 is dominant for low particle energies. In this region for different particles the slope is shifted for different masses. The energy loss reaches a minimum for $\beta\gamma \approx 3.5$ with $-\left\langle \frac{\mathrm{d}E}{\mathrm{d}x}_{\mathrm{MIP}} \right\rangle = 1.5\,\mathrm{MeV\,g^{-1}\,cm^{-2}}$. For most materials these minimum ionising particles (MIP) are used as estimation for the smallest signal of a charged particle in a detector. The loss increases steadily with higher momentum due to relativistic effects and reaches a plateau. The different regimes are shown in Figure 4.1 for muons in copper.

Applied to the ATLAS detector, muons of typical energies are for example minimum ionising and therefore show the MIP-like deposit in the calorimeter. In general, as soon as a particle is no longer minimal ionising, it will lose energy drastically and finally be stopped in the material within a short distance. This principle is used in calorimeters. Most of the energy is deposited near the stopping point, which can be described by the Bragg-curve.

For thick detector layers the energy loss, which is a statistical process, can be described by a Gaussian distribution where the mean is given by Eq. (4.1).

Thinner detectors, such as the tracking system, do not completely stop a particle. The probability distribution of the energy loss is described by the Landau distribution [127–129] which has a long tail towards high energy loss. The asymmetry originates from the different rates of high and small energy transfer collisions. Because of the asymmetry, the mean energy loss is higher than the most probable energy loss.

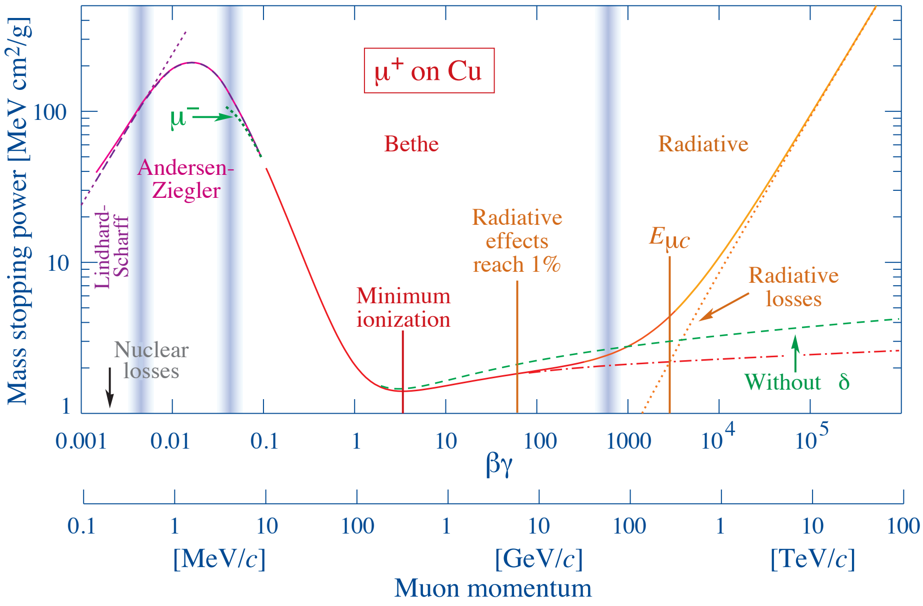

Figure 4.1: Mass stopping power for muons in copper. Radiative losses dominate for higher energy [56].

4.1.2. Electrons

Due to the much smaller mass of electrons and positrons and the fact that incident particle and the shell electron are quantum mechanically indistinguishable, Eq. (4.1) describing the ionisation is only valid with modifications and only in the low energy regime. The main contribution, however, is bremsstrahlung, electromagnetic radiation that is emitted when an electron is scattered, as long as it is above the critical energy

$$E_\mathrm{c} \approx \frac{800}{Z}\,\mathrm{MeV}\,.$$

The energy loss is

$$-\left\langle \frac{\mathrm{d}E}{\mathrm{d}x} \right\rangle = \frac{E}{X_0}\,,$$

where the material dependent radiation length X_0 can be defined, which is the mean distance after which the energy is reduced by a factor of $\frac{1}{e}$ due to bremsstrahlung:

$$X_0 \approx \frac{1}{4\alpha n Z^2 r_e^2 \ln(287/Z^{1/2})}\,,$$

where n is the number density of nuclei. For silicon, which is used in the tracking detectors of ATLAS, the radiation length is 9.36 cm, which shows that also electrons and positrons easily pass the $\mathcal{O}(100\,\mu\mathrm{m})$ thick sensors.

4.1.3. Multiple Scattering

Apart from losing energy as described in the sections above, charged particles also scatter off the nuclei. The small deflections lead to the particle taking a zigzag path from which an overall scattering angle can be defined. The scattering angle after a distance is statistically distributed and the cross section of the elastic scattering via the Coulomb potential with the nuclei can be described with the Rutherford formula as

$$\frac{\mathrm{d}\sigma}{\mathrm{d}\Omega} = z^2 Z^2 r_e^2 \frac{(m_e c/\beta p)^2}{4\sin^4(\theta/2)} \,,$$

where θ is the mostly small scattering angle, which is shown by the $\sin^4(\theta/2)$ dependence, z and Z are the charges of the scattered particle and the nucleus and p is the momentum of the scattered particle.

For pixel detectors this is of importance as the incoming and outgoing particles might be separated by an angle which complicates reconstruction.

4.1.4. Photons

Photons cannot be detected directly, but have to create charged particles which in turn ionise the material and give an electrical signal. There are three interactions of photons with matter with increasing energy: photoelectric effect, Compton scattering and pair production.

The intensity of a photon beam decreases exponentially with distance x:

$$I = I_0 e^{-\mu x} \,,$$

with the initial intensity I_0 and the material specific attenuation coefficient μ. Photons can either be absorbed completely or scattered and thus changing their energy.

In the *photoelectric effect* the photon is absorbed by an electron. The electron is ejected with the energy of the photon minus the binding energy that was needed to free the electron from its bound state. For conservation of momentum, the recoil momentum is taken by the nucleus the electron is bound to. Photons with low energies have a large cross section, which decreases with energy. However, once the energy is large enough to excite an electron from a lower shell, the cross section rises again with a step. This behaviour is dependent on Z. Figure 4.2 shows the interactions of photons with matter for the example of carbon and lead.

With higher energies the photons scatter on electrons instead of being absorbed. The process is described by *Compton scattering*. Energy is transferred to the electron, depending on the scattering angle. When the photon is back scattered it deposits the maximum energy, which is called Compton edge.

At even higher energies of more than twice the electron mass, e^+e^-*-pair production* is the dominant process. For momentum conservation it requires a nucleus or another electron to take the recoil. The photon is converted into an electron-positron pair which then radiates photons again due to bremsstrahlung, as described in Section 4.1.2.

The radiation length X_0 is 7/9 of the mean free path for pair production λ_{pair} [56]. The

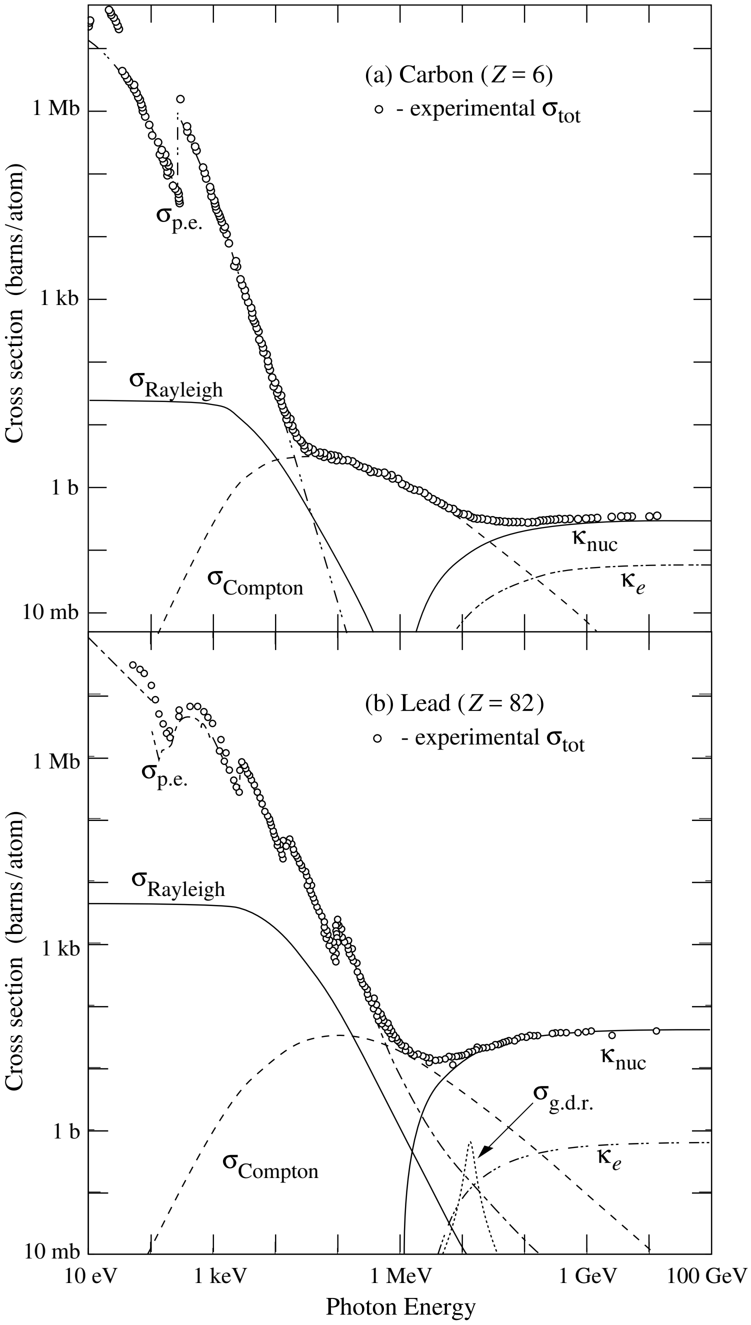

Figure 4.2: Cross section of different photon interactions in carbon and lead. The photoelectric effect is dominant in the low keV energy regime, Compton scattering is dominant for medium energies up to 1 MeV and pair production for higher energies above 1 MeV. Depending on the atomic number Z of the material, the amount of cross section steps for the photoelectric effect differs depending on the number of shells in the atom [56].

cross section for pair production and bremsstrahlung both scale with Z^2.

Pair production and bremsstrahlung are the two processes which lead to electron-photon showers in the electromagnetic calorimeter. With either a photon or an electron the shower is initiated. The energy of the particles is then gradually decreased until the threshold for pair production or bremsstrahlung is reached and the other interactions become dominant.

4.2. Principles of Semiconductor Detectors

In semiconductor material passing charged particles ionise the semiconductor and create weakly bound electron-hole pairs. A signal current is induced on the electrodes when the electron-hole pairs are separated by an applied external electric field and drift towards the electrodes.

Semiconductors are usually described within the context of the band model with a valence and a conduction band which are separated by a gap. In the lattice of a semiconductor, the discrete energy levels that the valence electrons occupy in an atom, which correspond to the orbitals, turn into quasi-continuous energy bands in the valence band. Available energy states are located in the conduction band. The energy difference between the valence band and the conduction band is $E_\mathrm{G} = 1.12\,\mathrm{eV}$ in silicon. Ionisation due to passing particles can be understood as electrons in the valence band being excited into unoccupied higher energy levels in the conduction band, leaving a hole in the valence band. Due to the small band gap, the charge carriers can recombine easily, unless an external field is exerted on them, as is the case in a detector.

Silicon is commonly used for pixel detectors in high energy physics. Due to its small band gap, silicon requires only an average energy of $3.61\,\mathrm{eV}$ for the creation of an electron-hole pair and therefore yields comparably high signal charges with respect to other semiconductors. This electron-hole pair creation energy is more than the gap energy as additional momentum transfer to the lattice is required as silicon has an indirect band gap. According to the interactions described in Section 4.1 material with high atomic numbers causes higher energy deposition and increases the material budget of the detector. For tracking detectors, however, a low material budget which reduces multiple scattering is preferred. This also favours silicon with an atomic number of $Z = 14$.

The motion of the particles in a semiconductor can be described by two different processes. *Diffusion* describes carrier concentration driven movement of the electrons or holes to the side of smaller concentration, which is permanently present in a semiconductor. The holes move in the valence band while the electrons move in the conduction band. Due to collisions with the atoms their energy is reduced until they recombine. *Drift* describes movements of free charge carriers under the influence of an electric field $\boldsymbol{E}$. They are accelerated along the field lines and can likewise collide with atoms which reduces their velocity. The drift velocity $\boldsymbol{v}_\mathrm{D}$ can be defined, which is the mean value of the velocity distribution. While the drift is dominant, diffusion nonetheless affects the charges and causes them to spread out. This effect becomes more prominent with time.

4.2.1. The pn-Junction

In intrinsic silicon, the number of electrons and holes is equal and induced by thermal excitations and impurities in the crystal. The charge carrier density is $n_i = 9.65 \times 10^9\,\mathrm{cm}^{-3}$ at 300 K [130]. In these conditions ionisation due to traversing particles cannot be detected as it is orders of magnitude smaller than the intrinsic number of free charge carriers.

The charge carrier density can, however, be changed by doping the material. In n-doped material, donor atoms with one additional valence atom are inserted in the crystal lattice, while p-type material is doped with acceptor atoms which are lacking one valence electron, in comparison with the substrate. Silicon as substrate material with four valence electrons has as typical n-type dopants Phosphorus and Arsenic with five valence electrons, while Gallium, Aluminium, Indium and Boron with three valence electrons are typical p-type dopants. In n-type material a quasi-free electron is introduced with an energy level close to the conduction band. The introduced hole in the crystal in p-doped material creates an additional energy state just above the valence band. With n- or p-doped sections in the semiconductor, the heart of all silicon detection devices, the pn-junction, can be established.

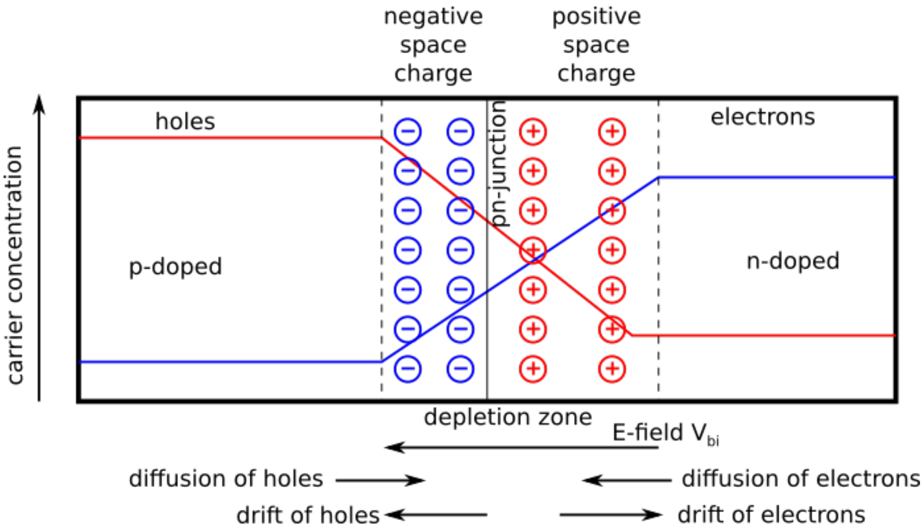

Figure 4.3: A pn-junctions forms between regions of different doping. The holes from the p-type material diffuse towards the n-region and vice-versa. A negative space charge is built on the p-side and a positive space charge on the n-side, which creates a field with a potential difference called the built-in voltage V_{bi}. This leads to a drift current. Between the two doped regions develops the depletion zone, which is vacant of free charge carriers.

A pn-junction forms naturally when differently doped areas interface, as shown in Figure 4.3. With different concentrations of electrons and holes, the holes from the p-type material diffuse towards the n-region and vice-versa. While electrons and holes recombine at the junction, a negative space charge is built on the p-side and a positive space charge on the n-side, which creates a field with a potential difference called the built-in voltage V_{bi}. This leads to a drift current. An equilibrium establishes between diffusion and the drift current induced by the electric field. Between the two doped regions develops the depletion zone, which is vacant of free charge carriers and has a higher resistivity then the initial material. The intrinsic width of the pn-junction is determined by the doping concentration, but can be increased with a reverse bias voltage, thus increasing the potential across the junction. With negative potential applied to the p-region and ground or positive potential on the n-region, holes from the p-region and electrons from the n-region are attracted towards their respective terminals and the depletion zone is increased. In Figure 4.5 the depleted regions for a p-type bulk (left) and an n-type bulk (right) are shown. In terms of detector operation, the depletion zone is called sensitive volume of the detector and is desired to be as large as possible. The pn-junction provides efficient charge collection when incoming particles ionise atoms in the depletion zone, as a reverse biased pn-junction is very little conductive. Respectively, when applying forward bias the pn-junction becomes conductive.

The width d of the pn-junction with dependence on the bias voltage is [131]

$$d = \sqrt{(V_{\mathrm{bi}} + V_{\mathrm{B}}) \frac{2\epsilon}{e} \frac{(N_{\mathrm{A}} + N_{\mathrm{D}})}{N_{\mathrm{A}} N_{\mathrm{D}}}}\,,$$

where ϵ is the electric permittivity, e the charge of the electron, N_{A} and N_{D} the acceptor and donor concentrations and V_{B} the bias voltage. In the case of very different doping concentrations the depletion zone spans unevenly mainly into the lower doped side of the junction as the free charge carriers fill a larger volume by recombination before an equilibrium settles. This is used for detector design. In the case of a high bias voltage compared to the built-in voltage, and a p-bulk, the width can be approximated with the majority charge carriers being electrons as

$$d \approx \sqrt{\frac{2\epsilon V_{\mathrm{B}}}{e N_{\mathrm{D}}}}\,. \tag{4.4}$$

Regarding the capacity of the sensor, it can be understood as a plate capacitor where the depleted width of the sensor volume corresponds to the dielectricum and the edges of the depleted region to the plates in the capacitor. With larger bias voltage and therefore larger depletion zone the capacitance decreases until the sensor is fully depleted and there is no further effect on the capacitance. The different capacitance regimes can be determined with Eq. (4.4) to be

$$C \approx \begin{cases} A\sqrt{\frac{\epsilon e \cdot N_{\mathrm{D}}}{2|V_{\mathrm{B}}|}} & \text{for } |V_{\mathrm{B}}| \leq |V_{\mathrm{depl}}|\,, \\ \epsilon \frac{A}{D} & \text{for } |V_{\mathrm{B}}| > |V_{\mathrm{depl}}|\,, \end{cases} \tag{4.5}$$

with the thickness D and the surface A of the sensor.

4.2.2. Signal Formation

In the following, the signal formation in silicon detectors is discussed.

With the external electric field, the electron-hole pairs from ionisation of passing particles are separated. They drift towards the electrodes, creating a current according to the

Shockley-Ramo theorem [132, 133]:

$$i = q\boldsymbol{E}_{\mathrm{w}}(r(t))\boldsymbol{v}_{\mathrm{D}}(r(t))\,,$$

with the current i induced by a charge q and the drift velocity $\boldsymbol{v}_{\mathrm{D}}$ of the charge carriers with the weighting field $\boldsymbol{E}_{\mathrm{w}}$ of the electrode. The weighting field is defined by the geometrical effects of the electrode on the electric field of the sensor. It can be determined by setting the electrode of interest to unit potential and all other electrodes to ground, thereby removing all free charges.

In the case of detector operation with an external bias voltage, the current-voltage characteristic shows the exponential behaviour [134]

$$I = I_{\mathrm{S}}\left(e^{eV_{\mathrm{B}}/kt} - 1\right)\,, \tag{4.6}$$

where k is the Boltzmann constant and I_{S} the saturation diffusion current for reverse bias. For reverse biased and depleted sensors, the current is thus expected to be rising until settling at a plateau as described by the exponential function for the negative exponent values (coming from the negative bias voltage). The voltage at which the current settles and the sensor is fully depleted is called the depletion voltage V_{depl}.

In order to be able to detect the signal charge from the traversing particles, the leakage current I_{leak} in the detector needs to be as small as possible. This current originates from thermal excitation in the depleted zone, diffusion currents from minority charge carriers at the junction (electrons in the p-type or holes in the n-type part) or diffusion currents in undepleted volume in the detector. Thermal excitation especially happens at lattice defects which are multiplied due to radiation damage, as explained in Section 4.2.3. The dependency on the temperature and the band gap energy E_{G} is [134]

$$I_{\mathrm{leak}} \propto T^2 \exp\left(\frac{-E_{\mathrm{G}}}{2kT}\right)\,. \tag{4.7}$$

At very high voltages the pn-junction breaks down and a very strong current can traverse the sensor. This can be caused by uncontrolled charge multiplication (avalanches) where electrons and eventually holes are accelerated in the very strong electric field and themselves create electron-hole pairs. This voltage is referred to as breakdown voltage V_{bd}.

4.2.3. Radiation Damage

Over time, the radiation traversing the detector material leads to radiation damage, which alters the signal. There are two different types of damages: *surface defects* and *bulk defects* which are caused by ionising energy loss and non-ionising energy loss, respectively. Both, sensors and readout chips are subject to radiation induced defects. Surface defects are mainly relevant for the readout electronics and bulk defects for the sensors.

Two types of defects can be created within the bulk of the material. The lattice atoms can be displaced to form vacancies and interstitials in the lattice, as shown in Figure 4.4. Induced by the displaced atom, further defects can be induced, creating a cluster.

Viewed from the band model, the defects create new energy levels between the valence and

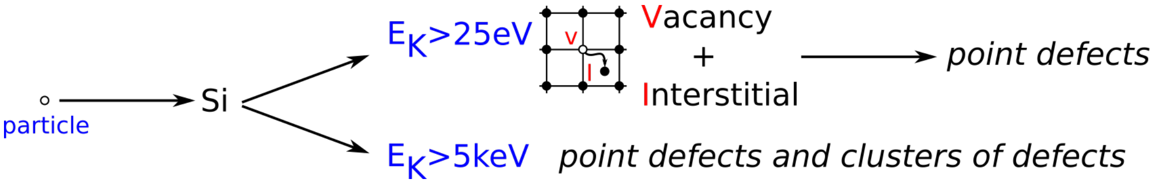

Figure 4.4: Lattice defects of a silicon sensor.

the conduction band. With a smaller necessary energy for the excitation to the conduction band, thermal excitations become more likely and the leakage current rises. Cooling of the sensor counterbalances this effect. The leakage current has thus also a $\propto \sqrt{V_{\mathrm{B}}}$ dependence on the bias voltage, as the size of the depletion region affects the number of additional energy levels.

Another type of effect is charge trapping, where electrons or holes are trapped in energy levels near the bands. When they are released with a delay while another particle passes, this signal is increased artificially. The actual signal of this particle, however, is decreased. This effect determines the charge collection efficiency of the detector.

The introduction of electrically charged defects can alter the effective doping concentration. For silicon, an n-type sensor can be converted to a p-type sensor after a high enough particle flux, as most defects are acceptor like, which means that electrons are removed from their atoms. For n+-in-n pixel sensors of the ATLAS PIXEL Detector the type inversion and its effect on the depletion region is shown in Figure 4.5. The depletion zone grows from the backside before type inversion, which means that only at full depletion it reaches the pixel implants, which is required for operation. After type inversion, the depletion zone grows from the pixel side and allows operation even if the bulk is not fully depleted.

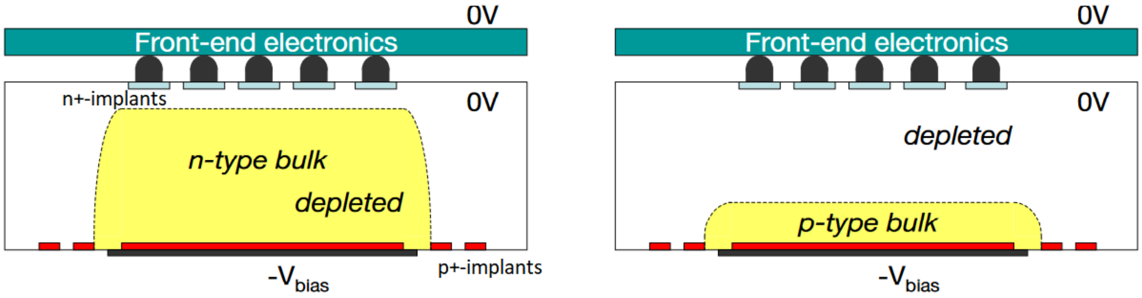

Figure 4.5: **Left:** In an n+-in-n pixel sensor the depletion zone grows from the backside before type inversion. Only at full depletion it reaches the pixel implants, which is required for operation. **Right:** After type inversion the depletion zone grows from the pixel side and allows operation even if the bulk is not fully depleted [95].

Additionally, with a higher doping concentration, the bias voltage needs to be higher for full depletion. The bias voltage is, however, limited by the breakdown of the sensor.

Particles of different types and energy cause different damage, hence the fluence is recalibrated into the equivalent fluence if the particles were neutrons. The increase of the leakage current is dependent on the sensor volume V, the radiation damage rate α and the

1 MeV neutron equivalent fluence Φ_{eq} as [135]

$$\Delta I_{\text{leak}} = \alpha V \Phi_{\text{eq}} \,. \tag{4.8}$$

At room temperature or higher temperature, the defect structure in the silicon lattice can change and repair defects. The simplest example is Frankel-pair recombination, where interstitials and vacancies recombine due to increased lattice mobility. This is called beneficial annealing. However, leaving the sensor for a long time at higher temperatures, new defects can develop which have a more negative effect than the original damage. This is called reverse annealing and must be avoided. The radiation damage rate is dependent on the annealing time and temperature and hence influences the leakage current. Detailed studies can be found in [135].

Surface defects are mainly caused by actual surface distortions or debris on the sensor. However, as for the bulk defects, radiation induces ionisation and therefore displacement of the crystal structure. Due to the proximity of the surface, usually high electric fields prevent the created electron-hole pairs from recombining. This leads to long lasting and spatially confined charge carriers which can even change the effective doping concentration. The characteristic linear dependence on the bias voltage is also different compared to the bulk defects.

4.2.4. Noise

There are always sources of noise in the detector that limit the smallest detectable signal and resolution. The noise is commonly stated relative to the measured quantity, the charge. It is quantified as Equivalent Noise Charge (ENC) and is the amount of charge when the signal to noise ratio turns one. The total ENC is the square sum of the individual contributions. Three of them are briefly discussed.

Thermal noise is caused by thermal motion of charges in a conductor. These random fluctuations of the electron distribution cause a leakage current which is proportional to the temperature, as shown in Eq. 4.7. This is present at all frequencies. As discussed, the depletion region stretches further into the sensor volume with higher applied reverse bias voltage. This has an effect on the capacity of the sensor, as shown in Section 4.2.1. As the noise is dependent on the capacitance, for a fully depleted detector volume, the noise is lower.

The *shot noise* is proportional to $\sqrt{I_{\text{leak}}}$, which increases with temperature. It is intrinsic to the discrete nature of charge carriers and the statistical fluctuations of the number of charge carriers passing through a conductor.

Unlike the other types of noise, *flicker noise* originates from the electronics in the detector. The noise power spectrum has an approximate $1/f$ dependence, where f is the frequency. Origin is the charge trapping by crystal defects in semiconductors, and especially transistors, which are then randomly released with a delay. Given the frequency dependence, flicker noise can be dominant at low frequencies.

The silicon tracking detectors used in ATLAS are built based on the principles discussed above. Important is their high charge collection efficiency and small noise, even after operation within ATLAS and receiving high radiation doses. In order to reduce the data rates, the silicon detectors are often read out binary, which is explained in more detail in Section 5.2.

CHAPTER 5

Hybrid Pixel Detectors for the ITk

The focus in the previous sections was on the sensor properties and its behaviour with particles. In this section a more technical introduction to the modules for the ITk is given.

Pixel detectors can be realised on the one hand as hybrid pixel detectors and on the other as monolithic pixel detectors. Monolithic pixel detectors have active and passive parts integrated on the same Application-Specific Integrated Circuit (ASIC) silicon chip so that the signal created in the passive part from passing particles is directly transformed and read out in the active part. Hybrid pixel detectors on the contrary, are made from two different silicon chips, where the sensor chip is passive and an active readout chip is bump bonded to the sensor pixels, pixel by pixel.

The main purpose of a pixel detector, the detection of particle tracks with high spatial resolution, is obtained by its segmentation in pixels - on the sensors and respectively on the readout chip. For the ATLAS PIXEL Detector and the ITk hybrid pixel modules in several layers are and will be used, which allow to measure the trajectory of passing particles.

A full hybrid pixel module comprises a sensor - readout-chip hybrid glued and wire bonded to a flexible PCB. The sensor - readout-chip hybrid is also known as *bare module* and the flexible PCB commonly called *flex*. The flex provides the connections to the readout system and the power supplies. Moreover, signals between the flex and the sensor and readout chip are routed through the aluminium wire bonds.

Hybrid modules with sensors bump bonded to the FE-I3 [136] or FE-I4 readout chips are used in the current ATLAS PIXEL Detector. The segmentation of the pixels in the sensor is achieved with implants of dedicated doping. That is why each pixel has an individual pn-junction which needs to be read out separately.

In Figure 5.1 one can see on the left a single pixel cell with a bump bond in between the bare sensor and the readout chip. The different doping which defines a pixel is indicated with different shades of grey. The bump bond is conductive material, either indium or tin-silver. On the right, a detector module with all of its components is shown. Additionally to the components in the figure on the left, the flex with its wire bond connections to the readout chips is shown. Also, the local support, a mechanical structure each module is

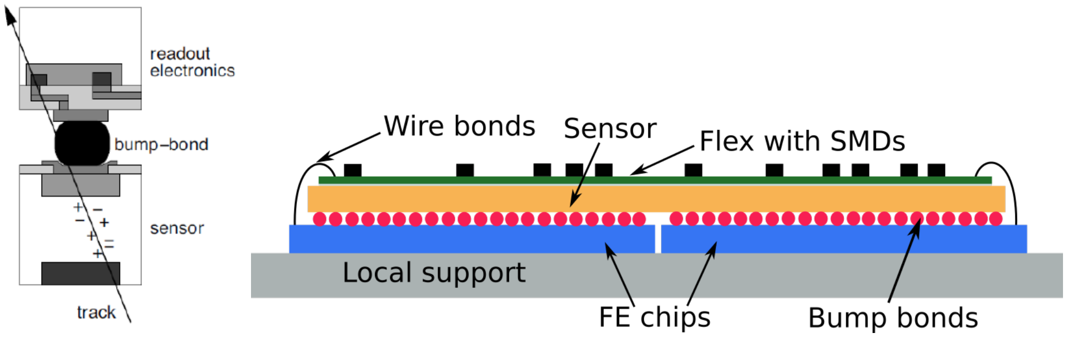

Figure 5.1: **Left:** A single pixel of a hybrid pixel detector with the active sensor volume where a passing particle creates an electron-hole pair and the bump bond connection to the readout chip [95]. **Right:** A pixel module with its components: sensor, readout chips and flex. The module is wire bonded and on a local support.

connected to, is displayed.

As described in Section 4.2.1, the sensor is operated in reverse bias to deplete the detector volume. Electron-hole pairs from passing particles are separated and drift towards the electrodes where a current is created that is routed via the bump bond to the readout chip. The readout chip processes the created charges for each pixel separately.

In general, for all readout chips used in this thesis, the readout path comprises an analog and a digital part. The analog part consists of an amplifier and a threshold discriminator which generate a pulse with a pulse length proportional to the charge signal. As every pixel has its own readout but all pixels need to be comparable, the discriminator thresholds and the return to baseline of the amplifier need to be adjusted to equalise the pixel response. The digital part measures the pulse width. The processed data is passed to a buffer which is shared between several pixels. Also, in order to achieve the high bandwidth required in the detector, parallel readout is needed.

For tracking of particles, multiple layers of silicon detectors are used. As mentioned in Section 4.1, the path of the particle can be altered by multiple scattering or energy loss. To counterbalance these effects the sensor must be as thin as possible to provide sufficient electron-hole pairs and signal but limit the interactions with the material.

5.1. ITk Pixel Sensors

The ITk features two different types of sensors. In all layers but the inner layer, planar sensors with p-bulk material and n-implants are used. The inner layer will be equipped with 3D sensors. Both are explained in the following.

A huge advantage of planar sensors is their easier processing mechanism so that they can be produced by multiple vendors in high quality with high yield and low cost. For the ITk, where an area as large as $13\,\mathrm{m}^2$ will be covered with Si pixel modules, they will therefore be used for the larger portion of the modules.

5.1.1. Planar Sensors

Planar sensors have layers of different doping, considering the sensor volume from backside to the top, as indicated in Figure 5.1 on the left. The bulk of the sensor is doped with one type in concentrations of typically $\approx 10^{12}\,\mathrm{cm}^{-3}$ [131]. With implants on the top- and/or backside with higher doping concentration, typically $> 10^{18}\,\mathrm{cm}^{-3}$ [131], the pn-junction is built up. As the depletion zone mainly spans into the less doped side, the bulk volume of the sensor can be depleted.

The planar sensors for the ITk are n-in-p sensors, where the silicon substrate is a boron doped p-type crystal with orientation (100) [137]. N-type implants with phosphorus coupled to an aluminium readout pad form a pixel. With another p-implant called p-stop or p-spray, depending on the type, the inter-pixel resistance is achieved that isolates the pixels from each other. Another p+-doping at the backside of the sensor improves the ohmic contact to the metallisation with aluminium. On the frontside an oxide layer, called passivation, is applied which protects the sensor from scratches.

The pixel size is $(50 \times 50)\,\mu\mathrm{m}^2$ for a sensor thickness of 150 µm and $(25 \times 100)\,\mu\mathrm{m}^2$ pixel pitch on the sensor with 100 µm thickness in the outer layer of the inner system, respectively. Guard rings for high voltage (HV) stability and low current operation are implanted around the active area and cause inactive areas on the sensor edges. On the sensors Under Bump Metallisation (UBM) for improved electrical contact is applied to prepare the hybridisation process where the readout chips are bump bonded to the sensor. The hybridisation is done after dicing, which describes the cutting out of the sensors or readout chips from the silicon wafer.

Compared to the FE-I4, with the change from n-in-n to n-in-p technology for the planar sensors, the guard ring structures are on the pixellated face of the sensor, as shown in Figure 5.2. This means that the sensor bias voltage is present at the perimeter of the pixellated surface on the sensor which is only the bump bond height (10 µm to 25 µm) [138] away from the readout chips which are at ground potential. Therefore, HV insulation is required to protect the readout chips for bias voltages higher than 200 V. This will be done with Parylene coating, which is applied on the whole module except for the connectors after wire bonding, and simultaneously protects the wire bonds and provides HV insulation.

In order to bias the whole pixel matrix with applying external voltage for laboratory tests, different techniques are employed. A temporary metal can be applied on the frontside which shorts all the pixel cells and allows to measure current voltage characteristics. This must be removed before hybridisation. Another option is a bias grid on the frontside with so-called *punch-through* (PT) dots at regular distances of 100 µm in the pixel matrix where an electric potential is directly applied to bias the sensor. An example is shown in Section 6.1.2 where measurements on ITk sensors are discussed. A last option is using poly-silicon bias resistors.

5.1.2. 3D Sensors

A different implantation technique is used for 3D sensors. Instead of stacking different layers, so-called electrodes are doped into the bulk material. The shape and number of electrodes can vary as well as the depth of the electrodes into the bulk material. The layout for the 3D sensors for the ITk can be found in [139] and is shown in Figure 5.3. Pixel

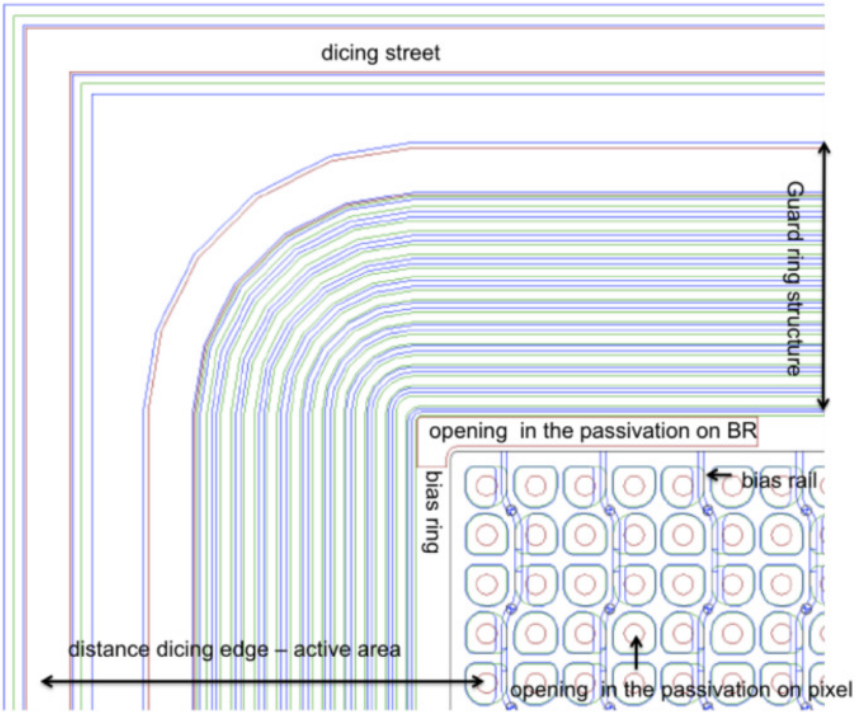

Figure 5.2: Layout of a corner of a planar sensor for the ITk. (50 × 50) µm² pixels are depicted, with a common dot for PT biasing. The passivation opening for sensor tests is on the bias ring.

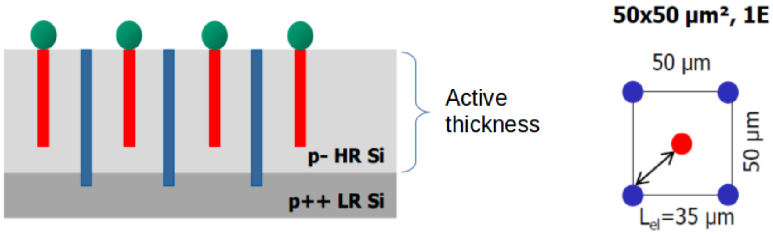

Figure 5.3: **Left:** A 3D sensor layout [139]. The readout columns (n+) are indicated in red. The ohmic columns (p+) are connected to the bulk region which is biased from the backside. **Right:** The top view of the (50 × 50) µm² pixel, where the inter-electrode distance is indicated.

geometries of (50 × 50) µm² are planned for the end-cap region and (25 × 100) µm² for the barrel region in the innermost layer.

3D sensors are more radiation hard as the close spacing between the implanted electrodes requires smaller bias voltage and hence results in a smaller leakage current which requires less cooling. This also counters charge trapping. Also, the depletion voltage is smaller compared to planar sensors, even at high irradiation dose. Most importantly, thickness of the sensor, needed for signal creation and the aforementioned electrode distance are decoupled, which allows for thicker radiation hard sensors. In opposition to all their advantages, 3D sensors are still expensive due to the more complex fabrication process which often includes double sided processing of the silicon.

5.2. ITk Pixel Readout Chips

Advances in ASIC-design as well as ever changing requirements regarding radiation hardness or noise, promote new readout chip designs for the detectors at ATLAS. In this thesis, the FE-I4 and the RD53A readout chip are used for measurements. For the sake of completeness the new ITkPix readout chip for the ITk is also introduced in the following sections.

5.2.1. FE-I4 Readout Chip

The FE-I4 readout chip was designed for the ATLAS IBL [96] to cope with the increasing hit rates closer to the interaction point and the hence required higher radiation hardness and efficiency.

Its pixel matrix has 80 × 336 pixels with pitches of 250 µm and 50 µm, respectively. Compared to the FE-I3 readout chip with pitches of 400 µm × 50 µm, the spatial resolution is increased. Two columns are grouped to form 40 double-columns which are divided into 2 × 2 pixel regions with four separate analog pixels and one common Pixel Digital Region where hits and timing information is stored.

In the analog pixel electronics the charge signal from the sensor electrodes gets shaped from current to voltage in a two-stage amplifier. In the discriminator, the analog signal is converted into a digital square wave signal, where the output is on only when the signal is above a certain threshold. The pulse width, the time over the threshold (ToT), is likewise measured with the discriminator and proportional to the charge deposited in the sensor.

Calibration of the chip is done globally and per pixel with programmable registers. Test charges can be injected into both, the analog and the digital part, of each pixel. With the known amount of charge, the global and local pixel registers are tuned based on the response to the known charge.

The chip is powered with digital and analog voltage directly. However, the FE-I4 modules are also capable to be operated in serial powering with other modules. This means that a shunt low dropout voltage regulator (Shunt-LDO or SLDO) voltage regulator is implemented in the chip which can generate the digital and analog voltages needed for the chip from a supply with constant current. Serial powering is exploited in the demonstrator programme, as reported in Chapter 8. Extensive studies on the SLDO and serial powering in general can be found in [124].

5.2.2. RD53A Readout Chip

The smaller pixels on the sensors for the ITk require new readout chips with not only smaller pixel sizes but also higher bandwidth and new electronics which can handle the new data acquisition (DAQ) and trigger protocols from the new trigger architecture, as mentioned in Section 3.4.1 and detailed in [120].

The RD53A readout chip is a prototype ASIC where three different design variations, different analog FE types, are used in the chip for technology validation on the same chip [121]. The synchronous, linear, and differential FEs are arranged on the chip as shown in Figure 5.4. The chip has a width of 20 mm and a height of 11.6 mm with a pixel matrix of 400 × 192 columns and rows. The lower edge has a row of pads for wire bonding, circuitry for biasing, configuration and readout.

According to Ref. [121], the differential FE uses a differential gain stage in front of the discriminator and implements a threshold by unbalancing the two branches, the linear FE features a linear pulse amplification in front of the discriminator, which compares the pulse to a threshold voltage and the synchronous FE uses a baseline "auto-zeroing" scheme that requires periodic acquisition of a baseline instead of pixel-by-pixel threshold trimming. As for the FE-I4, the pulse width, also called the ToT, is measured with the discriminator and proportional to the charge deposited in the sensor. In order to equalise the pixel response, tuning is also necessary for this chip. Details on this procedure can be found in Section 7.3.2.

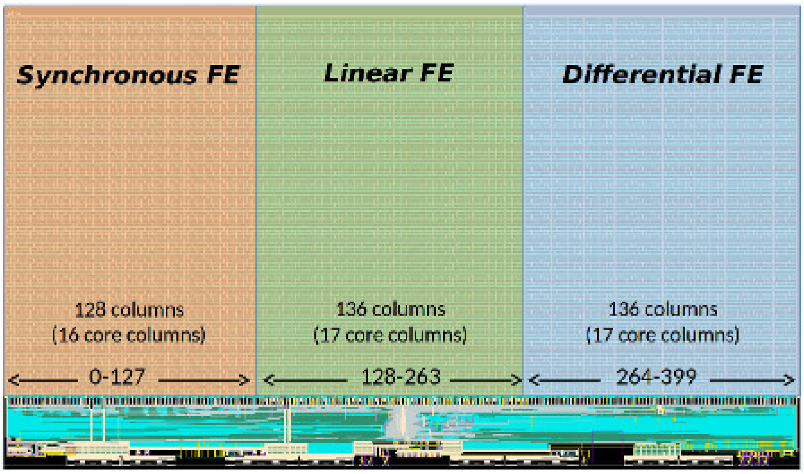

Figure 5.4: Three different FE types: synchronous, linear, and differential.

Similar to the FE-I4 chip, the pixel matrix is split in cores of 8 × 8 pixels, which are synthesised as one digital circuit. The analog FEs are grouped together in sets of four. The digital configuration to the analog FEs is provided by the core, which also receive the digital outputs from the FEs. Via a single 160 Mbit/s link the chip is controlled and the data can selectively be output through one to four links at a data rate up to 1.28 Gbit/s each. As the FE-I4, the RD53A chip is designed for serial powering with an integrated SLDO, which is supplied with constant current. Serial powering reduces power losses in cables and the material budget. For testing purposes direct powering is also possible and achieved by bypassing the regulators. Analog and digital voltages of 1.2 V each are needed to power the chip. More information on the powering is provided in Section 7.3.

5.2.3. ITkPix Readout Chip

The RD53 collaboration was founded to produce the readout chip for both, ATLAS and CMS based on a common design, adjusted to the specific needs [140]. It is sometimes called

RD53B, but for ATLAS now commonly ITkPix. The ITkPix readout chip has the differential FE as the by ATLAS chosen design of the analog FE. It is full size, which means that the pixel matrix is 400 × 384 pixels. The baseline pre-production chip is the ITkPixV1.1. Due to imperfections in the chip design, a revised version was produced and thus ITkPixV1.0 and ITkPixV1.1 exist. For the ITk the final chip ITkPixV2 will be used. In the following this readout chip in general will be referred to as ITkPix.

Compared to the RD53A, the ITkPix provides improvements, such as enhancements of the serial powering regulators, the clocking, a new triggering and readout scheme, new data encoding and most importantly data merging [141]. This means that up to four ITkPix chips can be connected together. The data from the slave chips, which are connected to the input lanes, are merged into the output of one master chip, which is called link-sharing.

5.3. ITk Pixel Module Types

The modules planned for the ITk or used within the studies towards the ITk can be grouped into different types by the number of readout chips bump bonded to the sensor. Based on the size of the bare module, different types of module flexes have been produced.

5.3.1. Single Chip Modules

Single chip modules are not actually planned for the ITk any more as they were used in the IBL. Solely for R&D single chip modules are used. As explained in Section 5.2, the RD53A readout chip is only half of the size of the final ITkPix chip. Apart from modules with a sensor and readout chip of exactly the RD53A size, for tests with the real geometry, full size RD53A sensors have been produced, providing thus only an area of about $1 \times 2\,\mathrm{cm}^2$ of active area. The other part of the sensor is inactive silicon.

For single chip modules bare modules are wire bonded to a rigid PCB to assemble a module with higher robustness. These test modules are built by the ITk institutes and used in lab tests and test beams. An example is shown in Figure 5.5 on the left.

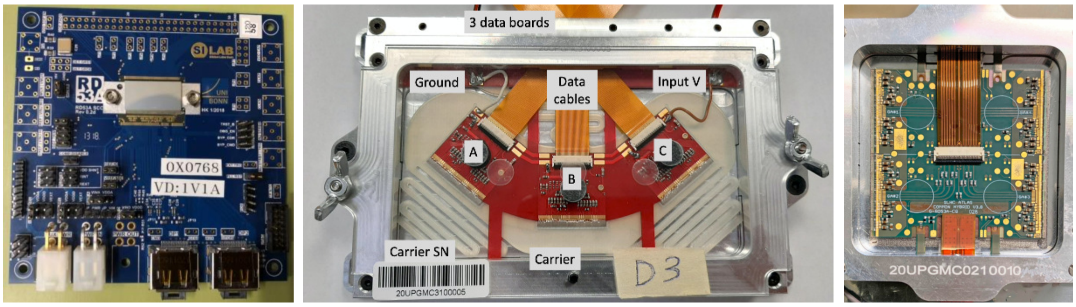

Figure 5.5: **Left:** Single chip module for test beam measurements. **Middle:** Triple chip module for the inner layer of the ITk. **Right:** Quad chip module in a module carrier for the outer layers of the ITk.

5.3.2. Triple Chip Modules

So-called triplets are used in the innermost layer of the ITk, in layer L0, with 3D sensors. The active sensor thickness is 150 µm with an additional support of 150 µm. Three readout chips are arranged as shown in Figure 5.5 in the middle.

5.3.3. Quad Chip Modules

In order to minimise complexity, quad chip modules are built, where one large sensor is connected to four readout chips, as shown in Figure 5.1. Modules with further readout chips are disfavoured due to powering and readout constraints. The chips on the module are powered in parallel which makes a large number of chips very difficult. As for the readout constraints, the data rate is 1.28 Gbit/s per chip (see Section. 5.2) which means that by reading out the data through the master only link, the readout time multiplies by the number of chips.

A multi layered flex is glued and wire bonded to the bare module. There exist several different versions of the flex, as detailed in Section 7.1.1, where the assembly of quad modules is discussed. For all flex versions, the wire bond pads and rails are implemented on the flex edges, as can be seen in Figure 5.5 on the right. Ground, digital and analog potentials for the readout chips are distributed via the rails. A direct connection through a hole in the flex delivers bias voltage for the sensor. The temperature of the module is monitored with two NTCs (negative temperature coefficient sensors) on the flex. Probe pads for the analog and digital voltage generated by the SLDOs are available and used for module building. The two rectangular shapes connect to ground, for example. For easier handling and stability the flex comes in a frame to which it is connected with so-called tabs. In the picture the frame is hidden under the module carrier. There are different areas which can be defined on the flex and come in handy later. The wire bonding area on both sides of the flex, the keep clear area, inside the four circles, and the connector and capacitor areas. The connector is white and in the middle and connects to the readout. With two types of connection flexes, called pigtails, the module is powered and the data is routed to the readout system, coming from the connector. The large filtering capacitor is hidden under the data pigtail on the top, between chip 1 and 4. It is connected in parallel to the power rails to assure stable power supply to the digital components across the board. A capacitor acts as a charge reservoir which can quickly provide currents and prevent current surges.

Quad chip modules of two different sensor thicknesses are used in the planned ITk, as discussed in Sec 3.4.2. Thinner thicknesses are used in the inner system in layer L1, to minimise the leakage current and the material budget in the detector. Also, as mentioned, the inner system will be replaced after having received half of the expected integrated luminosity. However, the inner layers are expected to be exposed to a higher fluence of $1 \times 10^{16}\,\mathrm{n_{eq}/cm^2}$ during their lifetime, compared to the fluence in the outer layers of maximal $4 \times 10^{15}\,\mathrm{n_{eq}/cm^2}$. The outer layers L2-L4 therefore need to be radiation harder to withstand the harsh conditions for longer, up to integrated luminosities of $4000\,\mathrm{fb^{-1}}$.

CHAPTER 6

Planar Sensors for the ITk

As introduced in Section 5.1.1, planar sensors for quad chip modules will be used in the outer layers of the ITk pixel barrel detector. In this chapter, the qualification measurements of these sensors which were performed in Göttingen are discussed.

From the initial decision on the sensor specifics which was finalised before the scope of this thesis to the actual production of the sensors it is a long way. In a so-called market survey, potential vendors of sensors were specified and their sensors were tested and validated. Based on different mechanical and electrical tests it was decided whether the potential vendors pass the criteria for production or not. For the ITk pixel modules sensors from six potential foundries (*ADVACAM*[1], *HLL*[2], *FBK*[3], *HPK*[4], *LFoundry*[5], *Micron Semiconductor Ltd*[6]) were measured and compared to effectuate a decision on the vendor. Every vendor, which during the tests had to stay confidential, was asked to produce ten RD53A single chip (SC) and 20 double chip (DC) sensors, fitting in size the RD53A chip and compatible with the specifications needed for the ITk as documented in [137] and updated for the price inquiry at the vendors [142]. SCs have hence pixel matrices of 192 × 400 pixels and DCs matrices of 192 × 800 pixels. As at the time of the market survey the decision for the pixel size was not yet made, pixel sizes of $(50 \times 50)\,\mu\text{m}^2$ and $(25 \times 100)\,\mu\text{m}^2$ were investigated for two sensor thicknesses.

The concept of the market survey was to divide the participating institutes in clusters of two, which were assigned to one or more foundry and had to perform cross checks of the results. Göttingen cross checked results with Dortmund for initially two of the six vendors. With the start of the pandemic and changing laboratory access conditions in the various countries, eventually, sensors from four vendors were measured and analysed in Göttingen.

The required measurements include leakage current-voltage (IV), capacitance-voltage

---

[1] https://advacam.com/

[2] Halbleiterlabor der Max-Planck-Gesellschaft (https://www.hll.mpg.de/)

[3] Future Built on Knowledge, Fondazione Bruno Kessler (https://www.fbk.eu/en/)

[4] Hamamatsu Photonics K.K. (https://www.hamamatsu.com/jp/en.html)

[5] http://www.lfoundry.com/

[6] http://www.micronsemiconductor.co.uk/

(CV) and leakage current-time measurements (It) as well as height and bow measurements to assure the silicon sensor quality. Depending on the vendor, bare sensors or wafers with or without UBM were set under test. The hit efficiency and position resolution of the sensors was additionally measured in test beams.

In general, the sensors were first tested in table top laboratory experiments, described in Section 6.1 and 6.2, and afterwards in test beam experiments which will be explained in Section 6.3.

The laboratory measurements comprise:

- Visual Inspection
- Thickness measurements
- Planarity measurements
- Current-Voltage characterisation (at 20 °C and relative humidity (RH) $< 50\%$)
- Current-Time measurement for 48 h
- Capacitance-Voltage characterisation

Mechanical measurements were performed only on the DC sensors, electrical tests on SC and DC sensors and test beam measurements only on SCs.

6.1. Mechanical Tests and Visual Inspection

Mechanical tests on the sensors are performed to assure that bump bonding with the readout chip is possible. The bow of a sensor is an indication for the stress that is enforced on the bump bonds and must therefore be $< 25\,\mu\mathrm{m}$ for both, the thin and the thick sensors. An overall envelope of a module is defined to make sure that the module physically fits in the designated space in the detector. Hence, the thickness of all the components needs to be controlled, also requiring thickness measurements of the sensors.

6.1.1. Setup and Measurement Technique

Visual inspection and thickness and planarity measurements are performed with a microscope (VISION ENGINEERING / HAWK Mono Dynascope). Different lenses with magnification of 10×, 20×, 50×, 100×, 200×, 500 × and 1000× are available. The height is measured via the focus of the light. Hence, in order to measure the thickness, the sensor is flattened with underpressure by applying vacuum to the backside through a chuck with vacuum openings. The height of the chuck and the height of the sensor are each measured with four points as there is no automatic measurement available on the microscope. With these four points the planes of the sensor and the chuck are defined by the measurement programme and the distance between these planes is calculated and interpreted as the sensor height. The measurement points are as depicted on the left in Figure 6.1.

Compared to other sites performing metrology measurements with an automatic microscope, the measurement described above with the manual instrument is considered as

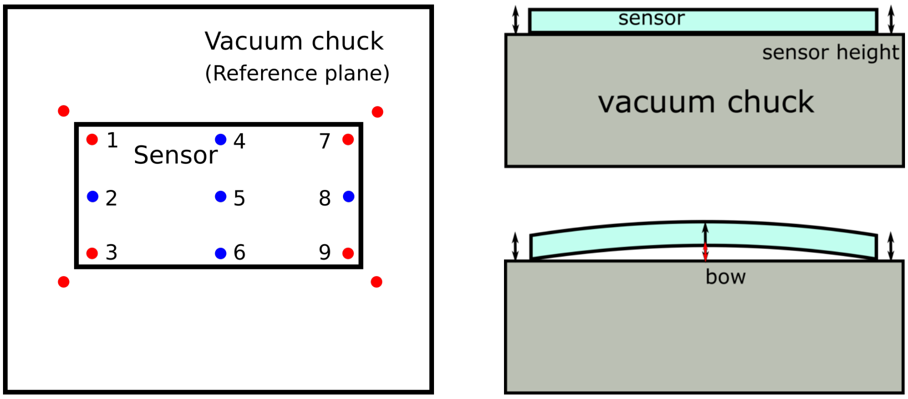

Figure 6.1: **Left:** The red measurement points are used for the height measurement. The blue and the red measurement points for the determination of the sensor bow. **Right:** In order to measure the height, the sensor is flattened with vacuum. For the bow measurement the vacuum is turned off.

baseline and the minimum requirement as stated in Ref. [137]. With this method, small variations in the thickness cannot be detected. However, large deviations across the sensor can be determined.

The standard deviation of a single height measurement σ_{h_1} was obtained by measuring one point h_1 ten times to be

$$\sigma_{h_1} = \sqrt{\frac{1}{n}\sum_i \left(h_{1i} - \overline{h_1}\right)^2} = 1.44\,\mu\text{m}\,.$$

It being so small tells that the judgement of the experimenter if the object that is measured is in focus or not is only causing a small systematic error. Systematic uncertainties due to the limited number of measurement points need to be taken into account. When all four measurements are largely deviating, the thickness determination as average of the four measurements should be taken with care. Especially as the standard deviation is small and with error propagation for only four height measurements the thickness error stays as small as

$$\sigma_h = \sqrt{\sum_{i=1}^{4} \sigma_{h_i}^2} = 2.9\,\mu\text{m}\,.$$

The bow is obtained by measuring nine points on the sensor without vacuum being applied and calculating the sagitta of the sensor. In Figure 6.1 the nine measurement points for the sagitta are depicted, both, the red and the blue measurement points on the sensor have to be measured. The sagitta with the propagated error is calculated as

$$\begin{aligned}\text{bow} &= \frac{z_4 + z_5 + z_6}{3} - \frac{z_1 + z_2 + z_3 + z_7 + z_8 + z_9}{6}\,,\\ \sigma_{\text{bow}} &= \sqrt{\sum_{i=1}^{6} \sigma_{h_i}^2} = 3.5\,\mu\text{m}\,.\end{aligned}$$

Table 6.1: Height and bow measurements of three calibration samples for qualification of the market survey institutes.

	Thin_1	Thin_2	Thick_1
Height	(101 ± 3) µm	(102 ± 3) µm	(150 ± 3) µm
Bow	(1.2 ± 3.5) µm	(2.2 ± 3.5) µm	(4.0 ± 3.5) µm

While the absolute values of the uncertainties seem small, it should be mentioned that they amount to 11% and 14% for the height and the bow, with respect to the tolerance of the height measurement of 15 µm and the maximal bow of 25 µm.

Visual inspection is also performed with the same microscope, using 200× and 10× magnifications for detailed pictures of probable scratches and residues from production or overview images, respectively. The implants and the aluminium layer on the pixel must be clean to prevent any shortages between individual pixels. No more than 0.1% of the pixels must show defects.

6.1.2. Samples and Results

Before measuring sensors from the qualifying vendors for sensor production for the ITk, calibration samples were shared amongst the participating institutes. By comparison of the results on the calibration samples the setups of the sites were qualified. Given the non-detailed measuring of the height at the microscope in Göttingen, any further sensor thickness measurements in Göttingen were omitted after confirming that the measurement is in principle possible and comparable to the results in Dortmund. Hence, only calibration samples were analysed regarding the height and the bow.

Two sensors with a defined height of 100 µm and one with 150 µm were analysed in terms of thickness and bow and the results are shown in Table 6.1. All measurements lie well within the required bow of ≤ 25 µm and thickness deviations of ≤ 15 µm [137]. Given that the uncertainty of the bow is the same order of magnitude as the measurement value, a better measurement device should be used.

While no further height and bow measurements were performed on market survey sensors, these measurement techniques were extensively used and developed for module building, as presented in Section 7.1.2.

In Figure 6.2 microscope images from visual inspection show two different types of defects. The pixel geometry of (50×50) µm^2 pixels with bias rails is also visible. Darker rings around the pixel metallisation show that UBM is already applied on the pixels. Large contaminations as the round stain on the right, which looks like glue, have only been observed on calibration samples and are therefore not worrying. Small debris was also observed on actual market survey sensors but never caused an effect in any of the measurements.

6.2. Electrical Measurements

With electrical tests on the sensors, their capability of particle signal processing is tested, following the procedure in Ref. [137]. Tests are conducted with SC sensors before irradiation

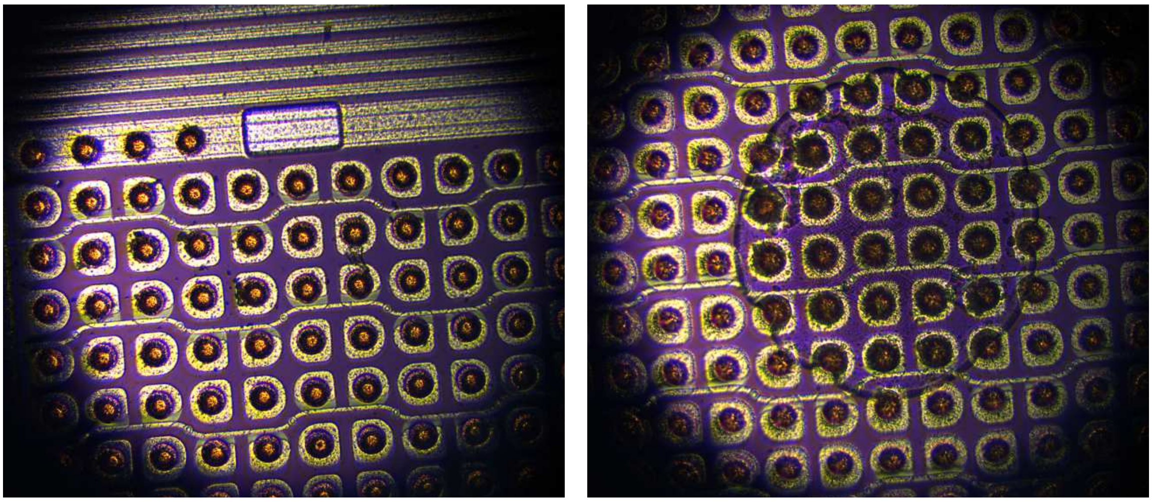

Figure 6.2: Different kind of defects detected by visual inspection. The pixel geometry of $(50 \times 50)\,\mu\mathrm{m}^2$ pixels with bias rails is also visible. Also, UBM is already applied on the pixels, seen as darker ring around the pixel metallisation. **Left:** Small residues spanning only one pixel. The passivation opening for electrical measurements is also visible. **Right:** Large stain, maybe glue, spanning several pixels.

and after. DC sensors are only tested before irradiation.

The sensors are sent[7] to be irradiated to fluences of $2 \times 10^{15}\,\mathrm{n_{eq}/cm^2}$ (1 MeV neutron equivalent) and $5 \times 10^{15}\,\mathrm{n_{eq}/cm^2}$ after the initial measurements and after return measured again. These irradiation fluences are chosen to match the fluences the sensors will receive during their life time when operated in the ATLAS Detector in the HL-LHC. Sensors in layer 1 and 2 receive fluences of up to 5×10^{15} and $2 \times 10^{15}\,\mathrm{n_{eq}/cm^2}$, respectively.

For unirradiated sensors all measurements are taken at relative humidity RH $< 50\%$ and a temperature of 20 °C. In IV tests, the leakage current dependence on the voltage is measured by probing the sensors directly. Before irradiation, sensors are required to have a leakage current of less than $0.75\,\mu\mathrm{A\,cm^{-2}}$ at a bias voltage of $V_\mathrm{bias} = V_\mathrm{depl} + 50\,\mathrm{V}$, where V_depl is the full depletion voltage. As explained in Section 4.2.1, the pn-junction should fully deplete the sensor for best signal formation. This happens at the depletion voltage V_depl. With a CV measurement of the sensor the voltage at full depletion can be determined. Also, the stability of the current must be better than 20% within 48 h when biased with $V_\mathrm{bias} = V_\mathrm{depl} + 50\,\mathrm{V}$. The breakdown voltage V_bd, which is defined as increase of the leakage current of more than 20% over a voltage step of 5 V must be $V_\mathrm{bd} > V_\mathrm{depl} + 70\,\mathrm{V}$. Tests before irradiation are discussed in Section 6.2.2.

In order to make sure that the sensors are still sensitive to the traversing particles in the detector, the leakage current must not surpass the defined limits. This is why the change of the leakage current I_leak due to irradiation is investigated. Also, I_leak is temperature dependent, as shown in Eq. 4.7, which requires that cooling of the module to $T = -10\,°\mathrm{C}$ at the module NTC is applied during operation. Hence, the sensors are also measured at

---

[7] The University of Birmingham (UK) and the CYRIC irradiation facility (Japan) irradiate the sensors with proton beams. The corresponding dose in $\mathrm{n_{eq}/cm^2}$ is calculated.

cold temperatures to understand their behaviour at real detector conditions.

The number of defects increases due to irradiation. During annealing, defects in the sensor can repair and thus the leakage current caused by irradiation can decrease, as mentioned in Section 4.2.3. However, annealing is dependent on time and temperature. The requirement of the market survey is to measure after ten days of annealing at room temperature.

After irradiation and annealing the following requirements at a sensor temperature of $T = -25\,°\mathrm{C}$ should be met by the different sensors and fluences:

- 150 µm thick sensors:
  - $I_\mathrm{leak} < 25\,\mathrm{\mu A\,cm^{-2}}$ at 400 V for $\Phi = 2 \times 10^{15}\,\mathrm{n_{eq}/cm^2}$
  - $I_\mathrm{leak} < 45\,\mathrm{\mu A\,cm^{-2}}$ at 600 V for $\Phi = 5 \times 10^{15}\,\mathrm{n_{eq}/cm^2}$
- 100 µm thick sensors:
  - $I_\mathrm{leak} < 20\,\mathrm{\mu A\,cm^{-2}}$ at 300 V for $\Phi = 2 \times 10^{15}\,\mathrm{n_{eq}/cm^2}$
  - $I_\mathrm{leak} < 35\,\mathrm{\mu A\,cm^{-2}}$ at 400 V for $\Phi = 5 \times 10^{15}\,\mathrm{n_{eq}/cm^2}$

These limits are needed to keep the compliance with the predicted performance of the cooling system as otherwise the power dissipation is too large. The measurements are performed at a sensor temperature of $T = -25\,°\mathrm{C}$ to assure that annealing processes are as small as possible. This allows to take a snap-shot of the sensor performance at defined conditions. Section 6.2.3 discusses the results on irradiated sensors. Additionally to the tests requested by the market survey, further complementary temperature, time and annealing tests have been undertaken and are also presented in Section 6.2.3.

6.2.1. Setup

A semi-automatic probe station with temperature controlled chuck (PA 300 Probe Shield) is used for the electrical measurements. HV is commonly applied via the chuck with a Keithley 2410 and the ground terminal is connected to the probe needle to prevent arc-overs. The current is measured with the same Keithley. A CV measurement is performed with an HM8118 LCR meter and a Keithley 6487 as HV supply. The impedance of the sensor is measured at a frequency of 1 kHz and converted to capacity.

The temperature of the chuck is controlled with a chiller (Huber unistat with unistat control) with hydrofluoroether Novec 7200 as cooling liquid. Both, temperature measurements inside the chiller and directly on the probe station chuck with a PT1000 temperature sensor are used for the setting of the temperature. Humidity control is not possible in the probe station, but can be measured with an HIH4000 humidity sensor. Dry air can be used to flush the whole volume, which reduces the relative humidity RH to a value of ≈ 3% which is measured with a humidity sensor inside the probe station volume. All sensor readouts are performed with multimeters.

The system should by design be light tight when the probe station is closed. See Figure 6.3 for photos of the probe station, the internal microscope used for approaching the sensor with the needle, and an open view on the sensor positioned on the chuck. The circular pattern on the chuck are the vacuum supply channels, where the hole connected to the vacuum pump is right below the sensor in the middle.

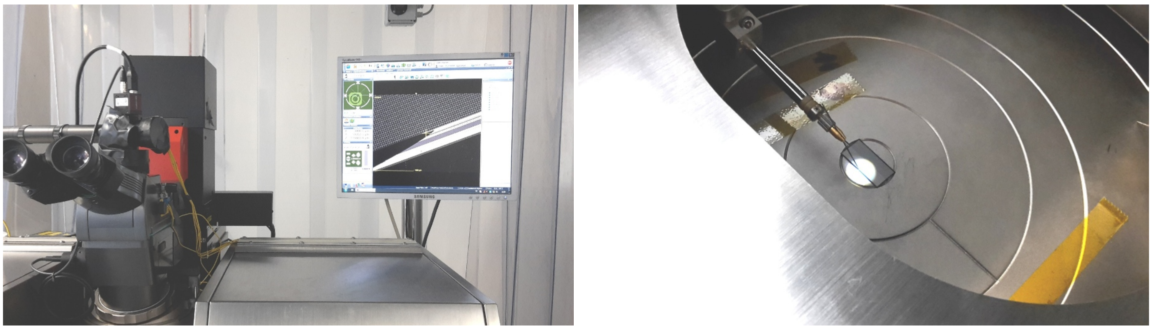

Figure 6.3: Photos from the closed and open probe station, where the microscope picture with the needle on the sensor is shown on the left.

6.2.2. Before Irradiation

As for the mechanical measurements, before measuring sensors from market survey vendors, the calibration sensors were measured to verify the setup.

Leakage Current Characterisation

In general, the measurement is performed by taking current measurements every 5 V steps and averaging over 10 measurement points until 600 V or compliance is reached. A compliance of 10 µA is set to avoid higher currents of breaking sensors. As soon as the compliance is reached, the voltage is ramped down. A short wait time of 10 s is used to separate the ten measurements and after each ramp step. The uncertainty of a current measurement for one voltage step is as low as $\mathcal{O}(0.01)$ nA for all of the measurements. It is hence not visible in any of the plots and not noted for any of the given current values in this chapter.

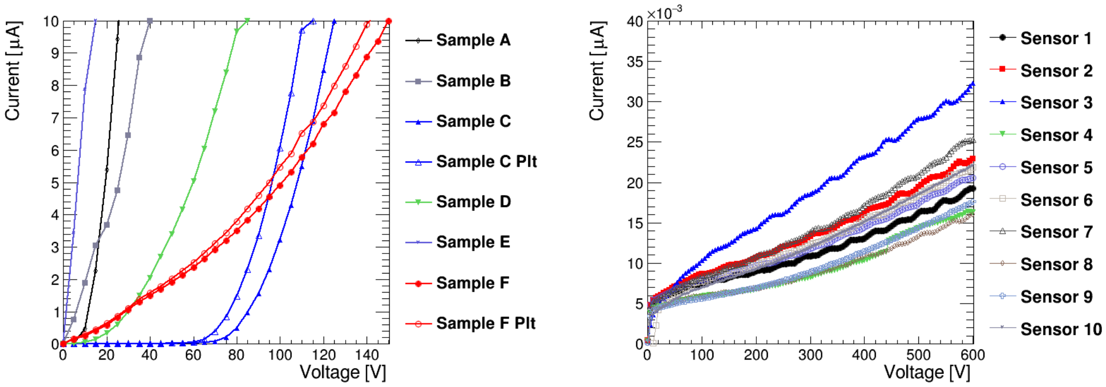

Figure 6.4: **Left:** IV curves of the six calibration sensors with a breakdown. **Right:** The sensors from the market survey show small currents up to voltages of 600 V.

There are six qualification samples and two of them have been measured twice, once before long-term studies and once afterwards. This is marked in Figure 6.4 on the left as PIt (post It). For the market survey ten SC sensors from vendor 4 were tested. In Figure 6.4 the IV-behaviour of the qualification sensors is shown on the left and the market survey sensors on the right. Compared to the qualification measurements, the characteristics of

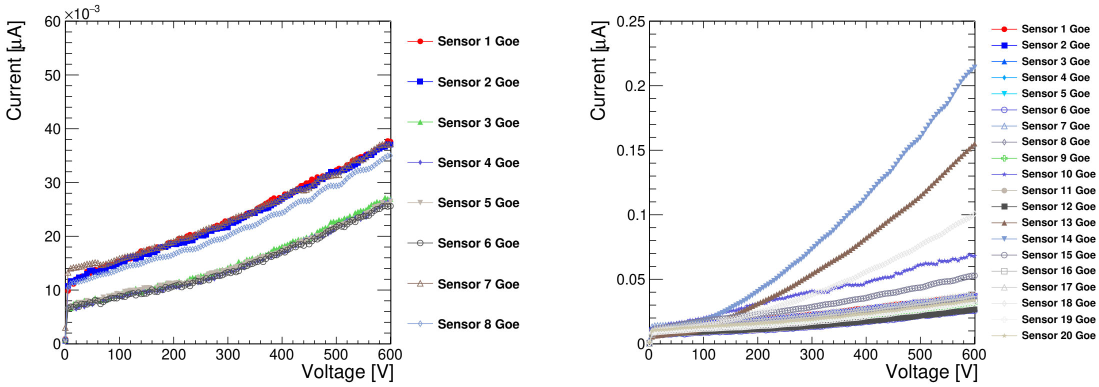

Figure 6.5: IV measurements on the DC sensors. **Left:** The first eight sensors seem to follow two different trends, about 10 nA apart. **Right:** All further sensors show different trends and higher leakage currents.

the market survey sensors show much better sensor quality.

It is visible that the qualification sensors all show a steep current rise, the so-called breakdown, while the market survey sensors do not show any breakdown and only very low currents (nA). On the right one can also see that the current is fluctuating, which is due to the cycles of the chiller. The leakage current dependence on the temperature is directly visible.

As presented in Section 4.2.2 a plateau region is expected to be seen in the current while there is no charge multiplication. This is not visible for either of the sensors, instead, the current is constantly slowly rising for the market survey samples. Possible reasons could be that edge and surface contributions increase the current. As the measurement is performed with only one probe needle, there is no separate guard ring current which would protect the main part of the sensor from these contributions.

In Figure 6.5 the IV data for DCs from vendor 4 are shown and it is visible that the first eight measured sensors have all low leakage currents without breakdown. The sensors seem to follow two different trends, about 10 nA apart. All further sensors show different trends and higher leakage currents.

Within the supervision of a Bachelor's thesis [2], algorithms determining the breakdown voltage according to the market survey criterion were used on this data. Sensor 4 of the SC sensors was assigned a breakdown voltage of 525 V, 530 V or 555 V, depending on the algorithm. However, there is only a step visible in the measurement and no actual breakdown. Sensor 9 was also assigned conflicting breakdown voltages of 405 V, 460 V and 530 V due to fluctuations in the measurement, while no actual breakdown is visible. With these algorithms none of the DC sensors are characterised as having a breakdown.

Depletion Voltage Characterisation

For the CV characteristic and determination of the depletion voltage of a sensor, every 5 V a measurement point is taken up to voltages of 200 V. In order to determine the depletion voltage, the capacitance is plotted as $\frac{1}{C^2}$ as a function of the bias voltage and supposed to

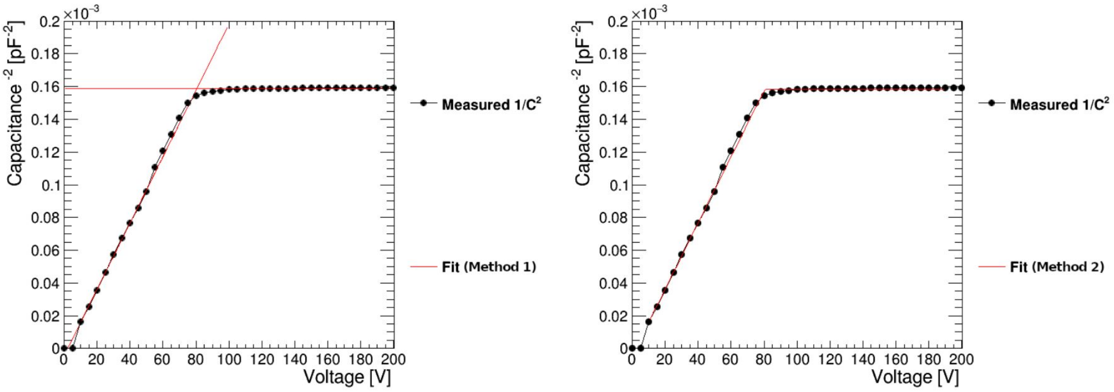

Figure 6.6: Two different fits of the CV measurement of SC sensor 1 from vendor 4 [2]. **Left:** Two separate straight lines are fitted to the measurement. **Right:** A continuous function is fitted to the measurement.

Table 6.2: Depletion voltages for the SC sensors at 10 kHz.

Sensor	V_{depl} [V]
Sensor 1	80.30 ± 0.03
Sensor 2	83.31 ± 0.02
Sensor 3	83.80 ± 0.02
Sensor 4	73.54 ± 0.03

follow Eq. 4.5. For voltages smaller than the depletion voltage V_{depl} the plotted function $\frac{1}{C^2} \propto V_{\mathrm{B}}$ and for higher voltages the dependency stays constant. The depletion voltage is hence extracted as the voltage at which the capacitance becomes constant. This is achieved by fitting straight lines to the linear and the constant part of the function and extracting the intersection of the two lines. Within the supervision of the Bachelor's thesis [2], two fitting methods were compared: the aforementioned method with two straight lines to a continuous function that describes both sections in one function. The two different fits of sensor 1 from vendor 4 are shown in Figure 6.6. Both methods yield good results, however, the fitting with two separate lines is more stable and was used for the determination of the depletion voltage. It is also the method which is recommended by the RD50 collaboration [143].

The measurements for the SC and DC sensors from vendor 4 are shown in Figure 6.7. In the plot on the left for the SC sensors, the measurements for 1 kHz and 10 kHz of four different sensors are shown. The behaviour is similar for both frequencies, as expected. Table 6.2 summarises the depletion voltages for the SC sensors at 10 kHz. On the right in Figure 6.7, the CV data for 17 DC sensors at 1 kHz is displayed. The few outstanding points originate from connection issues between probe and sensor.

However, data taking with the setup described in Section 6.2.1 was causing serious problems, which is why only the CV measurements shown in the plots for the market survey sensors were taken. Data taking was complicated by faulty hardware and for many measurement trials a default value instead of real data points were output. This problem was solved by subsequent users of the setup.With results from Dortmund and a valid cross check for the available data, it was not problematic that no further measurements were taken.

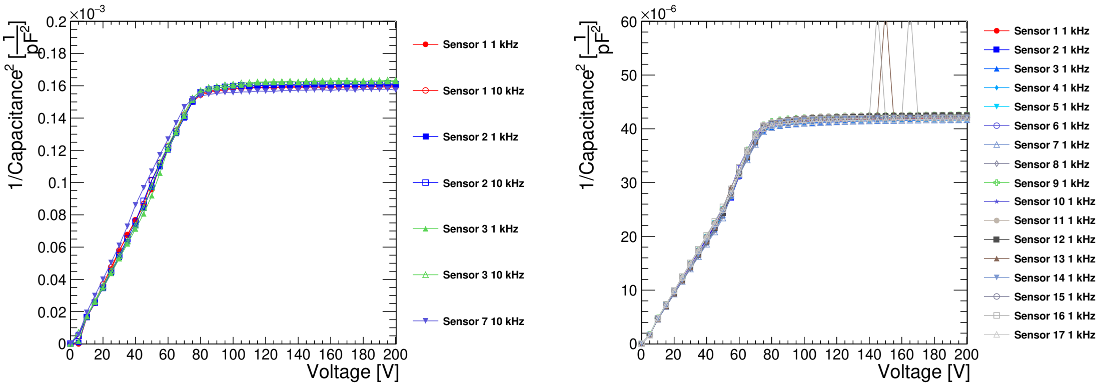

Figure 6.7: CV curves of the market survey sensors. **Left:** Four SC sensors CV measurements at two different frequencies of the LCR meter. The lines are fitted to the two parts of the curve to extract the depletion voltage at their intersection. **Right:** 17 DC sensors CV measurements at 1 kHz. All sensors of the same type show similar behaviour.

Current Stability

In order to determine the long-term behaviour of the sensors when powered, the current is measured over 48 hours with measurement points being taken every 10 min. Figure 6.8 shows the long-term measurements of the current and the humidity over time for five different market survey sensors at $T = 20\,°\mathrm{C}$. With the requirement of a measurement

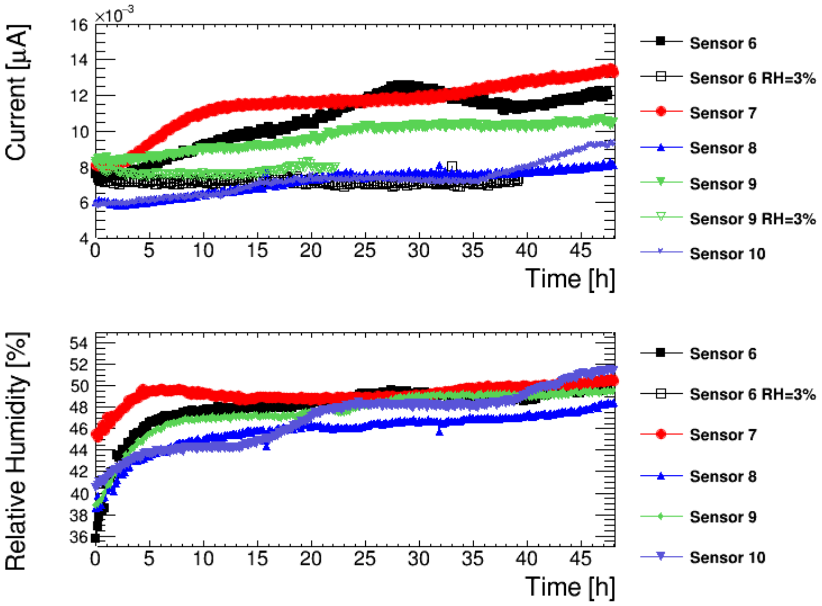

Figure 6.8: **Top:** IT curves of the market survey sensors. An unstable behaviour with variations of up to 63% can be observed. **Bottom:** Behaviour of the relative humidity over time. Variations between 36% and 52% are observed over the course of 48 hours.

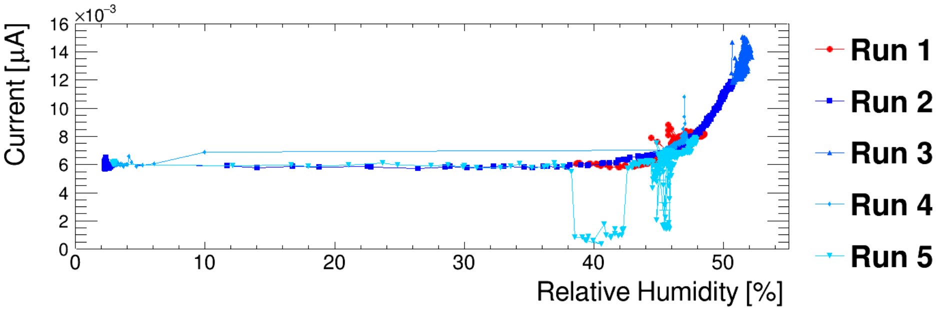

Figure 6.9: Current behaviour versus relative humidity for sensor 8. The current is stable up to RH ≈ 40% and afterwards strongly rising.

at RH $<$ 50%, all sensors are measured without RH control. Additionally two sensors are measured at RH ≈ 3%, obtained by flushing the probe station volume with dry air. It can be seen for the uncontrolled measurements that towards the end of the long-term measurement the RH was surpassing the limit. Also, the currents for all non-controlled measurements are varying more than the permitted 20%. Exemplified for sensor 7, the current rises from ≈ 8 nA to ≈ 13.5 nA, which corresponds to an increase of 59%. Seeing variations of even 63% for sensor 8, the dependence on the relative humidity was investigated with dedicated tests on this sensor.

As can be seen in Figure 6.9, the current is a function of the relative humidity. In five separate runs it could be shown that the current is stable up to RH ≈ 40% and afterwards exponentially rising. The points with currents close to zero originate from bad contacts between needle and sensor and should be ignored. Given the dependency on the relative humidity, the long-term measurements are better to be performed at relative humidities RH $<$ 40% where they are stable.

The origin of the humidity dependence of the current is not clear. However, it has been seen by other groups [144–146]. One reason could be that positive hydrogen ions accumulate in the passivation layer of the sensor. This induces conductive layers between the implants of the guard rings and the dicing edge which was shown to reduce the breakdown voltage in [144].

6.2.3. After Irradiation

After irradiation no more CV and It studies are performed, only IV measurements. CV measurements are not meaningful after irradiation due to high leakage currents. Long term studies after irradiation are in principle of interest, but not part of the market survey study. These measurements are, however, taken in further studies towards production of the sensors.

In Figure 6.10 a comparison of the leakage current at $T = -25\,^\circ\mathrm{C}$ after ten days of annealing at room temperature of vendor 1, 2, 3 and 4 for sensors with a thickness of 150 µm is shown for both irradiation fluences. For every vendor two functioning sensors were measured, except for vendor 3, where the other sensor is broken from previous tests at another institute. For the thinner sensors of 100 µm, only samples from two vendors were

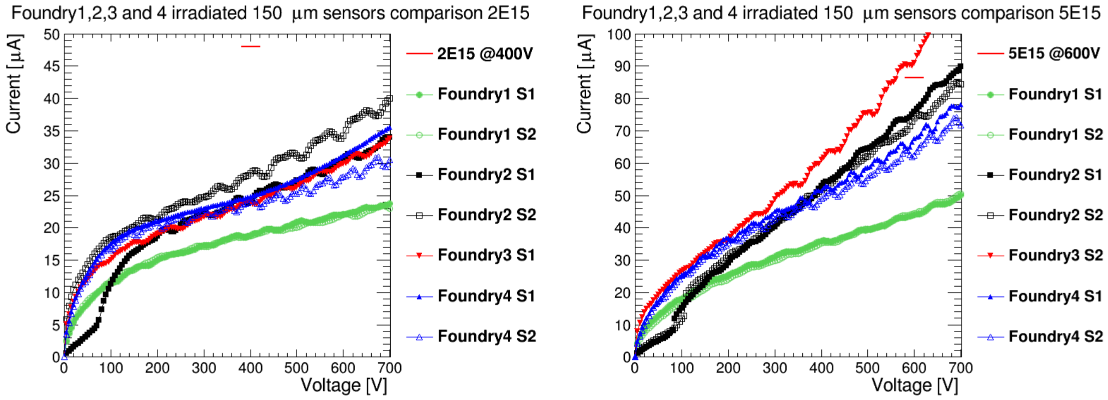

Figure 6.10: Comparison of IV curves for four different vendors and 150 µm thick sensors that were irradiated with fluences of $2 \times 10^{15}\,\mathrm{n_{eq}/cm^2}$ and $5 \times 10^{15}\,\mathrm{n_{eq}/cm^2}$. For every vendor two functioning sensors were measured, except for vendor 3, where only one sensor was provided. The sensor from vendor 3 is the only one which shows slightly higher currents than accepted by the market survey requirement. Both sensors with pixel geometries of $(25 \times 100)\,\mu\mathrm{m}^2$ (vendor 2 S2 (left) and vendor 2 S1 (right)) show slightly higher leakage currents than the respective sensors with $(50 \times 50)\,\mu\mathrm{m}^2$ from the same vendor.

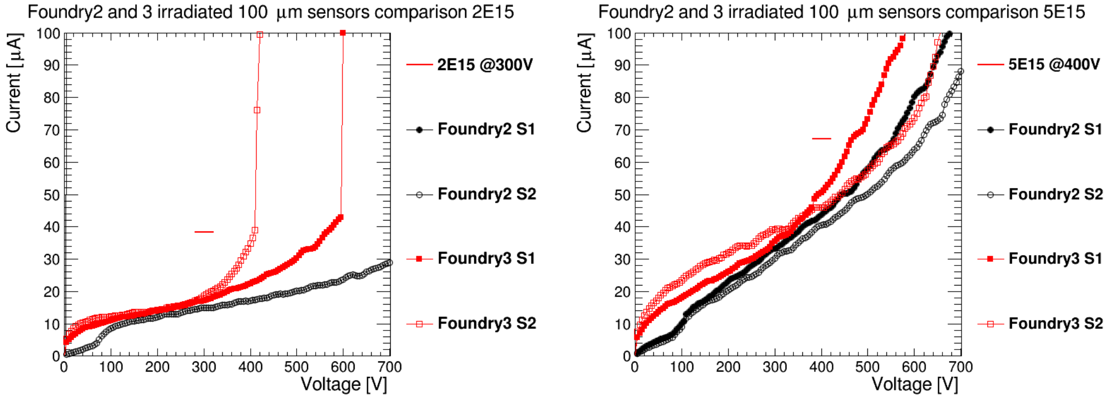

Figure 6.11: Comparison of IV curves for two different vendors and two 100 µm thick sensors each that were irradiated with fluences of $2 \times 10^{15}\,\mathrm{n_{eq}/cm^2}$ and $5 \times 10^{15}\,\mathrm{n_{eq}/cm^2}$. Sensor 1 from vendor 2 is broken from previous tests at another institute, which is seen from the breakdown directly at the first current measurement (next to the y-axis). The sensors from vendor 3 show breakdown at voltages higher than the required minimal voltage.

measured at $T = -25\,^\circ\mathrm{C}$. The comparison of two sensors for vendor 2 and 3, each, is shown in Figure 6.11 for both fluences.

In Figure 6.10 and 6.11 the red line indicates the leakage current limit defined by the market survey. The voltage at which the current limit is defined corresponds to the expected bias voltage needed for full depletion after irradiation. From the CV measurements the minimum breakdown voltage is calculated to be $V_{\mathrm{min\_bd}} = 80\,\mathrm{V} + 70\,\mathrm{V} = 150\,\mathrm{V}$.

Almost all the thick sensors fulfil the market survey requirements, except for the sensor from vendor 3 and in general the sensors show a similar behaviour for all vendors with only

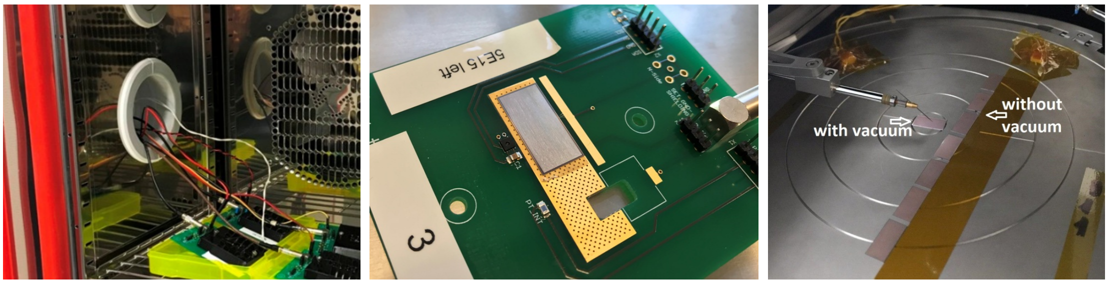

Figure 6.12: **Left:** The climate chamber setup with four modules in a plastic box. **Middle:** Simple PCB for sensor tests in the climate chamber. **Right:** The probe station setup with Kapton tape to allow measurements of eight sensors with only cooling the probe station once.

slight differences. Both sensors with pixel geometries of $(25 \times 100)\,\mu\text{m}^2$ show slightly higher leakage currents than the respective sensors with $(50 \times 50)\,\mu\text{m}^2$ from the same vendor. This is sensor 2 for lower irradiation and sensor 1 for higher irradiation of vendor 2. Of the other sensors it is unkown which pixel geometry they have. For the thin sensors, sensor 1 from vendor 2 is broken from previous tests at another institute. This is seen from the breakdown directly at the first current measurement, a steep current rise directly next to the y-axis. The sensors from vendor 3 also experience a breakdown, however, after the required minimal breakdown voltage for the market survey.

Comparison of Probe Station and Climate Chamber

Given that not all institutes have a probe station with T-controlled chuck, an alternative setup is tested. The sensor under test is glued and wire bonded to a PCB that allows to apply the voltage and then cooled in a climate chamber to allow comparisons.

In Figure 6.12 the climate chamber and the PCB with the sensor as well as the probe station are shown. The temperature measurements in the climate chamber are taken with a PT1000 temperature sensor inside the chamber volume (white cable in the picture on the left in Figure 6.12). In the top left corner of the probe station the yellow cables lead to the PT1000 used for the chuck temperature measurements inside the probe station.

It is important that the PCB conductive parts have no connection with the climate chamber, thus the PCBs are arranged on plastic boxes and only the connecting cables are routed outside. While in a climate chamber easily several sensors at once can be cooled and measured, in the probe station usually only one sensor can be measured.

To facilitate the measurement of up to 8 sensors at the same time in the probe station, a Kapton tape is used as alignment barrier towards which the sensors are pushed with the probe needle. In this configuration the sensors are not connected with vacuum to the probe station, but only touching the chuck due to gravity and the touch of the needle. In order to check if this method is proper or if the difference in temperature is large when using vacuum and when not, the measurement on sensor 2 of vendor 2 was repeated with and without vacuum and shows almost no difference. Hence the thermal contact of the sensor is also given without vacuum, as shown in Figure 6.13.

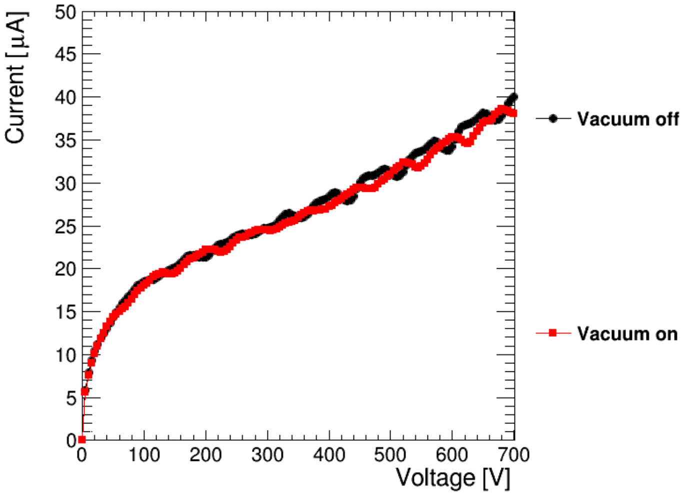

Figure 6.13: Comparison between IV measurements when vacuum and no vacuum is used for fixing sensor 2 of vendor 2 on the chuck of the probe station. The curves agree very well.

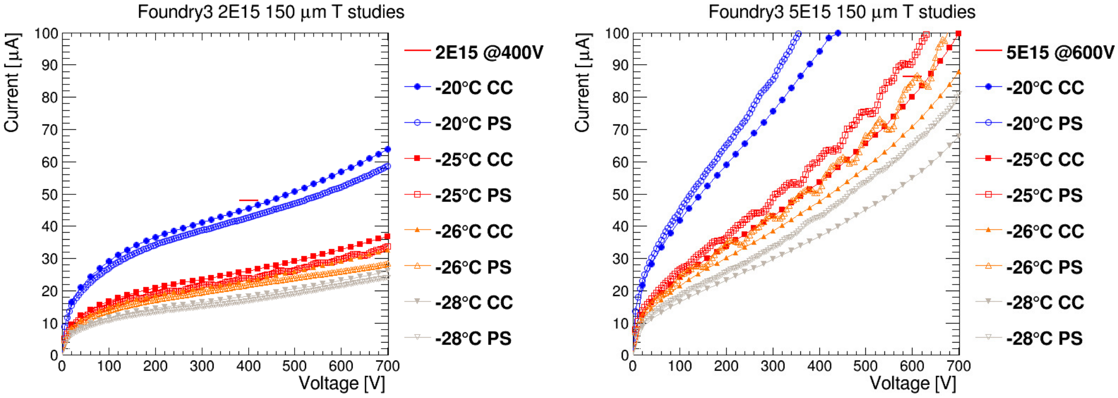

Figure 6.14: Probe station (PS) and climate chamber (CC) comparison measurements on sensors that were irradiated with fluences of $2 \times 10^{15}\,\mathrm{n_{eq}/cm^2}$ and $5 \times 10^{15}\,\mathrm{n_{eq}/cm^2}$. Measurements in the climate chamber are taken faster to avoid thermal runaway and have hence fewer measurement points. The opposite behaviour for low and high irradiation originates from bad thermal contact in the PS for the highly irradiated sensor.

Comparison measurements in the probe station and in the climate chamber are shown in Figure 6.14. In general there is a good agreement between the measurements in the climate chamber and in the probe station. Close analysis shows, however, that for the lightly irradiated sensor the same set temperature in the climate chamber is about 1 K higher than in the probe station. Also, this temperature behaviour seems opposite for the highly irradiated sensor, where the measurements at −26 °C in the probe station agrees well with the −25 °C measurement in the climate chamber. This originates from the fact that the thermal contact of the highly irradiated sensor in the probe station was not perfect, thus resulting in slightly higher temperatures and thus higher currents. The not ideal thermal contact occurred as one edge of the sensor slipped onto the Kapton tape used for alignment

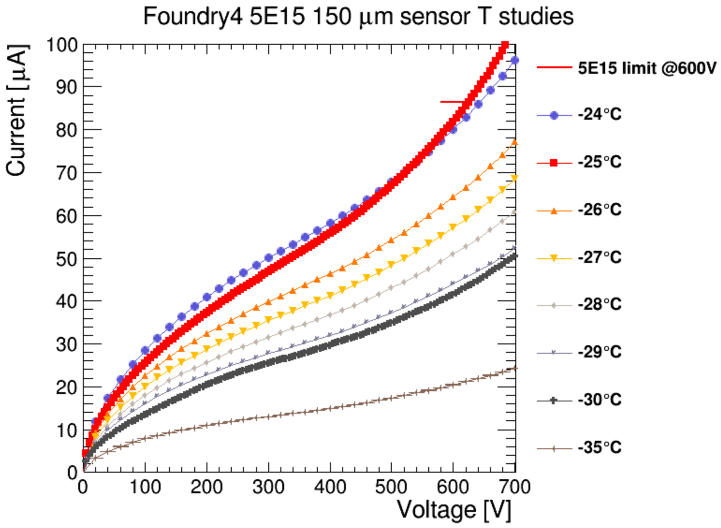

Figure 6.15: Climate chamber (CC) comparison measurements for different temperatures on one sensor that were irradiated with fluences of $5 \times 10^{15}\,\mathrm{n_{eq}/cm^2}$. Fast measurements in the CC are compared to one slow measurement in the CC, on which thermal runaway can be observed (red curve).

of the sensors in the probe station.

Leakage currents of irradiated sensors generate heat inside the sensor. When the sensor heats up, the leakage current increases and a runaway can occur. In order to avoid this thermal runaway, measurements in the climate chamber are taken faster than in the probe station. The cooling of the probe station acts directly via a cold chuck on the sensor. Compared to the indirect cooling with cold air in the climate chamber, the probe station is more efficient and can handle a slower measurement. An example of thermal runaway for measurements in the climate chamber can be seen in Figure 6.15. The slower measurement curve in red shows a steeper slope than the fast measurements.

Temperature Studies on Irradiated Sensors

In Figure 6.16 temperature studies on thick and thin sensors in the probe station from vendor 3 are shown. Due to a cyclic cooling behaviour of the chiller in the probe station, slowly taken measurements show fluctuations in the current, as seen in Section 6.2.2. The currents are larger for higher temperatures and irradiation with higher fluences, as shown in Eq. 4.7 and Eq. 4.8. This is expected as higher irradiation fluences cause more damage in the silicon crystal that lead to an increase in leakage current. The thin sensor with lower irradiation shows an unexpected breakdown behaviour, which, however, occurs after the current limit set for the market survey. Also, the sensors irradiated with a smaller fluence are for much higher temperatures of −20 °C still under the market survey limits. Better temperature performance is also visible for the thinner highly irradiated sensor, while the thick one requires cooling of −26 °C to meet the market survey requirements.

In order to understand the behaviour of irradiated sensors under different temperatures better, further studies have been performed within the supervision of the Bachelor's the-

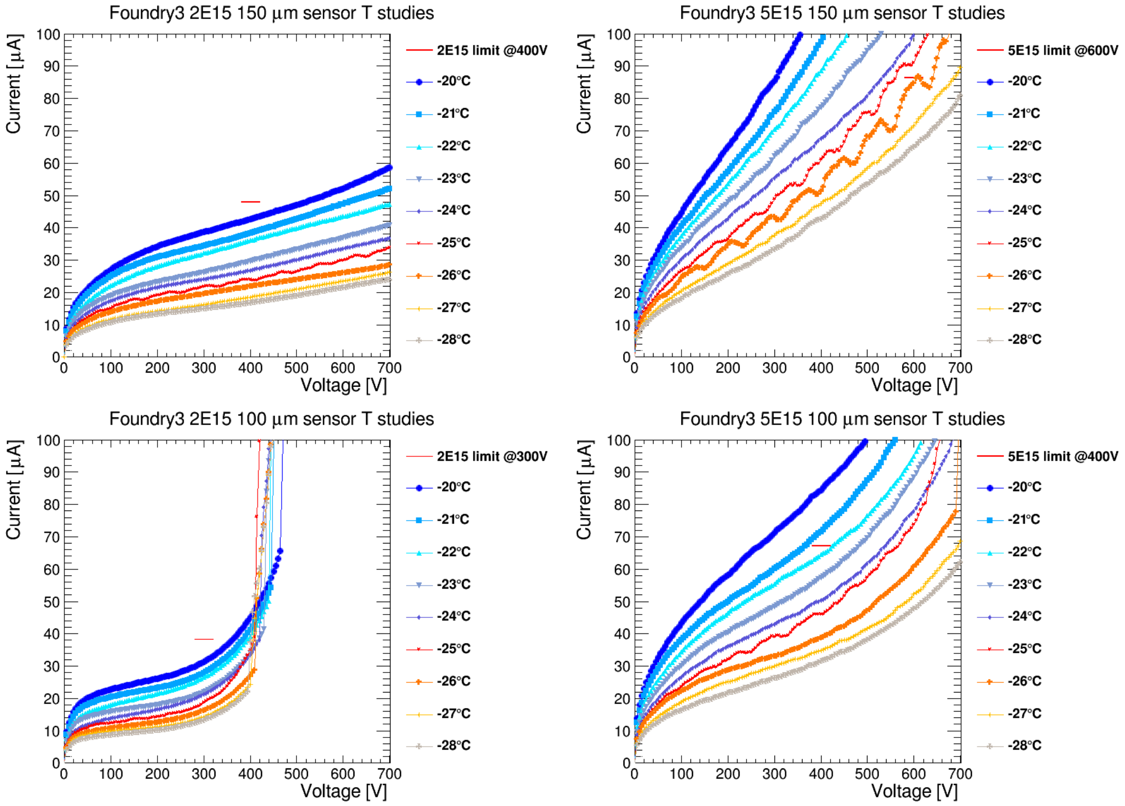

Figure 6.16: Temperature studies on sensors that were irradiated with fluences of $2 \times 10^{15}\,\mathrm{n_{eq}/cm^2}$ and $5 \times 10^{15}\,\mathrm{n_{eq}/cm^2}$. Fluctuations in the measurements originate from the cycle of the chiller.

sis [2]. The scaling behaviour of the leakage current with temperature was analysed with regard to the predicted behaviour from Eq. (4.7). For this purpose the relative temperature dependence between different measurements was calculated and compared to the measurements. Overall there is good agreement between the theoretical expected value from Eq. (4.7) and the experimental results. Larger temperature differences cause larger deviation from theory which is especially visible for highly irradiated sensors. This hints that contributions from surface and edge currents rise with irradiation.

Studies on Different Annealing Times

The requirement of the market survey was to measure sensors after ten days of annealing at room temperature. Ten days are chosen as it approximately corresponds to the time the actual sensors in the detector will be without cooling during shut downs. However, having to wait for ten days, easily another measurement for comparison could be taken several days earlier. Further measurements are interesting to understand the annealing effect over time.

In Figure 6.17 the currents for four sensors after three and ten days of annealing at room temperature are shown. Overall the currents after longer annealing times are lower, this is especially visible for the two sensors with higher irradiation. However, the breakdown voltages of the two sensors with lower irradiation are smaller for longer than for shorter annealing times. This trend is also visible for sensor 2 exposed to higher fluence.

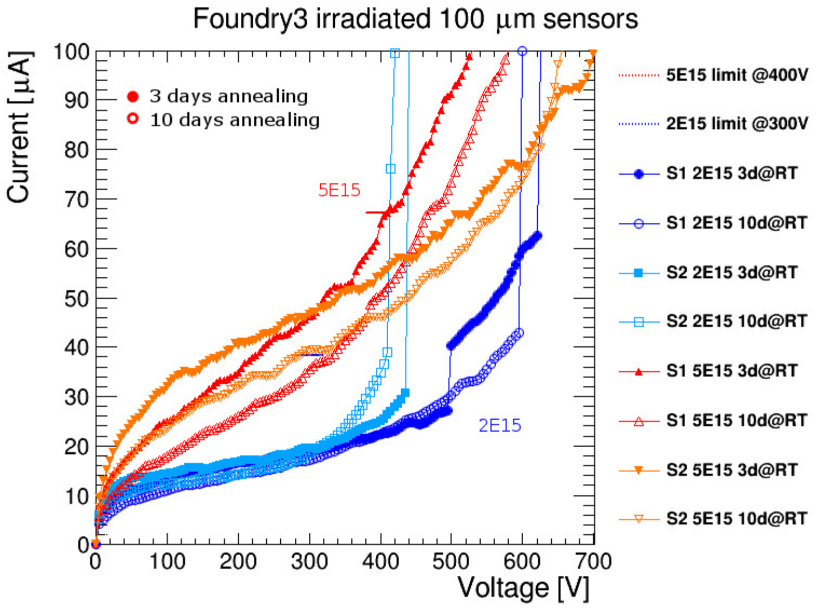

Figure 6.17: Annealing studies on sensors that were irradiated with fluences of $2 \times 10^{15}\,\mathrm{n_{eq}/cm^2}$ and $5 \times 10^{15}\,\mathrm{n_{eq}/cm^2}$. Longer annealing times, marked with open symbols, lead to lower leakage currents.

6.3. Test Beam Measurements

In addition to the laboratory tests on the bare sensors, test beam measurements for the market survey are performed at DESY on the SC sensors. These kind of tests expose the sensors to particle beams to study their behaviour in situations similar to real operation conditions. In order to be able to test the sensors, single chip modules are built as explained in Section 5.3 and shown in Figure 6.19 on the right.

The measurement of interest is the hit efficiency ϵ at perpendicular incidence. The acceptable hit efficiency of 97% has to be reached at the same voltage where the leakage current requirement is defined, which is dependent on the thickness and the irradiation dose. For thin sensors the voltages are 300 V and 400 V and for thick sensors, 400 V and 600 V for fluences of $\Phi = 2 \times 10^{15}\,\mathrm{n_{eq}/cm^2}$ and $\Phi = 5 \times 10^{15}\,\mathrm{n_{eq}/cm^2}$, respectively. For non-irradiated samples the targeted hit efficiency is 98.5%.

For samples with PT bias structure, inefficiencies around these structures are expected. With the test beam tests it is possible to validate if the efficiency of sensors biased with PT is overall high enough or if the biasing scheme must be changed for the production of sensors for the ITk.

The following sections introduce the experimental setup at DESY, explain the analysis and finally discuss the results.

6.3.1. Test Beam Infrastructure

Three main components are needed for test beams: the beam itself, a beam telescope and the data acquisition hardware and software.

Particle Beams

The particle beam is initiated in the synchrotron DESY-II which typically runs electron beams with oscillating energies from 0.45 – 6.3 GeV [147]. However, the electrons are not directly used, instead bremsstrahlung photons are generated with a fibre target in the beam orbit which are consecutively brought to collision with a secondary target where electron-positron pairs are created. The electrons and positrons pass a dipole magnet which by deflection sorts the particles by type and momentum in a collimator. Finally, in three independent beam lines and four test beam areas electron or positron beams are available with selectable energies from 1 – 6 GeV.

In Figure 6.18 the test beam generation and the test beam area at DESY are depicted. The measurements discussed in this thesis are performed with a 5 GeV electron beam to have a sufficiently high particle rate with not too much multiple scattering.

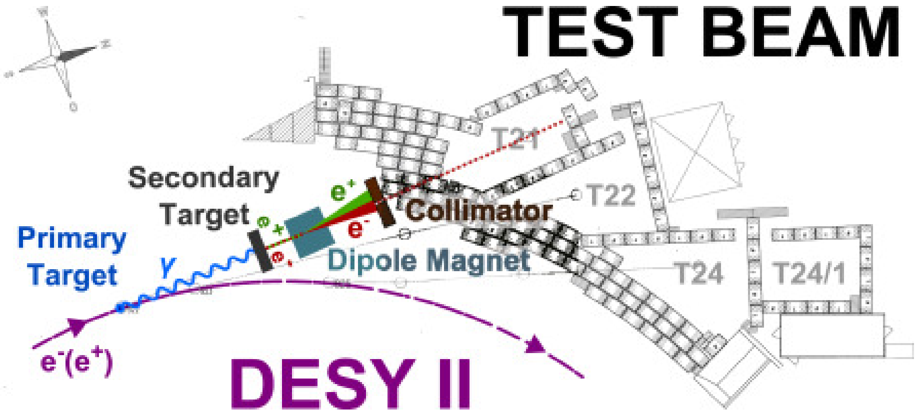

Figure 6.18: Test beam area at DESY with the different beam lines and the scheme of the test beam generation [147].

Beam Telescope

The actual measurement takes place in a EUDET-type beam telescope [148], which is an array of reference detectors along the beam line. Six reference planes, detectors based on the MIMOSA26 silicon sensor with an active area of $(2 \times 1)\,\mathrm{cm}^2$, quadratic pixels of 18.4 µm pitch and a thickness of 50 µm [149, 150], are aligned before and after the module, the so-called device under test (DUT). The readout of the MIMOSA26 sensors is done in rolling shutter mode where the rows of the pixel array are read out one after another. This consecutive readout leads to long integration times of 115.2 µs for the readout of the whole pixel matrix. Figure 6.19 shows the EUDET-type beam telescope used at DESY on the left. In the telescope two SC cards are mounted. The large aluminium jigs house the MIMOSA26 sensors and provide cooling. A thin Kapton foil protects the sensor from light

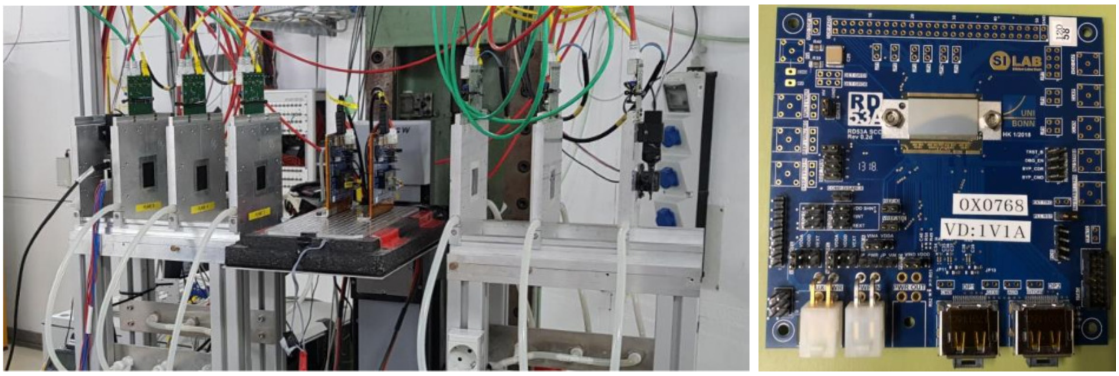

Figure 6.19: **Left:** EUDET-type beam telescope with 6 MIMOSA26 reference planes and two mounted SC cards as DUTs at DESY. The FE-I4 reference module is downstream (left) behind the telescope and just after two scintillators. Two other scintillators at a right angle are at the very front, upstream the telescope. **Right:** SC card for test beam measurements.

and minimises the material budget and thus multiple scattering. The DUT is placed on a micrometer stage to allow precise alignment in the beam between the telescope arms. A photo of one DUT, an SC card, is shown on the right in Figure 6.19. A styrofoam box offers light protection and also allows cooling with dry ice. The temperature range obtained with this passive cooling is approximately between −20 °C and −50 °C. Another reference module at the end of telescope is equipped with a FE-I4 readout chip operating at 40 MHz to set a time stamp for reconstruction as explained in Section 6.3.2.

Data Acquisition

Module Readout and Tuning. There are many different readout systems for different module types and different purposes. This section is supposed to serve as a short introduction of the systems used for the market survey, more detailed information for other setups is given in the respective chapters.

RD53A modules are read out with common ITk software (ITkSW) which is based on YARR [151]. The software called Yet Another Rapid Readout (YARR) was developed by Berkeley for the common use of the ITk community.

The readout chips of the DUTs are tuned to thresholds of 1000 e or 1500 e. The charge response, the ToT, is tuned to seven bunch crossings (7 bc) for an injected charge of 10 ke for all samples. This means that for seven bunch crossings, so $7 \cdot 25\,\mathrm{ns} = 225\,\mathrm{ns}$, the charge is above the threshold. Before data taking all noisy pixels are masked. This so-called tuning and masking is done with the ITkSW. Further details on this can be found in Section 7.3.2. The FE-I4 time-reference module has a planar silicon sensor with n-in-n doping. It is tuned to a threshold of 1500 e and a ToT of 7 bc for 14 ke. A bias voltage of 80 V is applied for full depletion.

Triggering. For the data acquisition triggering is necessary. Four scintillators with an active area of $(20 \times 10)\,\mathrm{mm}^2$ are hence mounted at the beginning and the end of the telescope in pairs of two. The trigger signal is transmitted to the Trigger Logic Unit (TLU) [152]. In the case of coincidence of the MIMOSA26 and the trigger, the trigger signal is distributed to the readout systems of the telescope planes and the DAQ system of the DUTs and the FE-I4 reference module. For the FE-I4 module the USBPix system [153] is used with the STControl software which is a small scale readout system for a limited number of FEs. A detailed description can be found in [154]. The DUTs with RD53A sensors are read out with YARR [151].

For the synchronisation of the readout trigger numbers are sent to all DAQ systems. The integration of the different DAQ systems is done with the EUDAQ framework [155, 156]. Within a graphical user interface the systems can be connected and controlled and data taking can be started and stopped. With an online monitor the data quality can be checked on the fly.

6.3.2. Test Beam Analysis

In four test beam campaigns unirradiated and irradiated samples from five of the six vendors have been measured. The test beam data is processed with the analysis and reconstruction software EuTelescope [157]. MIMOSA hits coinciding with scintillator hits are reconstructed with the General Broken Line (GBL) [158] algorithm. These reconstructed tracks are then matched to corresponding hits in the DUTs with the tbmon2 analysis framework[8].

The hit efficiency ϵ at perpendicular incidence is defined as the number of registered hits by the DUT divided by the total number of reconstructed tracks by the beam telescope:

$$\epsilon = \frac{\text{tracks in region with matched hit in DUT}}{\text{total tracks in region}}.$$

The sensors have different biasing mechanisms. For sensors with PT biasing, inefficiencies around this structure are expected, as discussed above. In order to obtain a valid assessment of the efficiency of the sensor under test if it was without bias structure, fiducial regions excluding these structures have been defined. These regions are dependent on the sensor design, as can be seen in Figure 6.20 for the two different sensor geometries. Based on the fiducial region, the fiducial efficiency ϵ_{fid} is defined in contrast to the global efficiency ϵ_{glob} for the whole sensor. Should the global efficiencies be below the accepted threshold, sensors with valid fiducial efficiencies could still be candidates for the ITk under the constraint that the bias mechanism is changed.

The sole purpose of the market survey test beams is the validation of the sensor vendors. Validation of the readout chips or the hybridisation are done in other campaigns. In order to focus on the sensor, masks are created to exclude bad areas from the experimental RD53A chip from the analysis. Pixels are masked during tuning (light blue) as can be seen in Figure 6.21 and was mentioned above. For the analysis the adjacent pixels of the pixels masked during the tuning are added to the mask. This is shown in dark blue in Figure 6.21. On the left the linear and the differential FE are used for analysis and on the right only the differential, which is baseline for the test beam tests and hence done for all other tests shown in the following.

---

[8] The code can be found in https://gitlab.cern.ch/tbmon2/tbmon2.

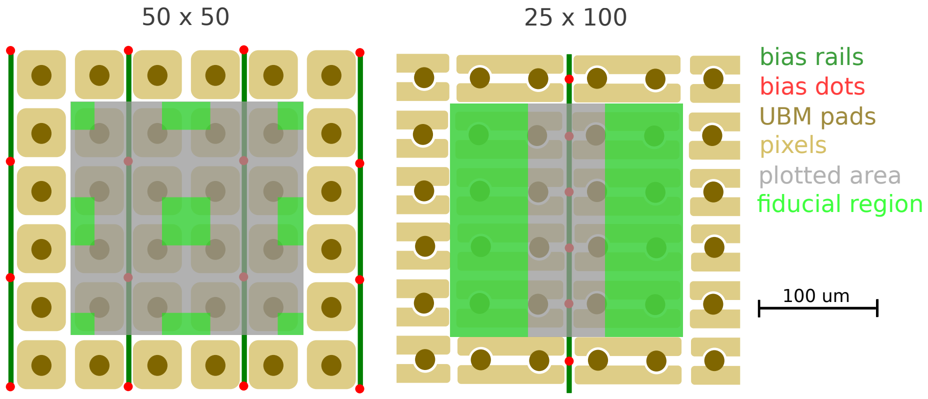
50 x 50
25 x 100
bias rails
bias dots
UBM pads
pixels
plotted area
fiducial region
100 um

Table 6.3: Hit efficiency measurements of all the modules from the planar sensor market survey. The unit of the irradiation fluence Φ is $10^{15}\,\mathrm{n_{eq}/cm^2}$. Under geometry the sensor thickness in µm and the geometry of the sensor pixels in the format pixel-length [µm] × pixel-width [µm] are given. Possible PT is marked in the column labelled PT. The masking described as unknown results from the fact that for these measurements the linear FE was used instead of the differential FE. The masks are by default determined on the differential FE and therefore no results for the linear FE are available.

ID	geometry		PT	Φ	V_B [V]	ϵ_{glob} [%]	ϵ_{fid} [%]	masked pixels	
V1S01	150	50 × 50	yes	0	90	99.3685	99.7424	803	3.18%
V1S02	100	50 × 50	yes	0	35	99.2435	99.8837	unknown	unknown
V1S03	150	50 × 50	yes	0	90	99.2962	99.7780	unknown	unknown
V2S01	150	25 × 100	yes	0	150	99.7347	99.7222	33	0.13%
V2S03	150	25 × 100	yes	0	150	99.7860	99.7779	0	0.00%
V2S11	100	25 × 100	-	0	100	99.8014	-	1702	6.75%
V2S12	100	50 × 50	-	0	150	99.8134	-	9	0.04%
V2S13	100	25 × 100	-	0	100	99.9166	-	934	3.70%
V2S14	100	25 × 100	-	0	75	99.9211	-	13	0.05%
V3S05	150	25 × 100	yes	0	80	99.4554	99.8802	988	3.92%
V3S06	150	25 × 100	yes	0	80	99.9494	99.9180	19757	40.02%
V3S13	100	50 × 50	-	0	80	99.8382	-	1960	7.77%
V4S01	150	100 × 25	-	0	150	99.7371	-	14324	56.81%
V4S02	150	50 × 50	-	0	150	99.6611	-	10617	42.11%
V4S03	150	100 × 25	-	0	150	99.8133	-	7612	30.19%
V4S06	150	100 × 25	-	0	150	99.2934	-	13687	54.29%
V6S02	150	25 × 100	yes	0	130	98.8287	99.8658	69	0.27%
V6S04	150	50 × 50	yes	0	130	98.6014	99.7185	21	0.08%
V6S05	150	50 × 50	yes	0	130	98.3357	99.7831	15	0.06%
V6S12	100	50 × 50	-	0	80	99.1251	-	648	2.57%
V6S13	100	50 × 50	-	0	80	99.5421	-	71	0.28%
V1S01	150	50 × 50	-	2	400	98.9955	-	1849	7.33%
V2S05	150	25 × 100	-	2	400	99.4303	-	5127	20.34%
V2S11	100	25 × 100	-	2	300	29.6496	-	24967	99.03%
V3S01	150	50 × 50	-	2	400	99.8105	-	10090	40.02%
V3S12	100	50 × 50	-	2	300	99.6079	-	950	3.77%
V4S01	150	50 × 50	-	2	400	98.9362	-	25166	99.82%
V6S02	150	25 × 100	-	2	400	82.0036	-	9868	39.14%
V6S11	100	50 × 50	-	2	300	99.3817	-	5148	20.42%
V1S02	100	50 × 50	yes	5	400	98.7103	99.7791	5895	23.38%
V1S03	150	50 × 50	-	5	550	098.5852	-	21821	86.55%
V2S03	150	25 × 100	-	5	600	99.3142	-	10723	42.53%
V2S13	100	25 × 100	-	5	350	99.1978	-	20116	79.79%
V3S02	150	25 × 100	-	5	600	99.7043	-	3565	14.14%
V3S03	150	50 × 50	-	5	600	99.6966	-	1368	5.43%
V3S11	100	25 × 100	-	5	400	99.0070	-	10034	39.80%
V3S14	100	50 × 50	yes	5	350	92.5727	0.967016	22020	87.34%
V3S1x1026	100	25 × 100	yes	5	400	98.8372	99.6258	8042	31.90%
V3S1x1028	100	50 × 50	yes	5	400	96.2227	99.0838	6475	25.68%
V4S03	150	50 × 50	-	5	600	99.8658	-	23238	92.17%
V6S03	150	25 × 100		5	600	97.5980	-	12924	51.26%
V6S05	150	50 × 50	yes	5	600	97.7773	99.6792	1232	4.89%
V6S16	100	50 × 50		5	400	99.1557	-	4567	18.11%

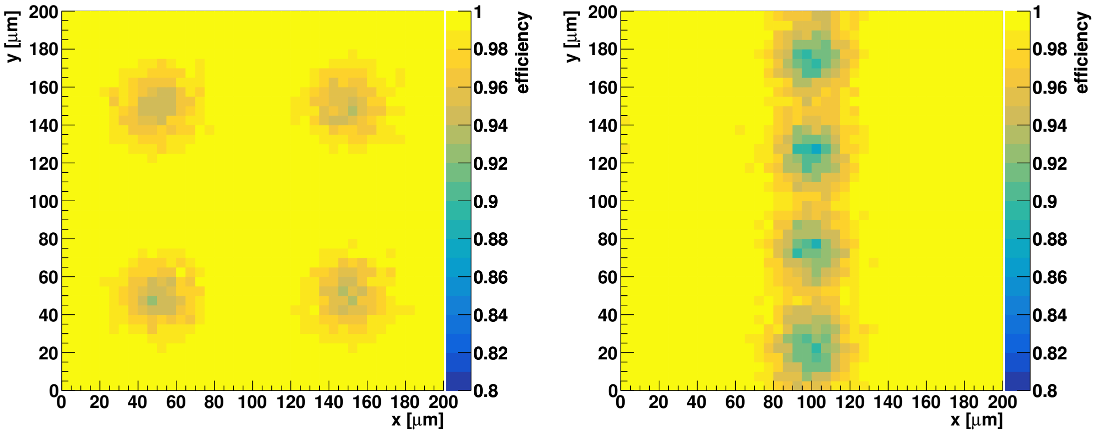

$\epsilon_{\text{glob}} = 99.2\%$, $\epsilon_{\text{fid}} = 99.9\%$ $\epsilon_{\text{glob}} = 98.8\%$, $\epsilon_{\text{fid}} = 99.8\%$

Figure 6.22: Hit efficiency maps for two different sensors with both geometries. On the left is sensor V1S02 with $(50 \times 50)\,\mu\text{m}^2$ geometry and on the right sensor V6S02 with $(25 \times 100)\,\mu\text{m}^2$ geometry. Both sensors are unirradiated. The global and the fiducial efficiencies are indicated, corresponding to the areas in Figure 6.20.

a cross check of the results.

In Figure 6.22 two efficiency maps are shown. On the left is an unirradiated 150 µm thick sensor with $(50 \times 50)\,\mu\text{m}^2$ pixel layout and PT bias. The bias regions show as circular regions with reduced efficiency. An unirradiated module with 150 µm thick sensor and $(25 \times 100)\,\mu\text{m}^2$ geometry is shown on the right. The plotted area corresponds to the grey section, indicated in Figure 6.20. All pixels over the full sensor area are measured and then folded onto the 4×4 or 2×8 pixel matrix to obtain the hit efficiency map. It should be pointed out that the scale of the colour axis has as lowest value 0.8 and not 0.

The summarised results in Table 6.3 are structured by the irradiation fluence Φ that the sensors were exposed to before the measurement. The thickness and the sensor geometry are noted in the format pixel-length [µm] × pixel-width [µm] as the rectangular pixels were available in different orientations. In the table the units are omitted because of space constraints. For the market survey sensors with PT bias structure the global and the fiducial efficiencies are calculated. PT is indicated in the respective column. Efficiencies which do not comply with the market survey criteria are marked in red, others in green. The bias voltage V_{bias} for the unirradiated sensors is set according to the requirement of $V_{\text{bias}} = V_{\text{depl}} + 50\,\text{V}$ at room temperature. For the irradiated samples, the setting of the required testing voltage was not always possible due to high leakage currents. In this case, the voltage is marked in red. In the last column, the number of masked pixels from tuning and the analysis is indicated. These pixels are hence either dead, noisy or masked by the analysis. The leakage current and the masks have a dependency. High leakage currents disturb the electronics as the random fluctuations will be too large and therefore pixels are marked as noisy. With a so-called leakage current compensation, which is a setting on the chip that can be adjusted, this can be reduced. If this fails, the bias voltage, and with it the leakage current, need to be reduced to obtain valid measurements. In total only five of

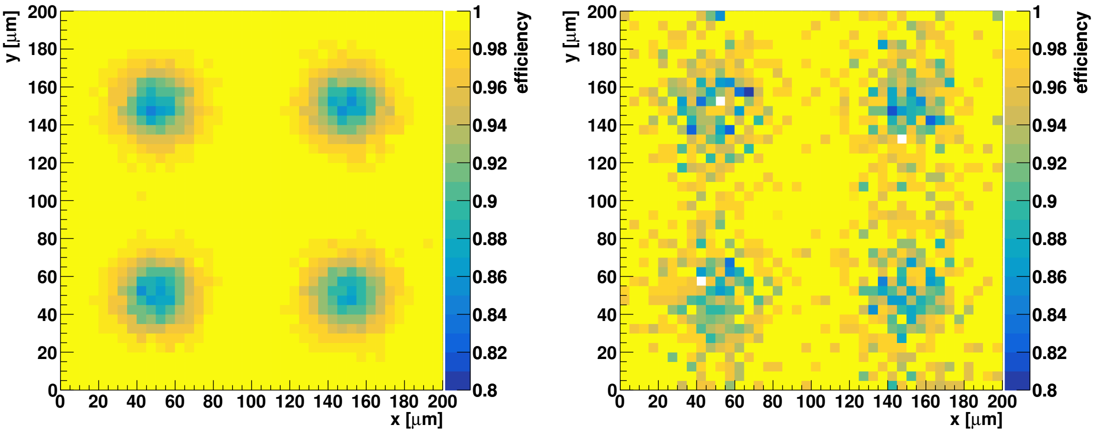

$\epsilon_{\text{glob}} = 98.3\%$, $\epsilon_{\text{fid}} = 99.7\%$

$\epsilon_{\text{glob}} = 97.7\%$, $\epsilon_{\text{fid}} = 99.6\%$

Figure 6.23: Hit efficiency maps of V6S05 before irradiation and irradiated to $5 \times 10^{15}\,\mathrm{n_{eq}/cm^2}$. The deterioration of the sensor around the PT structure after irradiation can be seen.

the samples do not pass the global efficiency market survey criteria.

In fact, there are two modules where only the global efficiency but not the fiducial efficiency is lower than the market survey requirement. V6S05 before irradiation has an efficiency of 98.3% which is, however, only 0.2% below the requirement. The fiducial efficiency $\epsilon_{\text{fid}} = 99.7\%$ meets the requirement. Also, a later measurement of the sensor irradiated to $5 \times 10^{15}\,\mathrm{n_{eq}/cm^2}$ yields both efficiencies above the threshold, as shown in Figure 6.23. The deterioration of the sensor around the PT structure after irradiation can, however, be seen.

For the actual detector operation, where perpendicular incidence is rare and usually clusters of two to three pixels detect a hit, the degradation due to the PT is not problematic.

For the other three sensors with lower efficiencies, there is a pattern visible in the mask used for the analysis. V2S11 was irradiated to $2 \times 10^{15}\,\mathrm{n_{eq}/cm^2}$ and $\epsilon_{\text{glob}} = 29.6\%$. It is expected that the number of pixels masked increases with irradiation, however, for this sensor nearly all pixels are masked, as shown in Figure 6.24, while before irradiation there were almost no pixels masked. Also, for the test beam measurements only the differential FE of the RD53A chip was measured. The synchronous and the linear FE are thus completely masked in the plot. The different origins of the masks are indicated in the plot.

The other sensor V6S02, irradiated to $2 \times 10^{15}\,\mathrm{n_{eq}/cm^2}$ and with $\epsilon_{\text{glob}} = 82.0\%$, is not nearly completely masked but has instead a masking pattern, as shown in Figure 6.25. As discussed in Section 7.3.2, the pixels with no hits can have different reasons. The digital or analog part of the chip can be broken, but also the bump connection between sensor and readout chip might be the cause. A possible cause for a higher number of disconnected bumps in the test beam samples could also be the shipping and handling during irradiation and measurements. Similar for V3S14, irradiated to $5 \times 10^{15}\,\mathrm{n_{eq}/cm^2}$, a masking pattern is seen. It masks almost the entire sensor.

However, there is another notion which should not be ignored: The effective voltage a

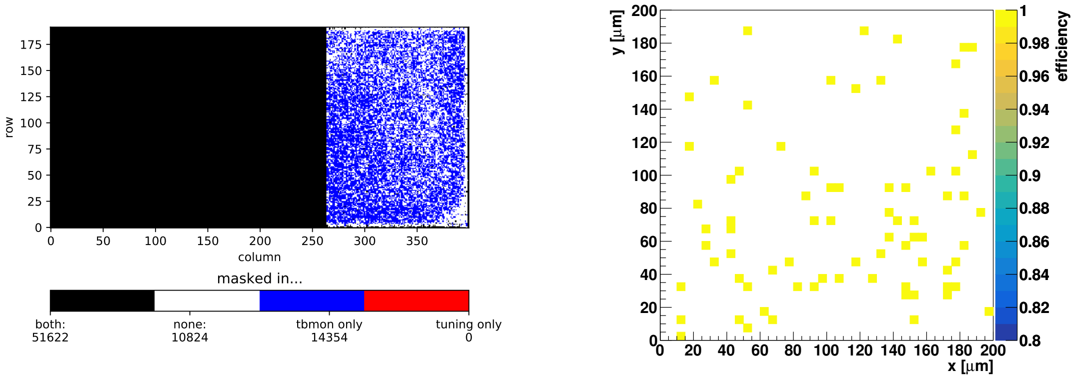

Figure 6.24: Masks and hit efficiency for V2S11. Almost all pixels are masked and the global efficiency is only $\epsilon_{\text{glob}} = 29.6\%$.

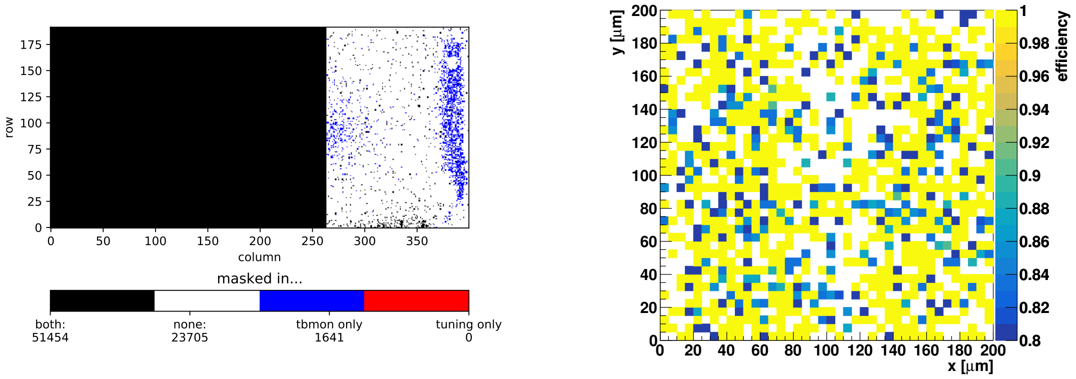

Figure 6.25: Masks and hit efficiency for V6S02. A pattern is visible in the mask which might originate from broken bump bonds. The global efficiency is $\epsilon_{\text{glob}} = 82.0\%$.

sensor is biased with is reduced for very high leakage currents. This means that the sensor behaviour is not actually measured at the voltage it is supposed to, but at a lower voltage, even though the correct voltage is set on the power supply. The effective voltage can be calculated as

$$V_{\text{eff}} = V_{\text{set}} - R \cdot I_{\text{leak}},$$

where $R = 200\,\text{k}\Omega$ is the module resistance. Very high leakage currents were present for V3S14, V1S03 and V2S13, which means that they were effectively not measured at the required voltage. However, with leakage currents at $\mathcal{O}(500\,\mu\text{A})$, the effective voltage can end up being higher when a lower voltage is set. Because of this, the three sensors were measured at a $50\,\text{V}$ lower set bias voltage. Summarising, for sensors with high leakage current the results are not completely trustworthy. Anyhow, V1S03 and V2S13 are marked as passing the requirements. In total there were 20 out of 21 sensors which passed the global requirements without irradiation. Six of eight passed after being irradiated to fluences of $2 \times 10^{15}\,\text{n}_{\text{eq}}/\text{cm}^2$ and twelve out of 14 for fluences of $5 \times 10^{15}\,\text{n}_{\text{eq}}/\text{cm}^2$.

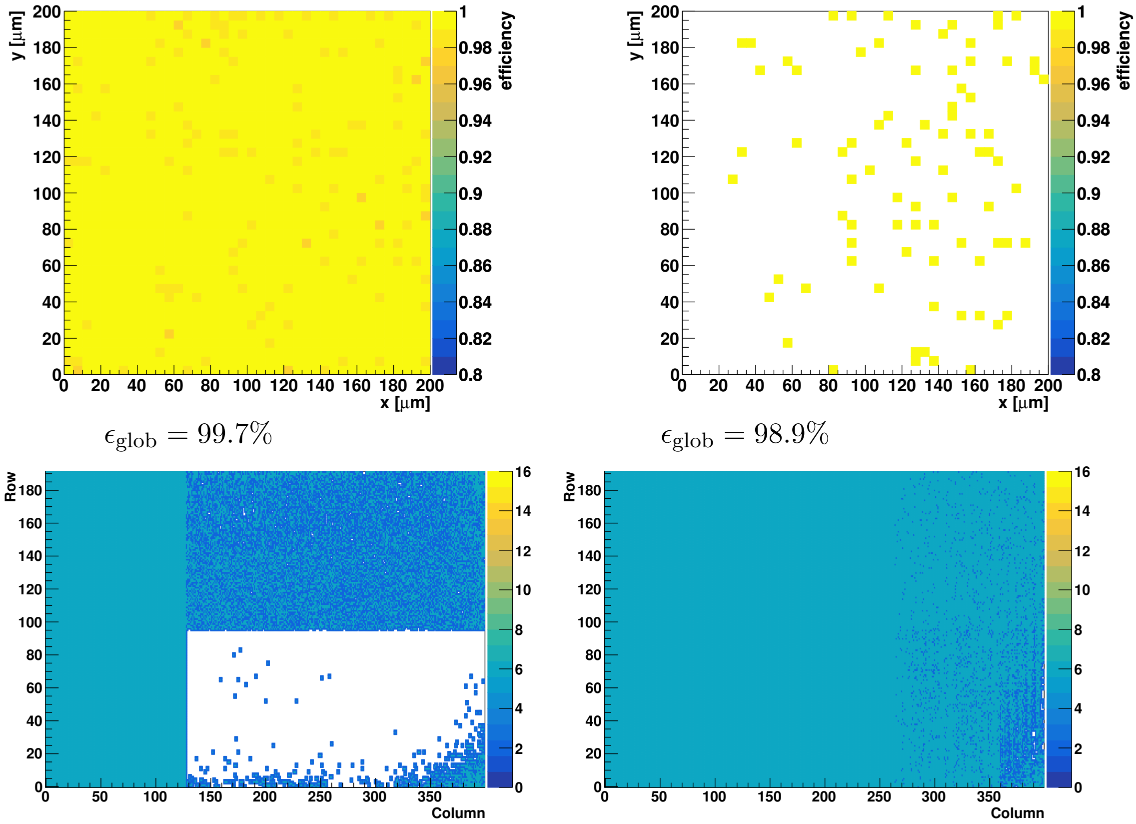

$\epsilon_{\text{glob}} = 99.7\%$

$\epsilon_{\text{glob}} = 98.9\%$

Figure 6.26: Efficiency maps and masks for V4S01. Unirradiated measurements are on the left. Measurements after irradiation to $2 \times 10^{15}\,\text{n}_{\text{eq}}/\text{cm}^2$ on the right.

Concerning the masks, it also should be mentioned that sensor V4S01 is heavily masked and the results, which pass the requirements, are thus only obtained from a few pixels. Hence these measurements may not necessarily be entirely reliable. For an example see Figure 6.26 of sensor V4S01, where the hit efficiencies before and after radiation and the respective masks are shown. For the unirradiated sensor, a global efficiency of $\epsilon_{\text{glob}} = 99.7\%$ and for the sensor irradiated to $2 \times 10^{15}\,\text{n}_{\text{eq}}/\text{cm}^2$ an efficiency of $\epsilon_{\text{glob}} = 98.9\%$ was determined. It can be seen that even though the upper part of the sensor is already almost completely masked before irradiation, there are sufficient pixels to obtain a filled hit map. After radiation, however, there are almost no unmasked pixels left.

For this vendor it is known that there is a bias structure applied only to the upper part of the sensor which induces noise. Therefore, this part of the sensor is almost completely masked.

6.4. Conclusions

Measurements within the scope of the ITk planar pixel market survey were dedicated to the qualification of vendors for ITk pixel sensors. In laboratory and test beam measurements, the performance of sensors was evaluated and suitable vendors were identified.

Through visual inspection, it could be confirmed that the yield of sensors free from defects or debris on the UBM needed for bump bonding is large enough. Also, the mechanical properties of sensors, as measured by other institutes, are good enough to allow bump bonding to the readout chip. The current characteristics of sensors measured before and after irradiation to two different fluences, also cross checked by other institutes, show that the sensors fulfil the requirements of the market survey. Thermal runaways of leakage currents and unstable currents due to higher humidities are not relevant for operation in the ATLAS detector as long as cooling and humidity control are provided.

Sensors are bump bonded to readout chips and SC card assembled which are used in test beam measurements. In test beams the hit efficiency was measured before and after irradiation. Most modules passed the requirements, however, efficiency degradation around PT bias structure could be observed. In order to determine the performance without PT bias, the efficiency in a fiducial region was defined which excludes the areas affected, and was mainly meeting the requirements.

Also, heavy masking of the sensor, possibly due to disconnected bumps and high leakage currents affects the sensor efficiency measurements. Not only are the efficiencies lower, but also the statistics and therefore the credibility of the results.

Overall, the measurements have shown a good performance of the sensor prototypes for the ITk and have resulted in three vendors to be chosen. *FBK*, which was labelled as vendor 3 will be a vendor for 100 µm sensors with temporary metal for biasing. This vendor is not qualified for the production of thick sensors and as shown in Figure 6.10 one thick sensor from vendor 3 was not meeting the requirement in the laboratory tests. *Micron Semiconductor Ltd* will be vendor for 100 µm and 150 µm thick sensors and was labelled as vendor 6. It uses PT bias structure on its sensors as they have shown to perform sufficiently well with this design. The last vendor is *HPK*, vendor 4 for 150 µm with poly silicon for biasing. As shown the PT biasing structure tried on one part of the sensors was not performing.

Concluding, in all the measurements presented above, it could be shown that the vendors qualified for the respective production meet the requirements. As of now, a pre-production of sensors is ongoing. The next step towards the ITk is the assembly and quality control of actual ITk modules, which is covered in the next chapter.

CHAPTER 7

Modules for the Outer Barrel

As discussed in Section 5.3, pixel quad modules are going to be built for all but the innermost layer of the pixel detector. The final module components will be the ITkPixV2 chip with a suitable sensor and the final design of the flex. In ATLAS, before starting the production of the actual ITk modules, several qualification steps have to be passed. Due to delays in the design and delivery of the final chip and flex, it was decided that design qualification of the modules is to be done with the prototype chip RD53A. Based on this decision, the RD53A module campaign was started which evaluates the module building process and the subsequent testing. After the successful completion of the RD53A programme, a pre-production with 10% of the total number of ITkPix modules, counting the RD53A modules, is currently ongoing to validate the findings of the previous campaign on the almost final detector components. The real production for the ITk starts only after this step is passed and the final readout chip becomes available.

In the following sections, different steps of the RD53A campaign are discussed.

7.1. Module Assembly Tooling

As the ATLAS collaboration must guarantee ten years of functionality of the ITk detector, the modules have to meet a set of specifications as defined in [159]. Ideally, all quad chip modules used in the ITk are comparable in dimensions and electrical functionality. Given the large collaboration, a common tooling was developed for a well-defined module building process and is desired to be used by all contributing institutes.

Building modules means that the flex is attached to the bare module with adhesive applied by a stencil and later wire bonded after curing. About 200 wires are bonded in a defined order which prioritise ground and reference voltage connections to prohibit electrostatic discharges that might destroy the chip. The wire bonding scheme can be found in [160] and references therein.

The tooling for quad module assembly was developed at the University of Göttingen to be used as the default tooling for the ITk pixel collaboration. It is based on an initial

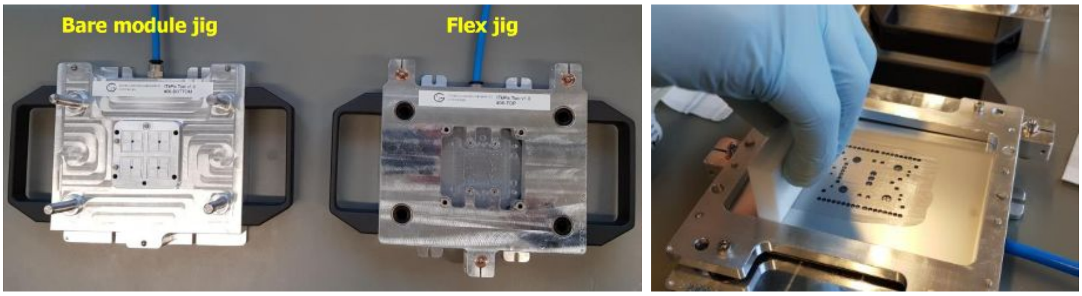

Figure 7.1: **Left:** The tooling for the quad module building comprises two jigs, one for the flex and one for the bare module. **Right:** Adhesive is spread on the flex with the help of the stencil tooling.

concept which stems from the IBL module production [161] and was developed for the FE-I4 modules as described in [5]. In parallel, a tooling was designed and produced in Japan, then underwent upgrades for the different module components. This tooling is being qualified to be used in Japan and will not be discussed any further. Similar, in Oxford, a specific tooling for their laboratory equipment exists and is being qualified for them to be used.

Based on lessons learnt from the initial toolings, a more advanced version was developed by the workshop of the II. Institute of Physics of the University of Göttingen. This first RD53A tooling has undergone some development so that there exists another version now, which is adjusted to the final module components. In this work the main focus is on the RD53A version of the tooling as during the course of this thesis only RD53A modules have been built. So the reader should assume that whenever a tooling is mentioned, it is the RD53A version of the tooling.

The tooling for quad module building comprises two jigs that carry the flex and the bare module and allows to place them on top of each other with 50 µm precision through rods and ball bearings. With an additional stencil tooling and a spatula, a predefined amount of adhesive can be spread on the flex before closing the tooling for attaching and curing. Compared to the manual glue deposition for the FE-I4 module building this constitutes a large improvement. Also, the legacy tooling had only one jig where the bare module was aligned and the flex positioned on top, thus aligning the flex and mating of the two components was done in one step. The disentanglement of the flex positioning with small pins and the overall positioning of the flex with respect to the bare module with larger rods is an advantage over the FE-I4 tooling. Also, the alignment of the bare module and the flex itself was improved by the use of pins with soft coating and perfectly fitted stainless steel alignment pins, respectively.

The tooling and an example of spreading the adhesive with the stencil tooling can be seen in Figure 7.1. Technical drawings and descriptions for the RD53A tooling can be found in [162] and likewise for the ITkPix tooling in [163].

In Figure 7.2 the module building setup of the University of Göttingen is shown with two jigs, vacuum suction, glue gun, stencil frame, precision shims and dial gauge. The module components for a dummy module are shown on the jigs. This will be explained in Section 7.1.1.

In the following sections, after detailing the specifications of the module and its compo-

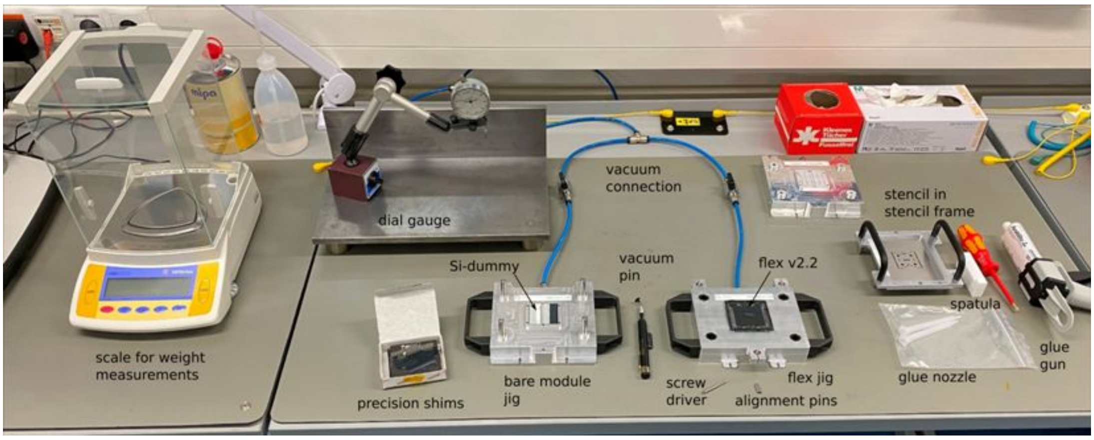

Figure 7.2: Göttingen module building setup in the lab with two jigs, vacuum suction, glue gun, stencil frame, precision shims and dial gauge. A dummy bare module and a flex v2.2 are shown on the jigs.

nents, the module assembly procedure is presented.

7.1.1. Assembly Specifications

Before building RD53A quad modules, module assembly sites have to undergo a qualification process where they show that they are capable of building modules that fulfil the general requirements. For this purpose silicon dummies instead of bare modules and the preliminary version 2.2 (v2.2) of the common quad flex are used.

The actual RD53A quad module building is done with the fully functioning RD53A bare modules and version 3.8 (v3.8) of the common module flex. The drawings for the RD53A flex v3.8 can be found in [164].

Regarding the assembly itself, there are certain requirements which need to be met. In the following these different requirements and specifications are explained.

Component Specifications

In order to validate the functionality of the module assembly tooling, the exact dimensions of the bare components need to be known.

In terms of the bare modules, the overall flatness of the bare module and the Si-dummy should be $\pm 25\,\mu m$ and the coplanarity $\pm 50\,\mu m$. For the bare module the bump bond layer between FE and sensor should be between 10-25 µm. The specifications for outer barrel modules as of Ref. [165], which was used for the design of the tooling, are shown in Table 7.1.

The mechanical flex v2.2 was fabricated before all the details of the flex design were finalised and has a few significant differences with respect to flex version 3.8. Some SMD components, the temperature sensors (NTCs) as well as the HV hole changed location from v2.2 to v3.8. Additionally, the alignment holes on the frame were changed into slots on the diagonal for better alignment on the flex jig during assembly. The main change is, however, the size of the inner part of the flex, which is glued on the bare module, as listed in Table 7.1. Also, there were no tolerances specified for flex v2.2. Based on experience from flex validation sites, the vendor fabrication tolerances are about 100 µm[1].

Table 7.1: Specifications of the two different versions of the flex and the Si-dummy.

	y-dim.	x-dim.	Height
Si-dummy	(41.10 ± 0.05) mm	(42.20 ± 0.05) mm	$(325 + 55 - 40)$ µm
Flex v2.2	40.6 mm	40.4 mm	(160 ± 20) µm
Flex v3.8	$(40.4 + 0.04 - 0)$ mm	$(40.4 + 0.04 - 0)$ mm	(160 ± 20) µm
Distance dummy	0.5 mm	1.8 mm	

Assembled Module Specifications

For the assembled modules, in terms of mechanical requirements, a module needs to be attached with a precision of ±50 µm in x and y to guarantee wire bonding angles and suitable connector positions. For dummy modules the nominal x-distance between flex and Si-dummy on both sides of the module is 900 µm and the distance at the y-top is 250 µm. For real modules this should be the same, however, the module specifications have changed over time. The original tooling was designed with the specifications in [165] which correspond to the Si-dummy specifications as listed in Table 7.1. The actual production specifications of the bare module vendors are subject to small changes and given in Ref. [166].

In terms of height, the module envelope of 2.25 mm must be respected as defined in [167]. As the thickness of the module is mainly influenced by the adhesive, it is therefore subject to specifications. The coverage under the flex must be at least 80% without spreading beyond the edge of the flex to allow wire bonding and assure stability of the module. This leads to the requirement of an adhesive thickness of (40 ± 15) µm and a defined weight of the adhesive. Under the temperature sensors (NTCs) on the flex must be adhesive for good thermal connection to the sensor. Additionally, points of greater stress where the modules are picked up during loading must also be supported with adhesive.

The assembly procedure was developed to meet all these requirements and is presented in the following section.

7.1.2. Assembly Procedure

The assembly procedure differs slightly for dummy modules and real RD53A modules. As discussed in Section 7.1.1, the module components underwent changes. However, the module assembly with the Si-dummies and flex v2.2 is more challenging than what is expected with flex v3.8. Therefore, the successful site qualification with the dummy modules is more than sufficient to ensure a high yield with the RD53A quad modules.

As the module building qualification of the University of Göttingen and results from the later built real modules were done within the scope of this thesis, both are covered in the following. The Si-dummy will be referred to as dummy bare module, to make the descriptions easier.

The assembly process includes the calibration of the tooling but also measurements of the components before and after attachment. For all modules, the following measurements

---

[1] Private communication with project engineer Sneha Naik from the University of Glasgow.

are carried out:

- Measuring of the dimensions of the bare components before assembly.
- Weight of bare components and module after assembly.
- Measurements of height of the module and the adhesive in particular.
- Pull tests of the wire bonds.
- Visual inspection at various processing steps.

The content of the following sections is taken or adapted from the module assembly documentation [160].

Calibration of the tooling

In order to build a module with an even adhesive layer, it is important to calibrate the tooling. The important parts of the tooling to be parallel are the two surfaces of the jigs where (dummy) bare module and flex touch and this is assured by the mating principle with guide rods and bushings, not by their angle with the back plane of the respective tooling jigs. There is no need to specifically characterise the slope with respect to the back plane and if these planes are not parallel this does no harm to the module. Getting the surfaces of interest parallel to each other is obtained by calibrating the tooling with the three adjustment screws and precision shims with 40 µm thickness.

The calibration requires the following steps:

1. The flex needs to be aligned onto its respective jig by aligning the flex with two alignment pins and the aluminium block.
   - The flex is placed on the flex jig.
   - The frame-aligning pins are inserted according to the flex in use: for flex v2.2 the holes on the top left and bottom right corner, see Figure 7.3 on the left. For flex v3.8 the hole on the top right corner and the slot on the bottom right corner, see Figure 7.3 on the right.
   - The aluminium block is used to flatten the flex.
   - The vacuum is turned on to fix the flex on the jig.
   - Careful lifting of the aluminium block and removal of the frame-aligning pins from the flex jig.
2. The (dummy) bare module needs to be aligned on the bare module jig.
   - The (dummy) bare module is put on the bare module jig with the help of a vacuum pen.
   - The (dummy) bare module is positioned on the jig such that it touches all three alignment pins, see Figure 7.4.
   - Turning on the vacuum fixes the (dummy) bare module on the bare module jig.

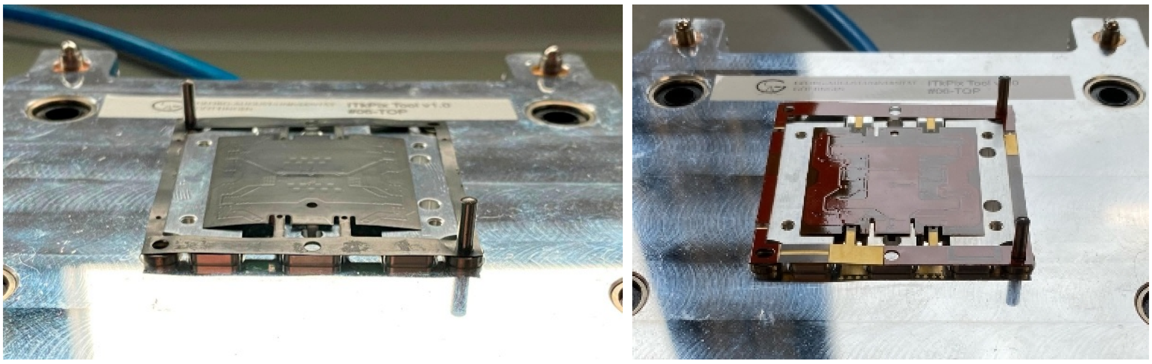

Figure 7.3: **Left** Positions of the alignment pins on the flex v2.2. **Right:** Position of alignment pins on the flex v3.8.

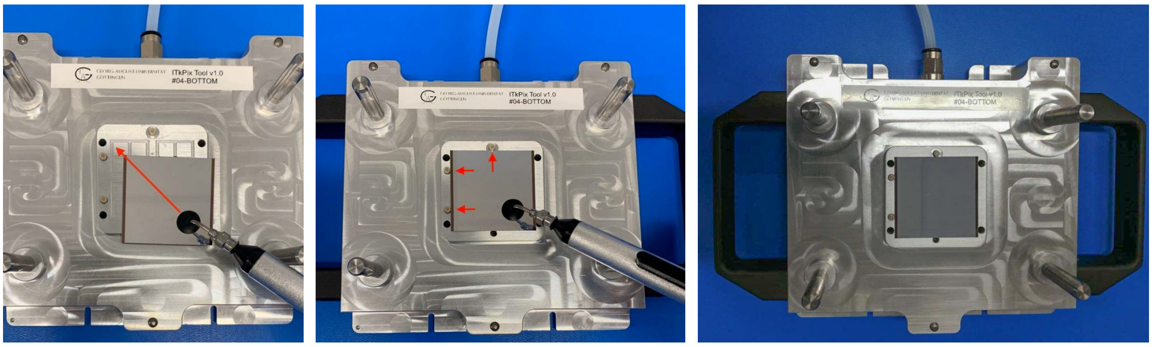

Figure 7.4: **Left:** The process of placing a dummy bare module on the bare module jig. **Middle:** Alignment of the dummy bare module to the alignment pins. **Right:** Dummy bare module aligned with alignment pins on bare module jig.

3. The adhesive height is set.
   - The precision shims are placed on top of the (dummy) bare module with the help of a vacuum pin.
   - The flex jig is placed very carefully onto the (dummy) bare module jig by mating the guide rods and the guide bushings.
   - Now the adjustable screws need to be screwed to the appropriate level with the help of a hex wrench and a dial gauge. Here it is most important that the screws are screwed very slowly and gently so that no movement is detected on the dial gauge. As soon as the slightest resistance is felt or a movement is detected, the screwing process needs to be stopped and reverted immediately. All three screws are lowered and then the locking nut is fastened. This should also happen with a lot of care.
   - Then the flex jig is removed from the bare module jig and the shims are removed.

To control the height of the adhesive, aforementioned adjustment screws set the distance between the jigs. As it became evident in first measurements that all institutes are tending to higher adhesive thicknesses than calibrated, the use of the dial indicating gauge was introduced. It is set up such that it monitors a point on the closed tooling surface, as shown in Figure 7.5. While screwing down the adjustment screws and tightening them, the

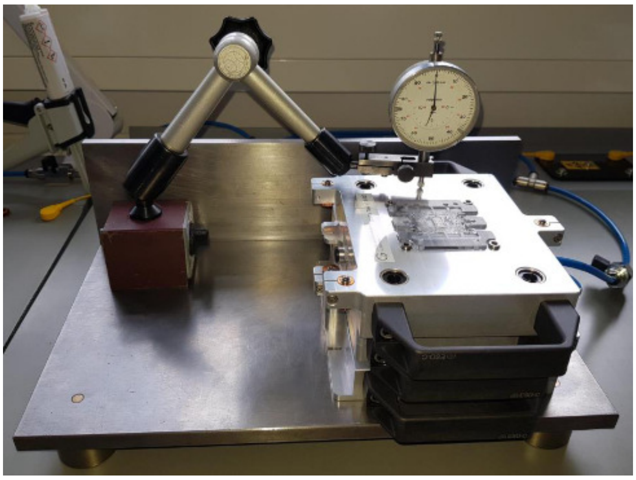

Figure 7.5: **Left:** A dial gauge is used for setting the adjustment screws. The needle is placed on the closed tooling with an additional jig on top and closely monitored when turning the adjustment screws.

dial gauge is constantly monitored and the screwing reverted in case any movement of the tooling surface is shown on the dial gauge. For this method to work well, a second flex jig with $\approx 1.2\,\mathrm{kg}$ as weight was put on top of the closed module.

Assembling the module

Within the course of module building experience, the stencil layout was changed several times to cover the full flex region with adhesive. In the photos in the following there are therefore various stencil designs shown. For the purpose of the pictures the design can be ignored, unless specifically mentioned. In Section 7.2.3 studies on the pattern are discussed in detail and it should be noted that the glue weight clearly differs for both versions.

Concerning the general attachment procedure, there is a set of steps to follow. It is assumed that the flex and the (dummy) bare module are still in position on their respective jigs after calibration of the tooling.

1. The stencil tooling is placed onto the flex jig. The stencil frame guide rods are such that only one orientation allows insertion into the flex jig. It is extremely important that the stencil is screwed correctly in the stencil frame.

2. The adhesive is distributed on the stencil using the mixing nozzle on the glue gun. Ideally the line should look like shown in Figure 7.6 in the middle.

3. With the spatula the adhesive is spread into the stencil holes in a controlled motion. The stencil looks afterwards like shown in Figure 7.6 on the right. Figure 7.7 shows a flex with adhesive distributed using the stencil method.

4. The stencil tooling is removed from the flex jig.

5. The flex jig is very gently placed onto the bare module jig, leaving vacuum active.

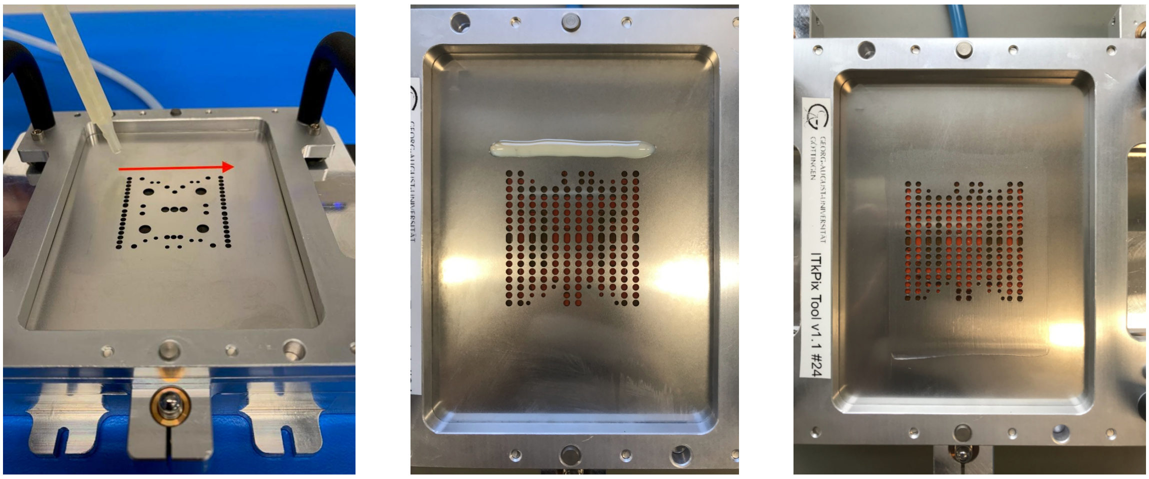

Figure 7.6: **Left:** The stencil tooling is placed on top of the flex jig. Putting the adhesive on the stencil. **Middle:** Adhesive distributed on one end of the stencil. **Right**: Adhesive spread across the stencil.

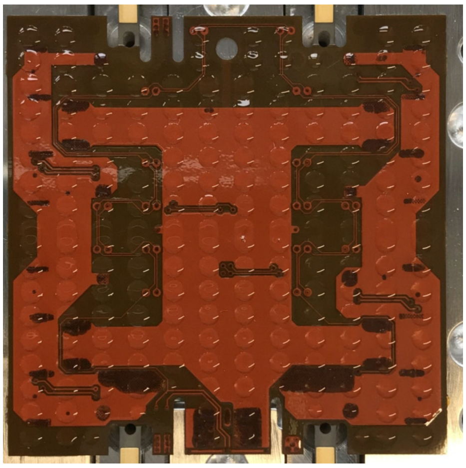

Figure 7.7: The adhesive pattern on a flex v3.8 (with the almost final stencil) distributed with the stencil method.

6. Leaving the flex jig on the bare module jig for at least 8 h at more than 21°C allows the adhesive to cure completely. An additional weight of ≈ 1 kg should be placed on top of the tooling so that any upwards force originating from the viscosity of the adhesive is counterbalanced. An additional jig can be used for that.

The mechanical assembly of a module is completed after the aforementioned steps. However, electrical functionality is only established after wire bonding. Dummy modules, even though in principle some electrical tests would be possible, are only wire bonded for practice and never tested electrically. Both module types undergo quality control (QC) measurements after gluing to analyse the assembly quality.

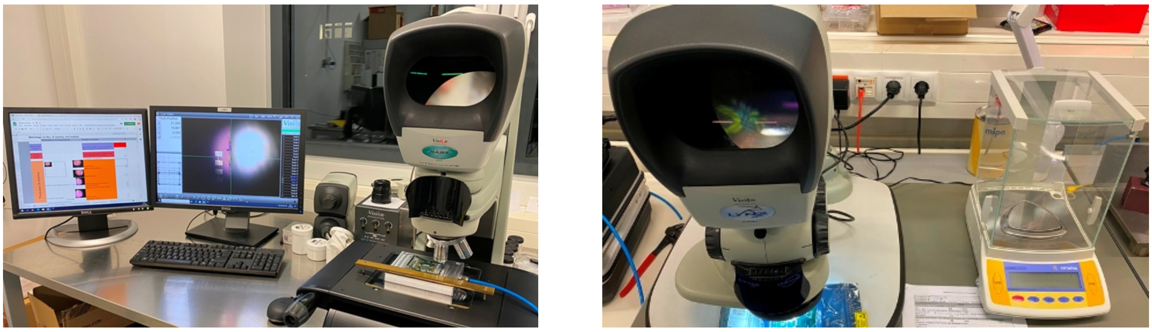

Figure 7.8: Microscope and stereomicroscope for metrology measurements and visual inspection.

7.2. Quality Assessment

In 2019 and 2020 Göttingen produced 24 version 1 toolings for 15 institutes worldwide, which all required validation before sending them out. The validation tests of the toolings were done using metrology on RD53A modules and dummy components with the metrology tools as described in Section 7.2.1 and are discussed in Section 7.2.2.

7.2.1. Measurement Setup

In the following, the measurement setup for all quality control tests, before and after gluing, is introduced. The metrology equipment for measuring the module and the module components in all dimensions and doing visual inspection especially for the wire bonding comprise a microscope with x-y-stage and adjustable focus for z-height measurements and visual inspection and a stereomicroscope for wire bond inspection. Both microscopes are shown in Figure 7.8. The metrology microscope is the same that is also used for the sensor market survey metrology measurements, as explained in Section 6.1.

Height measurements are performed with the dynascope that measures the height via the focus. The measurement vacuum jig of the dynascope is defined as reference plane for the measurements. Hence, in order to measure the height, the (dummy) bare module is flattened with vacuum on the vacuum chuck and the height of the module component is measured via a defined set of points on the surface. The height measurement is non-automatic, however, certain analysis functions are provided which are employed for the measurement of the height. With the defined points the (dummy) bare module plane is defined and the distance between the reference plane and the (dummy) bare module plane then results in the (dummy) bare module height. While the Si-dummy has constant height, for the bare module there are two measurements to be made: the height on top of the sensor and the height of only the readout chips. Figure 7.9 shows the measurement points for the Si-dummy and the bare module in the middle and on the left, respectively.

The bow is obtained by measuring nine points on the dummy (bare module) without vacuum being applied, and calculating the sagitta, as shown for the sensors in Section 6.1.

The flex height is also measured when the flex is held down with vacuum. For this measurement many more points are needed than for the sensor, as shown in Figure 7.9 on

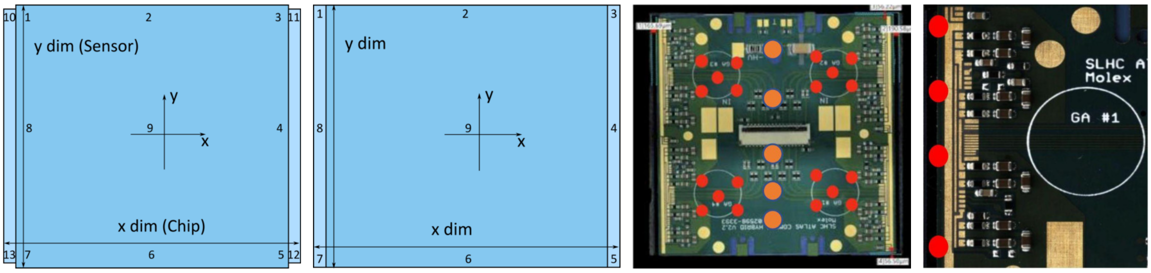

Figure 7.9: **Left:** Measurement points on a bare module. **Middle left:** Measurement points on a dummy bare module. **Middle right and right**: Measurement points on the flex. The wire bonding area is measured with four points, the keep clear areas with five measurements, the connector and the capacitor with two measurements each. For the bow of the assembled module a row of measurements is taken in the middle of the module.

the right two images. The flex is divided in different areas as introduced in Section 5.3.3. The wire bonding area is measured with four points, the keep clear areas with five measurements, the connector and the capacitor with two measurements each.

Height measurements on the assembled module are again performed with vacuum turned on with the exact same points as on the flex in order to extract the thickness of the adhesive between (dummy) bare module and flex by subtracting the heights of the bare components. For the bow a row of measurements is taken in the middle of the module, as indicated in Figure 7.9.

For a cross check the flexes and dummy bare modules were also measured with a micrometer screw before and after gluing. Consistent results were achieved so that the measurement with the micrometer screw that is more dangerous for the components was dropped for the real modules. An example for a cross check is shown in Section 7.2.2.

7.2.2. Module Assembly Process

The validation tests of the tooling comprises x-y-alignment and z-height tests and visual inspection, assuring the performance of the tooling to be within the required precision. For the tests a dummy bare module was used instead of a real bare module in combination with a flex v2.2. The same components were used for all the toolings to assure comparability.

First, in order to qualify the gluing procedure, repeated tests with one tooling have been conducted on the bare components and on the assembled module. The following two sections describe the x-y-alignment and z-height measurements.

z-height

As mentioned in Section 7.1.2, the adhesive height is set by calibrating the distance the two tooling jigs are apart when mating them. During validation, the adhesive height was causing the main problem as the actual obtained adhesive height is not the same across the module and also not necessarily as expected from the set distance. The aforementioned dial gauge with 0.01 mm accuracy was successfully used to cope with the problem by monitoring the setting of the distance between the jigs, see again Figure 7.5.

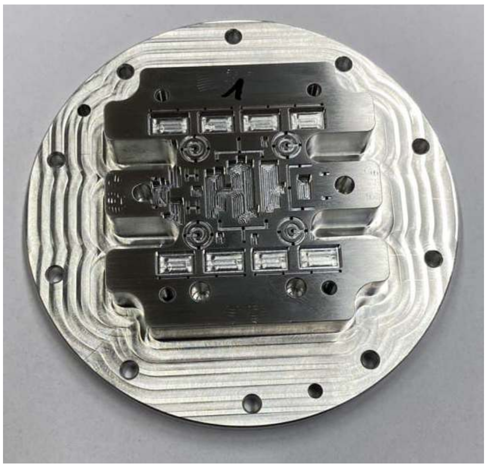

Figure 7.10: The new aluminium inlay for the flex jig of the tooling.

Table 7.2: Height measurements with micrometer screw and microscope in comparison. All values are in µm.

	All	Wire bonding area	Keep clear area	Connector	Capacitor
µm-screw	50.8 ± 8.2	54.9 ± 5.4	40.3 ± 5.9	51.0 ± 12.7	46.5 ± 3.4
Microscope	49.0 ± 10.4	51.9 ± 9.9	41.8 ± 7.2	55.8 ± 6.4	35.8 ± 4.9

Moreover, the adhesive height in the middle of the module has always been too high, unless some foam piece was inserted in the middle of the flex jig inlay to enforce pressure on the flex. It was realised that this was due to the instability of the flex inlay under vacuum which was made out of perspex. Consequently, new aluminium inlays (G.AL C210 DYNAMIC/ AW 5083-O3) were machined in the central workshop of the University of Göttingen, as shown in Figure 7.10 on the left. Plan parallelism and flatness have been measured on these inlays and are within tolerances. The validation of these new inlays was also done with gluing another dummy module.

The height measurements on the glued module, performed with a micrometer screw and the microscope for comparison, show very similar values all across the module surface. In Table 7.2 the results for the specific areas on the flex as introduced in Section 5.3.3 are shown. The adhesive weight was measured to be 25.3 mg.

x-y-alignment

On the left in Figure 7.11, the measured distances for the validation of the x-y-alignment on the upper left corner are shown. The image also indicates the bare module alignment pins existent on the bare module jig. First measurements were done on a spare bare module jig of the tooling, as shown in Figure 7.11 in the middle. The distances of interest for the measurement of the alignment on a dummy module as seen under the microscope are shown in Figure 7.11 on the right.

Example x-y-distance measurements for one glued module are presented in Table 7.3. Only one of the measurements is outside the tolerances, when comparing them to the

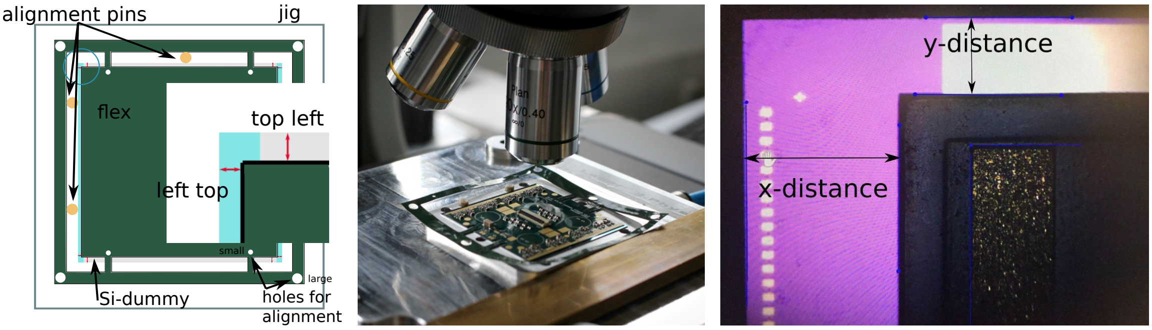

Figure 7.11: **Left:** The measured distances for the validation of the x-y-alignment and the alignment pins as existent on the jig of the tooling are shown. **Middle:** Setup for the microscope measurements of a glued module. **Right:** The distances of interest for the measurement of the alignment on a dummy module as seen under the microscope.

Table 7.3: Example x-y-distance measurements for one glued module. For each side two measurements have been taken and averaged. The precision for one distance measurement is 3.7 µm. For the values stated below the precision is therefore 5.2 µm.

Measurement	Mean [µm]	Nom. [µm]	Mean - Nom. [µm]
Top distance	283.5	350	-66.5
Right distance	919.3	900	19.3
Bottom distance	336.3	350	-13.7
Left distance	853.8	900	-46.2

nominal values as presented in Table 7.1.

However, deviations of the flex and dummy bare module geometries can also lead to x-y-distances between the separate components that are not within the tolerances. The dummy bare modules used within the scope of this thesis were found to be ≈ 50 µm larger in x- and y-direction.

In Figure 7.12 on the left the by the module component sizes defined distances and the derived distances are shown. Based on the alignment in the tooling with the pins on the left side and on the top for the bare module and the two pins for the flex, two distances between the flex and bare module edges are defined. The other two distances can be derived:

$$\begin{aligned}\text{distance}_{\text{right}} &= (x_{\text{measured\_Si}} - x_{\text{measured\_flex}}) - 900\\ \text{distance}_{\text{bottom}} &= (y_{\text{measured\_Si}} - y_{\text{measured\_flex}}) - 250\,.\end{aligned}$$

Given the detected deviation from the specifications, the actual distance should be taken into account for the analysis of the distance for the non-defined sides. Also, the relative distances between frame and flex inner part are not always according to the specifications. Hence, for each module, the actual expected target needs to be calculated as shown in Figure 7.12 on the right. The calculation is the following:

$$\text{Offset in flex} \;=\; \text{Distance hole-flex-edge - nominal value.}$$

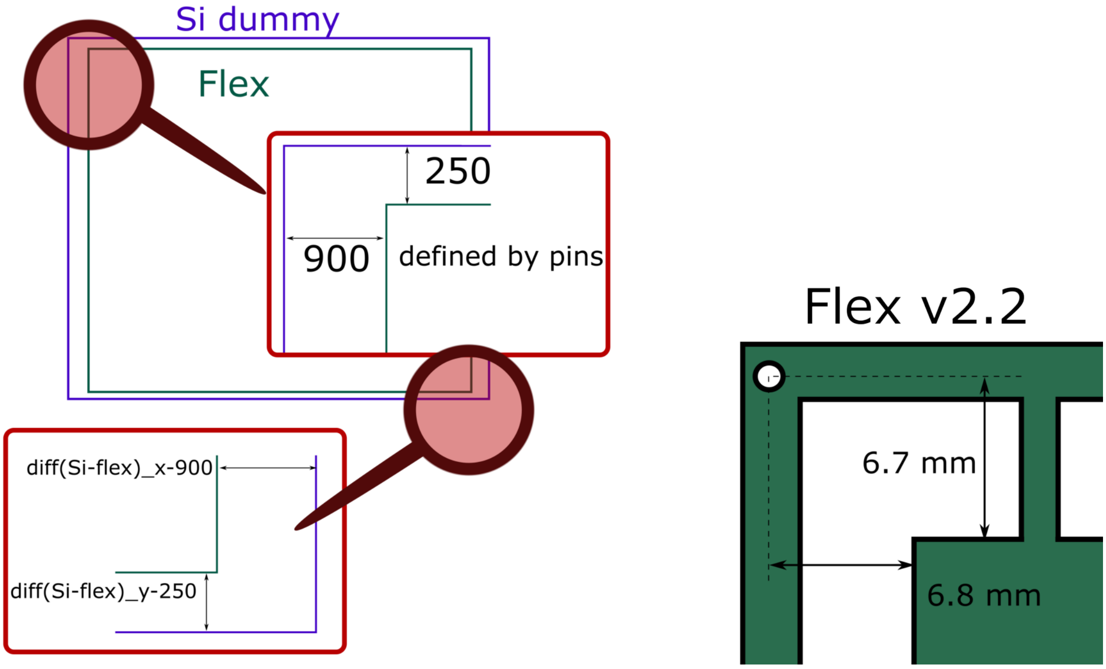

Figure 7.12: **Left:** Defined and derived distances for the relative alignment position of the flex and the dummy bare module. **Right:** Defined distances for the relative alignment position of the flex frame and the flex inner part.

This offset then needs to be subtracted (or added) for all sides. It could also be shown that the y-alignment at the top (distance hole and central flex edge) differs by $\approx 50\,\mu\text{m}$ for the flex v2.2.

By taking these measured distances of the glued module into account, the alignment capability of the tooling could be verified to be within $\pm 50\,\mu\text{m}$. Given the recent relaxation of the criterion, $\pm 100\,\mu\text{m}$ deviation instead of $\pm 50\,\mu\text{m}$, slight inconsistencies in the bare components can be seen as non-problematic.

Another value that needs to be determined is the distributed adhesive weight. Therefore the bare components are weighed before assembly and the glued module after assembly. Evidently the subtraction of both yield the adhesive weight. The nominal weight of the glue has changed frequently due to different versions of the stencil. For the five dummy modules used for the qualification of the University of Göttingen as module building site, the glue weights are listed in Table 7.4. The nominal weight of the glue with the stencil version that was used is 26.8 mg. Due to measurement problems on the components of the modules (not perfectly dry flexes), lower glue weights than expected are measured. Monitoring of the weight of the flex for 5 min results in smaller flex weights and the corresponding glue weight is marked in the table as "corrected".

Not actually counting to the metrology measurements, pull tests have to be performed on the wire bonds to test their strength. Some specifically for this purpose bonded wire bonds are pulled before setting the module under electrical tests. Within the scope of this thesis pull tests have only been performed on dummy modules and are hence not presented here.

Table 7.4: Glue weight of five modules with a flex v2.2 and a Si-dummy. Measured with a precise scale with uncertainty of 0.05 mg. All values in mg.

	1	2	3	4	5
Glue weight	17.7	15.3	32.1	12.6	11.9
Corrected glue weight					25.5

7.2.3. Delamination of Module Components

Modules might delaminate under temperature changes as expected during operation [168]. This comprises small range temperature changes from module operation between ≈ −40 °C and ≈ 25 °C, but also catastrophic scenarios such as CO_2 from the cooling leaking on the module and exposing it to temperatures of ≈ −55 °C or broken cooling and failing interlock which will heat up the modules to ≈ 60 °C. Simulations of the module with adhesive applied with the stencil pattern as depicted in Figure 7.6 on the left were a reason for concern. Hence, the stencil was improved to cover the full flex area with adhesive, as shown in Figure 7.6 in the middle and on the right, to reduce probable delimination. The design on the right was reworked several times with small changes to the hole diameter. The final version is not shown in this thesis.

In the following, validation tests of the new stencil will be presented and concluded by the delamination tests.

Stencil Validation Tests

For the new stencil several assemblies were performed in Göttingen with Si- or glass-dummies and similar adhesive layer thicknesses achieved as before. The results for the specific areas on the flex are shown in Table 7.5 and 7.6. As shown, the target adhesive weight of 50 mg was also reached.

Table 7.5: Height of a module with a flex v2.2 and a glass dummy. Measured with a micrometer screw. All values are in µm.

	All	Wire bonding area	Keep clear area	Connector	Capacitor
Height	49.4 ± 11.7	45.9 ± 9.9	48.8 ± 2.9	48.5 ± 0.7	72.0 ± 18.4

Table 7.6: Height of a module with a flex v2.2 and a Si-dummy. Measured with a micrometer screw and the microscope for comparison. All values in µm.

	All	Wire bonding area	Keep clear area	Connector	Capacitor
µm-screw	43.9 ± 16.2	35.4 ± 9.1	47.8 ± 6.9	49.5 ± 10.6	81.5 ± 2.1
Microscope	51.5 ± 17.2	49.8 ± 17.5	44.1 ± 6.2	50.8 ± 10.6	80.8 ± 2.1

For a glass dummy the height of the glued module was measured with a micrometer screw. The adhesive weight is 50.1 mg.

For the Si-dummy bare module the height of the glued module was measured with a micrometer screw and the microscope for comparison. The adhesive weight is 50.8 mg and the height of the bare components is for the Si-dummy $(318.8 \pm 6.7)\,\mu\text{m}$ and for the flex $(199.7 \pm 10.4)\,\mu\text{m}$.

In order to validate the stencil, several groups of institutes in ITk conducted assembly trials. The judgement was based on the glue pattern either visible through the glass or after removing the flex from the dummy bare module. A coverage of 80% of the module area with adhesive is required. In order to evaluate the gluing several times, it was decided that the modules should not be cured completely to allow reuse of the components.

Among the institutes very short times of $\approx 30\,\text{min}$ and longer curing times were tried. In order to obtain valid results, the adhesive must not be altered between gluing and judging the glue pattern. Possible issues are that the flex can bend once the vacuum is released and thereby exert a force on the adhesive and make it spread. Additionally, a very soft glue might be compressed further by the weight of the glass dummy itself.

To tackle these problems the vacuum should only be released of the bare module jig (and not of the flex jig) after mating the jigs to avoid bending of the flex. Also, the curing time should be at least long enough to prevent the glass dummy from compressing the glue. For the evaluation of the pattern a picture analysis is suggested as the other option would be a judgement by eye.

Based on these suggestions to the assembly procedure and the evaluation of the adhesive coverage, an evaluation of the adhesive pattern without distorting the pattern is feasible. Studies with different curing times using plexiglass and flex v3.8 were performed and are presented in the following.

On the example of a short curing time of 15 min the analysis procedure is explained. To see how the adhesive behaves, initially, only the vacuum on the bare module jig is released. The pictures of the adhesive coverage are shown in Figure 7.13.

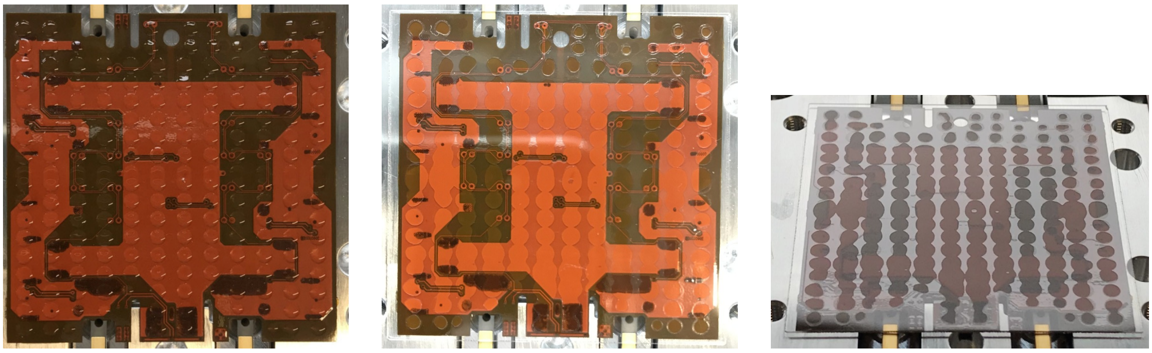

Figure 7.13: **Left:** Gluing pattern after application. **Middle:** Gluing pattern after 15 min curing time and only releasing the vacuum on the bare module jig. **Right:** Gluing pattern as seen from the side for contrast between adhesive covered area and free space.

A python script, partly written by the author, and a picture editing programme are used to analyse the adhesive coverage. First, based on the colours of the image pixels, black and white areas are defined. Then, a central part to be used for the analysis is defined as the full module surface makes the calculation difficult and imprecise, as shown in Figure 7.14. The whole image yields $\approx 55\%$ coverage and the central part $\approx 67\%$ - both are not meeting the requirements. After releasing the vacuum from the flex jig and waiting for ≈ 1 min it can be observed in Figure 7.15 that the adhesive is compressed.

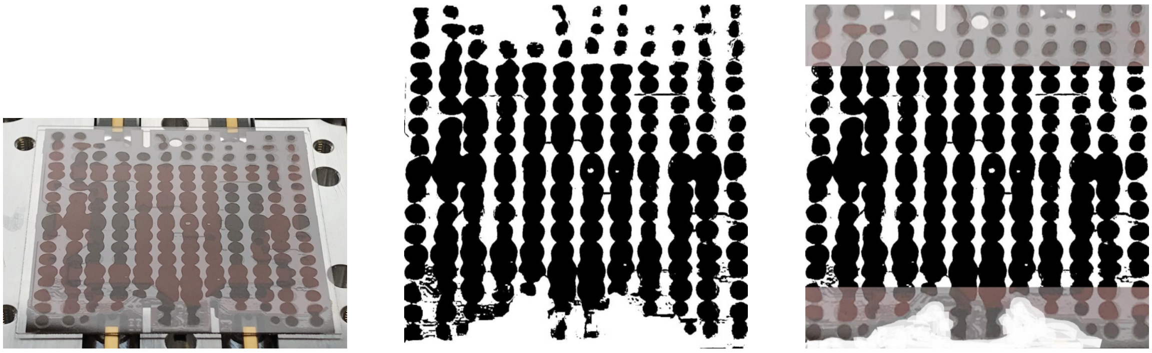

Figure 7.14: Analysis of the adhesive pattern after a curing time of 15 min without releasing vacuum on the flex jig. **Left:** Gluing pattern as seen from the side for contrast between adhesive covered area and free space. **Middle:** Transformation of the full image with the python script and a picture editing programme. **Right:** Definition of an analysis area.

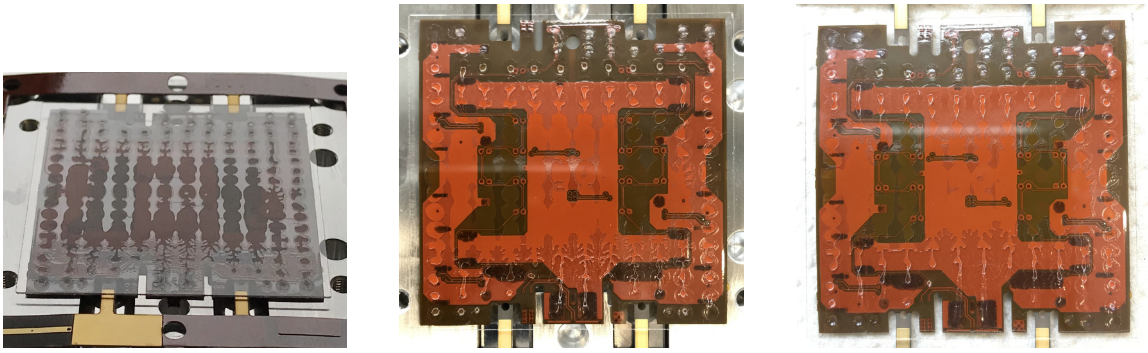

Figure 7.15: The adhesive is pressed together after releasing vacuum on the flex jig and waiting for 1 min for a curing time of 15 min.

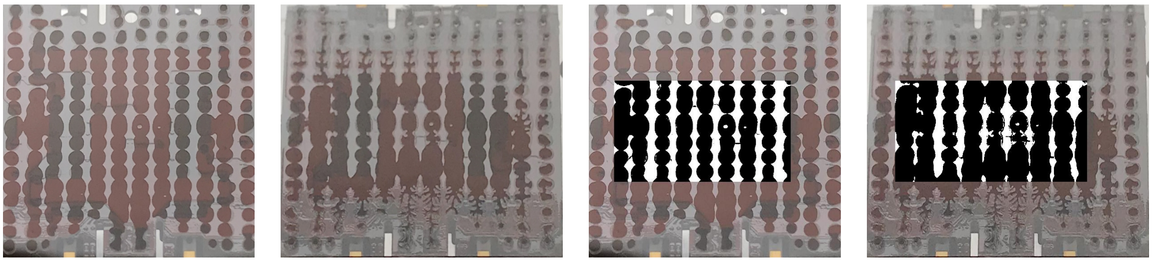

Figure 7.16: Comparison of the adhesive coverage before and after release of the vacuum in the flex jig shows that the alleged glue coverage is augmented once the vacuum is completely released from the tooling jigs.

Figure 7.16 shows the comparison of the adhesive coverage before and after the release of the vacuum on the flex jig. The central selected area adhesive coverage yields 67% before vs. 77% after the release of the vacuum.

Further tests with 30 min and 60 min curing time were performed. Additionally, the

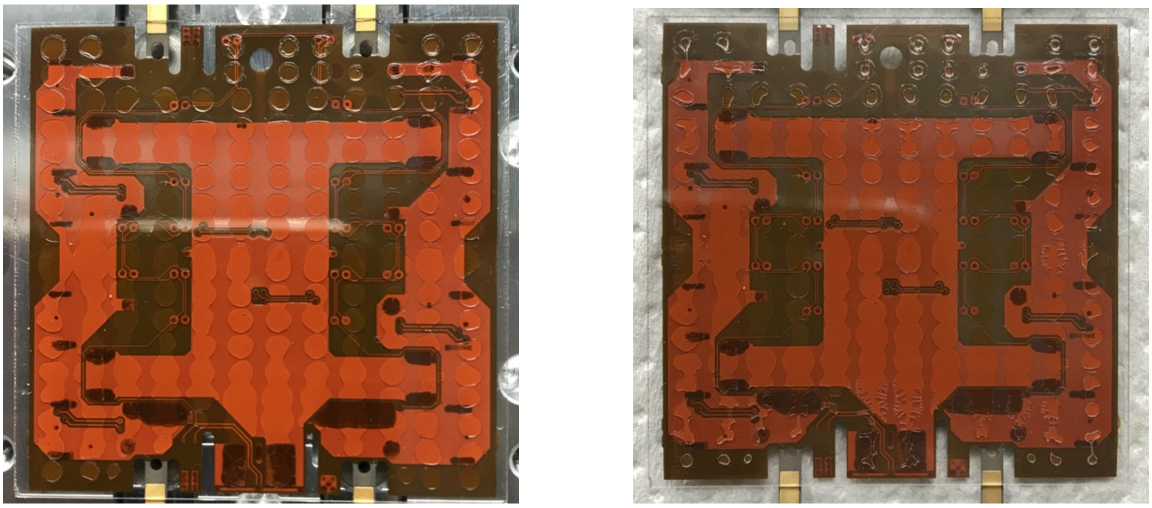

Figure 7.17: After letting the adhesive cure for 60 min, the adhesive does not spread much more when the vacuum is released on the flex jig. **Left:** Gluing pattern after 60 min curing time and only releasing the vacuum on the bare module jig. **Right:** Gluing pattern after 60 min curing time and releasing the vacuum on both sides of the jig. The glue pattern changes only slightly and mainly on the outer edges, hence leaving the area of interest in the middle of the module unchanged.

dependence on the time the nozzle used for the application of the adhesive is not used (and the adhesive curing inside) is also evaluated.

Leaving the adhesive cure for a longer time (with a nozzle that was exposed to air for 20 min) the adhesive does not spread as much anymore after the vacuum is released from the flex jig, see Figure 7.17. Several other compositions of curing time and nozzle age were tried and a curing time of at least 60 min seems advantageous for stable glue dots while measuring, still allowing to remove the glue completely to perform several tests.

Delamination Tests with Dry Ice

After gluing of modules, the actual delamination tests were performed to understand if the bump bonds resist temperature cycles. For the test, the modules undergo 1, 5 and 10 cycles between dry ice (reaching approximately $(-60 \pm 5)\,^{\circ}\mathrm{C}$) and room temperature, monitored with a humidity and a PT1000 temperature sensor that are glued in the testing bag close to the modules and read out with an arduino. A soak time of 5 min was applied to the modules after reaching $-55\,^{\circ}\mathrm{C}$ or room temperature, respectively. The bag is flushed with dry air to avoid condensation and ice on the modules, as shown in Figure 7.18. Two dummy modules with flexes without SMD components (1, 2) and one module with SMD components but one side where the Si-dummy was damaged (3) were treated with dry ice.

To probe potential delamination, manually 24 points on the flex were pinched with the needle of the probe station after each set of cycles, as shown in Figure 7.19. A movement of the flex can be observed as change of light in the microscope image.

The modules were inspected before the first cycle: **module 1** showed slight movements on one side close to the edge, **module 3** also showed movement on the side with the broken

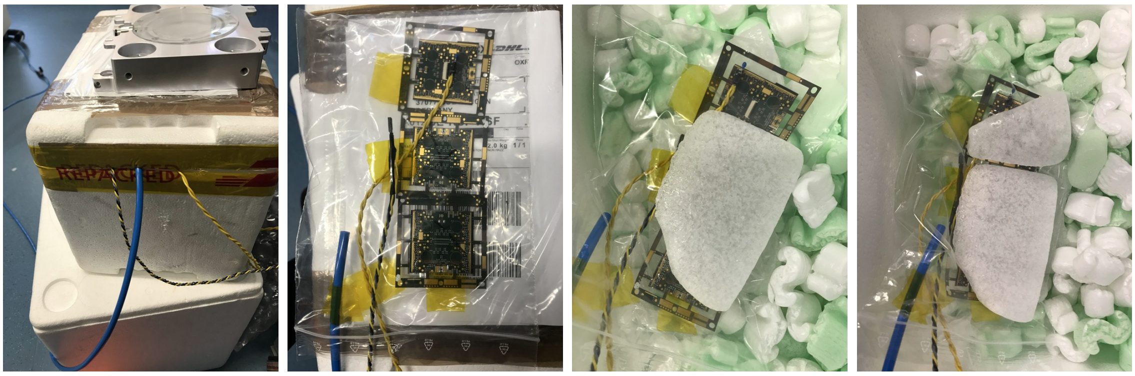

Figure 7.18: Foam box used for the cycling tests with dry ice. The dry air supply and the sensors inside the bag are used to monitor and maintain appropriate environmental conditions.

Si-dummy, **module 2** looked perfect with no movement observed anywhere on the module. Table 7.7 lists the additional contact points showing movement after cycling. It should be taken into account that SMD components on the flex do alter the behaviour of the flex under cooling and warming up and also initially broken components are more error prone as the silicon structure might be damaged further inside than visible.

In combination with results from other sites, it was, however, concluded that the stencil design is sufficient to prevent large delamination.

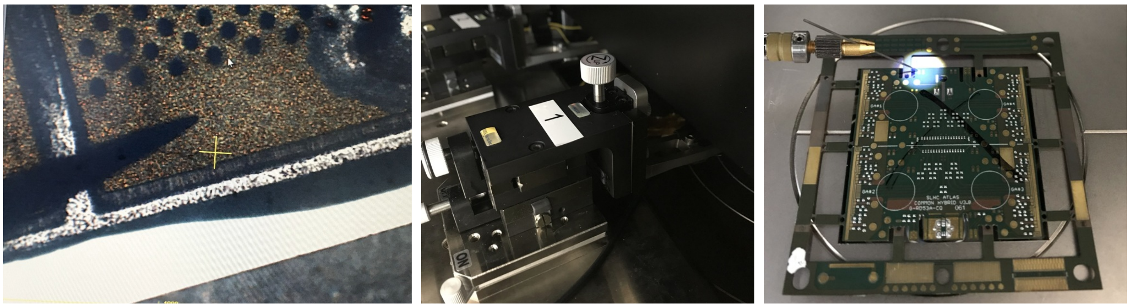

Figure 7.19: Delamination measurements are performed by manually pinching the flex with the probe needles in the probe station and observing the change of light. **Left:** The view through the microscope where the change of light is judged. **Middle:** The micrometer screws for manually moving the probe needle. **Right:** One position on the flex, where the delamination is probed.

Table 7.7: Additional contact points showing movement when pinching with a probe station needle after thermal cycling with dry ice.

	Module 1	Module 2	Module 3
1 Cycle	0	0	0
5 Cycle	2	1	4
10 Cycles	2	2	8

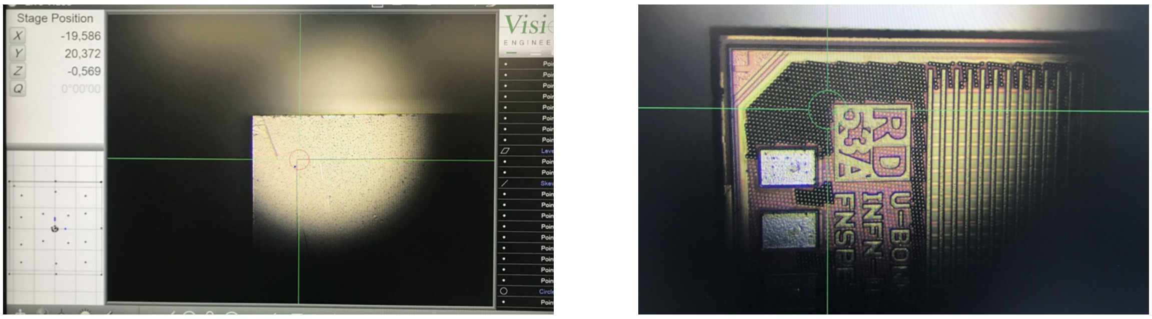
Stage Position
X -19,586
Y 20,372
Z -0,569
Q 0°00'00

Figure 7.20: Measurement points on the sensor part of the bare module and the readout chip part.

Table 7.8: Nominal values for RD53A bare modules. The separate dimensions for FE and sensor in the bare module are given according to Ref. [165]. All measurements are in µm.

Sensor height	FE height	Flatness	x-dim. sensor	y-dim. sensor	x-dim. FE	y-dim. FE
$575 + 75 - 40$	$400 + 25 - 10$	± 25	$39.5 + 0.05$	$41.1 + 0.05$	$42.2 + 0.05$	$40.3 + 0.05$

7.2.4. RD53A Module Assembly

Specifically for the purpose of providing modules for the outer barrel demonstrator programme, RD53A modules were built and tested mechanically and electrically in Göttingen. The mechanical tests follow the mechanical tooling validation tests and the electrical tests follow the description in [169].

In the following, the results for the first real module gluing in Göttingen are presented. The mean and standard deviation of specific parameters such as the module height in specific regions and the x- and y-dimensions and distances have been analysed.

The dynascope was used for the detailed inspection and measurement of the height of the bare module and the x- and y-dimensions of its components. Figure 7.20 shows some measurement points taken on three bare modules and one flex.

The nominal values of the module components are listed in Table 7.8. Actual measurements on the bare modules can be found in Table 7.9. There are two different flatness measurements shown. The flatness of the bare module determined when it was flattened with vacuum corresponds to the distance of separate height points on the sensor with respect to the mean sensor height. For the flatness measurement without vacuum the differences between measurements with and without vacuum are taken. This can result in large deviations as the bare module can bend and therefore lie at an angle with respect to the measurement jig surface. This way the measurement must not necessarily reflect the actual bare module flatness.

To actually determine the bare module flatness, the distances between each height point are measured without vacuum with respect to a plane defined through these points. With this last measurement only four of 39 values are > 25 µm, which is the required flatness. These deviations are not of any concern as this bare module has a thick FE which is not used in the modules for the ITk.

It can be concluded that the x-dimension of the sensor is 58 µm too small while the

Table 7.9: Bare module and flex measurements for module assembly.

	BM1	BM2	BM3	Specifications
Height and flatness of bare module [µm]				
Sensor height	576.2	578.0	583.7	$575 + 75 - 40$
FE height	401.8	403.8	408.5	$400 + 25 - 10$
StdDev sensor height	8.9	8.8	8.8	
StdDev FE height	2.5	2.2	6.0	
Min flatness BM with vacuum	-8	-12	-15	-50
Max flatness BM with vacuum	20	16	14	50
Min flatness BM without vacuum	-2	-1	5	-25
Max flatness BM without vacuum	86	105	88	25
dimensions of sensor [mm]				
x-dim	39.442	39.443	39.436	$39.5 + 0.05$
y-dim	41.052	41.053	41.044	$41.1 + 0.05$
Stdev x	0.001	0.001	0.006	
Stdev y	0.004	0.002	0.007	
dimensions of FE [mm]				
x-dim	42.177	42.181	42.184	$42.2 + 0.05$
y-dim	40.320	40.320	40.322	$40.3 + 0.05$
Stdev x	0.013	0.003	0.013	
Stdev y	0.001	0.004	0.008	
dimensions of flex [mm]				
x-dim.	40.402			$40.4 + 0.04 - 0$
y-dim.	40.423			$40.4 + 0.04 - 0$

y-dimension of the sensor is almost always within tolerances (48 µm too small). The x-dimension as well as the y-dimension of the FEs is very similar for all bare modules, around 20 µm too small or too large, respectively. These deviations are also of no concern as these bare modules are not used for the real ITk. The relevant values for the alignment of the bare module to the flex in the tooling are the y-dimension of the sensor and the x-dimension of the FEs. What should be mentioned is that the tolerances for BM1 and BM2 are in general smaller than for BM3, as a close up function for focus setting on the microscope was used.

Table 7.10: Measurements of the glue height after gluing on the first RD53A module (BM1). All measurements in µm.

	All	Wire bonding area	Keep clear area	Min.	Max.
Glue height	44.0 ± 10.9	45.8 ± 9.5	40.0 ± 10.7	21	63

The measurements of the x- and y-distances between the module components and the glue height after gluing of module 1 are shown in Table 7.3 and 7.10. The glued module fulfils all but one of the distance requirements as listed in Section 7.1.1. The distance on the top is outside of the tolerances. Looking at the bare module measurements, the distances on the right and on the bottom were expected to be too small due to the actual dimensions of the bare module. However, it was observed that the top and left distances are too small.

A possible explanation would be that the module was rotated for these measurements as the RD53A bare modules do not have any marking so that rotating by 180° could be excluded. The average glue height is within the specifications of $(40 \pm 15)\,\mu\mathrm{m}$, however, there are outliers. The smallest measured thickness is 21 µm and the largest 63 µm.

The flatness of the module is 43.7 µm on average and has a maximum of 91 µm and is thus not within the tolerances. Also, the adhesive weight is 45.8 mg, which is below the specifications. This is not a problem as the gluing process for the real ITkPix modules has been improved with the new version of the tooling.

In total, however, it can be concluded that the module building process is understood and possible limitations are known. In the next section the electrical tests after module building are discussed.

7.3. Module Electrical Testing

For the production phase, an electrical test system is employed to ensure the operational quality of the modules. The key points are the electrical testing of the proper functionality of the readout chips by tuning them and the bump bonding quality checks which may involve the sensor. The sensor quality after module assembly is validated with an IV measurement. The full testing procedure is defined in Ref. [169] and includes thermal cycling tests ($-55\,^\circ\mathrm{C}$ to $60\,^\circ\mathrm{C}$ and $-45\,^\circ\mathrm{C}$ to $40\,^\circ\mathrm{C}$) and measurements at operation temperature which require a setup with cooling options. Section 7.3.2 explains the module testing itself. The following section describes the setup. And in Section 7.3.3 the testing results are presented.

7.3.1. Electrical Test Stand

The FE-I4 testing setup as shown in [5] with a custom designed cooling jig was used for initial tests of the RD53A modules at the University of Göttingen. The cooling jig which was originally designed for FE-I4-modules is, however, not suitable due to changes in module geometry.

For the electrical testing of RD53A-modules a cooling unit was designed at the University of Bergen, intended to be used by all ITk institutes. It is used for the removal of heat from the power consumption of the module. The cooling unit comprises a foam housing with a cooling chuck inside which is cooled by an external silicon oil chiller (Huber Unistat 705). Inside is a stack of a Peltier element for precise temperature control, a cooling chuck and a vacuum chuck which holds the module. Vacuum and dry air tubes as well as the module data and power pigtails are routed through the housing.

The cooling unit setup can be seen in Figure 7.21. In the open cooling unit at the right of Figure 7.21 part of the stack can be seen. On the white jig at the bottom of the cooling unit the cooling chuck is placed, which is connected to a chiller and hidden. Above this, the Peltier and finally the vacuum chuck are stacked, which are also hidden. The module is placed in the frame of the module carrier without the bottom part on the vacuum chuck to guarantee direct contact of readout chips to the vacuum chuck. Dry air supply to the module is obtained with the transparent pipe connected to the module carrier. The blue pipe is the connection to the vacuum pump.

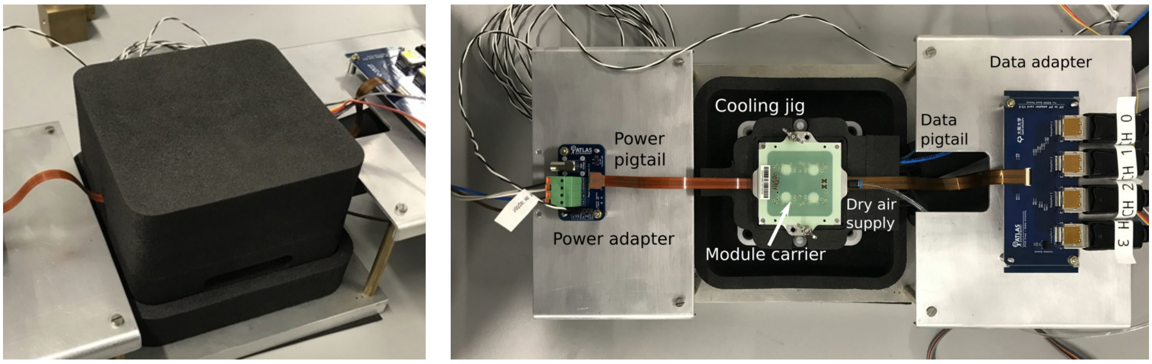

Figure 7.21: Cooling unit with foam housing and connections to a vacuum pump, a chiller, dry air, power supplies, sensors and the readout PC.

The electrical connection of the module is obtained with data and power pigtails, which are flexible PCBs that connect the two small rigid PCBs, shown on the left and right of the picture on the right in Figure 7.21. Power and NTC readout is routed through the smaller PCB on the left. The data pigtail is connected to the adapter board on the right, which routes the signal to four display port cables which are connected to the readout PC.

Within the scope of this thesis the cooling unit was installed and commissioned for Göttingen. This comprised the installation of temperature and humidity sensors in the cooling unit on the vacuum chuck, the cooling chuck and close to the module itself and the commissioning of the software. For the temperature and humidity readout an Arduino Mega[2] is used which is run with labRemote, a common ITk software package[3]. The same holds for the control of the power supplies, used for biasing the sensor and powering the module. The scripts running labRemote were configured to the needs of the power supplies for the cooling unit and the Arduino sensor readout was set up within the scope of this thesis.

The readout for the actual module testing was also commissioned. Module readout systems aim at collecting the detector FE hit data that will be stored, waiting for further processing later. The readout chain is composed of a DAQ software communicating with a dedicated hardware, usually FPGA-based, which is connected to the FEs. Two readout systems can be used for RD53A readout, the YARR [151] or the BDAQ53 readout system [170, 171]. YARR is a software that supports different hardware (HW) platforms, PCI Express FPGA boards, e.g. Spec, Tef1001, XpressK7, KC705. It can also support other FPGA platforms like BDAQ53 board and RCE HW (ZCU102). BDAQ53 is another python based software[4] which uses a BDAQ53 board connected to the PC through Ethernet connection. The aforementioned YARR based software is referred to as ITkSW. The single module test setup for RD53A modules in the cooling unit was commissioned with a BDAQ53 board and the common ITkSW, for the first time demonstrating that the HW and SW combination is fully functioning.

---

[2] Arduino Mega https://docs.arduino.cc/hardware/mega-2560.

[3] Git repository of labRemote ITk software for power supply and sensor readout control in https://gitlab.cern.ch/berkeleylab/labRemote and the common scripts in https://gitlab.cern.ch/berkeleylab/labremote-apps/pixelmoduleqc.

[4] The BDAQ53 python based software is available at https://gitlab.cern.ch/silab/bdaq53.

The original plan was to install several cooling units for parallel testing in a radiation shielded box which used to house the FE-I4 testing jig to allow for source scans which are needed to test bump bond connectivity of the bare modules. However, only one cooling unit could be installed within the time frame of this work.

7.3.2. Testing Procedures

Electrical testing procedures are subject to regulations to ensure comparable procedures at all ITk sites. As explained in Section 5.2, the RD53A chip has an analog and a digital part. In order to perform measurements, the chips on the module need tuning to equalise the response of every pixel. Apart from the tuning and the subsequent scans, the sensor properties also need to be tested again in IV scans.

In general, all tests were supposed to be performed at three different temperature: 20 °C, 30 °C and −15 °C. However, the regulations were changed due to time constraints to require only one complete set of measurements at 30 °C.

First, the functionality of the readout chips needs to be assured. As a first step the wire bonding is visually verified. In particular, wire bonds defining the 2 µA current reference and the chip ID selection should be checked. Then, before performing any tuning on the module, the voltages provided by the SLDO for the digital and the analog part of the module have to be verified. For this purpose and in general for the module testing, the readout chips are serial powered with 4.6 A [169] to ensure that the voltage at the SLDO input of the module is $\approx 1.6\,\mathrm{V}$. To protect the readout chips, a voltage limit of 2 V is set on the LV power supply. The sensor is reverse biased with $V_{\mathrm{depl}} + 50\,\mathrm{V}$ and a current compliance is set to 100 µA at the most to protect the sensor. The analog and digital voltages supplied by the SLDO can then be obtained manually from the respective probe pads on the module flex. If not already at the recommended voltage of 1.2 V, register values are adjusted in the chip configuration files. Settings of the registers from wafer probing of chips are used as a starting point.

The turn-on behaviour of the SLDO in the RD53A chip is unstable. It therefore needs to be determined for each chip separately to understand at which temperatures the chip can be used. This comes from the fact that the SLDO for serial powering mode does not work as expected and hence does not reliably provide the chip voltage at all temperatures. For system tests (explained in Chapter 8) modules have to be used at cold temperatures, which is only possible when they properly turn on. VI scans have to be taken, where the chip voltage is monitored as a function of the input current of the power supply. This VI scan has to be repeated at −35 °C and if not successful at higher temperatures in 15 °C steps to understand at which temperature the readout chips turn on.

Following these initial tests on the chips, verifying that they are powered correctly, the tuning and testing procedure starts. The testing procedure requires scanning the occupancies of digital and analog injections, doing threshold scans and performing threshold and charge response tuning. Scans simply describe procedures performed by the readout system where the response of the front-end chip for different parameters is measured. The sequence of the electrical measurements is as defined in [169] and available in the YARR git repository[5].

In the following subsections the explicit testing scans are explained.

Digital- and Analog Scan

Basic operation of all pixels is tested with these scans. The digital or the analog injection mechanism is used to inject hits into all pixels of the FE. For the analog test the injected charge needs to be above the discriminator threshold.

For the analysis of the occupancy scans a defined number of hits is injected and the response of the respective part of the pixel measured in digital- and analog scans. For the digital part of the chip a perfect response is expected. The analog part of the pixel is subject to noise, thus some pixels with non-perfect response are expected.

Typically, for YARR 100 triggers are injected. For a response of $98 \leq \text{hit number} \leq 102$, the pixel is called "*good*". If less than 98 or more than 102 electrons are measured, the corresponding pixel is excluded from other measurements and called a "*bad*" pixel. Pixel with no hits are referred to as "*dead*".

Threshold Scan

The discriminator in the FEs is used to suppress noise below a defined threshold. This threshold can be adjusted. In an ideal world, the pixel would never fire for signals below the threshold and always fire for signals above. This behaviour could be described by a step function.

A real discriminator, however, is influenced by noise in the system, as explained in Section 4.2.4. Therefore a so-called s-curve describes the turn-on behaviour of a pixel. The hit probability is described by

$$P_{\text{hit}}(Q) = \frac{1}{2}\text{Erfc}\left(\frac{Q_{\text{threshold}} - Q}{\sqrt{2}\sigma_{\text{noise}}}\right) ,$$

with the charge Q, the discriminator threshold $Q_{\text{threshold}}$ which is defined as the point with a hit probability of 50%, the noise σ_{noise} and the complementary error function Erfc

$$\text{Erfc(x)} = \frac{2}{\sqrt{\pi}} \int_{x}^{\text{inf}} e^{-y^2} \text{d}y \, .$$

The functionality of the threshold scan is in principle the same as for the analog and digital scans. In this case, however, the occupancy is measured at different injected charges for a fixed threshold. For a FE tuned to 1000 electrons one would expect every pixel to register charges above 1000 electrons as hit. By fitting the hit probability curve the threshold is interpreted as the charge value with 50% hit probability and the width of the curve as the noise. The projected distribution of the thresholds and the noise for all pixels is a Gaussian distribution. Fitting these distributions with the mean and the width the threshold and the noise are characterised.

---

[5] Tuning script for module QC in https://gitlab.cern.ch/YARR/YARR/-/blob/master/scripts/rd53a-module_tuning.sh.

Noise Scan

A noise scan is used for masking of pixels firing without a physical signal. When a pixel registers a hit in the absence of a signal, which is more likely to occur at low discriminator thresholds, the pixel should be masked to avoid overloading the readout bandwidth. This means that this pixel is disabled and excluded from any further scans. To perform this scan, trigger commands are sent to the FE at a fixed frequency. As soon as hits from noise, random coincidence between trigger, cosmic radiation or broken pixels surpass an occupancy of 10^{-6} hits per bunch crossing, the pixel is masked. The noise is stated per bunch crossing, but it is essentially a specific trigger time in which the number of hits is counted.

Source Scan

With a source scan where a radioactive source is positioned above the module all pixels are expected to see hits. If this is not the case, the pixel is counted as not-connected or dead.

In this scan physical hits from the sensor from a radioactive source or an X-ray source are measured. As preparation the noisy pixels are masked with a noise scan. The hits issue triggers to the FE chip and are read out. As components on the flex attenuate radiation this is visible in the histogram of the scan.

There are also other scans for the same purpose, they work, however, all without an external source and use internal injection mechanism of the chip. The scans are the disconnected bump scan and the crosstalk scan. Both work via crosstalk, which is expected to be seen between neighbouring pixels. By injecting in the four adjacent pixels and reading out the pixel in the middle, information about the bump connection can be gained. The same criteria for sorting pixels in “good”, “bad” or “dead” are applied as for the analog and digital scan. However, as the injection is performed via the adjacent pixel, for any pixel with “bad” or “dead” neighbours, the pixel must be marked as “unknown”. A last option are threshold scans where the modules are forward-biased and one also expects to see the disconnected bumps.

Tuning

As introduced in Section 5.2, the discriminator threshold and the time over threshold are adjustable to compensate for manufacturing variations and radiation damage in the readout chip.

The tuning procedure starts with configuring the FEs with default configuration. This means that an arbitrary value for the global threshold is set and and the per pixel threshold trims are set to the center of the range. First the global threshold is adjusted so that the average is at the desired threshold. However, the shape is still a wide Gaussian. In consecutive steps the individual pixel thresholds are tuned which narrows the width. For the ToT tuning a similar procedure is performed. As ToT and threshold tuning influence each other, the threshold fine-tuning is repeated after the ToT tuning. The resulting difference in the distribution is exemplified shown for FE 4 of a module from Paris[6] in Figure 7.22.

---

[6] The module from Paris is used by the author for system tests as later described and therefore used here

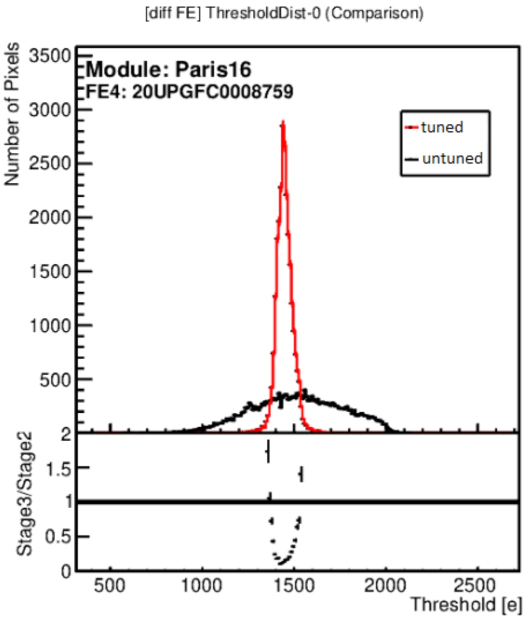

Figure 7.22: An example tuning to 1500 e for one FE compared to the untuned distribution.

7.3.3. Module Testing Results

Similar to the market survey on the sensors, sites have to qualify for the testing of modules. Within the scope of this thesis, the testing qualification of the University of Göttingen was performed with two *digital* modules that were built and successfully wire bonded at the University of Göttingen[7]. For *digital* modules a glass substrate replaces the sensor.

The digital quad modules under test have functioning RD53A readout chips, functioning flexes with SMD components, wire bonds, power connected via the power pigtail and the readout pigtail connected with the connector on the middle of the module, but, glass instead of a sensor. Hence, all scans except for IV and bump connection testing scans can be performed on these modules.

As explained, for the digital part of the chip, a perfect response is expected. Figure 7.23 shows the digital and analog scan occupancy with a few noisy pixels in the analog scan. The other two histograms on the right show that the chip was successfully tuned to a threshold of 1000 electrons and a charge response that leads to the ToT to be 7 bunch crossings (bc).

Apart from the tuning, VI measurements were performed that check the turn-on behaviour of the SLDO in the chips and all measurements were repeated at different temperatures.

The second part of the qualification for module testing requires the successful performance of a source scan and cycling of the module between temperatures of -55°C and 60°C. These tests were finalised outside of the scope of this thesis, showing that all required tests for module QC can be performed at the University of Göttingen.

The results of the RD53A modules built in the University of Göttingen are allocated to a

---

as example.

[7] The bonder model is FEK Delvotec 56xx WEP-00002 F/S Bondtec Ultrasonic Bonder with the bondhead 5630 and the pull head PH-100.

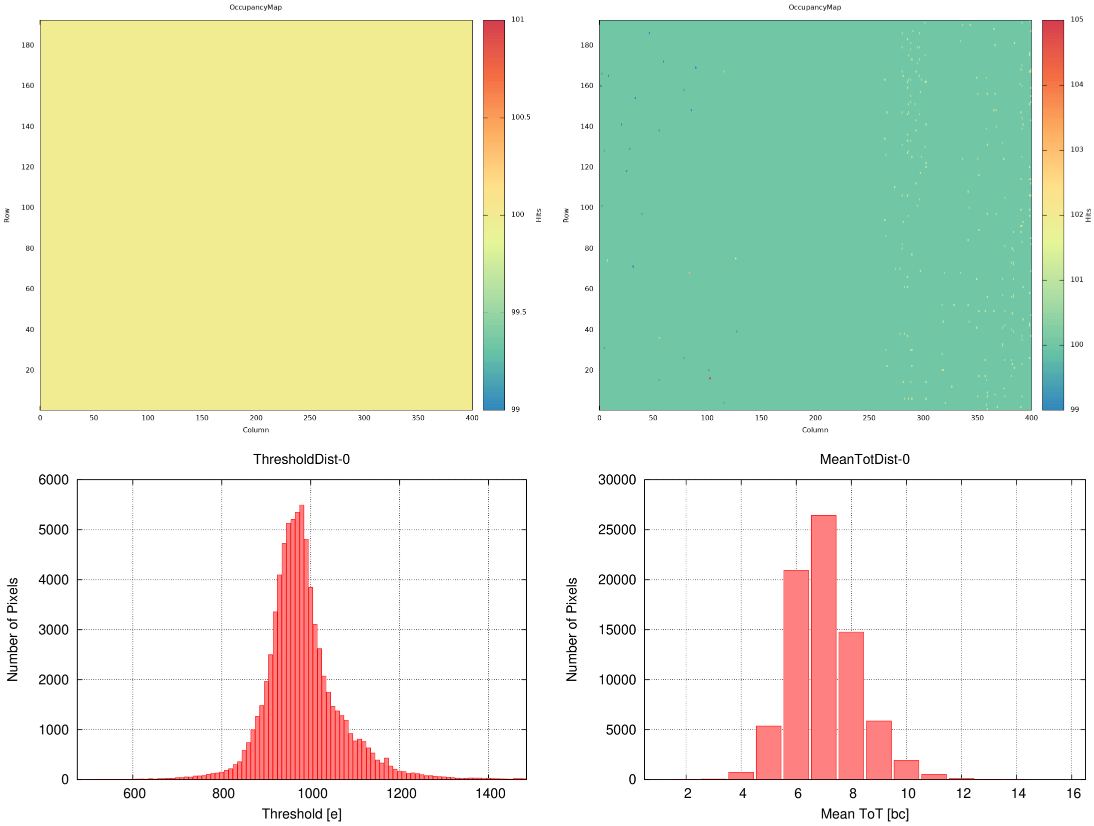

Figure 7.23: An example tuning for one of the chips of the digital modules showing the digital and analog occupancy scan and the successful tuning to a threshold of 1000 electrons and a ToT of 7 bc.

thesis still to come at a later stage and will include sensor-related measurements. As these modules have been sent to CERN for further processing and to be used on the demonstrator, testing results for these modules are among those presented in Chapter 9. However, for the sake of discretion, the modules are not explicitly marked.

7.4. Conclusions and Outlook

Within the RD53A module building campaign, many modules were built and tested, out of which five from the University of Göttingen. However, several shortcomings could be identified. It was shown that deviations of the flex and dummy bare module geometries can lead to x-y-distances between the separate components on the glued module that are not within the tolerances. Regarding the adhesive and module thickness, there have also been large variations among the groups. Coupled with the adhesive thickness is the coverage of the adhesive. Depending on the user, the adhesive weight, spread and height vary: At times, judged by the weight, more adhesive than expected with the stencil was applied. Hence, larger adhesive coverage with similar thicknesses was obtained. As a consequence, the stencil was subsequently further improved to anticipate a coverage of $< 80\%$ while keeping the wire bonding areas free of adhesive. Apart from that, manufacturing tolerances affecting the precise closing of the tooling and the uncontrolled closing mechanism by hand might also be the origin of some of the adhesive thickness or x-y-distances deviations.

Nonetheless, even modules outside the tolerances after gluing were wire bonded successfully, leading to a relaxation of the x-y-distance requirement from a precision of $\pm 50\,\mu\mathrm{m}$ to $\pm 100\,\mu\mathrm{m}$. The earlier requirement of an adhesive thickness of $(40 \pm 15)\,\mu\mathrm{m}$ has also been dropped. However, a minimal adhesive thickness of $10\,\mu\mathrm{m}$ remains and the requirement for the entire module thickness to be smaller then the module envelope.

For the RD53A modules, especially with the lowering of the requirements, a sufficiently high yield of modules for loading and serial powering studies could be obtained. However, the procedure would benefit from simplification in view of production. Thus, a new version of the tooling was developed which will be used for module building with ITkPix components. The idea is to have a more elaborate and automated version of the tooling which leads to less room for user mistakes. The stencil tooling is also completely reworked to discard any room for handling mistakes so that, in principle, all sites should yield the same amount of glue spread on the flex.

When it comes to module testing, a test setup has successfully been installed in Göttingen which allows performing module QC. The common cooling unit was installed and equipped with sensors for environmental conditions monitoring and the respective ITkSW configured. With this cooling unit, electrical tests of the modules at all required temperatures of $20\,^{\circ}\mathrm{C}$, $30\,^{\circ}\mathrm{C}$ and $-15\,^{\circ}\mathrm{C}$ can be conducted. It was shown that the module tuning could be performed at these temperatures successfully. Also, in order to build electrically functional modules, the wire bonds need to be analysed and the chip registers set correctly by probing the SLDO voltage values. It was shown that this is possible by using digital quad modules from Göttingen. This was a requirement to qualify the laboratory at the University Göttingen for further module building and module testing.

Outside of the scope of this thesis, two further requirements for module testing were fulfilled. The capability of source tests was shown and thermal cycling of the module. While with the cooling unit in principle also the thermal cycling tests are possible, another setup involving a shock chamber at Göttingen was commissioned for this purpose.

Overall, Göttingen is since the end of 2019 qualified to build quad modules and from the beginning of 2021 also fully qualified to test quad modules.

CHAPTER 8

Outer Barrel Demonstrator

8.1. Demonstrator Programme

As described in Sec 3.4.2, the ITk PIXEL Detector will be built of around 10000 modules which are arranged in 5 layers, powered with serial powering and read out at 1 MHz.

The already mentioned demonstrator programmes are being conducted at CERN to test integration and system aspects in detail to validate the design and detector concept before the start of the large scale production. They comprise the building and study of the basic building blocks of the ITk for a prove of concept. This is for example the serial powering in a realistic setting with several serial powering chains, the HV powering of the sensors and the cables and connections between modules and power supplies.

The final ITk PIXEL Detector will be built with ITkPixV2 modules. As these are not yet available, the demonstrator projects are using preliminary modules.

The first version of the demonstrator was built with FE-I4-based modules, see also Section 5.2. This is the readout chip used in the IBL in the current inner detector. The main focus of this demonstrator was the prove of concept of serial powering for multiple parallel chains with common ground (GND). The modules are loaded on pyrolitic graphite tiles and then mounted on a longeron with cooling pipes. A longeron is an elongate light carbon fibre composite truss structure for mechanical support while introducing a small material budget [172]. This loaded longeron is housed in a light tight Faraday cage, referred to as the environmental box. With CO_2 cooling and dry air supply controlled environmental conditions are available for electrical tests on the demonstrator.

With the current demonstrator with RD53A modules the final design of the outer barrel is prototyped. Hence, not only a longeron but also a half-ring are commissioned with modules and a new cabling and connector scheme (called services) to validate the design of the ITk. This goes hand in hand with the qualification of the loading of the modules on cells which are needed to integrate the modules on the mechanical support. In Figure 8.1 a computer animated drawing of the loaded longeron is shown. The modules are on the bottom of the structure. On the right in the figure, two modules (in purple) are shown on cells (grey)

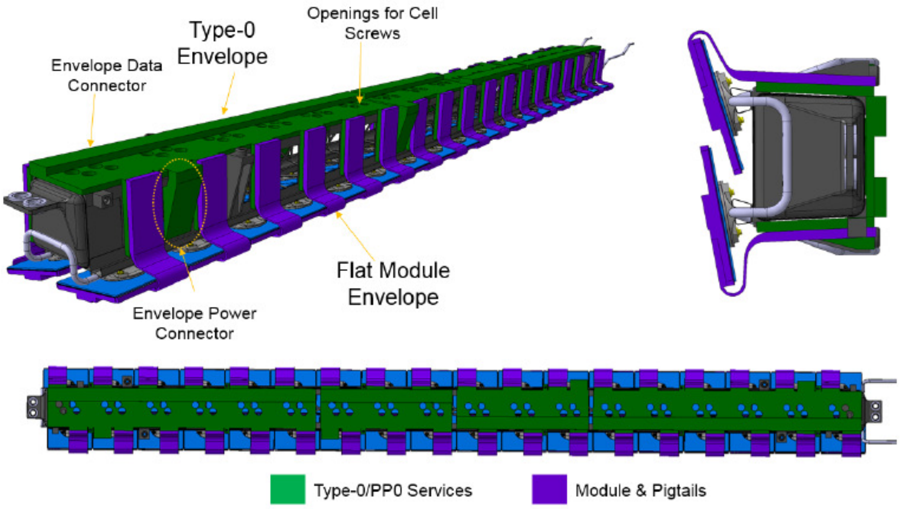

Figure 8.1: Computer animated design of a loaded longeron of the RD53A demonstrator. The modules are on the bottom of the structure. On the right, two modules (in purple) are shown on cells (grey) and screwed onto the mechanical support. The services are shown in green [172].

and screwed onto the mechanical support. The services are shown in green [172]. The demonstrator replaces the previous FE-I4 demonstrator longeron in the environmental box.

The modules for the demonstrator are being built in different production sites and being processed in various steps. In order to assure that the production yield of the modules allotted to the real detector is large enough, the full procedure is rehearsed already now for the demonstrator. This means that the modules undergo the full production chain and are tested at every step. On the RD53A demonstrator they are also tested on system level. The evaluation of the results from this version of the demonstrator are required to go into the final design review (FDR) of the loaded local supports.

The exchange of the current RD53A modules on the demonstrator to later ITkPix modules is in principle feasible due to the cell loading concept.

In the following, first, the serial powering concept will be explained. Then, different aspects regarding the setups, the commissioning and the results of the demonstrator programmes are discussed.

8.2. Serial Powering Chains

In a serial power chain (SP-chain) the modules are powered in series with a constant current [117–119]. Overcurrents need to be absorbed by the SLDO to assure that the readout chip stays safe. The schematics of the powering scheme for the demonstrator are shown in Figure 8.2. In serial powering, the local GND of one module is the input potential of the next module in the chain. Thus each module has a different local GND potential. As can be seen, the LV return line is connected to GND. This ensures that the GND of the module with the lowest local GND is equal to the system GND, which is in Figure 8.2 the

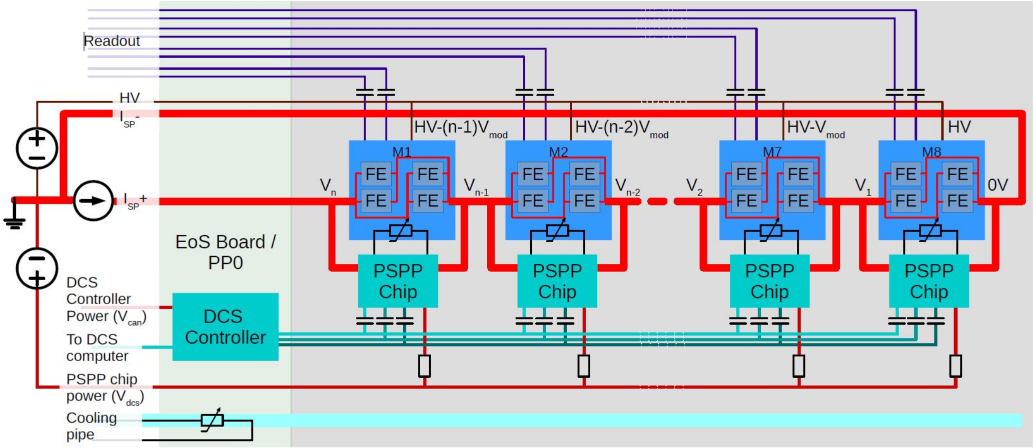

Figure 8.2: Powering scheme of the demonstrator according to Ref. [113].

module furthest to the right. In Figure 8.2, all modules are connected to the same HV input potential. The HV return line is connected to the LV return line. As a consequence of the shift in local module GND, each module sees a modified HV:

$$\mathrm{HV}_{\mathrm{mod}} = \mathrm{HV} - (n-1)\cdot V_{\mathrm{mod}}\,,$$

where n is the number of modules between the point of interest in the chain and the LV return. Thus, for the module on the right, the HV value stays unchanged. For the demonstrator, there are two HV lines for a single SP-chain, like in the detector in the outer barrel.

Results of tests with SP-chains in the FE-I4 demonstrator are discussed in the following section.

8.3. FE-I4 Demonstrator

The FE-I4 demonstrator is a longeron loaded with dual chip and quad chip FE-I4 modules, as introduced in Section 5.3. The modules are powered in up to six SP-chains with five, seven, eight and 16 modules.

On the FE-I4 demonstrator several different tests were done. Noise and threshold analyses were performed at warm (17°C CO_2 temperature) and cold (-25°C CO_2 temperature) to evaluate the module performance in SP-chains. The grounding concept of the ITk Pixel Detector was validated as well. Apart from this, the module performance at different integration stages was compared.

Overall, with these tests, serial powering was demonstrated in a large test system environment and the FE-I4 demonstrator measurements were providing invaluable experience in cable and connector design.

In the following sections the setup, studies on the SP-chains and grounding measurements will be presented that were conducted by the author.

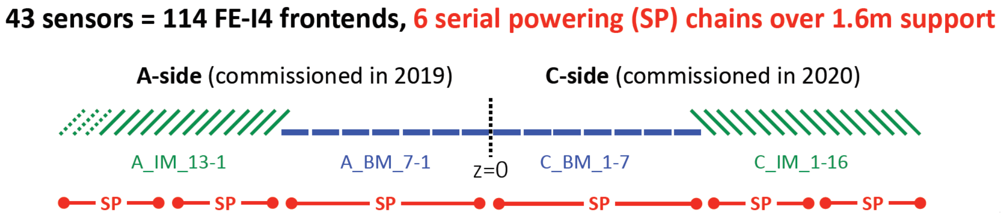

Figure 8.3: Schematic view of the demonstrator with the SP-chains on both of its sides.

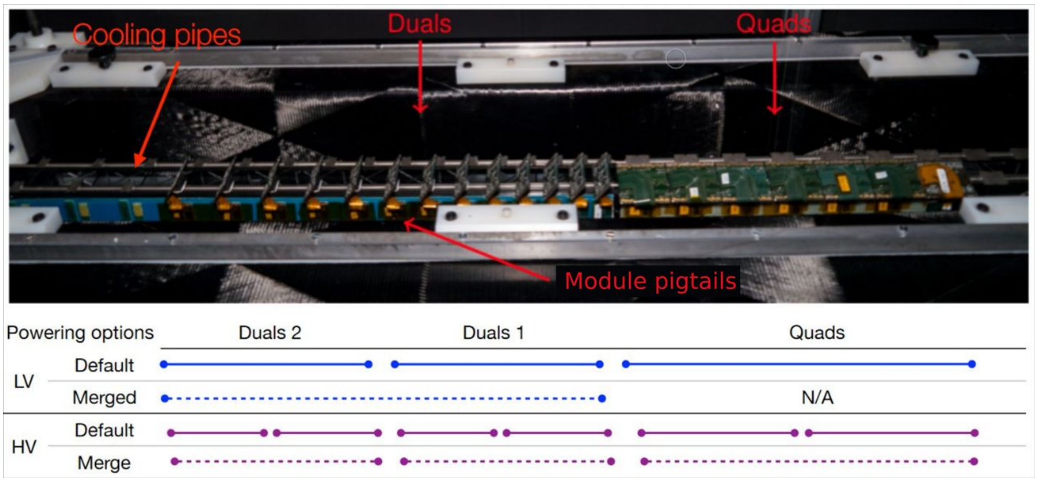

Figure 8.4: **Top:** Photo of the A-side of the demonstrator shows the quad barrel module on the right and the inclined dual modules on the left. **Bottom:** HV and LV powering options for the default mode and merged SP-chains. Default HV powering uses two HV lines for one SP-chain.

8.3.1. Setup

The longeron is divided in two sites, the A-side and the C-side, according to the ATLAS geometry. The FE-I4 system has 7(A) + 7(C) quad chip barrel modules (BM) on a flat central section and 13(A) + 16(C) inclined dual chip modules (IM) towards the ends of the longeron, see Figure 8.3. On the A-side are only 13 modules because three of the delivered 16 modules broke during further processing. Naming of the modules follows the scheme of *side_module type_FE number*. The names for the quad modules are hence A/C_BM_1-7_1-4 and the names for the inclined dual modules A/C_IM_1-13/16_1-2.

All modules are powered in 4-6 SP-chains with coupled grounds, as explained in Section 8.2. The inclined chains can be split to 8 + 5(8) modules in separate chains or be combined, as shown in Figure 8.4 on the bottom. For each SP-chain there exist two HV groups.

Concerning the sensors, all of the BMs are n-in-p modules. The IMs are of n-in-n type for the C-side and of n-in-p type for the A-side. Depending on the side, the modules use either spare sensors from the IBL, as on the C-side, or specifically produced sensors for the demonstrator, as on the A-side. In principle, with IBL sensors, more modules could have been produced for the A-side. However, the flexes needed for the IMs on the A-side and the C-side are mirrored. As there were no further flexes for the A-side available, only 13

Table 8.1: HV power settings for the six HV chains of the C-side. In the first HV chain in SP-chain 3 the voltage needs to be reduced because of an early breakdown around -60 V. For the second HV chain in this SP-chain even lower voltages of -20 V must be set to avoid a breakdown.

SP-chain	SP-chain 1		SP-chain 2		SP-chain 3	
HV chain	HV 1	HV 2	HV 1	HV 2	HV 1	HV 2
Value [-V]	80	80	80	80	60	20

modules could be mounted on the demonstrator.

Additionally, some of the sensors break down at a bias voltage of 0 V. This is the case for modules 11, 12 and 13 on the A-side (A_IM_11, A_IM_12 and A_IM_13) which are hence not powered with HV at all as otherwise the per pixel current limit of 9 nA would be surpassed. Other HV constraints can come from early breakdowns of the sensors. For C_IM_16 a low HV of -20 V needs to be set as the module breaks down at -30 V. A_IM_09 has a breakdown between -60 and -70 V and therefore also cannot be biased with the foreseen -80 V.

In the following, results are only shown for the C-side of the demonstrator as it has more functioning modules. The HV power settings for the six HV chains of the C-side are depicted in Table 8.1. It is known from module QC that the depletion voltage for these modules is about -30 V. Hence, the last four modules in the third SP-chain will not be fully depleted.

The detector control system (DCS) which controls the SP-chains uses Pixel Serial Power Protection (PSPP) chips [122, 173, 174]. PSPP chips monitor the module and can bypass it if necessary. They will, however, not be used in the real detector, but were foreseen when the FE-I4 demonstrator was built. Integrated in the DCS is the interlock to prevent damage to the modules and operators. An interlock acts for example on the power supplies. When environmental parameters like temperature or humidity change into an unsafe state for module operation, the power supplies will turn off. The same holds when the environmental box is opened and contact with components at a high electrical potential would be possible. Interlocked power supplies stay turned off until the trigger of the interlock is not valid any more **and** the interlock is unlocked by a user.

In the final detector, supply voltages, data uplinks and command downlinks are routed via type-0 electrical connections from the module to Patch Panel 0 (PP0). Each SP-chain is connected to one PP0. The type-0 connections are also called module pigtails. From PP0 a type-1 bundle goes to another Patch Panel (PP1). Type-1 bundle describes a cable which transmits CAN, Interlock, LV and HV signals. From PP1 the signals are transmitted via another type-2 bundle to PP2, from which then type-3 cables go to the interlock, the power supplies and the DCS (CAN) separately. This path is depicted in Figure 8.6 at the bottom.

At the time of the FE-I4 demonstrator the patch panels were not yet available. Instead, a cable saver board (CSB) was used to split the combined cables in the type-1 bundle to separate cables. A sketch of the cables and connections as used in the FE-I4 demonstrator is shown in Figure 8.6 on the top. The FE-I4 demonstrator measurements before the scope of this thesis showed that cross talk occurred between too close lines in the PP0. This led to an update of the design of the PP0.

While in the lab readout chains the FEs are directly connected to the ITk DAQ HW as explained in Section 7.3, the detector readout requires indirect connection through long optical fibre connections and transceiver and/or aggregator hardware. As these devices are inside the detector, they must be radiation hard. For the FE-I4 demonstrator the readout is instantiated with high speed *gigabit transceiver* (GBTx) ASICs [175] which serialise the electrical signals from the modules. In *versatile transceiver* (VTRx) chips [176, 177] the electrical signal is translated to optical signals and vice-versa. The optical signals then go in the DAQ system. Details and studies on the DAQ system can be found in [123, 178].

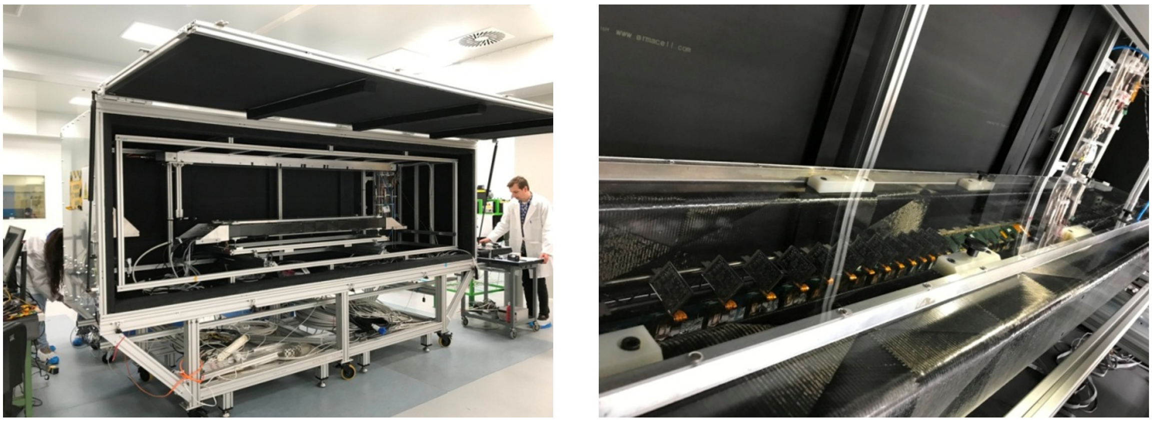

Figure 8.5: **Left:** The demonstrator testing box with the longeron. In a light tight environmental box the longeron is shielded from external factors and CO_2 cooling and dry air supply allowed controlled environmental conditions. **Right:** A view on the demonstrator with the inclined modules visible on the left side.

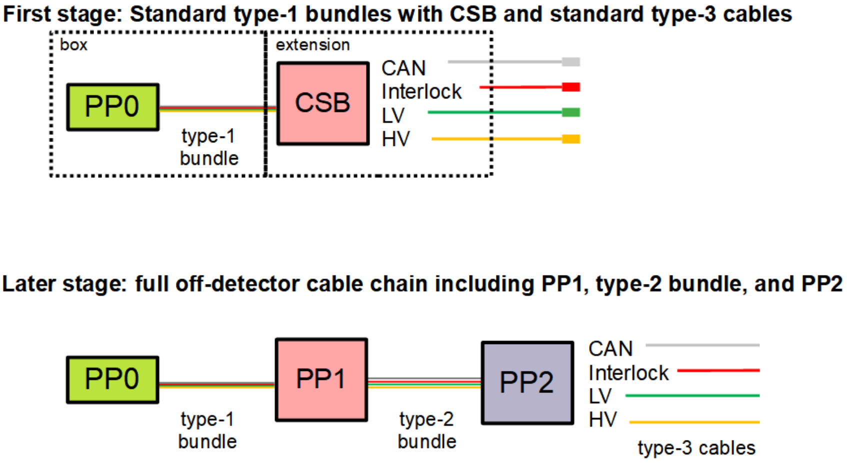
First stage: Standard type-1 bundles with CSB and standard type-3 cables

Later stage: full off-detector cable chain including PP1, type-2 bundle, and PP2

Figure 8.6: The schematics for the cables and connectors for the demonstrator are shown. On the top is the first stage where a cable saver board (CSB) is used instead of a PP1 and a PP2 which are not yet available. The type-1 bundle transmits power, interlock and monitoring data (via Controller Area Network (CAN)) and at the CSB separate cables go to the respective receivers.

Before conducting final measurements, the demonstrator had to be moved between two different labs at CERN, so that the system had to be recommissioned. This included recabling of the interlock and powering system, and reinstalling the detector readout. Also, the CO_2 cooling system had to be reconnected to the setup. A rapid pressure drop was noticed at the CO_2 inlet, which required checking the CO_2-system for leaks with a CO_2-sensor. The measured pressure drop over time for 20 days is shown in Figure 8.7. In orange is the temperature measurement over the same time frame. As the system was subject to temperature changes, the pressure normalised to the temperature is also shown in red. One single fit (dashed line) and two separate fits (orange and yellow), starting at the large change in temperature were performed. From the fits it can be concluded that the pressure drop rate was $\approx 160 - 170\,\mathrm{bar\,d^{-1}}$ which does not allow operation of the CO_2 cooling system. After the replacement of a ceramic electrical break, the CO_2 cooling was recommissioned and no further leaks detected so that the final tests could be conducted.

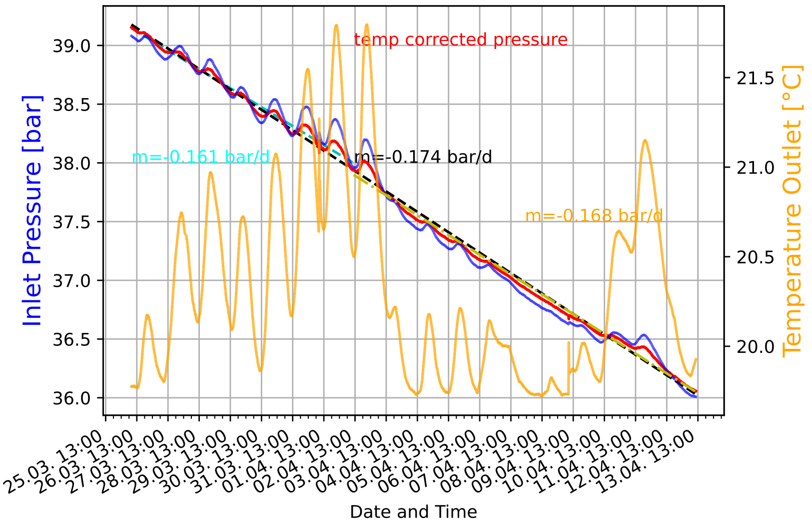

Figure 8.7: CO_2 leak data. The pressure on the CO_2 inlet is plotted for 20 days, showing a decrease over time (blue). In orange, the temperature is plotted. Because of high temperature changes the pressure normalised to the temperature is also plotted, which is then fitted. One single fit (dashed line) and two separate fits (blue and yellow) are shown and the slope of the fits is indicated in matching colours.

8.3.2. Study of Serial Powering Chains

In order to characterise the performance of modules in SP-chains and understand the independence of separate SP-chains, the SP-chains were tested in several different configurations on the A- and C-side of the demonstrator.

Table 8.2: Overview of the possible different powering combinations on any side of the demonstrator, labelled as scenario "S1" to "S7", that are used to test the stability and independence of the serial powering scheme of the demonstrator. The "✓" symbol indicates a powered SP-chain, while the "×" symbol corresponds to a deactivated chain.

Scenario	SP-chain / HV-chains 1	SP-chain / HV-chains 2	SP-chain / HV-chains 3
S1	✓	✓	✓
S2	✓	✓	×
S3	✓	×	✓
S4	✓	×	×
S5	×	✓	✓
S6	×	×	✓
S7	×	✓	×

Measurement Methods and Powering Configurations

As shown in Table 8.2 there exist seven possible different powering configurations for all separate HV and LV chains (one for the barrel modules and two for the inclined modules) on each side of the demonstrator. The powering configurations are called scenario "S1" to "S7". The "✓" symbol indicates a powered SP-chain, while the "×" symbol corresponds to a deactivated chain. Both sides of the demonstrator are tested separately.

The tests of interest are threshold and noise studies, where the average noise level of the module, the measured leakage current of the sensors and the voltage drop over the FEs at each module (measured with the PSPP chips) are used to evaluate the behaviour of the demonstrator under the various scenarios. Apart from the different scenarios it also needs to be verified that the two demonstrator sides are independent of each other. Hence, the measurements were performed once with the other side being fully powered and once with it being turned off completely. The aim for the measurements within the scope of this thesis was to do a final evaluation of noise and thresholds for different powering configurations of the inclined and barrel SP-chains and to compare to measurements from 2020 for consolidation of results.

All tests were performed at $T_2 = 17°\text{C}$, which means that the modules are at a temperature of $T_{\text{mod}} \approx 30°\text{C}$. Before running the tests, all modules were retuned to a minimal threshold of $3000\,\text{e}$. In Figure A.1 a comparison of the average threshold and noise values before and after retuning are shown for comparison. Only very few modules in the inclined chains actually needed to be retuned.

The findings of these and especially the studies from 2020 will also be published in a paper by the collaboration.

Results

The results for the C-side with the A-side being turned on are shown in Figure 8.8 and 8.9. The uncertainty of the measurements is $\pm(0.01\% \cdot V_{\text{out}} + 0.01\% \cdot V_{\text{nom}})$, where $V_{\text{nom}} = 600\,\text{V}$

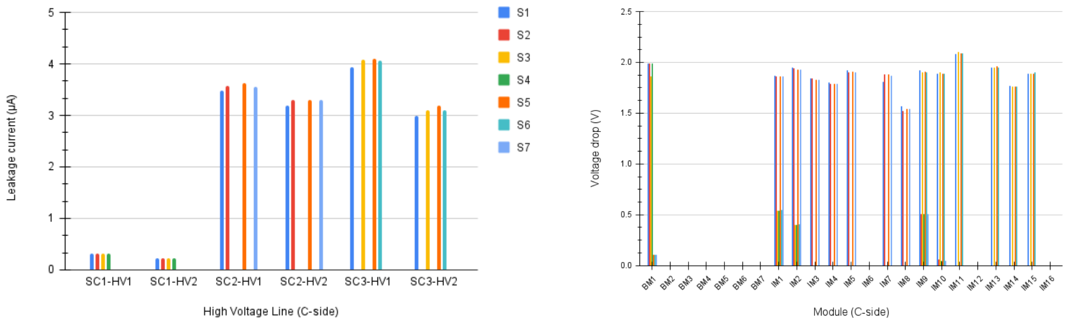

Figure 8.8: Results of the measurements performed on the C-side of the demonstrator. **Left:** The leakage currents for the six different HV chains are measured for all seven scenarios. They remain stable. The uncertainty of the measurements is $\pm(0.01\% \cdot I_{\text{out}} + 4\,\text{nA})$. **Right:** The voltage drop over the SP-chains is shown. Residual currents in the DCS line cause small voltage drops in the first two modules at the beginning of each chain, even when they are turned off. The uncertainty of the measurements is $\pm(0.01\% \cdot V_{\text{out}} + 0.01\% \cdot V_{\text{nom}})$.

is the nominal voltage of the power supply[1]. On the right in Figure 8.8 the measured voltage drops are shown for the IMs and the BMs. The chains start with BM1, IM1 and IM9 for the C-side. It can be noted that residual currents in the DCS line cause small voltage drops in the first two modules at the beginning of each chain. This behaviour was observed with inactive modules, as it is intrinsic to the PSPP chips. Apart from this, no significant differences between the scenarios were observed. Bypassed modules and broken PSPP chips, which are not returning valid measurements, are marked by -0.1. The leakage currents for the HV lines, as shown on the left, remain stable in all scenarios. The uncertainty of the measurements is $\pm(0.01\% \cdot I_{\text{out}} + 4\,\text{nA})$[2].

In Fig 8.9, the mean threshold and noise of the modules is shown. The mean values of threshold and noise are obtained by fitting a Gaussian to the per-pixel threshold and noise distributions, which are obtained using the s-curve method, as explained in Section 7.3.2. The errors are the fitted standard deviation. All values are stable for the different scenarios, except for FE chip C_IM_05_2 in scenario 5. This chip is known to be unstable. The high noise in the last modules originates from incompletely depleted sensors and will be explained in Section 8.3.2.

The measurements were repeated with the A-side being turned off and the results are compatible, as expected. For the A-side the same measurements were performed, once with the C-side active and once inactive. The two results are also compatible, as expected.

---

[1] The exact uncertainty is not known as the uncertainty specifications for the power supply are only guaranteed for one year. Also, the exact model of the power supply is not listed in the available manuals any more (https://iseg-hv.com/en/products/detail/EHS). However, the power supply belongs to the same series and hence the same specifications hold.

[2] Same comment as above.

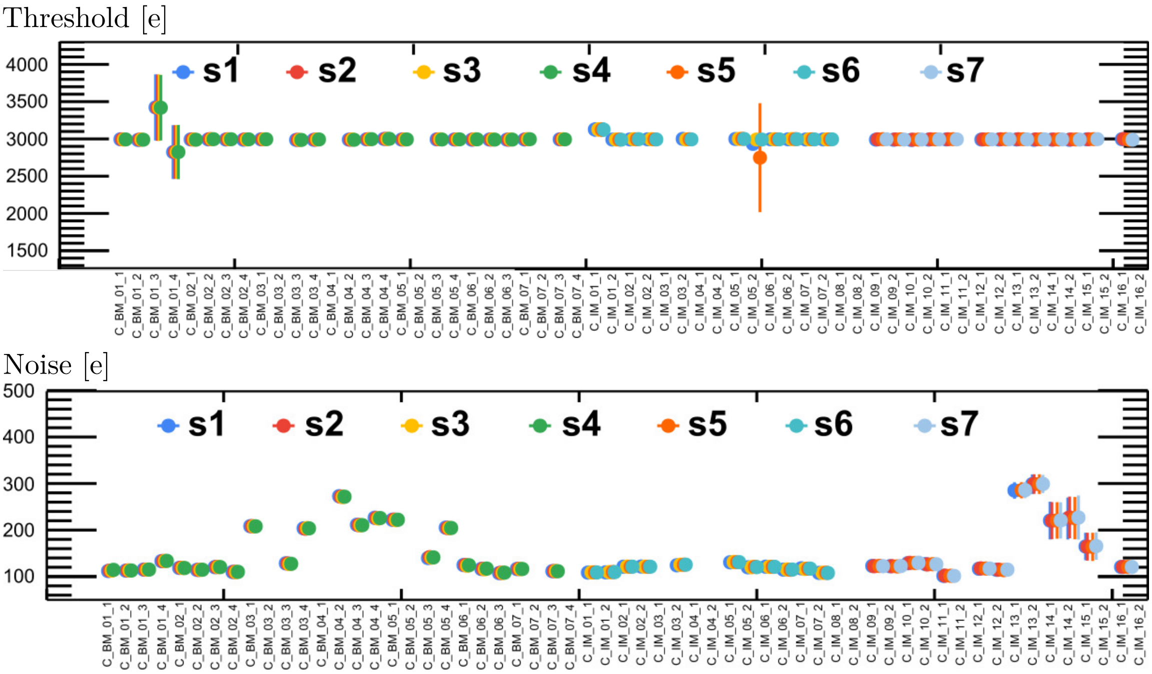

Figure 8.9: **Top:** Mean thresholds of the modules. **Bottom:** Mean noise measured for each module for the different serial powering scenarios. The mean values are obtained by fitting a Gaussian to the per-pixel threshold and noise distributions, which are obtained using the S-curve method. The errors given are the fitted standard deviation.

Measurement Methods - Serial Powering Configurations

In order to understand if there exist effects related to the number of modules in a single SP-chain, two different chain lengths were tested on the dual modules on the C-side of the detector. The nominal scheme, which is shown in Figure 8.3, where the first eight modules and the remaining ones are powered in different SP-chains was compared to the merged SP-chains. In the merged SP-chain tests the default HV powering scheme with four separate HV groups for the IMs was used and only the LV powering is changed, such as shown in Figure 8.4.

Results

The measurements for the C-side with the A-side inactive are shown in Figure 8.10 and 8.11. The missing voltage drop for IM15 is due to a breaking PSPP chip. Interestingly, 7.2 µA was measured for the last HV group for merged SP-chains, which is more than double the leakage current compared to separate chains. In the last HV chain are the modules C_IM_13-16. Also, the average noise for the last modules is lower in the merged scenario.

These results can be understood as indication that in the merged configuration the last modules are fully depleted and in the separate configuration not. That the modules are not fully depleted in the separate configuration is known. As shown in Table 8.1, the last HV line has a lower set value than the required voltage for full depletion of the sensor. Full depletion in the merged scenario is possible as the applied bias HV and the per-module

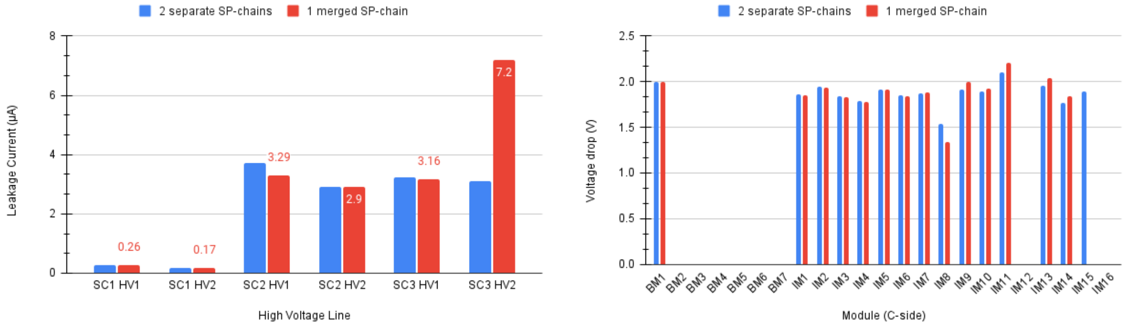

Figure 8.10: **Left:** Measured leakage currents for C-side modules under two different SP scenarios: separate and merge chains. For the last HV line the current is much higher when the LV lines of the inclined modules are merged as the sensor is effectively biased with a higher leakage current. **Right:** Voltage drops are slightly different in the later modules in the merged scenario. The missing voltage drop for IM15 is due to a faulty PSPP chip.

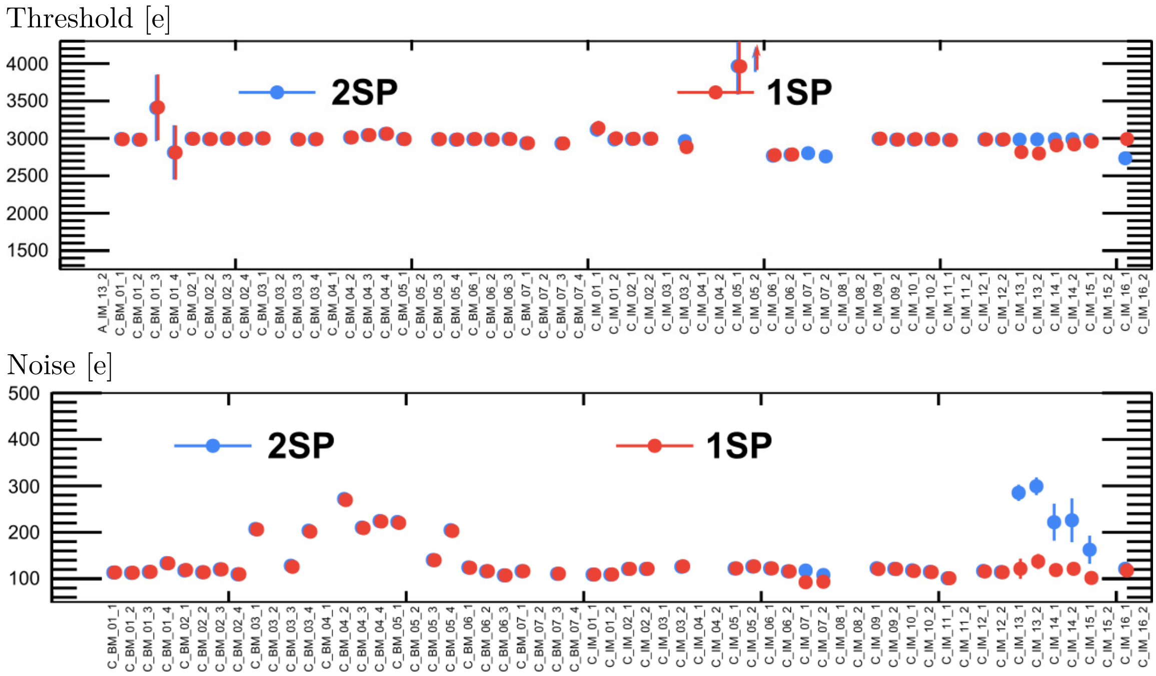

Figure 8.11: **Top:** The thresholds for the last modules are lower in the single merged SP-chain (1SP) compared to the separate SP-chains (2SP). **Bottom:** The average noise for the last modules is lower, indicating that in the merged configuration the last modules are fully depleted and in the separate configuration not.

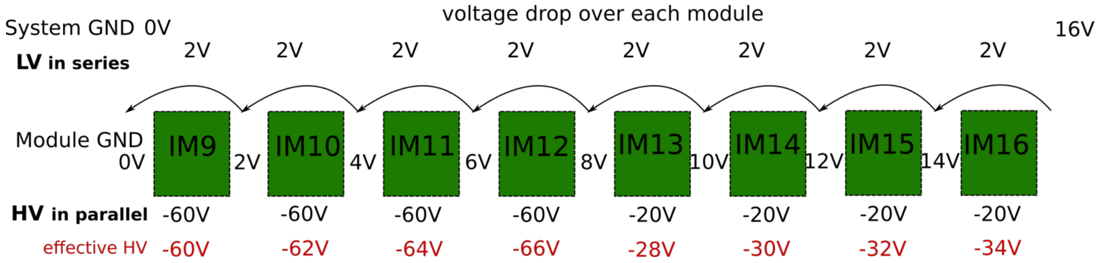

Figure 8.12: Bias HV levels and voltage drop in the last SP-chain exemplified for eight modules. The applied bias HV of -60 V or -20 V and the per-module variation of the ground potential add up to higher effective HV values for modules further back in the chain.

variation of the GND potential for the specific modules add up to higher values for the merged SP-chains compared to the separate SP-chains. This is common for SP-chains and explained in Section 8.2.

For the third SP-chain with inclined modules of the C-side of the demonstrator, the scenario is exemplified shown in Figure 8.12. An approximate voltage drop of 2 V is assumed and a chain length of eight modules. The SP-chain has two different HV lines, SC3-HV1 and SC3-HV2, both connected to four modules each. The first one at -60 V, the second at -20 V. As can be seen, the local GND of the second module in the chain is 2 V above the system GND. With the HV being referenced to the SP-chain ground, the sensor is exposed to an effective bias voltage of $\text{HV}_{\text{mod}} = \text{HV} + 2\,\text{V}$. Sensors further back in the chain are at even higher GND potentials. The last sensors in the second HV line are in this scenario at bias voltages around -30 V. With these effective higher HV biasing values, full depletion of the sensor is possible. In the real scenario the voltage drop is slightly lower as shown in Figure 8.10. Also, there are 16 modules in the chain, which means that the local ground is even higher towards the end of the chain.

The explanation for high leakage currents and low noise in the merged scenario can be concluded from the findings above. As explained in Section 4.2.1, the capacitance of the sensor changes with depletion. From Section 4.2.4 it is known that the capacitance has an impact on the thermal noise in the readout chip. Not fully depleted sensors thus have higher noise, which is what is observed in Figure 8.11. The higher leakage currents are also easily explained. Sensor C_IM_16 in the last chain experiences a breakdown at -30 V. With an effective HV close to the breakdown voltage the leakage current rises.

In order to verify the upper assumptions, in the default setup with two SP-chains the HV line SC3-HV2 for the modules C_IM_13-16 was varied form 20 V to 30 V in steps of 2 V. Closer to 30 V the noise and threshold values approach the noise and threshold values that were measured in the merged SP-chain scenario, as shown in Figure 8.11. The same holds for the leakage current.

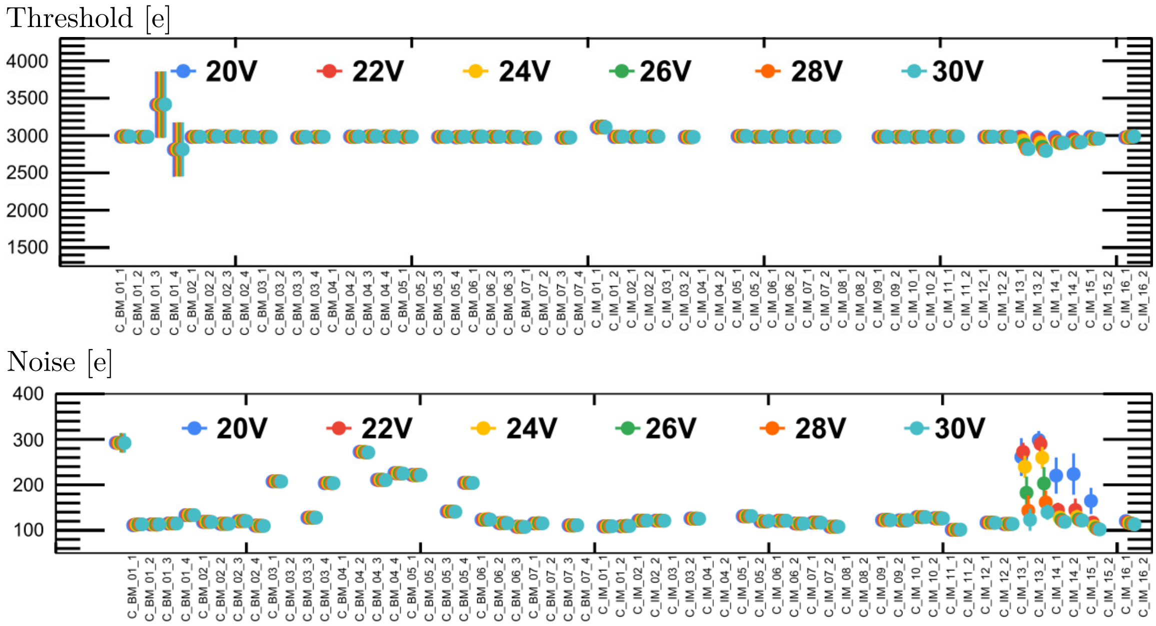

Figure 8.13: Average threshold and noise for the C-side modules for different HV values for the modules C_IM_8-16.

Conclusions

For the last four modules differences in terms of leakage current and average noise are seen when the length of the SP-chain is varied from eight to sixteen modules. This behaviour is, however, caused by the nature of the modules and the design of the SP-chains. The applied HV in a separate SP-chain is not high enough to fully deplete the sensor, while with the different per-module variation of the ground potential in the longer SP-chain it is. Due to high leakage currents the voltage in the separate SP-chain was kept at the lower value.

It was shown that in general the different SP-chain configurations do not have any effect on the module performance, as long as the HV supply of the modules allows full depletion.

8.3.3. Drain Wire Tests

In the following, the surge protection in the ITk is verified, for which a 3 m long wire with AWG 32 is foreseen. The one and only ground connection of the detector must survive a failure, such as the disconnection of the power supplies (I_{in} or I_{out}) in an accident. This requires that the highest maximal current on the drain wire does not damage the wire. For wires with AWG 32 the maximal current for separate wires is 0.53 A [179].

In order to mimic this failure, the current supply of the FE chips in the quad barrel SP-chain on the C-side of the demonstrator is cut. Tests are conducted for both separately, cutting I_{out} and I_{in}.

It should be mentioned already here that the currents of the FE-I4 readout chips are different, compared to the ITkPix currents. For a final evaluation of the results, the tests described in the following should be repeated with the final readout chips.

Measurement Methods

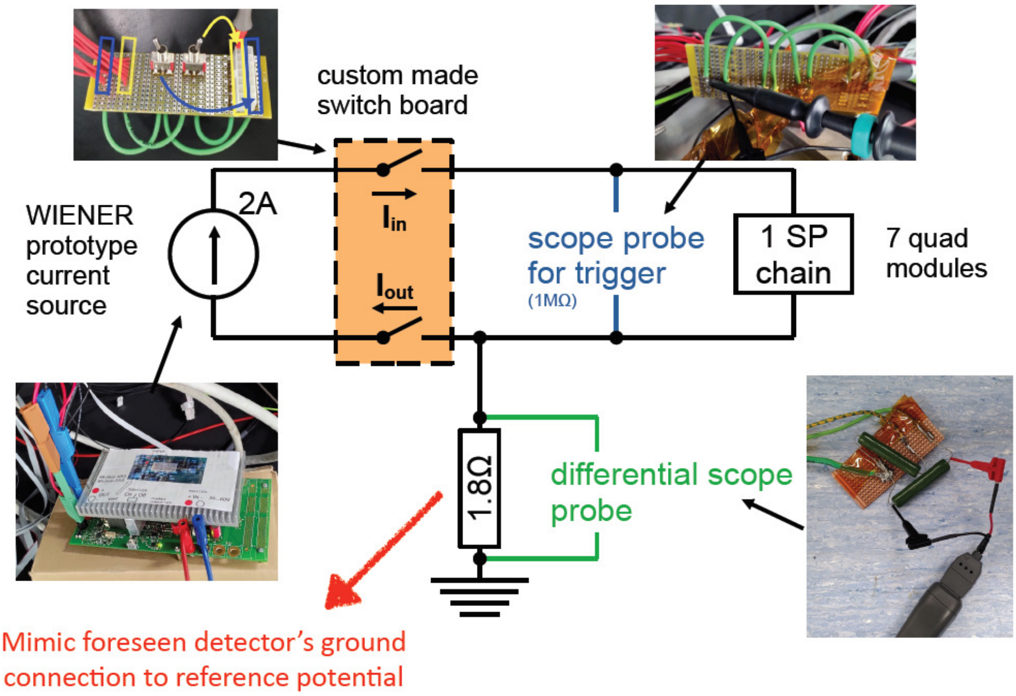

Figure 8.14: Setup for the grounding tests with a resistor mimicking the drain wire.

The demonstrator setup is prepared for the tests by disconnecting all parasitic grounding lines of the demonstrator in order to make sure only one well defined grounding line is left. The evaluation of the surge protection is then done in several steps. First, a 1.8 Ω resistor is connected as grounding line. It mimics the effective resistance of the foreseen drain wire of 3 m length with AWG 32. The resistance at 20 °C for AWG 32 is $0.538\,\Omega\,\mathrm{m}^{-1}$[179], hence the resistance for 3 m is

$$0.538\,\Omega\,\mathrm{m}^{-1} \cdot 3\,\mathrm{m} = 1.614\,\Omega\,.$$

The voltage drop in the resistor, when the current line is disconnected, is measured for three different supply currents ($I_{\mathrm{sp}} = 1\,\mathrm{A}$, 1.5 A and 2 A) with the probe of a scope with limited input bandwidth to suppress any high frequency noise pickup. Next, the resistor is exchanged by 3 m long cables with different wire gauges (AWG 32, 26, 20) to be realistic in terms of inductance of the wire. On these wires the voltage drop is measured again in the different disconnection scenarios.

The first part of the test with the resistor had been done before and was repeated for confirmation of the results. See Figure 8.14 for the setup of the measurements. A prototype WIENER current source is used which is connected to a switch board with mechanical switches. The switch board allows easily disconnecting the connection to either the input or the output line of the current source. A differential scope probe is connected in parallel to the resistor or the drain wire to measure the voltage drop over the wire. It is triggered on voltage changes.

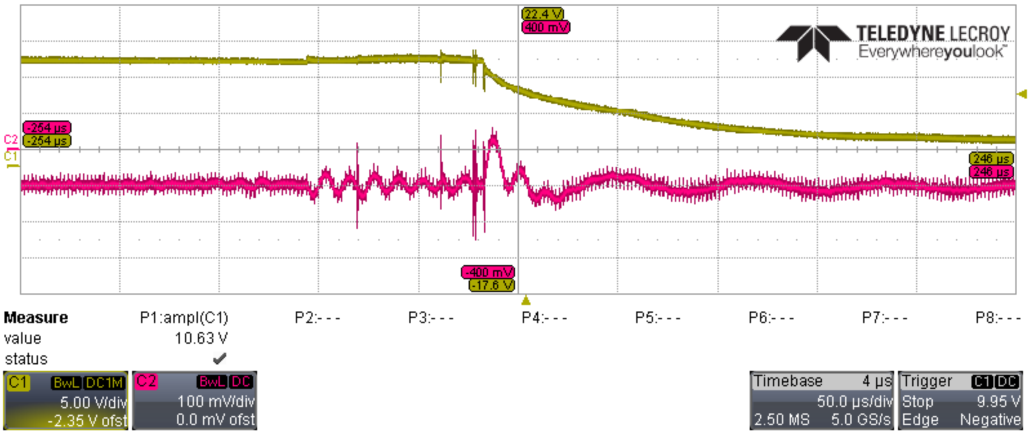

Measure P1:ampl(C1) P2:- - - P3:- - - P4:- - - P5:- - - P6:- - - P7:- - - P8:- - -
value 10.63 V
status ✓

C1 BwL DC1M 5.00 V/div -2.35 V ofst
C2 BwL DC 100 mV/div 0.0 mV ofst
Timebase 4 µs 50.0 µs/div 2.50 MS 5.0 GS/s
Trigger C1 DC Stop 9.95 V Edge Negative

Figure 8.15: Measured voltage drop in the probe in pink for cutting I_{out} with 2 A supply current and measuring over the resistor. The yellow curve shows the power supply terminal voltage.

Results

For $I_{\mathrm{sp}} = 2$ A and disconnecting I_{out} an oscillating voltage with a maximal positive amplitude of ≈ 130 mV is visible on the probe over the 1.8 Ω resistor, as shown in Figure 8.15 in pink. After the disconnection, a lower frequency oscillation remains. In yellow the power supply terminal voltage is shown. The moment the wires are disconnected is marked by the exponential drop of the voltage. It is unclear why there is a voltage drop of -100 mV over the resistor seen already before cutting the current line.

Before disconnecting the current and right when cutting it, there are also very short voltage peaks, which are interpreted to be related to the mechanical switch and its contact bounce. When the switch is being used, the momentum and elasticity of the switch mechanical components make the two components bounce apart several times. This causes switching between on and off before settling out of contact. After cutting the current this can be seen as spikes in the voltage. Touching the switch right before using it might also cause disturbances.

When disconnecting the incoming current line, there is no long lasting voltage drop measurable, as can be seen in Figure 8.16. Again, a very short peak is seen directly when cutting the lane and in the 100 µs afterwards from the contact bounce of the switch.

The two scenarios are repeated with $I_{\mathrm{sp}} = 1.5$ A and 1 A and the measured voltages are listed in Table 8.3. For lower supply currents the observed maximal positive current amplitude when cutting the outgoing current line reduces. When cutting the incoming current line only a very short pulse is visible in the probe exactly at the moment of the cut. For both cut scenarios and both voltages several voltage peaks from bounce can be seen.

For actual drain wires instead of the resistor, the scenarios look similar. The only difference is that the probe signal is much noisier. This results from the length of the wire and its capability of picking up other electrical signal from surrounding instruments.

See Figure 8.17 for the voltage measurement with a supply current $I_{\mathrm{sp}} = 2$ A and cutting I_{out} over a 3 m long wire with AWG32. On the probe approximately 120 mV are visible

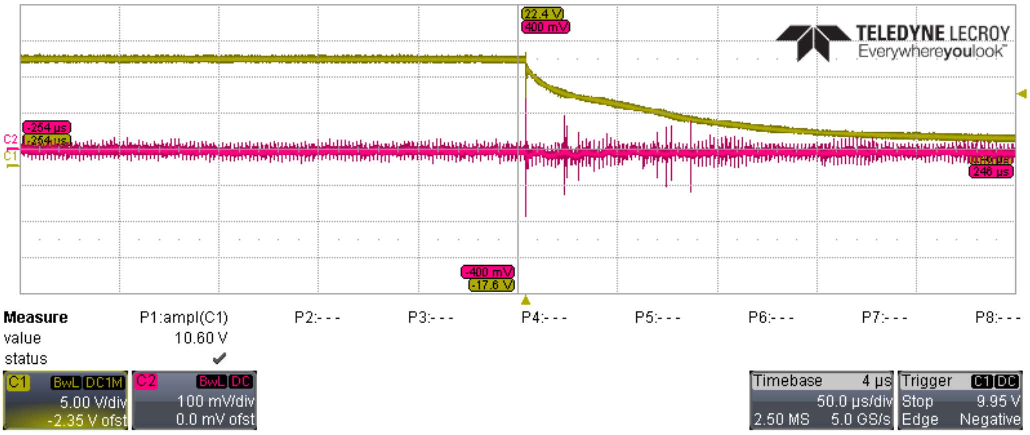

Figure 8.16: Measured voltage drop in the probe in pink for cutting I_{in} with 2 A supply current and measuring over the resistor. The yellow curve shows the power supply terminal voltage.

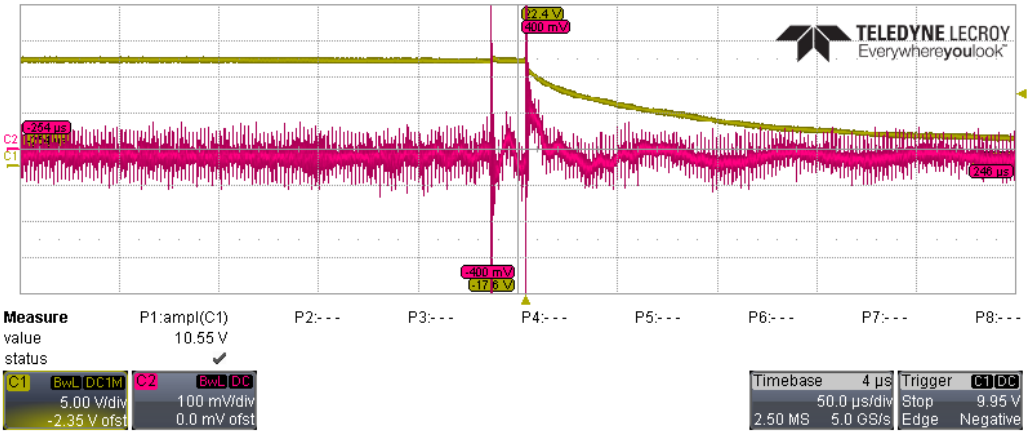

Figure 8.17: Measured voltage drop in the probe in pink for cutting I_{out} with 2 A current and measuring over a 3 m long wire with AWG 32.

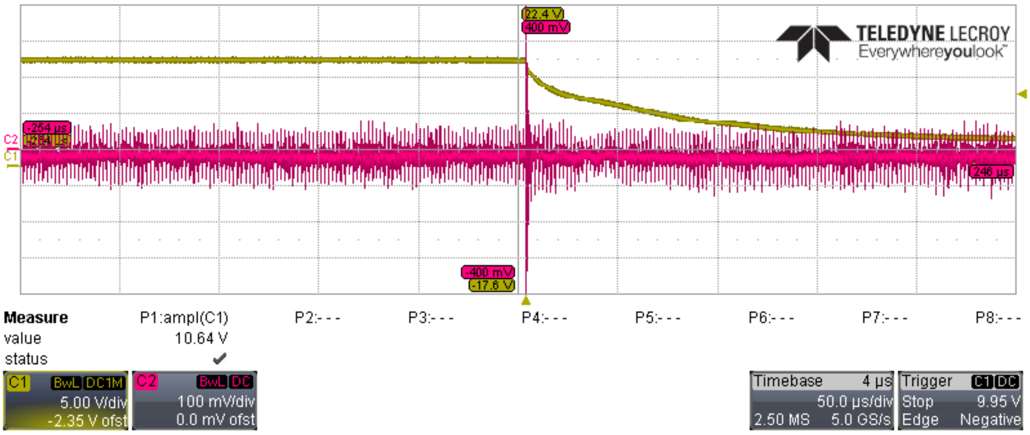

Figure 8.18: Measured voltage drop in the probe in pink for cutting I_{in} with 2 A current and measuring over a 3 m long wire with AWG 32.

Table 8.3: Induced voltages on the drain wire when cutting the output line of the current supply. The voltage drop scales linearly with an offset of -30 mV for the resistor. An uncertainty of ±20 mV for the measurements is assumed.

Wire gauge	I_{sp} [A]	Voltage drop [mV]	$\frac{\text{Voltage drop}}{1\,\text{A}}$ [mV A^{-1}]	$\frac{\text{Voltage drop}}{1\,\text{A}\cdot\text{FE}}$ [mV A^{-1}]
Resistor $R = 1.8\,\Omega$	2	130	40 (-30 mV offset)	2.32
Resistor $R = 1.8\,\Omega$	1.5	90	40 (-30 mV offset)	2.14
Resistor $R = 1.8\,\Omega$	1	50	40 (-30 mV offset)	1.79
32	2	120	60	2.14
26	2	60	30	1.07
20	2	≈ 0	≈ 0	≈ 0

and a seemingly unrelated short pulse before cutting the line. In Figure 8.18 the result for $I_{\mathrm{sp}} = 2$ A and cutting I_{in} over a 3 m long wire with AWG 32 is shown. Only a short pulse and noise from the bounce of the switch are visible on the probe.

For different wire gauges both disconnection scenarios are repeated with $I_{\mathrm{sp}} = 2$ A. The wire with AWG 26, which corresponds to a larger diameter of the wire, behaves as expected and shows a smaller voltage drop of ≈ 60 mV when cutting the outgoing line. Noise and short peaks can be measured when disconnecting the incoming line. The overall noise is also lower. For the wire with AWG 20 the noise is drastically reduced and only a short peak in the probe is measured for both scenarios at the time when the current is disconnected. This is expected as a much thicker wire has less resistance. The voltage drop values for these measurements can also be found in Table 8.3. In order to improve the measurement, the current should be directly measured with a current probe instead of a voltage probe over a very small resistance. Also, the voltage reading of the scope was done by eye. Based on the scale, the uncertainties of the measurements amount to ±50 mV. However, due to large scale width, they can be assumed to be ±20 mV.

Conclusions

For each measured voltage drop, over the resistor or the drain wire, the voltage drop corresponding to $I_{\mathrm{sp}} = 1$ A is calculated, as noted in Table 8.3. For seven modules in the SP-chain with four FEs each, 28 FEs in total, the voltage drop per ampere and FE can be calculated. It is stated in the last column of Table 8.3.

From the table it can be seen that the voltage on the GND line scales with the supply current. For each 0.5 A supply current the measured voltage drop rises by 40 mV. Extrapolating this, there is an offset of -30 mV for no supply current, which is surprising and might originate from improper calibration of the probe. The current on the grounding line for a voltage drop of 40 mV amounts to approximately 50 mA for $I_{\mathrm{sp}} = 0.5$ A. The values for grounding with resistor and corresponding drain wire diameter are consistent.

For larger wire diameters the voltage drop is lower, as expected. The resistance of the 3 m long wire with AWG 26 is $R_{\mathrm{AWG\,26}} = 0.134\,\Omega\,\mathrm{m}^{-1} \cdot 3\,\mathrm{m} = 0.402\,\Omega$ and of the 3 m long wire with AWG 20 $R_{\mathrm{AWG\,20}} = 0.033\,\Omega\,\mathrm{m}^{-1} \cdot 3\,\mathrm{m} = 0.099\,\Omega$. From the voltage drop over the wire with AWG 32, the expected voltage drop for the other two wires can be extrapolated. For the 3 m long wire with AWG 26 a voltage drop of 0.52 mV is expected, which is slightly below the obtained value. The negligible voltage drop for the wire with AWG 20 is also expected.

It could be shown that the foreseen drain wire with AWG 32 can withstand the current peak of a discharging FE-I4 SP-chain of seven quad modules without being damaged. Due to the linear scaling behaviour of the measured voltage drop, the expected current on the grounding line for higher supply currents for the ITkPix modules can be approximated. The exact supply current is not yet defined. Currents higher than 6 A can be critical. However, if the current on the drain wire will not exceed 500 mA, the drain wire with AWG 32 is also suitable for the ITk.

8.3.4. Summary and Outlook

The FE-I4 demonstrator has served to prove design concepts for the ITk and to define what needs to be checked on the RD53A demonstrator. Among these tests is the validation of the new PP0 which was improved with a thicker layer of Kapton after detecting crosstalk on the original version. Serial powering for multiple parallel SP-chains with coupled grounds and up to 16 modules was successfully demonstrated. The behaviour of the modules in the SP-chains is not influenced by the powering status of surrounding SP-chains. Changes in the length of an SP-chain also, in general, do not influence the module behaviour, except when the module sensors are not biased with a high enough HV to fully deplete the sensors. In this case, the, by design of the SP-chains, different local GND levels of the modules can have an influence on the module performance.

Another shortcoming of the FE-I4 modules is the LV connector, which will, however, only be replaced on the ITkPix modules and not on the RD53A modules yet. The modifications of the SLDO, based on findings from the FE-I4 demonstrator, can be tested with the RD53A modules. However, as mentioned in Section 7.3.2, the turn-on behaviour of the RD53A chips is unstable and this problem is only fixed in the ITkPix chip. The same holds for the correct handling of overcurrents in chips, which need to be absorbed by the respective SLDO to keep the SP-chain running.

It was also shown that the surge protection concept for the ITk with a 3 m long wire with AWG 32 sufficiently works for FE-I4 modules. An SP-chain powered with 2 A will induce a maximum current of approximately 200 mA on the drain wire. This does not break the wire. For higher currents, as needed for the ITkPix modules, the foreseen drain wire might be sufficient, depending on the final supply current and configuration. Other wire gauges were tested, so that a wire with smaller wire gauge could most likely also be chosen. Tests with the final system still have to be conducted once the HW is available. In the meanwhile these tests are also performed on the RD53A demonstrator.

8.4. RD53A Demonstrator

The purpose of the RD53A demonstrator is to refine the validation of ITk design, module loading procedures and to develop an infrastructure for the loaded local supports, to which the longeron and the half-ring count. Cables, connectors, power supply units, the DCS and also the cooling system comprise the infrastructure. The RD53A demonstrator is currently still in the construction phase.

8.4.1. Setup of the Demonstrator

The setup of the RD53A demonstrator evolves in a laboratory at CERN. It can very generally be split into these different components: the actual loaded local support with cooling pipes inside the environmental box, the interlock and the powering chain, and the readout chain. For the ITk titanium cooling pipes will be used, which are integrated in the mechanics.

All parts of the demonstrator setup are developed and prepared in different institutes and brought to CERN to commission the demonstrator. The RD53A demonstrator, as well as the previous demonstrator project, is therefore an enormous international teamwork throughout the outer barrel community.

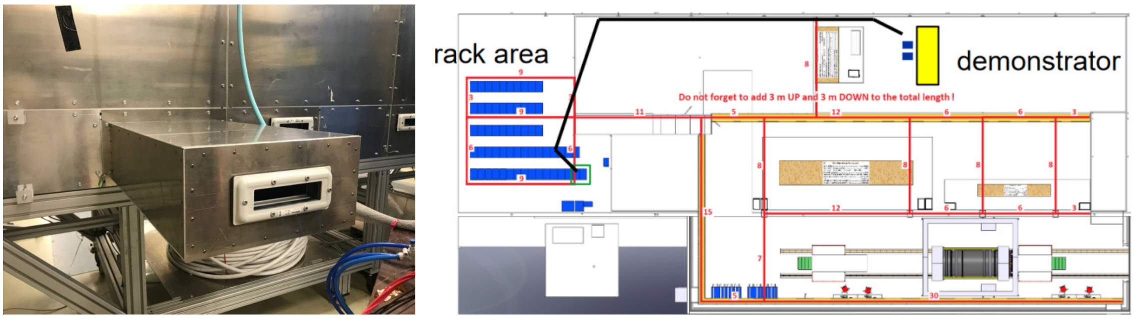

Figure 8.19: **Left:** Additional Faraday cage to the environmental box to house the CSB for the power cables and to mimic the PP1. **Right:** Overview of the locations of the demonstrator components. The yellow rectangle marks the environmental box, in blue are the racks with the interlock and additional power supplies.

While no components of the loaded local support of the previous FE-I4 demonstrator can be used any further, the environmental box, several power supplies and the interlock hardware can. Also, apart from the cooling system on the mechanics, the original available CO_2 cooling system in the laboratory is reused. Only a small additional box was added to the Faraday cage to house an adapter board for the power cables and to mimic the PP1, as can be seen in Figure 8.19. As for the FE-I4 demonstrator, the PP1 and PP2 as well as the cable bundles in between are replaced by an adapter board, again called CSB. The PP1 in the real detector functions as the end of the Faraday cage and can hence be simulated with this box. Given there is insulation between the small box and the environmental box, it can be opened during operations on the demonstrator. So from outside, the demonstrator setup will still look almost the same. Flushing with dry air and temperature control via the CO_2 cooling system to assure safe conditions for operating the modules is possible, just like for the FE-I4 demonstrator.

In order to develop the setup from FE-I4 to RD53A, all powering and readout cables and all mechanical structures belonging to the loaded local support of the previous version of the demonstrator had to be removed. Temperature and humidity sensors can be reused, however.

Different to the previous setup, the power supplies for the RD53A demonstrator are located in the so-called rack area, next door to the experimental hall with the environmental box.

The same holds for the readout PCs. 65 m long cables are used to connect the power supplies and readout PCs with the demonstrator. A map of the locations of the demonstrator components can be seen in Figure 8.19. The interlock keeps its previous position in the blue rack as indicated next to the demonstrator: analog signals from the sensors cannot be transported over that long distance, so the interlock signals will go from the experimental hall to the rack area and the power supplies.

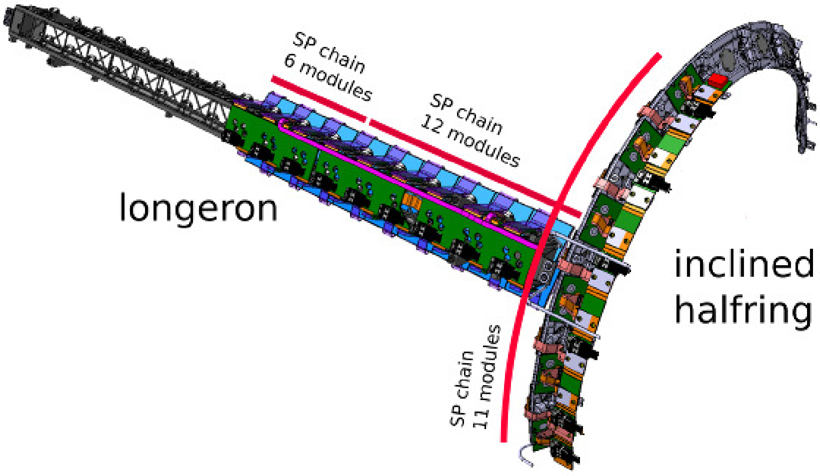

Figure 8.20: Sketch of the RD53A demonstrator setup.

The demonstrator itself will have at least 29 RD53A modules in three SP-chains. The maximal capacity is 40 modules. For prototyping the ITk, mechanics from layer 3 are used for one half populated inclined half-ring with one SP-chain of 11 modules and for a longeron with 2 SP-chains of 6 and 12 quad modules, as sketched in Figure 8.20. This will allow to test all three variations of SP-chains. The modules have 150 µm thick FEs and 150 µm thick sensors as planned for the outer barrel region. As mentioned in Section 8.1 the OB module loading concept allows that loaded cells can be easily installed and removed such that the OB demonstrator mechanics are in principle capable of housing ITkPixV1.1 modules once all tests on the RD53A modules are done. In Chapter 9, the modules for the demonstrator are discussed.

In the following sections the interlock and the readout system will be explained in more detail as this was the focus of the work within the scope of this thesis. The DCS and the monitoring system will also briefly be introduced.

Readout Chain, Monitoring and DCS

As explained in Section 8.3.1, the detector readout requires indirect connection through long optical fibre connections and transceiver and/or aggregator hardware between on-detector and off-detector readout parts.

For the demonstrator readout, the DAQ ITkSW communicates with a custom PCI Express FPGA board, called Front-End Link eXchange (FELIX) which is hosted in a FELIX Server.

FELIX is the interface to the on-detector readout components. It sends the configuration and control commands to the detector FEs through its fibre down-links. It also receives the aggregated FE data through its fibre up-links.

The first FELIX was installed in the Phase-I upgrade for the New Small Wheel and the trigger readout of the LAr calorimeter [180]. For the Phase-II upgrade of the ATLAS Detector, FELIX will be adopted as common readout system for ATLAS [181]. It will hence also be used for the ITk and therefore be tested on the demonstrator. The FELIX version used for the demonstrator builds on the initial version Phase-I FELIX [182].

From the FEs several 1.28 Gbit/s e-links are aggregated in one up-link which operates at up to 10.24 Gbit/s. Each module can use up to four e-links. If there are four e-links to transmit data, then each FE is associated with one e-link. If there are fewer e-links than FEs, a master FE can merge data stream from slave FEs. The number of e-links is dependent on the expected particle rate at the position in the detector. The e-link aggregation is performed in an lpGBT chip, an upgrade of the GBTx chip, [183][3]. This is an asymmetrical transceiver/aggregator ASIC with several configuration possibilities[4]. On the downlink, the lpGBT splits the bandwidth between up to 16 modules so that they receive commands at 160 Mbit/s each [183].

The e-link uplinks running at 1.28 Gbit/s each suffer from degradation through the electrical wires before arriving to the lpGBT aggregator. Equalisation is thus necessary to enhance the signal quality. This is done in a GBCR chip [184]. The lpGBT electrical high-speed up-link and down-link are transformed to/from optical signal through VTRx+ (another dedicated ASIC [185, 186]).

An opto board is a PCB on which up to four lpGBTs, GBCRs and one VTRx+ are assembled. For the demonstrator, an optobox with seven opto boards is used as shown in Figure 8.21. The optobox includes also a power board, a connector board, housing and cooling plate. Opto boards with only one or two lpGBT are used, which leads to a different mapping than in the final detector. The optobox needs auxiliary power (1.2 V) which is derived on the power board of the optobox by a system of DCDC converters.

The DCS controls the powering of the detector elements. It was written within the scope of the master thesis in Ref. [187]. The DCS is integrated into a finite state machine (FSM) with quick navigation and a control hierarchy, similar to the FSM that is used for the control of the current ATLAS detector. It keeps track of the states of all the components of the demonstrator and provides methods for the operator to send components from one state to another. GUI panels have been developed for all detector components to facilitate the operation. As an example, turning on and off several SP-chains is possible in a simple panel.

Detector module and optobox voltages as well as temperatures are monitored with a so-called MoPSHUB 4beginners. MOPS stands for *Monitoring Of Pixel Systems*. The MoPSHUB 4beginners differs from the final MoPSHUB in that it is controlled by a RaspberryPi, instead of an FPGA. The MOPS is an ASIC with an ADC and a CAN bus [188]. In Figure 8.21 the MoPSHUB 4beginners is shown with one CAN Interface Card (CIC) module and the

---

[3] The manual serves as the main reference: https://lpgbt.web.cern.ch/lpgbt/v1/.

[4] The up-link runs at 5.12 Gbit/s or 10.24 Gbit/s with two Forward Error Correction choices (FEC5, FEC12), whereas the down-link operates at 2.56 Gbit/s with FEC12.

Figure 8.21: **Left:** The MoPSHUB 4beginners, housing the RaspberryPi and a CIC card. **Middle and right:** Optobox with seven optobards, including power board, connector board, housing and cooling plate.

card with the RaspberryPi. Analog signals are measured and digitised and then routed to the DCS for monitoring. The interlock status and CO_2 cooling plant monitoring is also integrated into the DCS, where the first is shown in Figure 8.22. Signals from these units come from a different monitoring system intertwined with the interlock.

An overview of the infrastructure with off- and on-detector services is shown in Figure 8.23. The off-detector services describe the CSB and all the cables that connect the power supplies, the MoPSHUB 4beginners and the interlock. With respect to the FE-I4 setup, the HV power supply and the power supply for the MoPSHUB 4beginners are reused. A new LV Wiener power supply is used and the existing interlock is updated. Pigtails, PP0s and the type-1 cables belong to the on-detector services. All of them have been exchanged with regard to the FE-I4 demonstrator.

Interlock

The purpose of an interlock is to protect operators and the detector. It bypasses the DCS and blocks the power supplies (HV, LV, MOPS power (monitoring), opto system power) directly in case of need. The interlock is based on an Interlock Matrix Crate (IMC) with an FPGA as centrepiece, which is used in the current IBL and was also used for the FE-I4-demonstrator. The interlock program is, in fact, an updated version of the interlock already used for the FE-I4 demonstrator. Eventually, the interlock system is to be upgraded to a completely new Local Interlock & Safety System (LISSY) which is planned for the ITk [189]. This system will replace the current updated but preliminary system, however, it is not yet commissioned.

The general functionality of the interlock is the following: analog signals are routed to interlock cards where the signal is compared to a threshold. The output digital signals are routed into the FPGA of the IMC. Based on a logical OR of certain input signals an interlock decision for a certain component is made by the FPGA. This means that the FPGA has to be configured correctly to set the interlock dependencies for the RD53A demonstrator. The interlock signal is then distributed to the respective components which

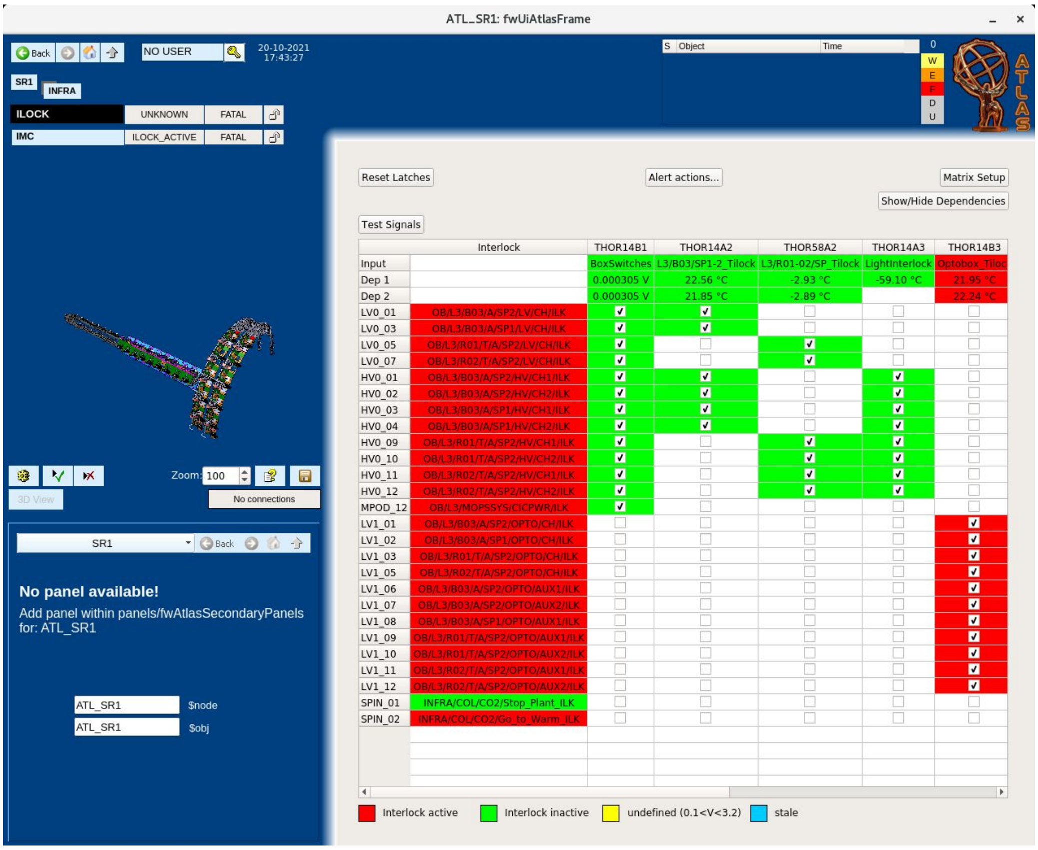

No panel available!
Add panel within panels/fwAtlasSecondaryPanels for: ATL_SR1

ATL_SR1 $node
ATL_SR1 $obj

	Interlock	THOR14B1	THOR14A2	THOR58A2	THOR14A3	THOR14B3
Input		BoxSwitches	L3/B03/SP1-2_Tilock	L3/R01-02/SP_Tilock	LightInterlock	Optobox_Tiloc
Dep 1		0.000305 V	22.56 °C	-2.93 °C	-59.10 °C	21.95 °C
Dep 2		0.000305 V	21.85 °C	-2.89 °C		22.24 °C
LV0_01	OB/L3/B03/A/SP2/LV/CH/ILK	☑	☑	☐	☐	☐
LV0_03	OB/L3/B03/A/SP1/LV/CH/ILK	☑	☑	☐	☐	☐
LV0_05	OB/L3/R01/T/A/SP2/LV/CH/ILK	☑	☐	☑	☐	☐
LV0_07	OB/L3/R02/T/A/SP2/LV/CH/ILK	☑	☐	☑	☐	☐
HV0_01	OB/L3/B03/A/SP2/HV/CH1/ILK	☑	☑	☐	☑	☐
HV0_02	OB/L3/B03/A/SP2/HV/CH2/ILK	☑	☑	☐	☑	☐
HV0_03	OB/L3/B03/A/SP1/HV/CH1/ILK	☑	☑	☐	☑	☐
HV0_04	OB/L3/B03/A/SP1/HV/CH2/ILK	☑	☑	☐	☑	☐
HV0_09	OB/L3/R01/T/A/SP2/HV/CH1/ILK	☑	☐	☑	☑	☐
HV0_10	OB/L3/R01/T/A/SP2/HV/CH2/ILK	☑	☐	☑	☑	☐
HV0_11	OB/L3/R02/T/A/SP2/HV/CH1/ILK	☑	☐	☑	☑	☐
HV0_12	OB/L3/R02/T/A/SP2/HV/CH2/ILK	☑	☐	☑	☑	☐
MPOD_12	OB/L3/MOPSSYS/CICPWR/ILK	☑	☐	☐	☐	☐
LV1_01	OB/L3/B03/A/SP2/OPTO/CH/ILK	☐	☐	☐	☐	☑
LV1_02	OB/L3/B03/A/SP1/OPTO/CH/ILK	☐	☐	☐	☐	☑
LV1_03	OB/L3/R01/T/A/SP2/OPTO/CH/ILK	☐	☐	☐	☐	☑
LV1_05	OB/L3/R02/T/A/SP2/OPTO/CH/ILK	☐	☐	☐	☐	☑
LV1_06	OB/L3/B03/A/SP2/OPTO/AUX1/ILK	☐	☐	☐	☐	☑
LV1_07	OB/L3/B03/A/SP2/OPTO/AUX2/ILK	☐	☐	☐	☐	☑
LV1_08	OB/L3/B03/A/SP1/OPTO/AUX1/ILK	☐	☐	☐	☐	☑
LV1_09	OB/L3/R01/T/A/SP2/OPTO/AUX1/ILK	☐	☐	☐	☐	☑
LV1_10	OB/L3/R01/T/A/SP2/OPTO/AUX2/ILK	☐	☐	☐	☐	☑
LV1_11	OB/L3/R02/T/A/SP2/OPTO/AUX1/ILK	☐	☐	☐	☐	☑
LV1_12	OB/L3/R02/T/A/SP2/OPTO/AUX2/ILK	☐	☐	☐	☐	☑
SPIN_01	INFRA/COL/CO2/Stop_Plant_ILK	☐	☐	☐	☐	☐
SPIN_02	INFRA/COL/CO2/Go_to_Warm_ILK	☐	☐	☐	☐	☐

🟥 Interlock active 🟩 Interlock inactive 🟨 undefined (0.1<V<3.2) 🟦 stale

Figure 8.22: Representation of the interlock in the FSM. The interlock input signals are seen in the top row and the output signals on the left. Red means that the output is interlocked or the input is invalid, green means that the output is not interlocked or that the input signal is valid.

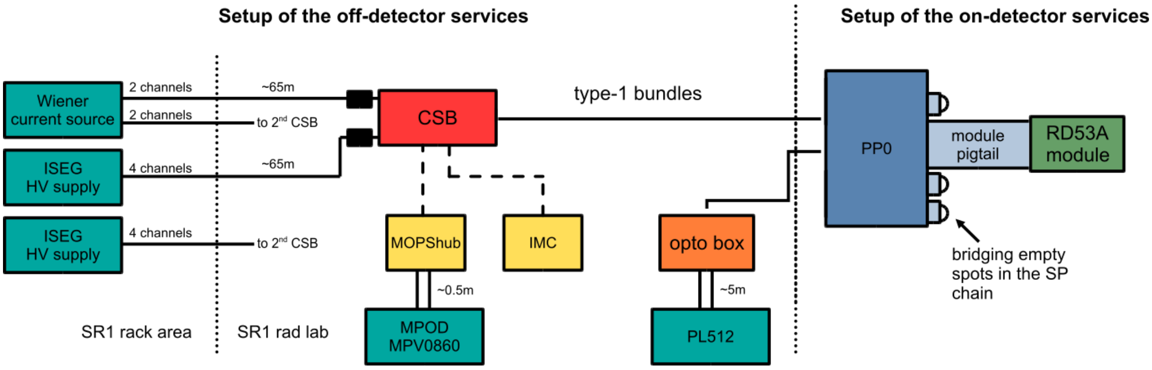

Figure 8.23: Sketch of the RD53A demonstrator infrastructure. The off-detector services describe all the cables and connectors that lead to the power supplies. Pigtails, PP0s and the type-1 cables belong to the on-detector services.

need to be interlocked, such as the power supplies. On the IMC are also monitoring units which transmit the interlock and cooling plant signals to the DCS, as mentioned before. Additionally, they provide the monitored temperature values. The monitoring units, however, cannot be used to change the interlock logic.

On the interlock cards specific thresholds can be set for the comparators. For the NTCs of the SP-chains a threshold of 40 °C is set. The opto board NTCs interlock at 30 °C. Two further sensors make sure that the box is closed and light-tight. There also exist specific interlock cards which handle these signals. The same holds for the humidity signals, which are reworked temperature interlock cards. Another input signal is the status of the cooling plant. The functionality of all cards is documented in Ref. [190].

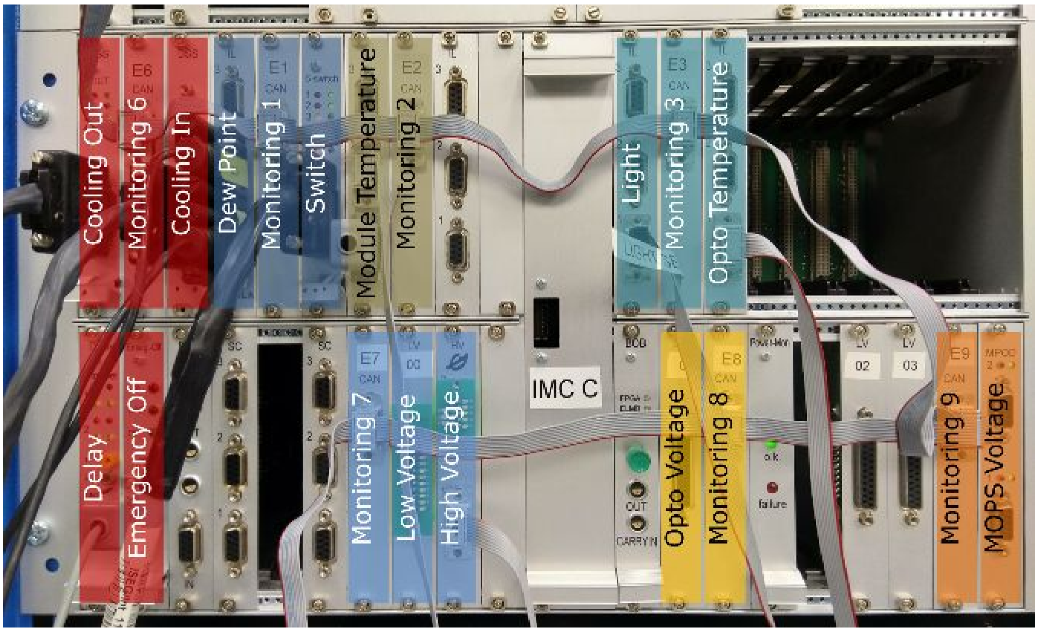

Figure 8.24: Photo of the IMC with schematic labelling of the components.

A photo with schematic labelling shows the interlock with the interlock cards in Figure 8.24. In the upper row, the input from the cooling plant, the dew point sensors, the door switches and the temperature sensors from modules and the optobox are mounted. In the lower row are the interlock output cards which transmit signals to the LV, HV, MOPS and opto power supplies. There is also a card which evokes a delayed signal for the LV power supplies as they need to be turned off with a delay with respect to the HV power supplies. For all other systems the monitoring cards are integrated.

It needs to be made sure that the right combination of signals leads to interlock outputs. In order to protect operators, it needs to be made sure that there is no high voltage potential on any part of the demonstrator which could accidentally be touched. This means that as soon as the box is opened up the module power needs to be turned-off immediately. Regarding the module side, threats are high humidity combined with cold temperatures, leading to condensation and possible ice on the module. This could induce mechanical stress or shorts on the module. Hence, humidities with respect to the cooling line temperatures and the temperature of the environment need to be controlled. For this purpose the dew point is measured and must never be above the module temperature. To assure that the leakage currents of the sensors are not too high, no light must be in the box which could cause an additional photo current.

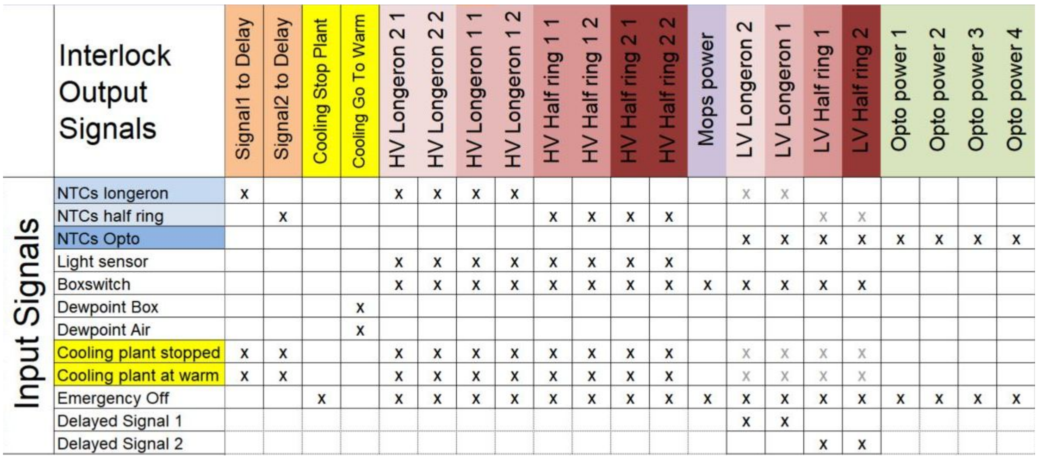

	Interlock Output Signals	Signal1 to Delay	Signal2 to Delay	Cooling Stop Plant	Cooling Go To Warm	HV Longeron 2 1	HV Longeron 2 2	HV Longeron 1 1	HV Longeron 1 2	HV Half ring 1 1	HV Half ring 1 2	HV Half ring 2 1	HV Half ring 2 2	Mops power	LV Longeron 2	LV Longeron 1	LV Half ring 1	LV Half ring 2	Opto power 1	Opto power 2	Opto power 3	Opto power 4
Input Signals	NTCs longeron	x				x	x	x	x						x	x						
	NTCs half ring		x							x	x	x	x				x	x				
	NTCs Opto														x	x	x	x	x	x	x	x
	Light sensor					x	x	x	x	x	x	x	x									
	Boxswitch					x	x	x	x	x	x	x	x	x	x	x	x	x				
	Dewpoint Box				x																	
	Dewpoint Air				x																	
	Cooling plant stopped	x	x			x	x	x	x	x	x	x	x		x	x	x	x				
	Cooling plant at warm	x	x			x	x	x	x	x	x	x	x		x	x	x	x				
	Emergency Off			x		x	x	x	x	x	x	x	x	x	x	x	x	x	x	x	x	x
	Delayed Signal 1														x	x						
	Delayed Signal 2																x	x				

Figure 8.25: Representation of the interlock matrix. On the left the inputs are listed, such as the temperature and humidity sensors, the door switches and the light sensor. On the top row the power supplies for HV, LV and opto power are represented. The matrix indicates by using crosses which sensor has an effect on which power supply channel, i.e. crosses mean that input will trigger output. Greyed out crosses are indirectly input signals to the interlock for the LV power supplies as LV is turned off with a delay with respect to the HV power supplies.

As the interlock is built based on a logical OR, one forbidden state triggers an interlock. These dependencies can be shown in a matrix, as in Figure 8.25. The inputs signals are listed on the left, such as the temperature and humidity sensors, the door switches and the light sensors. On the top row the power supplies for HV, LV, opto and MOPS power are represented. Crosses indicate which sensor affects which power supply's interlock. Greyed out crosses describe the input signals to the interlock for the LV power supplies, but routed through the delay modules [190] as they are turned off after the HV power supplies. These delay signals are used when the temperature rises beyond the threshold of 40 °C on the module NTC of the last module in the chain or the CO_2 cooling is stopped. The signals from the cooling plant are used in the interlock system such that all HV power supplies are stopped when the cooling plant is stopped. In a situation where the dew points are too high, the cooling plant is warming up and as soon as it is at warm, the HV power supplies will be interlocked as well. The HV power supplies are also interlocked when light falls into the box or the module NTCs show too high temperatures. The optobox is the only system that stays on when the box is opened and only interlocks when the optobox temperature exceeds the threshold temperature. In addition, an emergency button for the operator interlocks the full system, switching everything off.

This matrix has then been translated to verilog code and flashed on the FPGA within the scope of this thesis. Two files are needed, where one describes the inputs and outputs (I/O) on the FPGA and the other defines the logic between these. The version of the matrix in Figure 8.25 is used while operating the RD53A demonstrator. The pinouts of all the interlock cables at the IMC are also documented[5]. The existing interlock documentation

---

[5] Code and the pinouts are on gitlab: https://gitlab.cern.ch/atlas-itk-pixel-systemtest/imc-for-rd53a-demonstrator/-/tree/master.

was updated as IMC-V40 document in Ref. [190].

In order to commission the interlock, all I/O channels were tested separately. Custom-made connectors with LEDs show if a pin of a connector is active or not. These connectors were used to validate that the correct turn-on and turn-off signals are sent to the power supplies. The temperature and light sensors from the FE-I4 demonstrator have been used as inputs to test the temperature and light interlock settings. The CO_2 cooling system, the humidity sensors and the box switches were directly tested with the respective hardware. The emergency switch was also tested to turn off everything. As a final commissioning step, the representation of the interlock in the DCS was confirmed.

8.4.2. Commissioning of the Setup

After commissioning the interlock and DCS system, a preliminary demonstrator test setup was set up right outside of the environmental box to allow for commissioning the readout infrastructure of the RD53A demonstrator. The CO_2 cooling system was therefore not used for this setup, instead a small cooling chuck cooled with a chiller. However, the interlock, the MoPSHUB and the DCS were used to control the powering of the modules and the optobox.

Before using the final readout path with the PP0, preliminary readout paths were used to install and commission the DAQ system. This means that the opto boards and FELIX were used in the DAQ chain with cables and connectors from the module testing setups as the PP0 was not yet available. On the module side the opto boards are therefore connected to breakout boards which are linked with display port cables to the adapter board that is also used for module testing. The module testing pigtail then connects the modules. On the FELIX side, the final DAQ path is used with the fibre connections between optobox and FELIX. A sketch of this initial setup is shown in Figure 8.26.

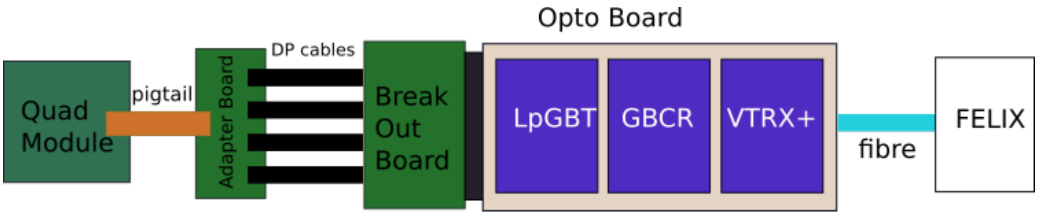

Figure 8.26: First setup with FELIX readout but not final hardware. The PP0 is replaced by break out and adapter boards.

In this preliminary test system, FEs of several modules could be read out. However, some issues were remaining. As depicted in Figure 8.27, the scans were imperfect, with lower than expected electron counts observed and multiple pixels disabled. A possible explanation is faulty hardware connecting the module pigtails with the opto boards. However, this hardware is not intended for further use in the detector. In order to rule out that the imperfect scans have another origin, the final pre-demonstrator setup was commissioned and tested once the PP0 became available. It is still outside the environmental box.

The pre-demonstrator is equipped with the full module readout path, which contains the opto boards, data and power cables directly from the PP0 and fibre connection from the

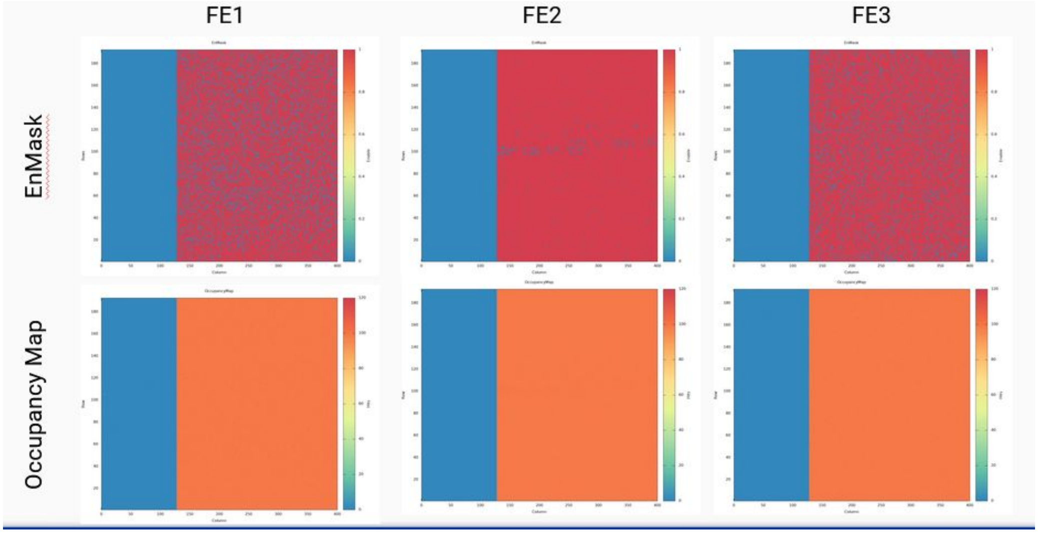

Figure 8.27: Imperfect digital scans with non final hardware.

optobox to the FELIX servers in the rack area, as shown in Figure 8.28.

One module is connected to the PP0, the green PCB in the photo. The final outer barrel pigtails are used, except that they are not bent yet, which is later needed on the loaded support. All green rigid PCBs on the PP0 are bridges on the positions where other modules can connect to. These slots need to be bridged as the PP0 is meant for serial powering and hence cannot have open circuits.

Because the PP0 services are built for the final ITkPix chip, which uses data merging, these services only route one or two uplinks out of a quad module, depending on the design and the layer of the outer barrel. However, the RD53A modules in use for the demonstrator do not have this data merging feature, as explained in Section 5.2. Therefore only two of the four chips can be read out. For this particular PP0 only one chip can be read out (chip 4). Also, only one module pigtail was available at the time of the measurements, so only one module was read out.

With the final hardware the readout chain was commissioned and validated by testing one digital module on all positions of the PP0. It was also tested in several module testing setups at CERN and the results compared. Robust communication and readout was possible to be established. The results of the comparison tests are shown in Section 9.5.

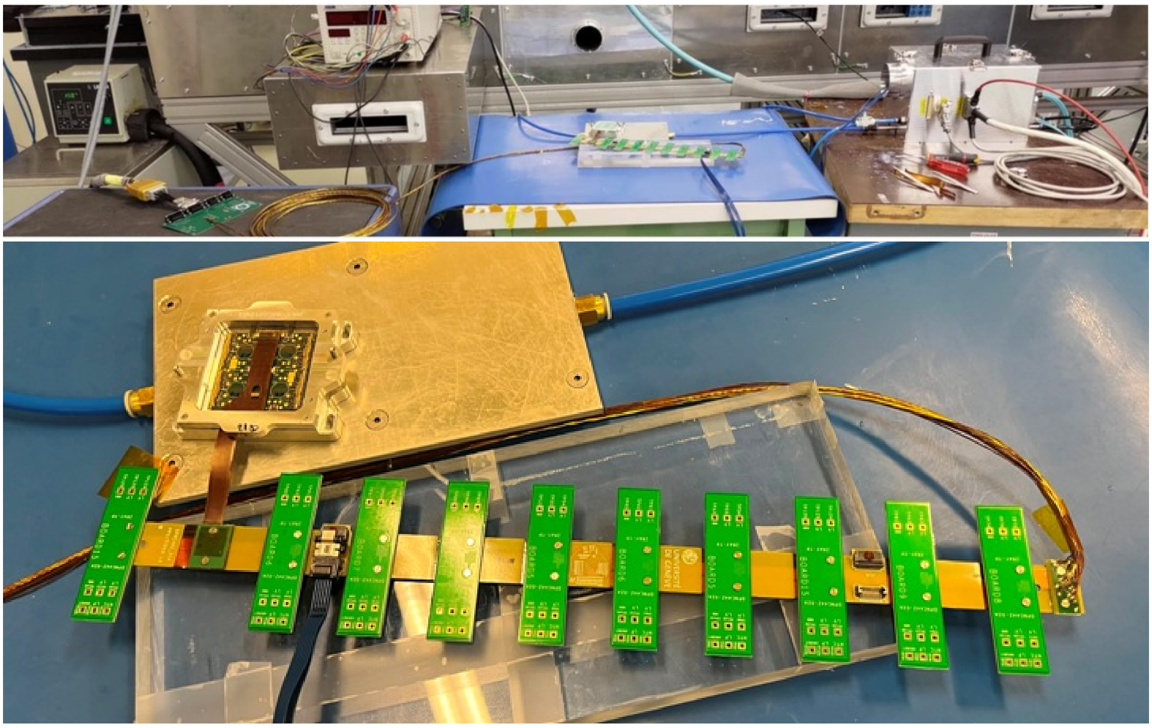

Figure 8.28: **Top:** Pre-demonstrator setup with full module readout path, which includes the PP0 of the inclined half-ring (in the middle and in close up below), opto boards in the optobox (on the right), data and power cables connected to the PP0 and the CSB and fibres from the optobox to the FELIX servers. All green rigid PCBs on the PP0 are bridges on the positions where other modules can connect to, in order to close the serial powering circuit.

8.5. Conclusions and Outlook

The RD53A demonstrator setup is still in the commissioning phase. Several aspects of the demonstrator setup were developed, implemented and tested within the scope of this thesis. The interlock system, based on the IMC used in the IBL, was adapted to the RD53A setup and is currently in use.

With the pre-demonstrator setup without the longeron mechanics, the full readout chain was validated. First tests with one module connected to the final DAQ hardware components have successfully been concluded, paving the way for measurements with several modules. In fact, since the measurements within the context of this thesis, the mechanics have arrived and the first SP-chain on the longeron was commissioned. First measurements are shown in Section 9.5 after discussing the modules, that are needed for the demonstrator in Section 9.2.

CHAPTER 9

Modules for the Demonstrator

As described in Section 8.4, at least 29 modules are needed for the OB RD53A demonstrator. CERN, Göttingen, Liverpool, Paris Cluster, Siegen and KEK have contributed as module building and testing sites. In order to assure quality standards for all modules, careful analysis of the module performance is done after assembly. The module QC needs to be done in a standardised way and with well-defined procedures to have a high yield of functioning modules and to assure comparability of the results. The procedure is as discussed in Section 7.3.2 and analyses the number of broken pixels regarding digital and analog behaviour of the chip. Apart from that the bumb bond quality and the sensor quality itself are of interest.

In Figure 9.1, the production flow of testing is shown. Module QC after production is referred to as first stage of testing. It is foreseen within the RD53A demonstrator programme that after passing the first stage all modules are delivered to CERN to pass further steps. While in the following the focus is on the electrical tests, metrology requirements are either checked at the production site or complemented at CERN. Ideally, all modules come from the production sites with the same set of tests. This means they have all undergone thermal cycling ($1 \times -55\,°\mathrm{C}$ to $60\,°\mathrm{C}$ and $10 \times -45\,°\mathrm{C}$ to $40\,°\mathrm{C}$) and full electrical tests, including

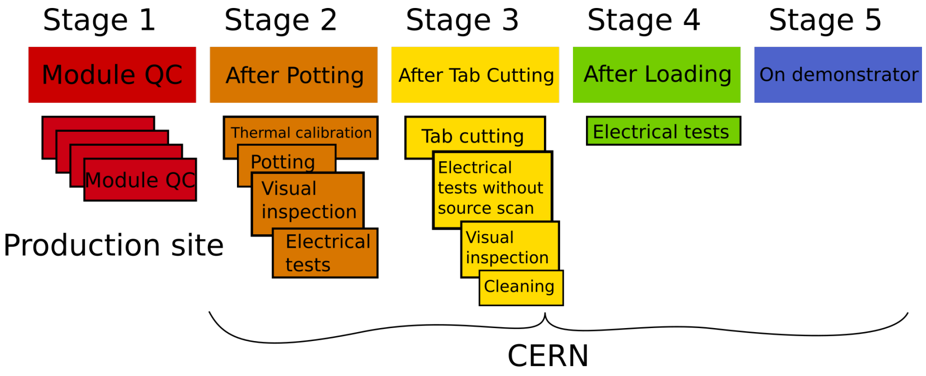

Figure 9.1: Production flow of RD53A quad modules.

source scans.

At the stage of reception at CERN the thermal calibration of the FE NTCs is performed in a thermally controlled reference environment. Based on that some of the register values of the chip are set which assure that the FE NTCs all show comparable results. In case module building sites could, however, not fulfil all QC measurements after assembly at their site, they are being completed at CERN. This mainly means additional thermal cycling and repeated electrical testing. In a next step the wire bonds are protected. Wire bond protection is crucial for demonstrator modules and is done by potting with Sylgard as the foreseen mechanical protection with a small carbon roof for the ITk modules was not yet available for all the modules at the time of the module reception. For the ITk the wire bonds will be protected with Parylene and the mechanical protection as Sylgard is not radiation hard enough. Parylene protects the bonds and at the same time provides HV shielding between readout chip and sensor. To make sure that no damage was done to the module during potting, visual inspection afterwards is crucial before passing the module to the electrical tests.

The tests after potting represent the second stage, where the full set of tests is repeated. For perfect comparison, the configuration files from the production sites are used for the tests at CERN.

The next step before the modules are ready for further handling outside CERN is the so-called tab cutting. Tab cutting refers to the process where the connection tabs of the flex are cut, which connect the inner relevant part with the flex frame for better handling. Tests after this stage are considered as the third stage of the modules.

After passing electrical tests after tab cutting, the modules go to cell loading. They are loaded on cells e.g. at the University of Geneva, before returning to CERN for further testing and mounting on the demonstrator. Once on the demonstrator further tests follow.

The main focus of this thesis is the comparison of the performance of the modules after potting and after tab cutting. Testing of loaded modules or modules integrated on the demonstrator was not performed within the scope of this thesis and is hence not part of the comparison.

The 29 modules for the demonstrator pass different stages. The criteria to pass the electrical module test sequence to be mounted on the OB demonstrator are that at least FE4 (and FE2) are fully functional, as the demonstrator readout is only possible for those two FEs. Apart from that, the sensor needs to be functioning and the turn-on behaviour of the FEs needs to be understood.

In Table 9.1, the specific features of the modules are listed, using the names of the modules on the demonstrator. So far only the first SP-chain with six modules is commissioned, all other modules are named M1-M23. In the table it is noted whether all four FEs of a module are functioning or only three. Specific comments for the behaviour of the modules or the number of the failing FE are also included in the table. Apart from that, the temperature at which the FEs turn on is given. The procedure to follow requested that the temperature is increased by 15 K if the module does not turn on [169]. However, not all of the module building institutes followed this recommendation. Therefore all different start-up temperatures were recorded. As mentioned in Section 7.3.3, the variation of the cold start-up temperatures of the modules is expected for the RD53A chip.

Table 9.1: Modules for the demonstrator. The number of working FEs and specific features.

	4 FEs	3 FEs	Cold start-up T [°C]	Comments
M-B-1	(x)	x	-35, -35, -35, -35	FE1 broken after loading
M-T-1		x	-35, -35, -35, -35	no FE1
M-B-2	x		-20,-21,-21,-21	works only with 16x1 FW
M-T-2	x		-35, -35, -35, -20	
M-B-3	x		-31, -31, -31, -	FE4 non-functional when too cold ($< 30\,°\mathrm{C}$)
M-T-3	x		-35, -35, -35, -35	
M1	x		10, 10, 10, 10	
M2		x	-35, -35, -25, -35	no FE2 (only for inclined)
M3	x		-3, -3, -3, 8	
M4		x	-35, -35, -35, -35	
M5	x		-35, -35, -35, -35	
M6		x	-35, -35, -35, –	no FE3, no FE4
M7	x		-35, -35, -35, -35	
M8	x		-20, -35, +10, +10	
M9	x		-35, -35, -35, -20	
M10	x		-35, -35, -35, -20	
M11	x		-35, -35, -35, +10	
M12	x		-35, -35, -35, -35	
M13	x		-24,+1,-9.7,+1	
M14		x	-,-26.5,-26.5,-26.5	no FE1
M15	x		-26,-26,-13,-26	
M16		x	-35, -20, - , -20	no FE3
M17		x	-23,-23,-14,-14	no tuning for FE3 possible
M18		x	-, -30, -30, -30	no FE1
M19	x		-13, -24, -13,-13	
M20	x		-26,-12,-26,0	large leakage curent
M21		x	-, -30, -30, -30	no FE1, large leakage current
M22	x		-35, -35, -35, -35	
M23	x		-35, -35, -35, -35	

9.1. Procedure, Comparison and Framework

The comparison of the modules' performance is undertaken in two steps. First, the electrical test data produced by the common testing procedure is analysed for the comparison of the performance of one module in different stages. Then, different modules are compared with each other.

For this purpose a framework was written[1]. With the framework an easy comparison of module performance for up to six stages for one module is possible. The analysis framework was initiated in a project for a CERN summer student, supervised within the scope of this thesis, and then further developed by the author of this thesis. The goal is to analyse the results from digital scans, analog scans, disconnected bump scans (discbump scans), crosstalk scans, source scans, threshold with noise scans, ToT scans, forward bias scans and IV and VI scans. For this purpose the *.json* files from the electrical tests are used.

---

[1] Version of the framework that was used for this thesis can be found in tag v2.1 in the git repository: https://gitlab.cern.ch/atlas-itk-pixel-systemtest/plotting/module-dossier/-/tree/master.

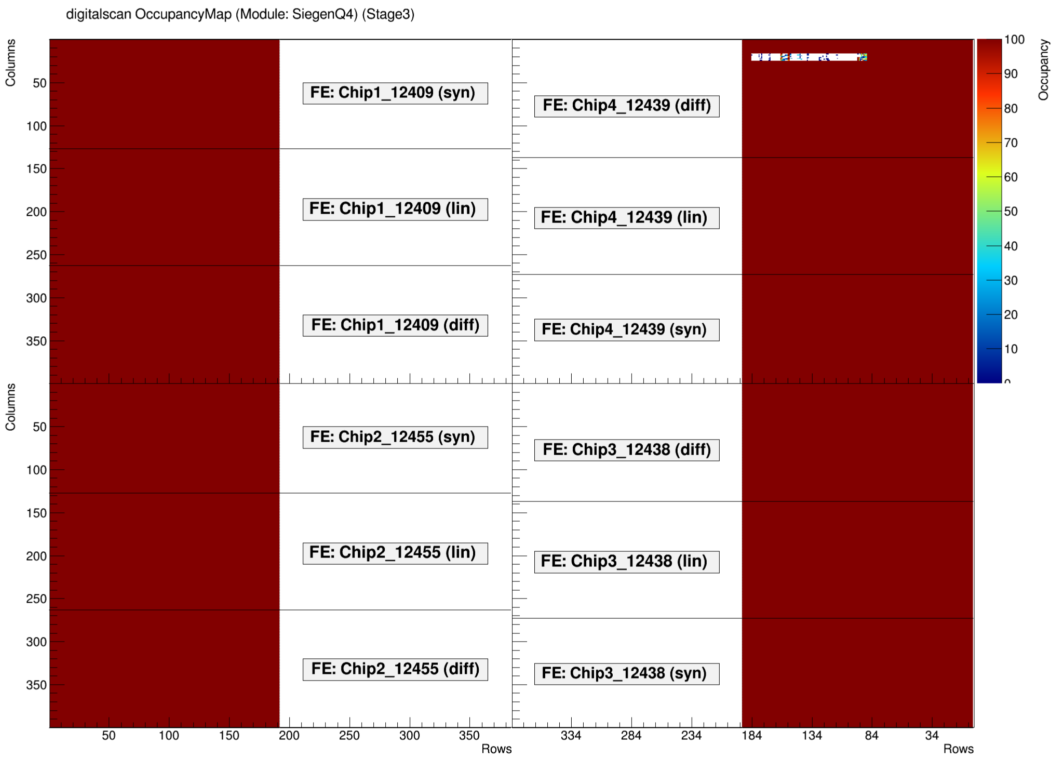

Figure 9.2: Example result for the module overview plot for module SiegenQ4. Two areas can be identified. The coloured area shows the active area of the RD53A FEs. In the middle of the module the sensor cannot be read out and the space is used for module information or analysis results. The chip number, chip identifier and the type of analog FE is displayed in this example. The FE numbers are defined anti-clockwise, starting at the top left. The digital scan shows a bad area in the differential FE of FE4. These can be identified by the colourful and white pixels which do not show the expected value of 100 e (dark red) as in all the other FEs.

For an overview of the module performance, the electrical data is plotted in module layout with top view. This is shown in Figure 9.2 for the module SiegenQ4 and a digitalscan. Two areas can be identified. The coloured area shows the active area of the RD53A FEs. In the middle of the module the sensor cannot be read out and the space is used for module information or analysis results. The chip number, chip identifier and the type of analog FE is displayed in this example. The FE numbers are defined anti-clockwise, starting at the top left. As explained in Section 7.3.2, pixels are evaluated as “good”, “bad” or “dead” depending on the occupancy or the number of hits in a pixel. Hence, specific data ranges (0 hits, 98-102 hits, . . .) are also plotted in top view to easily identify possible bad or broken areas in the module. This is shown in Figure 9.3, where it can be seen that there is an area with many dead or bad pixels in the differential FE of FE4. These can be identified by the colourful and white pixels which do not show the expected value of 100 e as in all the other FEs.

In the analog scan analysis plot in Figure 9.3 the number of pixels with zero hits are shown. As discussed in Section 7.3.2, pixels are masked when they are not classified as

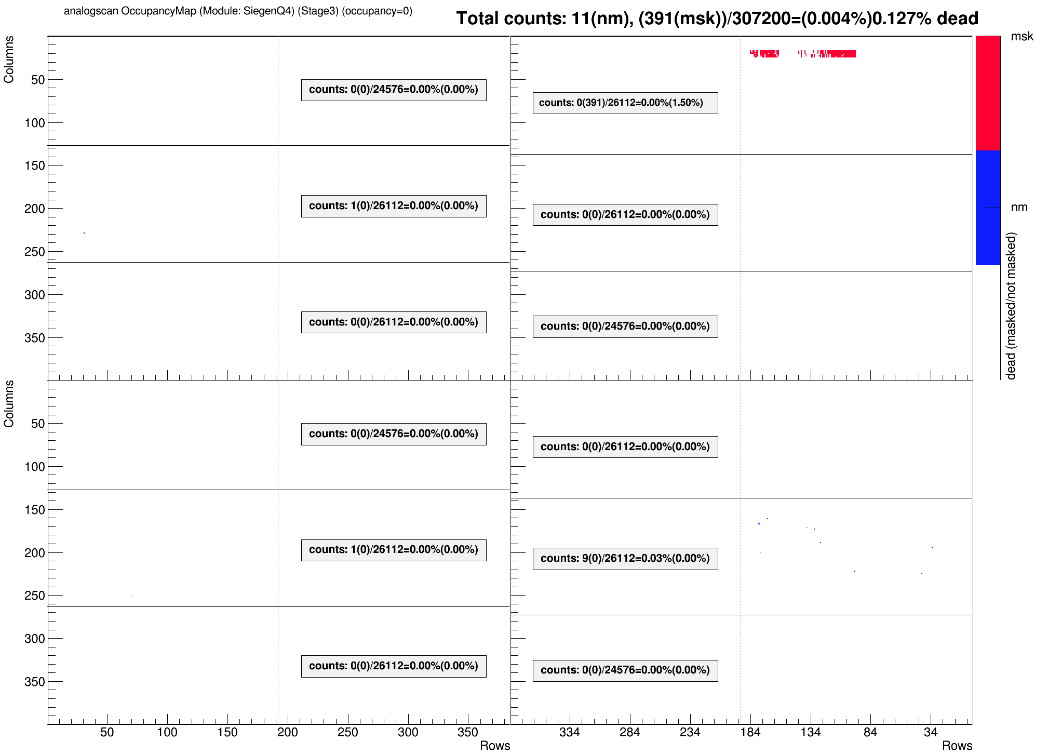

Figure 9.3: Example result for the range specific analysis plot for module SiegenQ4. Here the dead pixels in the analog scan are shown. Dead pixels are pixels with zero hits. They are marked in red and blue, while red pixels are masked (“msk”) from the digital scan before whereas others (blue) are only broken in the analog scan and hence not masked (“nm”). The number of masked and not masked pixels for each FE is shown in the FE sections and the sum over all FEs on the top right of the plot.

good in digital or analog scans. This means that bad or dead digital pixels are masked and therefore disabled in the analog scan and in all consecutive scans. Bad or dead analog pixels are additionally masked and disabled in all further scans, such as disconnected bump scans or crosstalk scans. For source scans, additionally, a noise scan is performed to mask noisy pixels before starting the scan with a radioactive source. According to the legend in Figure 9.3, there are many pixels which are masked (“msk”). This means that they are disabled in this scan. Additionally some pixels are marked as not masked (“nm”) but without hits. Pixels which are not masked but without hits were in previous scans considered to be good, but in the scan of interest show imperfections. They are hence considered to be dead.

To draw information from the aforementioned plots, the overview of the evolution of e.g. disconnected pixels over the stages is shown. An example for the disconnected bump scan which is marking disconnected bumps of module Paris6 is shown in Figure 9.4. The data from these plots is exported to *.csv* files, which are then needed for the next step.

The comparison of several modules is also evaluated per FE type and stage. Of interest are comparisons of the number of working FEs, leakage current values at 50 V and 100 V, threshold and noise distributions, number of zero hits in source scans (disabled or dead

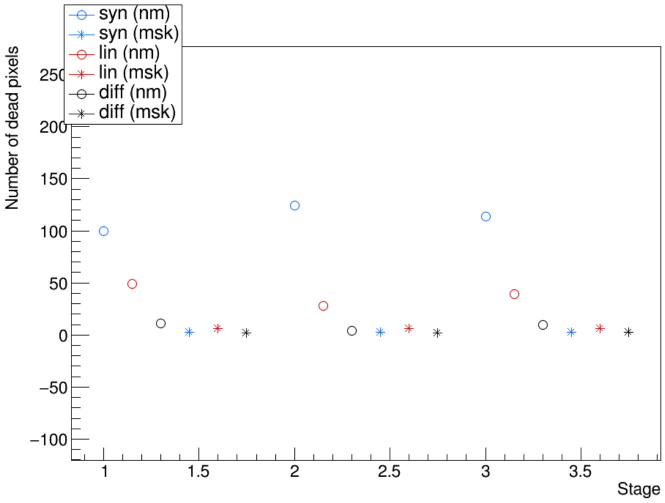

Figure 9.4: Example plot of the evolution of dead pixels for a disconnected bump scan of module Paris6 FE1. The dead pixels are marked as ("nm") and the disabled pixels as (msk). The analysis is done per FE which is why the numbers are also shown per analog FE.

pixels) and number of zero hits in disconnected bump scans (disabled or dead pixels). The analysis is not only aimed at comparing the different modules in different stages with each other, but also at identifying suitable methods to identify disconnected bump bonds between sensor and readout chip or other issues in a module.

9.2. Results of Electrical Measurements and Comparison

The electrical measurements on the demonstrator modules comprise the IV measurements of the sensors and all the aforementioned scans. In the following, the electrical results of the modules for the demonstrator and respective failures are explained. Additionally, the number of working FE chips per module is discussed. Based on this experience, the module building for ITk module production can be improved.

9.2.1. Current Voltage Behaviour

At first, the sensor IV is analysed for the 29 modules for the demonstrator. Of these 29 modules there are already six modules cell integrated in the longeron structure, therefore represented together in a plot. The other remaining modules are randomly attributed to plots with eleven and twelve modules to contribute to the SP-chains with elven and twelve modules. The final modules for the demonstrator chains have, however, not yet been decided at this stage, so these attributions should not be assumed to be in any way related to the final ones on the demonstrator.

The leakage current I_{leak} is normalised to 20 °C. An example plot for module SiegenQ1 is shown in Figure 9.5. The current rises with stage and a behaviour like a breakdown is visible after ≈ 70 V. The original requirement for sensors with a thickness of 150 µm

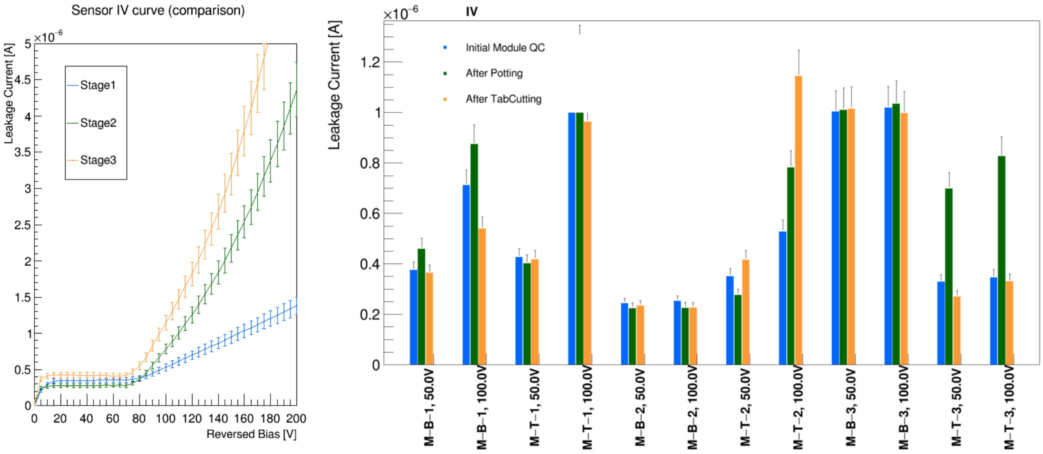

Figure 9.5: **Left:** Leakage current comparison for three different stages for one module. The current is normalised to 20 °C. A slight rise of the current with stage can be seen. **Right:** Comparison of different modules and their leakage currents for 50 V and 100 V, normalised to 20 °C.

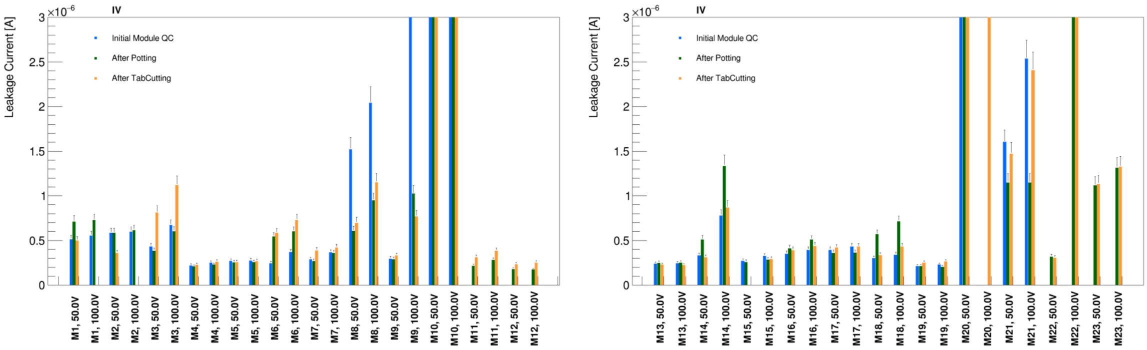

Figure 9.6: Comparison of leakage currents at 50 V and 100 V, normalised to 20 °C.

is $I_{\text{leak}} \leq 0.75\,\mu\text{A}\,\text{cm}^{-2}$ at $\text{V}_{\text{bias}} = \text{V}_{\text{depl}} + 50\,\text{V}$ and a $V_{\text{bd}} > V_{\text{depl}} + 50\,\text{V}$. According to these requirements, the breakdown of the sensor would qualify it as bad. For comparison with other modules the leakage current for a bias voltage of 50 V and 100 V is compared. Plots for six, eleven and twelve modules show the current for these two data points and the evolution over stage. The comparison for the modules for the short longeron SP-chain is shown as well in Figure 9.5. For the remaining modules the comparison is shown in Figure 9.6.

Some modules show higher leakage currents after tab cutting. In the tab cutting process with a pair of scissors the flex tabs are cut and very rarely it happens that the sensor is touched with the blades. This might be the reason for higher currents after the process.

Three modules show much higher leakage currents than the other modules as can be seen from the full range plots in Figure 9.7. M9 with higher leakage currents in the initial stage can, however, be ignored. As in later stages the current is low, the high current before either originates from measuring mistakes or the temperature allocated to the measurement was not correct so that the data was improperly scaled.

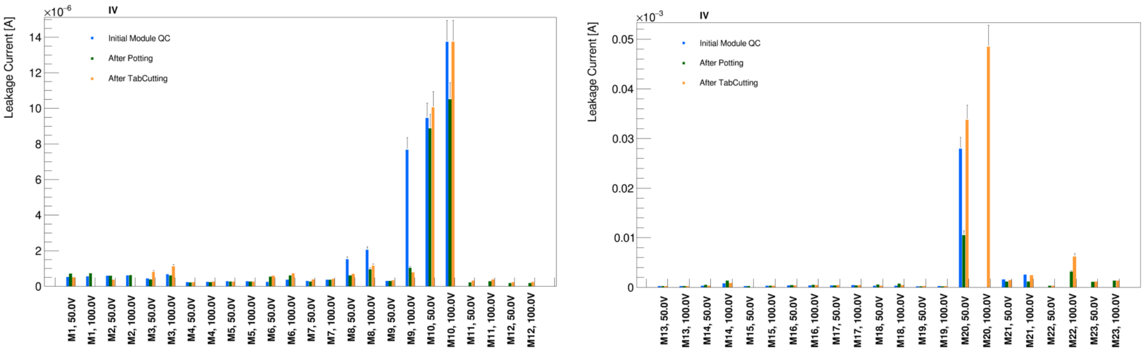

Figure 9.7: Full range comparison of leakage currents at 50 V and 100 V, normalised to 20 °C.

Concluding, there are several modules with higher leakage currents. For the purpose of the demonstrator tests, modules which do not fulfil the requirements can also be used. Regarding the modules later used in the ITk, the quality requirements are of course crucial.

9.2.2. Number of Working FEs

As a first step towards readout chip performance assessment, the number of working FEs in the different stages is compared.

In Figure 9.8, where the six modules are compared, it can be seen that one FE was broken in the initial module QC step but later worked again. This is the FE which was labelled as only working with temperatures > 30 °C, but could be used at the tests at CERN at 30 °C.

In Figure 9.9, the FE counts for the remaining modules are shown. Two modules lose one FE during tab cutting (stage 3), where due to handling mistakes the FEs were damaged. M16 also has one more FE in the second and third stage, which can be explained by missing wire bonds on one of the chips in the first stage, which were later added at CERN. In total there are seven modules that have only three working FEs: M2, M6, M14, M16, M17, M18 and M21.

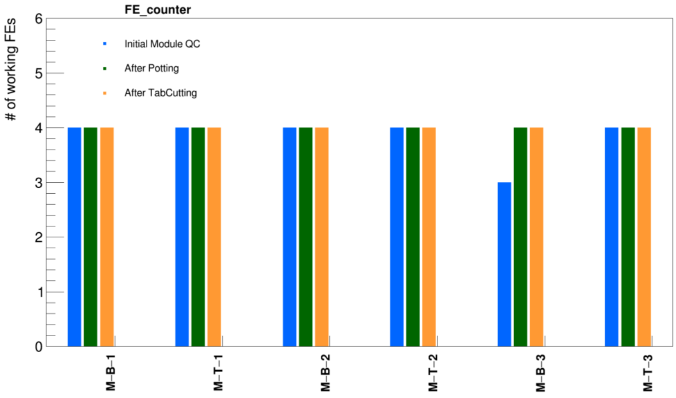

Figure 9.8: The overview of the working FEs per stage is shown for the six modules.

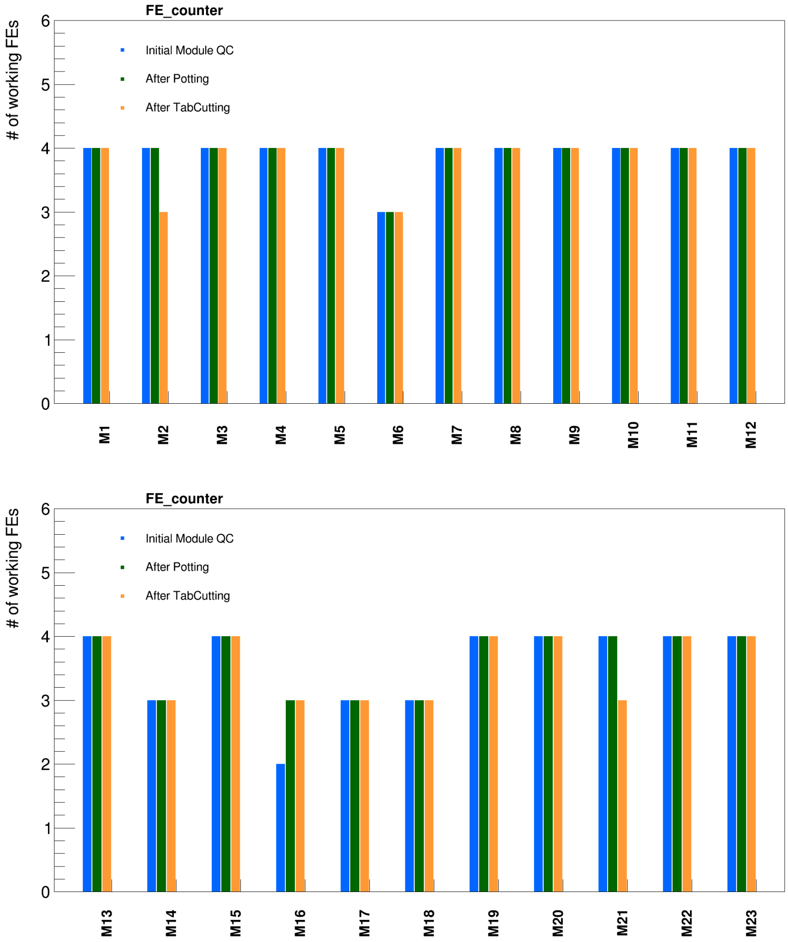

Figure 9.9: The overview of the working FEs per stage is shown for the remaining twelve and eleven modules.

9.2.3. Noise Distribution Comparison

The noise distribution of the FEs is very important to be low and similar for all modules as a higher noise can be an indication of introduced problems in e.g. the powering or the readout path. It is evaluated per analog FE and again shown for the three SP-chains separately. For the demonstrator all three analog FEs are used as the available area for measurements is already very small due to the small size of the RD53A chip and the limitations on the number of chips that can be read out simultaneously. However, as for the ITk only the differential FE (diff FE) will be used in the following the results for the differential FE are discussed, while all other measurements of the synchronous (syn) and the linear FE (lin FE) can be found in the Appendix B.

In Figure 9.10, the noise distribution for the differential FEs of the SP-chain with six modules and in Figure 9.11 and 9.12 the noise distribution for the SP-chains with eleven or twelve modules are shown. The value that is displayed is the fitted noise distribution for the differential FE with the error bars being the standard deviation calculated by ROOT. The mean noise distributions all show very similar noise values around 50 e.

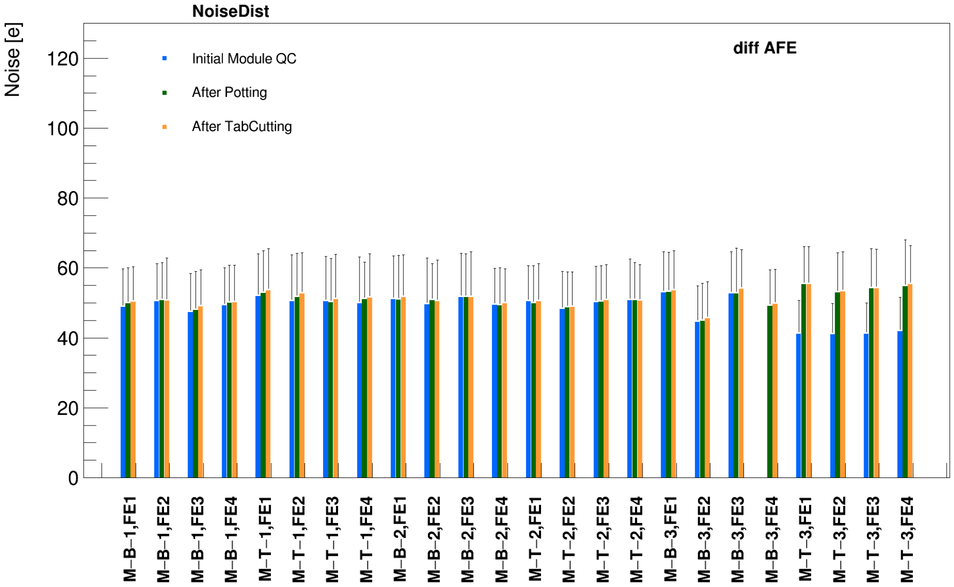

Figure 9.10: Mean noise distributions for the differential FEs of the modules for the short SP-chain.

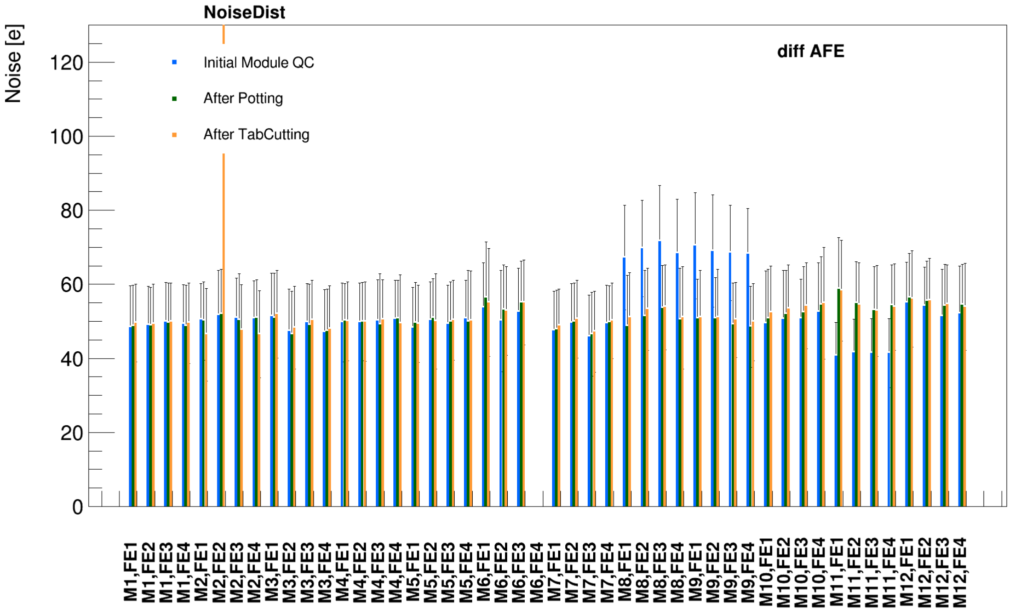

Figure 9.11: Mean noise distributions for the differential FEs of the modules of the twelve modules.

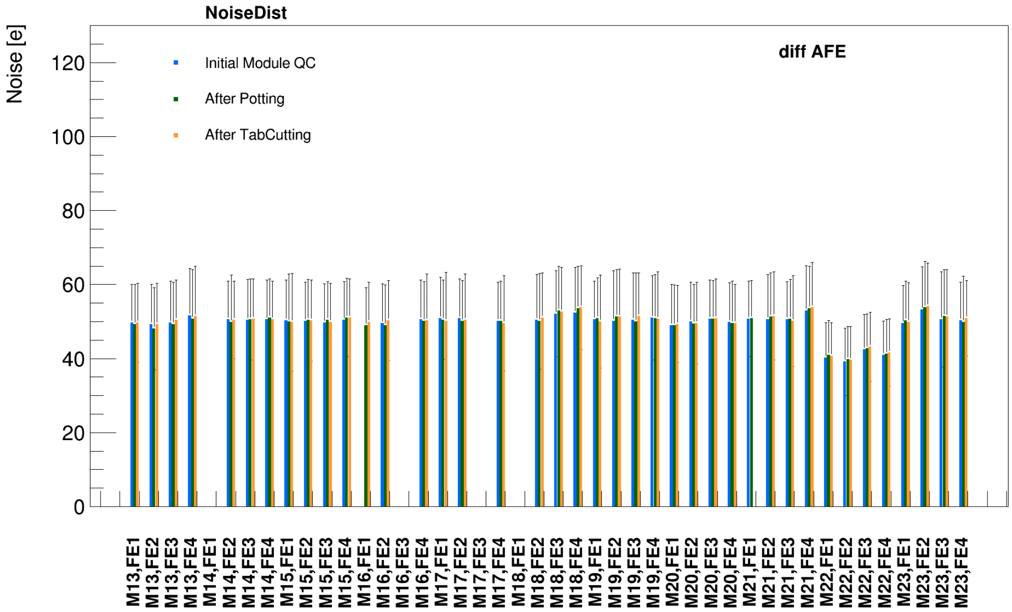

Figure 9.12: Mean noise distributions for the differential FEs of the modules of the remaining eleven modules.

The same analysis is made for the other FE types and shown in Appendix B.1.1 and B.1.2. Overall, the noise of the modules is low and stable for the different stages.

9.2.4. Source Scan Comparison

A very important property of a module is the goodness of the bump bonds. It can be evaluated with different scans as introduced in Section 7.3.2. An example source scan is shown in Figure 9.13 on the left, where an x-ray source was used to create electron-hole pairs in the module. It is visible where the active parts of the RD53A are and how the FE chips are arranged in a module. According to the absorption of hits, the SMD components on the flex and different structures within the flex can be identified. On the right is an analysis result for pixels which received zero hits. As mentioned before, pixels with zero hits are identified and marked as disabled or dead according to their status in the previous scans. Pixels are masked and hence disabled when they were considered as bad in digital or analog scans or noisy in a noise scan, as stated in Section 7.3.2. For the following scans, a noise scan is run for 5-15 min without source to identify noisy pixels which will be disabled for the actual source scan. Therefore, only the dead pixels are interesting in such that they give information about the status of the bump bonds.

The differential FE source scan for the six modules is depicted in Figure 9.14. FE2 of M-B-3 has a large area of dead pixels, as shown in Figure 9.15. This is most likely an area where the bump bonding is failing. Possible reasons are a strong bow of readout chip or sensor in this region, which push the bump bonds apart. Mistakes during the production process in the company are also possible. Compared to stage 1, in stage 2 additional pixels are disabled. These additional disabled pixels are an interesting feature and might

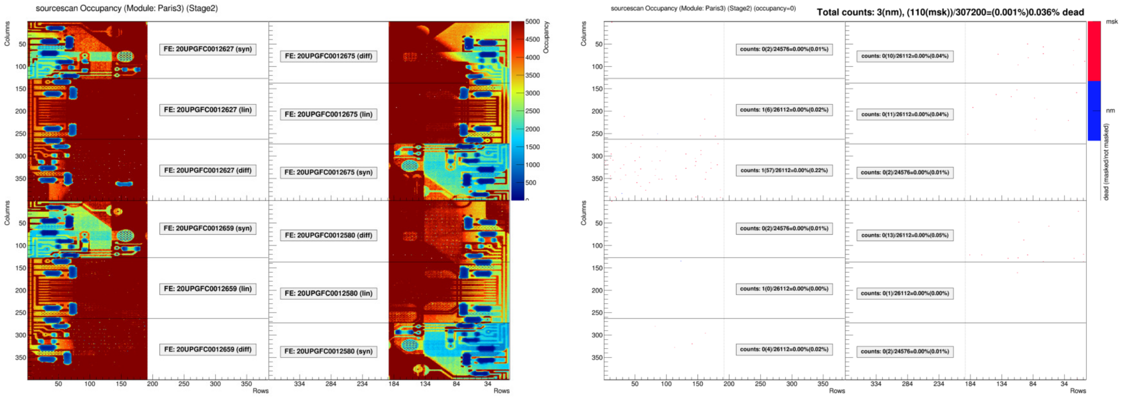

Figure 9.13: Source scan (left) and zero hit pixel analysis (right) of module Paris3 in stage 2. The pixels marked as not masked “nm” (in blue) in the plot correspond to the dead pixels. The masked (“msk”) pixels are disabled during the scan. There are 3 dead pixels and 110 pixels masked.

dead vs disabled pixels

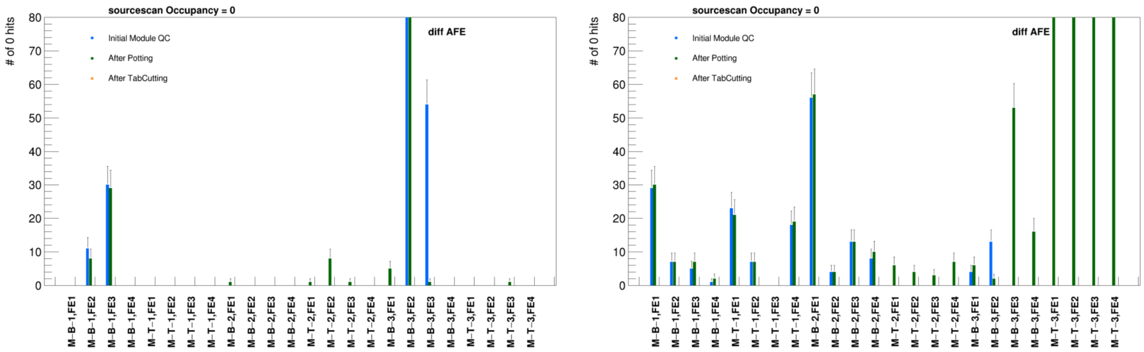

Figure 9.14: Source scan for the differential FE for the six modules.

be explained with the choice of the scans that are actually used for the analysis. The demonstrator team at CERN receives scan data which should be used for the analysis from the initial sites. Usually, the digital and analog scans are some of the first scans taken. In case a module degrades over time, in the scans from early stages broken pixels might not show up. In later stages and measurements at CERN new analog and digital scans are taken which then show these broken pixels. This results then in new masked pixels in the source scan.

M-B-1 and M-B-2 have several masked pixels from the analog scan, as shown in Figure 9.15. M-T-3 FE4 has a differential source scan where almost the whole area of all differential FEs is masked. There exists no source scans from the first stage for comparison, but for all stages the analog scans have lots of bad pixels, although no dead pixels.

For the twelve modules, Figure 9.16 shows the number of pixels with zero hits for the differential FEs. M11 has lots of masked pixels in FE2 from a bad digital scan. This is shown in Figure 9.17. M8 and M10 have lots of pixels masked, which is again explained by bad or dead analog pixel. In Figure 9.18, the source scan of the differential FEs of the eleven modules is shown. As can be seen M14, M16, M17, M18, M19 , M21 and M22 have

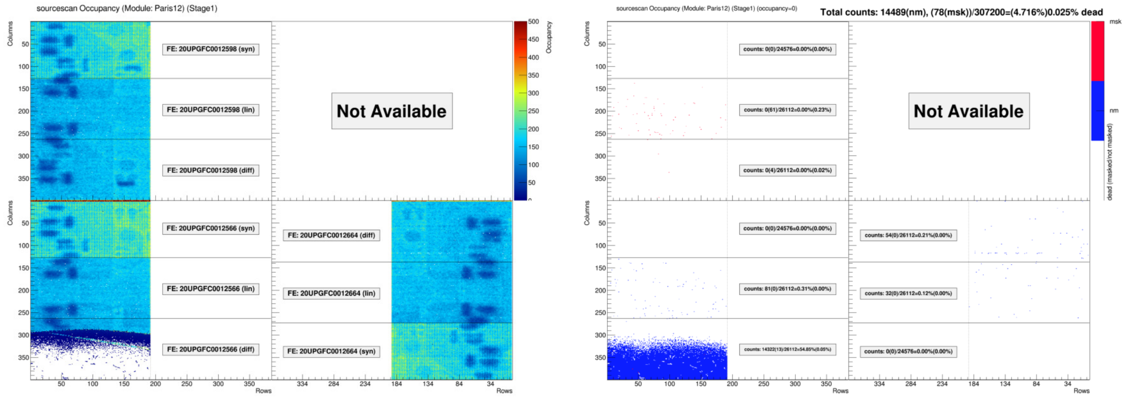

Figure 9.15: The source scan of M-B-3 shows a large broken area in FE2. The pixels marked as not masked "nm" (in blue) in the plot correspond to the dead pixels. The masked ("msk") pixels are disabled during the scan.

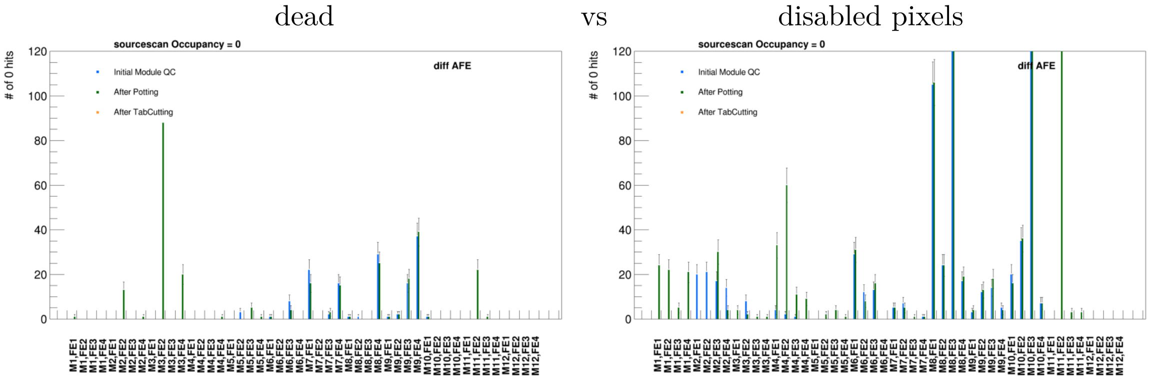

Figure 9.16: Differential source scans for the twelve modules.

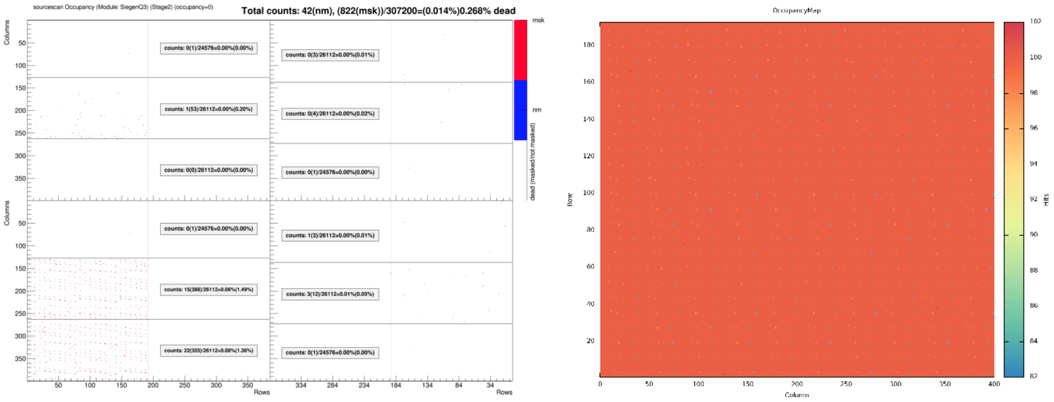

Figure 9.17: The pattern that is seen in FE2 of M11 is coming from the digital scan, as shown on the right. The pixels marked as not masked "nm" (in blue) in the plot correspond to the dead pixels. The masked ("msk") pixels are disabled during the scan.

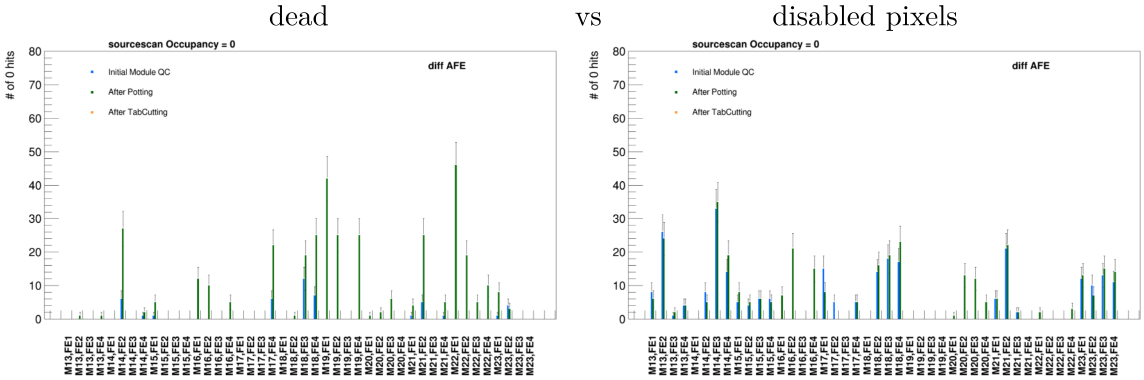

Figure 9.18: Differential sourcescan for the eleven modules. M14, M16, M17, M18, M19 , M21 and M22 have a few more dead pixel after the potting step.

a few more dead pixel after the potting step.

The same analysis is done for the other FE types and shown in Appendix B.2.1 and B.2.2. Similar problems as in the differential FE, such as scans of bad quality, lead to dead and disabled pixels. Overall, the number of dead and disabled pixels in the modules is not concerning and mistakes during the tests are understood.

9.2.5. Disconnected Bump Scan Comparison

A similar analysis is performed for the disconnected bump scan. The FEs are analysed separately and the pixels which give no hits are categorised in masked or not-masked pixels, hence disabled or dead, whereas the latter are again expected to be the pixels with disconnected bump bonds. In Figure 9.19, the disconnected bump scan of the differential FEs of the six modules is shown. It is evident that there are much more pixels marked with occupancy zero than in the source scans before. Also there are not as many masked and therefore disabled pixels. More pixels are classified as dead, i.e. have disconnected bump bonds.

For M-B-1 a pattern in the disconnected bump scan of stage 1 is visible. As this pattern

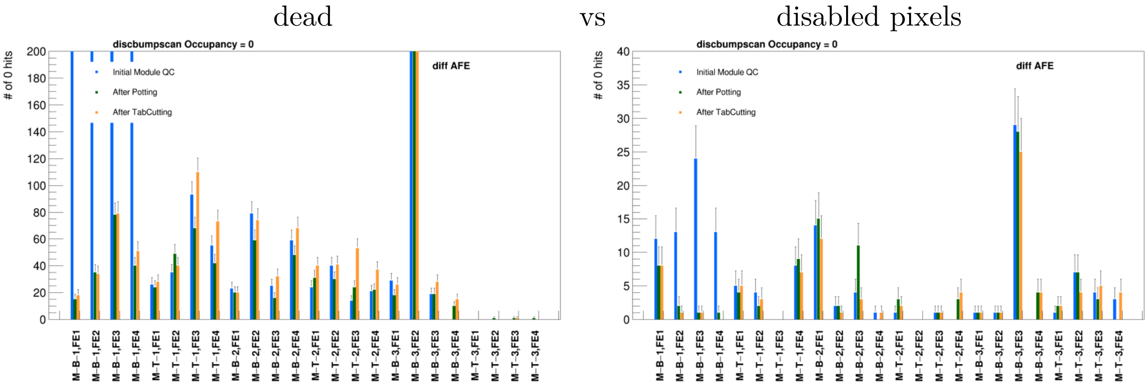

Figure 9.19: Disconnected bump scan of the differential FE of the six modules. There are many pixels in M-B-1 which are shown as dead.

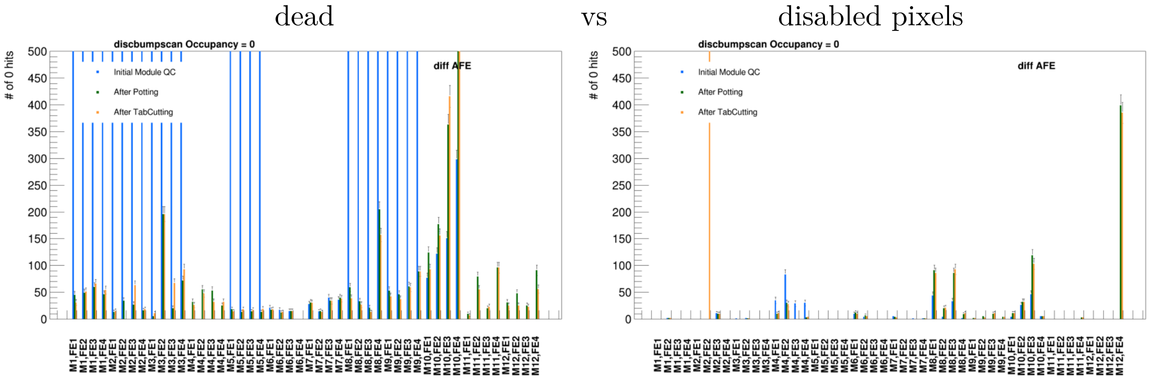

Figure 9.20: Disconnected bump scan of the differential FE of the twelve modules. There are many FEs with very high number of dead pixels. FE2 in M2 has a large number of disabled pixels.

is a known feature which sometimes can happen in disconnected bump scans, these pixels which are marked as dead pixels must not necessarily be dead. When comparing to the second and third stage, it is evident that the large number of dead pixels originated from a failure in the scan. In retrospective, the scan of stage 1 should have been repeated. Probably this was not done as it was not clear at the time of the measurement what was to be expected from the scan results. Other than that, only small variations between the stages are visible. For M-B-3 FE2 the large broken area causes lots of dead pixels. They have also been identified in the source scan, as depicted in Figure 9.14 and 9.15. In the disconnected bump scan 20969 pixels are identified as dead, while there are only 14322 dead pixels marked in the source scan.

In Figure 9.20, the disconnected bump scan of the differential FE of the twelve modules is shown. M1, M2, M3, M5, M8 and M9 have a pattern in stage 1 which leads to dead pixels, as for example shown for M1 and M2 in Figure 9.21. M10 has a pattern in stage 3 for FE4 and 3, FE2 of M2 is broken in stage 3, as was shown in the number of FE analysis in Figure 9.9. There is also shown M12, which has in FE4 a bad area in the digital- and analog scan and hence lots of disabled pixels in the disconnected bump scan.

In Figure 9.22 is the disconnected bump scan of the differential FE of the eleven modules shown. M16 has a pattern in stage 1 and M22 has a pattern in all stages. Other masked pixels originate from bad analog pixels.

The same analysis is done for the other two FE types and shown in Appendix B.3.1 and B.3.2. Similar problems as in the differential FE, such as scans of bad quality, lead to dead and disabled pixels. Overall, the number of dead and disabled pixels seems to be slightly higher in the linear and synchronous analog FE types.

9.3. Conclusion for Demonstrator Modules

After the third stage, 22 modules with four FEs and seven modules with three FEs are functional. 17 of these modules can be run with HV $\geq 100\,\mathrm{V}$, nine modules can only be operated with HV $\leq 80\,\mathrm{V}$, two modules show high leakage currents and one module breaks

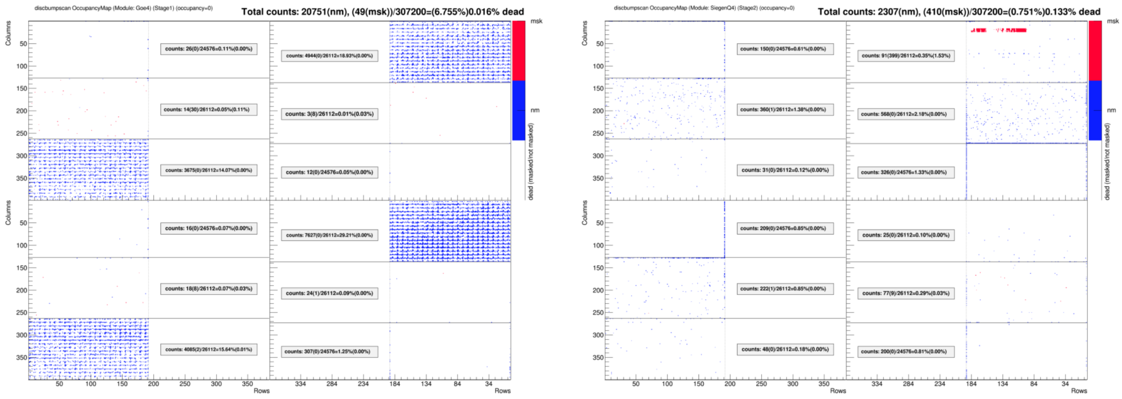

Figure 9.21: Pattern of M1 and M2 in stage 2 leading to dead pixels. The pixels marked as not masked "nm" (in blue) in the plot correspond to the dead pixels. The masked ("msk") pixels are disabled during the scan.

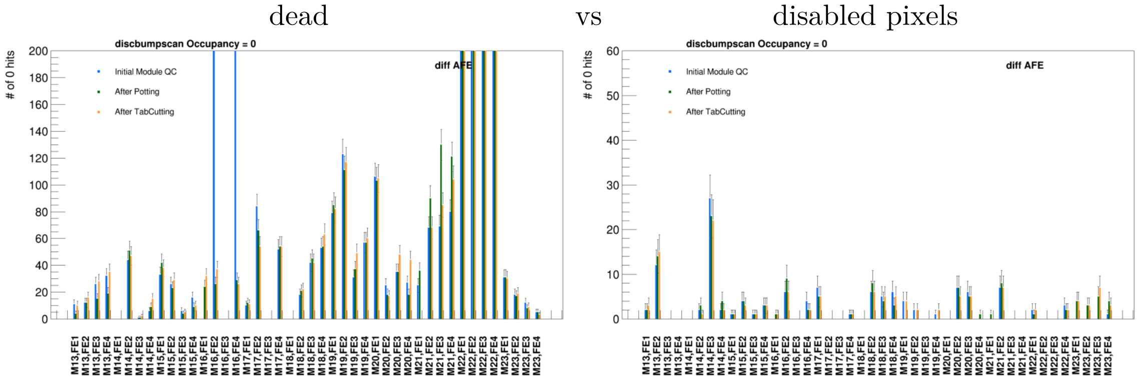

Figure 9.22: Disconnected bump scan of the differential FE of the eleven modules.

down below 20 V. For several modules the leakage current is higher after tab cutting. Due to these problems the HV requirement was dropped. It was put in place to make sure that the sensors do not show a breakdown within the operation range. This is justified as, for the demonstrator, sensor quality tests are of lower priority, and a high enough module yield is more important. Even with all care taken during the tests, two FEs were lost in module testing due to handling mistakes and following mechanical failures.

It can be observed that the noise levels stay similar at different module stages and also the number of pixels with no occupancy in source scans does not seem to change significantly over the stages. Some modules show large numbers of dead/disconnected pixels in source scans, which can, however, mostly be explained by mistakes made during testing, as discussed above. Additionally there are some modules with defects from the producer. Even though there are a number of dead or disconnected pixels in each module, these modules can still be used for tests on the demonstrator. It mainly needs to be understood if any of the steps the modules undergo introduce problems. These types of studies do not require perfect modules, but reliable comparisons between the different stages.

Disconnected bump scans show more disconnected pixels than source scans. However, only parts of them are corresponding to disconnected areas found in the source scans. The differential FE shows for several modules a pattern due to timing problems with the RD53A chip in disconnected bump scans, which is known and resolved for the updated readout chips. In general, the reliability of the disconnected bump scan is questionable. The source scan is the most reliable test of disconnected bump bonds as actual particles are passing the module. A test, such as the disconnected bump scan, which shows more disconnected pixels than in the source scans detected, is not favourable. Better agreement is expected for the ITkPix chips and needs to be studied in more detail.

9.4. Lessons Learnt

Most of the problems seen in the comparison of the modules originate from mistakes of the operator. Hence, clear instructions are required to get comparable data, which means that ideally all scans at all institutes should be run in exactly the same way, with the same parameters and settings as defined in Section 7.3.2. To achieve this can be seen as one of the big challenges of this highly decentralised production.

Apart from missing scans and the thereby created lack of information, non-ideal tuning also leads to incomparable results. This is the fact as a module cannot stay untuned in the later steps and needs to be retuned. After retuning, no full comparison with earlier stages is possible. To avoid these failures, the procedures have to be improved.

Moreover, masked and therefore disabled pixels can originate from digital or analog pixel parts being broken, which is what is expected. However, missing scans before the scan of interest can also lead to distorted results. All pixels in a missing scan are masked, which does, however, not give any physical information about the state of the pixels. Pixels with zero hits in the scan of interest might then be marked as disabled, even though they are actually dead. It is thus extremely important to do careful book-keeping, and systematic testing is essential. Best would be to adapt a tuning and testing routine where before doing a disconnected bump scan or a crosstalk scan, a new set of digital and analog scans is taken to update the masking.

Compared to the scans discussed above, for the source scan the masking is actively done by running a separate scan routine. It is extremely important that for the masking the source is turned off, as otherwise almost all pixels get masked, again, without any real physical meaning.

Concluding, a large number of modules has already passed the first three stages despite the aforementioned complications. A detailed understanding of the module behaviour in the first stages is available, as shown above. Based on this, in the latter stages, possible problems in the demonstrator setup can be distinguished from intrinsic problems of the modules. As of now, all demonstrator modules are already loaded and the first SP-chain is fully assembled.

In the last sections module results on the demonstrator are presented.

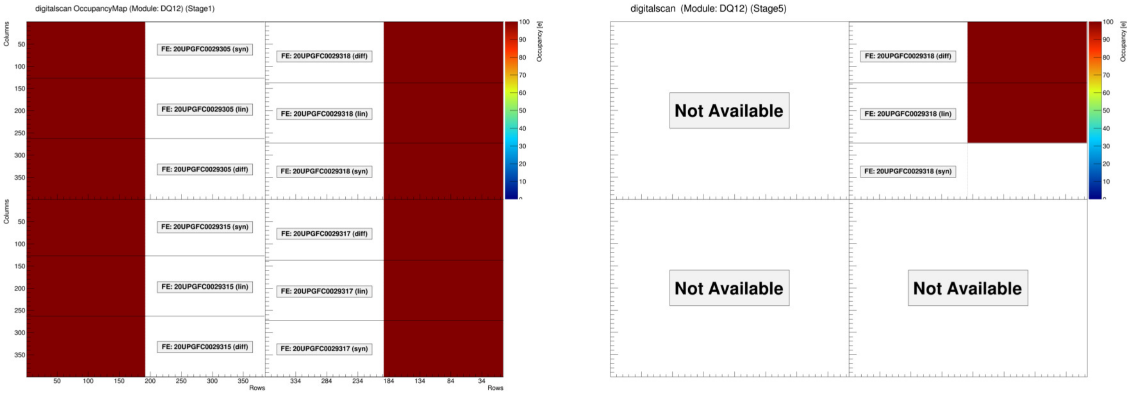

Figure 9.23: Digitalscans of the digital quad 12 used for the tests of the final readout path with the PP0. **Left:** In lab test setups all four readout chips can be read out. **Right:** In FELIX, by design, only one chips can be read out.

9.5. Measurements on the Demonstrator

The local support for the demonstrator was only provided mid-2022 which made it impossible to perform measurements on the loaded local support within the scope of this thesis. What could be achieved is a first measurement with a digital module in the final readout path, as explained in Section 8.4.2. In Figure 9.23, 9.24 and 9.25 results from digital and threshold scans (threshold and noise) of one FE taken with lab DAQ software and with the full FELIX readout chain are compared. Several different laboratory setups and two FELIX setups were used to evaluate the performance. These different measurements are referred to as different stages in the plots. The first two stages and the fourth stage are measured in laboratory setups. In the third stage a laboratory setup of FELIX without optoboards is used and in the fifth and sixth stage the pre-demonstrator with FELIX as well.

The digital scan is only shown for the final readout path and one laboratory setup, for comparison. In both setups perfect digital scans are possible, which means that communication could be established and readout is possible. Which is an important step in the validation of the demonstrator readout chain. The threshold values for FE4 are also very similar for all stages. In the first five stages the same tuning file is used, while the last measurement uses a new file, retuned with FELIX. All threshold and noise values are very similar. It is visible that after retuning with FELIX the threshold distribution is even narrower and the most probably value of the noise as well. With these measurements the validation of the readout system can be concluded.

As a preview to future doctoral theses, and to show that modules also perform in stage 5, first source scans of an SP-chain with six modules on the full demonstrator inside the box are shown in Figure 9.26. The plot is made with the analysis framework and with its adaptations shown in Ref. [191].

Conceptionally these measurements paved the road for the performance evaluation of the demonstrator through all production stages.

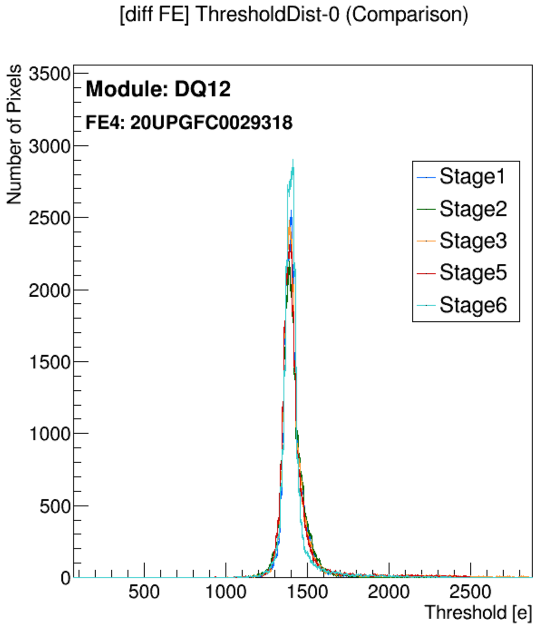

Figure 9.24: Threshold distributions of the differential FE of the digital quad in different setups. The threshold values for FE4 are very similar for all stages. In the first five stages the same tuning files are used. The first two stages are measured in different laboratory setups. In the third stage a lab setup of FELIX without optoboards is used. The fourth stage is again another lab setup and stage five and six are measurements on the demonstrator. The last measurement is after retuning with the FELIX system. All threshold distributions are very similar.

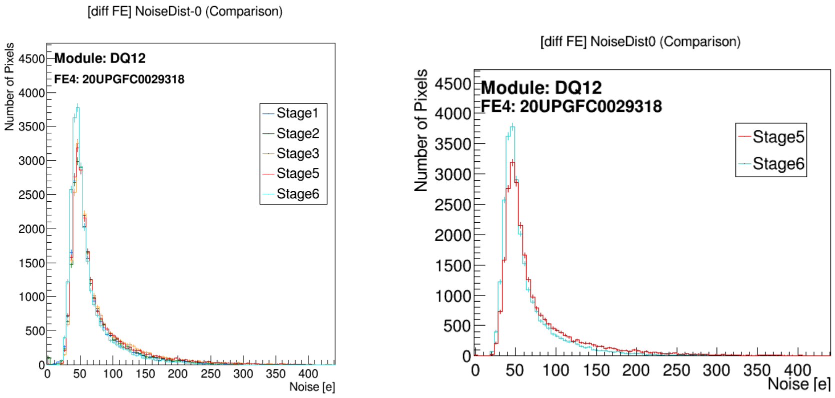

Figure 9.25: Noise distributions of the differential FE of the digital quad in different setups. The noise values for FE4 are very similar for all stages. In the first five stages the same tuning files is used. The first two stages are measured in different laboratory setups. In the third stage a lab setup of FELIX without optoboards is used. The fourth stage is again another lab setup and stage five and six are measurements on the demonstrator. The last measurement is after retuning with the FELIX system and the most probable value of the noise reduces.

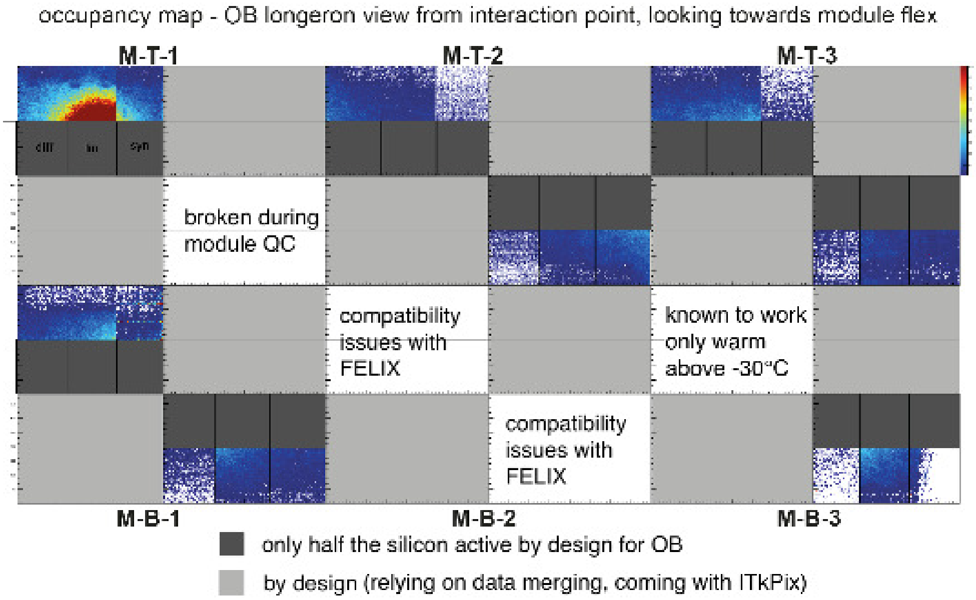

Figure 9.26: Source scan overview of six modules taken with the full readout chain on the actual demonstrator setup. Greyed out parts are FEs which cannot be read out by design. The partly inactive FEs due to the RD53A design are shown in dark grey. Other failures are marked in the respective FE positions.

CHAPTER 10

Summary and conclusions

This thesis made significant contributions to various aspects of the ITk pixel quad module production for the ATLAS upgrade for the HL-LHC.

10.1. Pixel Sensors

Modules of the outer barrel system and the outer layer of the inner system of the ITk comprise planar sensors. Within a sensor market survey mechanical and electrical tests were conducted on planar sensors from six different vendors. The market survey aimed at qualifying vendors for the production of sensors for the ITk modules. Based on the results from the market survey, the pre-production is currently ongoing as final validation step before production.

The work of this thesis shows important contributions regarding the electrical tests of the sensors before and especially after irradiation. Before irradiation, in IV, CV and It measurements, the leakage current behaviour, the depletion voltage and the long-term current behaviour was studied. A dependency of the leakage current on the humidity was demonstrated which led to a change in the testing requirements to yield comparable results. After irradiation, current characteristics for different temperatures, annealing times and test parameters were obtained for sensors from four different vendors.

In test beam measurements, together with an analysis and data taking team, the hit efficiency behaviour of sensors from five vendors were tested. The tuning of parameters of the readout chips of the modules in preparation for the data taking was one of the main responsibilities apart from the cross check of the reconstruction and analysis results of the modules themselves.

Based on all of these results the final decision on several vendors was taken.

10.2. Module Assembly

Module assembly is the next step from sensor to full detector elements. The assembly comprises gluing of the sensor - readout-chip hybrid, the bare module, to the flex with high precision and the subsequent wire bonding.

In order to assure module quality among all ITk production institutes, a common tooling was developed in the University of Göttingen. The validation of the tooling was shown, which resulted in several adjustments on the tooling until the requirements were fulfilled. In order not to violate the available detector space, there are height constraints on the module which entail requirements on the adhesive thickness between bare module and flex. With a more robust and stable aluminium inlay in the tooling and an additional dial gauge for monitoring the height setting, the required adhesive height could be obtained in repeated tests. Apart from the height, the x- and y-alignment of the two components to each other needs to be within the requirements. It was shown that the tooling is capable of precise gluing, provided the components are within specifications as there are no adjustment options for x- and y-alignment. Based on experience with this tooling a new version was designed which will be used for pre-production and production.

10.3. Module Quality Control

The University of Göttingen was qualified as assembly site for RD53A modules. Some example measurements of the adhesive height analysis and the x- and y-alignment are shown on dummy and on real modules. During the process of institutes getting qualified for module assembly, the stencil for the gluing pattern was adapted to limit delamination. Extensive studies were performed to assure a concise determination of the adhesive pattern and the covered area. A recommendation was therefore given to the community.

Part of quality control are also the electrical tests of modules. The installation of a cooling unit for the purpose of module testing in the University of Göttingen was shown. Also, the module testing capabilities were demonstrated and the University of Göttingen qualified as module testing institute. For the outer barrel demonstrator up to 29 modules are needed, originating from different ITk production sites. An analysis framework was developed and demonstrated for easy analysis and comparison of module testing data. This is in use to qualify modules for the demonstrator and was used to perform the analysis of data taken during the first assembly stages.

10.4. Outer Barrel Demonstrators

In the demonstrator setups system aspects are studied to validate the design of the ITk loaded local support, the services and the detector design concept. Final serial powering and grounding tests were performed on the FE-I4 demonstrator setup consolidating previous results. The functionality of serial powering for several module chains on common ground and a suitable grounding scheme were shown. For the RD53A demonstrator the interlock was programmed and validated with a pre-demonstrator setup. Besides, several commissioning studies paved the way to system tests, amongst which successful electrical scans with the full readout path were shown.

Bibliography

[1] S. Möbius (on behalf of the ATLAS ITk Group), *Module development for the ATLAS ITk pixel detector*, JINST 17 (2022) C03042

[2] J. Weller, *Characterisation of Pixel Sensors for the ATLAS ITk Upgrade*, II.Physik-UniGö-BSc-2020/04, BSc thesis, University of Göttingen, 2020

[3] T. Fitschen, *Search for semileptonic vector boson scattering with the ATLAS Detector using LHC Run-II data*, PhD thesis, Université Paris-Saclay & University of Birmingham (GB), 2022

[4] R. H. M. Taibah, *Upgrade of the ATLAS tracking detector in preparation for the High-Luminosity phase of the LHC : Planar pixel module characterisation and calibration for the current and future ATLAS inner tracker*, PhD thesis, 2021

[5] H. Beck, *Development of Pixel Module Assembly Processes for the Phase 2 Upgrade of the ATLAS Detector and Test Beam Measurements with Diamond Pixel Detectors*, II.Physik-UniGö-Diss-2019/08, PhD thesis, University of Göttingen, 2019

[6] T. H. Kwok, *2021 CERN Summer Student Report: Module Performance Evolution During Integration Steps*, CERN-STUDENTS-Note-2021-057, 2021

[7] J. W. von Goethe, *Faust. Der Tragödie Erster Teil*, Stuttgart: Reclam, 2000

[8] ATLAS Collaboration, *Observation of a new particle in the search for the Standard Model Higgs boson with the ATLAS detector at the LHC*, Phys. Lett. B 716 (2012) 1

[9] CMS Collaboration, *Observation of a new boson at a mass of 125 GeV with the CMS experiment at the LHC*, Phys. Lett. B 716 (2012) 30

[10] ATLAS Collaboration, *The ATLAS Experiment at the CERN Large Hadron Collider*, JINST 3 (2008) S08003

[11] CMS Collaboration, *The CMS experiment at the CERN LHC*, JINST 3 (2008) S08004

[12] S. L. Glashow, *Partial-symmetries of weak interactions*, Nucl. Phys. 22 (1961) 579

[13] G. 't Hooft and M. Veltman, *Regularization and renormalization of gauge fields*, Nucl. Phys. B 44 (1972) 189

[14] G. 't Hooft and M. Veltman, *Combinatorics of gauge fields*, Nucl. Phys. B 50 (1972) 318

[15] S. Weinberg, *A Model of Leptons*, Phys. Rev. Lett. 19 (1967) 1264

[16] A. Salam, *Weak and electromagnetic interactions*, Conf. Proc. C680519 (1968) 367

[17] S. L. Glashow, J. Iliopoulos, and L. Maiani, *Weak Interactions with Lepton–Hadron Symmetry*, Phys. Rev. D 2 (1970) 1285

[18] H. Georgi and S. L. Glashow, *Unified Weak and Electromagnetic Interactions without Neutral Currents*, Phys. Rev. Lett. 28 (1972) 1494

[19] D. J. Gross and F. Wilczek, *Ultraviolet Behavior of Nonabelian Gauge Theories*, Phys. Rev. Lett. 30 (1973) 1343

[20] H. D. Politzer, *Reliable Perturbative Results for Strong Interactions?*, Phys. Rev. Lett. 30 (1973) 1346

[21] G. 't Hooft, *Renormalization of massless Yang–Mills fields*, Nucl. Phys. B 33 (1971) 173

[22] G. 't Hooft, *Renormalizable Lagrangians for massive Yang–Mills fields*, Nucl. Phys. B 35 (1971) 167

[23] J. J. Thomson, *XL. Cathode Rays*, Phil. Mag. Ser. 5 44 (1897) 293

[24] E. Rutherford, *LXXIX. The scattering of* α *and* β *particles by matter and the structure of the atom*, Phil. Mag. Ser. 6 21 (1911) 669

[25] J. Chadwick, *Possible Existence of a Neutron*, Nature 129 (1932) 312

[26] N. Bohr, *I. On the constitution of atoms and molecules*, Phil. Mag. Ser. 6 26 (1913) 1

[27] N. Bohr, *XXXVII. On the constitution of atoms and molecules*, Phil. Mag. Ser. 6 26 (1913) 476

[28] N. Bohr, *LXXIII. On the constitution of atoms and molecules*, Phil. Mag. Ser. 6 26 (1913) 857

[29] A. Einstein, *Über einen die Erzeugung und Verwandlung des Lichtes betreffenden heuristischen Gesichtspunkt*, Ann. Phys. 322 (1905) 132

[30] M. Planck, *Ueber das Gesetz der Energieverteilung im Normalspectrum*, Ann. Phys. 309 (1901) 553

[31] A. Einstein, *Über die von der molekularkinetischen Theorie der Wärme geforderte Bewegung von in ruhenden Flüssigkeiten suspendierten Teilchen*, Ann. Phys. 322 (1905) 549

[32] A. Einstein, *Zur Elektrodynamik bewegter Körper*, Ann. Phys. 322 (1905) 891

[33] A. Einstein, *Ist die Trägheit eines Körpers von seinem Energieinhalt abhängig?*, Ann. Phys. 323 (1905) 639

[34] W. Heisenberg, *Über quantentheoretische Umdeutung kinematischer und mechanischer Beziehungen.* Z. Phys. 33 (1925) 879

[35] M. Born and P. Jordan, *Zur Quantenmechanik*, Z. Phys. 34 (1925) 858

[36] M. Born, W. Heisenberg, and P. Jordan, *Zur Quantenmechanik. II.* Z. Phys. 35 (1926) 557

[37] E. Schrödinger, *Quantisierung als Eigenwertproblem*, Ann. Phys. 384 (1926) 361

[38] P. A. M. Dirac, *The quantum theory of the emission and absorption of radiation*, Proc. R. Soc. A 114 (1927) 243

[39] P. A. M. Dirac, *The quantum theory of the electron*, Proc. R. Soc. A 117 (1928) 610

[40] W. C. T. Rees, *On a method of making visible the paths of ionising particles through a gas*, Royal Society 85 (1911) 285

[41] C. D. Anderson, *The Positive Electron*, Phys. Rev. 43 (1933) 491

[42] E. C. G. Stückelberg, *La signification du temps propre en mécanique ondulatoire*, Helv. Phys. 14 (1941) 322

[43] R. P. Feynman, *Space-Time Approach to Non-Relativistic Quantum Mechanics*, Rev. Mod. Phys. 20 (1948) 367

[44] S. Tomonaga, *On a Relativistically Invariant Formulation of the Quantum Theory of Wave Fields*, Prog. Theor. Phys. 1 (1946) 27

[45] J. Schwinger, *Quantum Electrodynamics. I. A Covariant Formulation*, Phys. Rev. 74 (1948) 1439

[46] J. Schwinger, *On Quantum-Electrodynamics and the Magnetic Moment of the Electron*, Phys. Rev. 73 (1948) 416

[47] R. P. Feynman, *Space-Time Approach to Quantum Electrodynamics*, Phys. Rev. 76 (1949) 769

[48] R. P. Feynman, *The Theory of Positrons*, Phys. Rev. 76 (1949) 749

[49] R. P. Feynman, *Mathematical Formulation of the Quantum Theory of Electromagnetic Interaction*, Phys. Rev. 80 (1950) 440

[50] F. J. Dyson, *The Radiation Theories of Tomonaga, Schwinger, and Feynman*, Phys. Rev. 75 (1949) 486

[51] F. J. Dyson, *The S Matrix in Quantum Electrodynamics*, Phys. Rev. 75 (1949) 1736

[52] M. Gell-Mann, *A schematic model of baryons and mesons*, Phys. Lett. 8 (1964) 214

[53] E. D. Bloom et al., *High-Energy Inelastic $e-p$ Scattering at 6° and 10°*, Phys. Rev. Lett. 23 (1969) 930

[54] B. R. Stella and H.-J. Meyer, Υ *(9.46 GeV) and the gluon discovery (a critical recollection of PLUTO results)*, Eur. Phys. J. H 36 (2011) 203

[55] P. Söding, *On the discovery of the gluon*, Eur. Phys. J. H 35 (2010) 3

[56] R. L. Workman et al. (Particle Data Group), *Review of Particle Physics*, PTEP 2022 (2022) 083C01

[57] CDF Collaboration, *Observation of Top Quark Production in $\bar{p}p$ Collisions with the Collider Detector at Fermilab*, Phys. Rev. Lett. 74 (1995) 2626

[58] DØ Collaboration, *Observation of the Top Quark*, Phys. Rev. Lett. 74 (1995) 2632

[59] M. Thomson, *Modern particle physics*, New York: Cambridge University Press, 2013

[60] P. W. Anderson, *Plasmons, Gauge Invariance, and Mass*, Phys. Rev. 130 (1963) 439

[61] F. Englert and R. Brout, *Broken Symmetry and the Mass of Gauge Vector Mesons*, Phys. Rev. Lett. 13 (1964) 321

[62] P. W. Higgs, *Broken symmetries, massless particles and gauge fields*, Phys. Lett. 12 (1964) 132

[63] G. S. Guralnik, C. R. Hagen, and T. W. B. Kibble, *Global Conservation Laws and Massless Particles*, Phys. Rev. Lett. 13 (1964) 585

[64] ATLAS Collaboration, *Standard Model Summary Plots February 2022*, ATL-PHYS-PUB-2022-009, 2022

[65] R. Davis, D. S. Harmer, and K. C. Hoffman, *Search for Neutrinos from the Sun*, Phys. Rev. Lett. 20 (1968) 1205

[66] Y. Fukuda et al. (Super-Kamiokande Collaboration), *Evidence for Oscillation of Atmospheric Neutrinos*, Phys. Rev. Lett. 81 (1998) 1562

[67] Q. R. Ahmad et al. (SNO Collaboration), *Direct Evidence for Neutrino Flavor Transformation from Neutral-Current Interactions in the Sudbury Neutrino Observatory*, Phys. Rev. Lett. 89 (2002) 011301

[68] N. A. et al, *Planck 2018 results. IV. Cosmological parameters*, A&A 641 (2020) A6, Erratum: A&A 652 (2021) C4

[69] F. Zwicky, *Die Rotverschiebung von extragalaktischen Nebeln*, Helv. Phys. Acta 6 (1933) 110

[70] F. Zwicky, *On the Masses of Nebulae and of Clusters of Nebulae*, Astrophys. J. 86 (1937) 217

[71] V. C. Rubin and J. Ford W. Kent, *Rotation of the Andromeda Nebula from a Spectroscopic Survey of Emission Regions*, Astrophys. J. 159 (1970) 379

[72] V. A. Kuzmin, V. A. Rubakov, and M. E. Shaposhnikov, *On anomalous electroweak baryon-number non-conservation in the early universe*, Phys. Lett. B 155 (1985) 36

[73] C. A. Baker et al., *Improved Experimental Limit on the Electric Dipole Moment of the Neutron*, Phys. Rev. Lett. 97 (2006) 131801

[74] L. Evans and P. Bryant, *LHC Machine*, JINST 3 (2008) S08001

[75] O. Aberle et al., *High-Luminosity Large Hadron Collider (HL-LHC): Technical design report*, ed. by I. Béjar Alonso et al., CERN Yellow Reports: Monographs, Geneva: CERN, 2020

[76] L. Arnaudon et al., *Linac4 Technical Design Report*, CERN-AB-2006-084, Geneva, 2006

[77] H. Damerau et al., eds., *LHC Injectors Upgrade, Technical Design Report, v.1: Protons*, CERN-ACC-2014-0337, 2014

[78] J. Coupard et al., *LHC Injectors Upgrade, Technical Design Report, v.2: Ions*, CERN-ACC-2016-0041, 2016

[79] CERN, *The Proton Synchrotron*, https://cds.cern.ch/record/1997189, 2012

[80] CERN, *The Super Proton Synchrotron*, https://cds.cern.ch/record/1997188, 2012

[81] CERN, *LEP design report v.1 : The LEP injector chain*, CERN-LEP-TH-83-29, Geneva, 1983

[82] CERN, *LEP design report v.2 : The LEP main ring*, CERN-LEP-84-01, Geneva, 1984

[83] ALICE Collaboration, *The ALICE experiment at the CERN LHC*, JINST 3 (2008) S08002

[84] LHCb Collaboration, *The LHCb Detector at the LHC*, JINST 3 (2008) S08005

[85] ATLAS Collaboration, *Luminosity Public Results Run 2*, URL: `https://twiki.cern.ch/twiki/bin/view/AtlasPublic/LuminosityPublicResultsRun2` (visited on Oct. 11, 2022)

[86] L. Wolfenstein, *Parametrization of the Kobayashi-Maskawa Matrix*, Phys. Rev. Lett. 51 (1983) 1945

[87] ATLAS Collaboration, *Letter of Intent for the Phase-II Upgrade of the ATLAS Experiment*, LHCC-I-023, Geneva, 2012

[88] ATLAS Collaboration, *ATLAS Phase-II Upgrade Scoping Document*, LHCC-G-166, Geneva, 2015

[89] ATLAS Collaboration, *ATLAS: technical proposal for a general-purpose pp experiment at the Large Hadron Collider at CERN*, LHCC-P-2, Geneva, 1994

[90] ATLAS Collaboration, *ATLAS detector and physics performance: Technical Design Report, 1*, ATLAS-TDR-14, 1999

[91] ATLAS Collaboration, *ATLAS Inner Detector: Technical Design Report, 1*, ATLAS-TDR-4, 1997

[92] ATLAS Collaboration, *ATLAS Inner Detector: Technical Design Report, 2*, ATLAS-TDR-5, 1997

[93] ATLAS Collaboration, *ATLAS Central Solenoid: Technical Design Report*, ATLAS-TDR-9, 1997

[94] B. Povh et al., *Teilchen und Kerne: Eine Einführung in die physikalischen Konzepte*, Springer, 2006

[95] ATLAS Collaboration, *ATLAS pixel detector electronics and sensors*, JINST 3 (2008) P07007

[96] ATLAS Collaboration, *ATLAS Insertable B-Layer Technical Design Report*, ATLAS-TDR-19, 2010, Addendum: ATLAS-TDR-19-ADD-1, 2012

[97] M. Garcia-Sciveres et al., *The FE-I4 Pixel Readout Integrated Circuit*, *7th International Symposium on the Development and Application of Semiconductor Tracking Detectors*, HSTD7 Hiroshima (Hiroshima, Japan, Aug. 29–Sept. 1, 2009), Nucl. Instrum. Meth. A 636, 2011, S155

[98] ATLAS Collaboration, *ATLAS Calorimeter Performance: Technical Design Report*, ATLAS-TDR-1, 1996

[99] ATLAS Collaboration, *ATLAS Liquid-Argon Calorimeter: Technical Design Report*, ATLAS-TDR-2, 1996

[100] ATLAS Collaboration, *ATLAS Tile Calorimeter: Technical Design Report*, ATLAS-TDR-3, 1996

[101] ATLAS Collaboration, *ATLAS Muon Spectrometer: Technical Design Report*, ATLAS-TDR-10, 1997

[102] ATLAS Collaboration, *ATLAS Magnet System: Technical Design Report, 1*, ATLAS-TDR-6, 1997

[103] ATLAS Collaboration, *ATLAS Barrel Toroid: Technical Design Report*, ATLAS-TDR-7, 1997

[104] ATLAS Collaboration, *ATLAS End-Cap Toroids: Technical Design Report*, ATLAS-TDR-8, 1997

[105] ATLAS Collaboration, *New Small Wheel Technical Design Report*, ATLAS-TDR-020, 2013

[106] ATLAS Collaboration, *Performance of the ATLAS trigger system in 2015*, Eur. Phys. J. C 77 (2017) 317

[107] ATLAS Collaboration, *ATLAS Liquid Argon Calorimeter Phase-I Upgrade: Technical Design Report*, ATLAS-TDR-022, 2013

[108] ATLAS Collaboration, *Technical Design Report for the Phase-I Upgrade of the ATLAS TDAQ System*, ATLAS-TDR-023, 2013

[109] J. Liouville, *Note sur la théorie de la variation des constantes arbitraires*, J. Math. Pures Appl. 1 (1838) 342

[110] B. Muratori and T. Pieloni, *Luminosity levelling techniques for the LHC*, *Proceedings of the ICFA Mini-Workshop on Beam-Beam Effects in Hadron Colliders* (CERN, Geneva, Switzerland, Mar. 18–22, 2013), 2014, arXiv: `1410.5646`

[111] *Schedule for the LHC and the HL-LHC*, 2022, URL: `https://hilumilhc.web.cern.ch/content/hl-lhc-project` (visited on Oct. 22, 2022)

[112] ATLAS Collaboration, *Technical Design Report for the ATLAS Inner Tracker Pixel Detector*, ATLAS-TDR-030, 2017

[113] ATLAS Collaboration, *Technical Design Report for the ATLAS Inner Tracker Strip Detector*, ATLAS-TDR-025, 2017

[114] ATLAS Collaboration, *Expected tracking and related performance with the updated ATLAS Inner Tracker layout at the High-Luminosity LHC*, ATL-PHYS-PUB-2021-024, 2021

[115] T. Sjöstrand et al., *An introduction to PYTHIA 8.2*, Comput. Phys. Commun. 191 (2015) 159

[116] A. Ferrari et al., *FLUKA: A multi-particle transport code (program version 2005)*, CERN Yellow Reports: Monographs, Geneva: CERN, 2005

[117] T. Stockmanns et al., *Serial powering of pixel modules*, Nucl. Instrum. Meth. A 511 (2003) 174

[118] D. B. Ta et al., *Serial powering: Proof of principle demonstration of a scheme for the operation of a large pixel detector at the LHC*, Nucl. Instrum. Meth. A 557 (2006) 445

[119] L. Gonella et al., *A serial powering scheme for the ATLAS pixel detector at sLHC*, JINST 5 (2010) C12002

[120] J. Chistiansen and M. Garcia-Sciveres, *RD Collaboration Proposal: Development of pixel readout integrated circuits for extreme rate and radiation*, LHCC-P-006, 2013

[121] RD53 Collaboration, *The RD53A Integrated Circuit*, CERN-RD53-PUB-17-001, 2017

[122] N. Lehmann, *Control and Monitoring for a serially powered pixel demonstrator for the ATLAS Phase II upgrade*, PoS TWEPP2018 (2019) 133

[123] E. Buschmann, *The Readout System for the ITk Pixel Demonstrator for the ATLAS High-Luminosity Upgrade*, II.Physik-UniGö-Diss-2019/10, PhD thesis, University of Göttingen, 2019

[124] F. Hinterkeuser, *Evaluation of a Serial Powering Scheme and its Building Blocks for the ATLAS ITk Pixel Detector*, PhD thesis, Rheinische Friedrich-Wilhelms-Universität Bonn, 2022, to be published.

[125] H. Bethe, *Zur Theorie des Durchgangs schneller Korpuskularstrahlen durch Materie*, Ann. Phys. 397 (1930) 325

[126] F. Bloch, *Zur Bremsung rasch bewegter Teilchen beim Durchgang durch Materie*, Ann. Phys. 408 (1933) 285

[127] L. D. Landau, *On the energy loss of fast particles by ionization*, J. Phys. 8 (1944) 201

[128] P. V. Vavilov, *Ionization losses of high-energy heavy particles*, Sov. Phys. JETP 5 (1957) 749

[129] H. Bichsel, *Straggling in thin silicon detectors*, Rev. Mod. Phys. 60 (1988) 663

[130] P. P. Altermatt et al., *Reassessment of the intrinsic carrier density in crystalline silicon in view of band-gap narrowing*, J. Appl. Phys. 93 (2003) 1598

[131] L. Rossi et al., *Pixel Detectors: From Fundamentals to Applications*, Particle Acceleration and Detection, Berlin: Springer-Verlag, 2006

[132] W. Shockley, *Currents to Conductors Induced by a Moving Point Charge*, J. Appl. Phys. 9 (1938) 635

[133] S. Ramo, *Currents Induced by Electron Motion*, Proceedings of the IRE 27 (1939) 584

[134] H. Kolanoski and N. Wermes, *Particle Detectors*, Oxford University Press, 2020

[135] M. Moll, *Radiation damage in silicon particle detectors: Microscopic defects and macroscopic properties*, PhD thesis, Hamburg University, 1999

[136] I. Perić et al., *The FEI3 readout chip for the ATLAS pixel detector*, *Proceedings of the International Workshop on Semiconductor Pixel Detectors for Particles and Imaging*, PIXEL 2005 (Bonn, Germany, Sept. 5–8, 2005), Nucl. Instrum. Meth. A 565, 2006, 178

[137] ATLAS ITk Collaboration, *Technical Specification and Acceptance Criteria for the Planar Pixel Sensors for the ITK project*, ATLAS internal note, `https://edms.cern.ch/document/1817538/1`, Geneva, 2017

[138] *Technical Specification and Acceptance Criteria for the Bump Bonding of the ITk pixel modules*, ATLAS internal note, `https://edms.cern.ch/document/1817526/3`, Geneva, 2020

[139] *Technical Specification and Acceptance Criteria for 3D Sensors for the ATLAS Pixel Tracker Upgrade*, ATLAS internal note, `https://edms.cern.ch/document/1817524/1`, Geneva, 2018

[140] F. Arteche Gonzalez et al., *Extension of RD53*, LHCC-SR-008, 2018

[141] M. Garcia-Sciveres (RD53 Collaboration), *RD53B Design Requirements*, CERN-RD53-PUB-19-001, 2019

[142] ATLAS ITk Collaboration, *Planar Pixel MS Technical Specification document*, ATLAS internal note, `https://edms.cern.ch/document/2040673/2`, Geneva, 2018

[143] *Recommendations towards a standardisation of the macroscopic parameter measurements - Part I: IV and CV measurements in Si diodes*, 2004

[144] J. Fernández-Tejero et al., *Humidity sensitivity of large area silicon sensors: Study and implications*, Nucl. Instrum. Meth. A 978 (2020) 164406

[145] C. Helling et al., *Strip sensor performance in prototype modules built for ATLAS ITk*, Nucl. Instrum. Meth. A 978 (2020) 164402

[146] F. G. Hartjes, *Moisture sensitivity of AC-coupled silicon strip sensors*, Nucl. Instrum. Meth. A 552 (2005) 168, ed. by E. Borchi and M. Bruzzi

[147] R. Diener et al., *The DESY II test beam facility*, Nucl. Instrum. Meth. A 922 (2019) 265

[148] H. Jansen et al., *Performance of the EUDET-type beam telescopes*, EPJ Tech. Instrum. 3 (2016)

[149] A. Himmi et al., *A Zero Suppression Micro-Circuit for Binary Readout CMOS Monolithic Sensors*, *Proceedings, Topical Workshop on Electronics for Particle Physics*, TWEPP2009 (Paris, France, Sept. 21–25, 2009), 2009

[150] J. Baudot et al., *First test results Of MIMOSA-26, a fast CMOS sensor with integrated zero suppression and digitized output*, *2009 IEEE Nuclear Science Symposium Conference Record (NSS/MIC)*, 2009, 1169

[151] T. Heim, *YARR - A PCIe based Readout Concept for Current and Future ATLAS Pixel Modules*, J. Phys. Conf. Ser. 898 (2017) 032053

[152] P. Baesso, D. Cussans, and J. Goldstein, *The AIDA-2020 TLU: a flexible trigger logic unit for test beam facilities*, JINST 14 (2019) P09019

[153] M. Backhaus et al., *Development of a versatile and modular test system for ATLAS hybrid pixel detectors*, *International Workshop on Semiconductor Pixel Detectors for Particles and Imaging 2010* (Grindelwald, Switzerland, Sept. 6–10, 2010), Nucl. Instrum. Meth. A 650, 2011, 37

[154] T. Bisanz, *Test beam studies of pixel detector prototypes for the ATLAS-Experiment at the High Luminosity Large Hadron Collider*, II.Physik-UniGö-Diss-2018/03, PhD thesis, University of Göttingen, 2018

[155] P. Ahlburg et al., *EUDAQ—a data acquisition software framework for common beam telescopes*, JINST 15 (2020) P01038

[156] Y. Liu et al., JINST 14 (2019) P10033

[157] T. Bisanz et al., *EUTelescope: A modular reconstruction framework for beam telescope data*, JINST 15 (2020) P09020

[158] C. Kleinwort, *General broken lines as advanced track fitting method*, Nucl. Instrum. Meth. A 673 (2012) 107

[159] R. Bates, *Technical Specification for ITk Pixel Modules*, ATLAS internal note, `https://edms.cern.ch/document/2019657/2`, Geneva, 2019

[160] J. Metcalfe et al., *RD53A Module Assembly*, ATL-COM-UPGRADE-2020-021, ATLAS internal note, Geneva, 2020

[161] ATLAS Collaboration, *Production and integration of the ATLAS Insertable B-Layer*, JINST 13 (2018) T05008

[162] *RD53A quad assembly tooling*, ATLAS internal note, `https://edms.cern.ch/document/2647640/1`, Geneva, 2021

[163] *ITkPix assembly tooling including instruction*, ATLAS internal note, `https://edms.cern.ch/document/2615861/1`, Geneva, 2025

[164] ATLAS Collaboration, *RD53A quad hybrid design*, ATLAS internal note, `https://edms.cern.ch/document/2391595/1`, Geneva, 2021

[165] *RD53A bare Module, Sensor and FE chip Engineering DWG*, ATLAS internal note, `https://edms.cern.ch/document/2016407/2`, Geneva, 2019

[166] *RD53A bare Module, Sensor and FE chip Engineering DWG*, ATLAS internal note, `https://edms.cern.ch/document/2016407/4`, Geneva, 2022

[167] *Envelope DWG of the RD53A Module Assembly*, ATLAS internal note, `https://edms.cern.ch/document/2115095/1`, Geneva, 2019

[168] E. Anderssen, G. Viehhauser, *ITk Operational Environments*, ATLAS internal note, `https://edms.cern.ch/document/1853235/2`, Geneva, 2019

[169] L. Meng, *RD53A Module Testing Document*, ATLAS internal note, `https://cds.cern.ch/record/2702738`, Geneva, 2021

[170] M. Daas et al., *BDAQ53, a versatile pixel detector readout and test system for the ATLAS and CMS HL-LHC upgrades*, Nucl. Instrum. Meth. A 986 (2021) 164721

[171] Michael Daas, *Characterization and Quality Control of RD53A Readout Chips and Modules for the ATLAS ITk Pixel Detector*, PhD thesis, Rheinische Friedrich-Wilhelms-Universität Bonn, 2021

[172] *Design Overview of Global Mechanics and Integration for the ITk Pixel Outer Barre*, ATLAS internal note, `https://edms.cern.ch/document/2438127/1`, Geneva, 2020

[173] N. Lehmann et al., *Prototype Chip for a Control System in a Serial Powered Pixel Detector at the ATLAS Phase II Upgrade*, PoS TWEPP2017 (2018) 026

[174] N. Lehmann, *Development of a Detector Control System Chip*, PhD thesis, Wuppertal University, 2019

[175] P. Moreira et al., *The GBT-SerDes ASIC prototype*, JINST 5 (2010) C11022

[176] J. Troska et al., *The Versatile Transceiver Proof of Concept*, *Proceedings, Topical Workshop on Electronics for Particle Physics*, TWEPP2009 (Paris, France, Sept. 21–25, 2009), 2009

[177] A. Xiang et al., *A Versatile Link for High-Speed, Radiation Resistant Optical Transmission in LHC Upgrades*, *Proceedings of the 2nd International Conference on Technology and Instrumentation in Particle Physics*, TIPP 2011 (Chicago, IL, USA, June 9–14, 2011), Physics Procedia 37, 2012, 1750

[178] E. Buschmann, *ATLAS Phase-II-Upgrade Pixel Demonstrator Read-out*, PoS TWEPP 2018 (2019) 046

[179] W. C. A. International, *ASTM B258-14 Standard Specification for Standard Nominal Diameters and Cross-Sectional Areas of AWG Sizes of Solid Round Wires Used as Electrical Conductors*, *Book of Standards*, **02.03**

[180] S. Ryu (on behalf of the ATLAS TDAQ Collaboration), *FELIX: The new detector readout system for the ATLAS experiment*, J. Phys. Conf. Ser. 898 (2017) 032057

[181] ATLAS Collaboration, *Technical Design Report for the Phase-II Upgrade of the ATLAS TDAQ System*, ATLAS-TDR-029, 2017

[182] C. Solans (on behalf ot the ATLAS Collaboration), *The FELIX detector interface for the ATLAS TDAQ upgrades and its deployment in the ITK demonstrator setup*, *19th International Workshop on Advanced Computing and Analysis Techniques in Physics Research* (Saas Fee, Switzerland, Mar. 11–15, 2019), J. Phys. Conf. Ser. 1525, 2020, 012033

[183] N. Guettouche et al., *The lpGBT production testing system*, JINST 17 (2022) C03040

[184] C. Chen et al., *Characterization of a gigabit transceiver for the ATLAS inner tracker pixel detector readout upgrade*, JINST 15 (2020) T03005

[185] *Versatile Link Plus Specification Part 1 System*, ATLAS internal note, `https://edms.cern.ch/document/1719328/1`, Geneva, 2019

[186] *Versatile Link Plus Specification Part 2.1 Front-end Versatile Transceiver*, ATLAS internal note, `https://edms.cern.ch/document/1719329/1`, Geneva, 2021

[187] H. Joos, *Development of the Detector Control System of the ITk Outer Barrel demonstrator for the ATLAS Experiment*, II.Physik-UniGö-MSc-2022/01, MSc thesis, University of Göttingen, 2022

[188] A. Walsemann et al., *A CANopen based prototype chip for the Detector Control System of the ATLAS ITk Pixel Detector*, PoS TWEPP2019 (2020) 013

[189] S. Kersten et al., *The ITk interlock hardware protection system*, Nucl. Instrum. Meth. A 1045 (2023) 167613

[190] *The Interlock Matrix Crate of the IBL*, ATLAS internal note, `https://edms.cern.ch/document/1302654/1`, Geneva, 2022

[191] R. Mueller (on behalf of the ATLAS Collaboration), *System Tests of the ATLAS ITk Planar and 3D Pixel Modules*, *Topical Workshop on Electronics for Particle Physics 2022*, TWEPP2022 (Bergen, Norway, Sept. 19–23, 2022), 2022

APPENDIX A

FE-I4 Demonstrator Additional Plots

A.1. SP-Chain Configuration Tests

In Figure A.1, the comparisons of the average noise and threshold values before retuning, after retuning and after doing the grounding tests are shown. A few modules, mainly in the duals of the C-side, needed retuning, while most others kept their tuning values. The grounding tests did not have any effect on the module performance. One exception is the breaking FE chip A_IM_05_2 which works unstably.

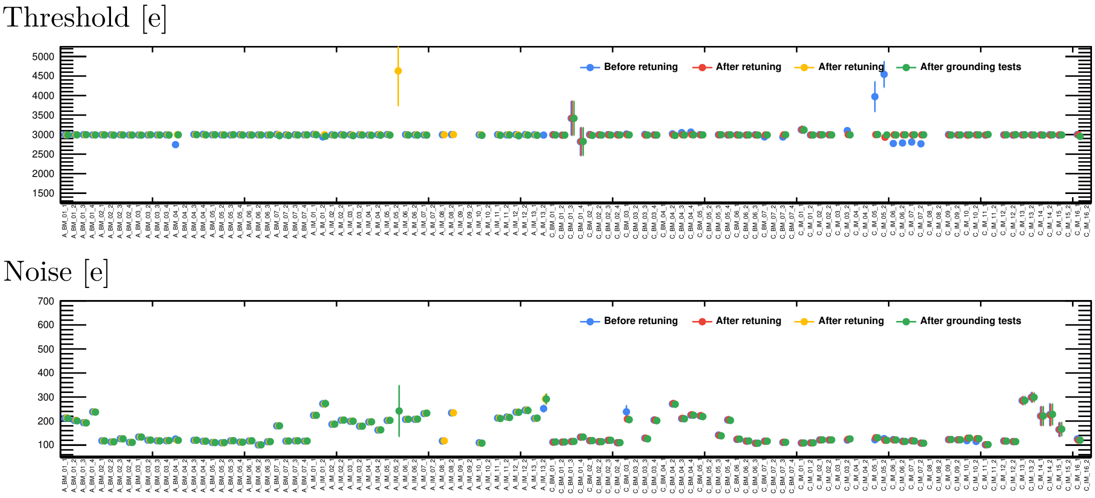

Figure A.1: Comparison of performance before retuning, after retuning and after doing the grounding tests. Some modules, mainly on the C-side, benefited from the retuning. The faulty FE chip A_IM_05_2 works unstably and shows higher results after retuning.

APPENDIX B

RD53A Demonstrator Additional Plots

B.1. Noise Distribution

B.1.1. Synchronous FE

In Figure B.1, the noise distribution for the synchronous FEs of the SP-chain with six modules is shown. The value that is displayed is the fitted noise distribution for the synchronous FE with the error bars being the standard deviation calculated by ROOT.

The noise values are all ≈ 120 e, except for M-T-2. The tuning of the initial stage has either failed or was not done for the synchronous FE of M-T-2, resulting in a more wide spread noise distribution in the following stages. Also, there are no valid scans from the

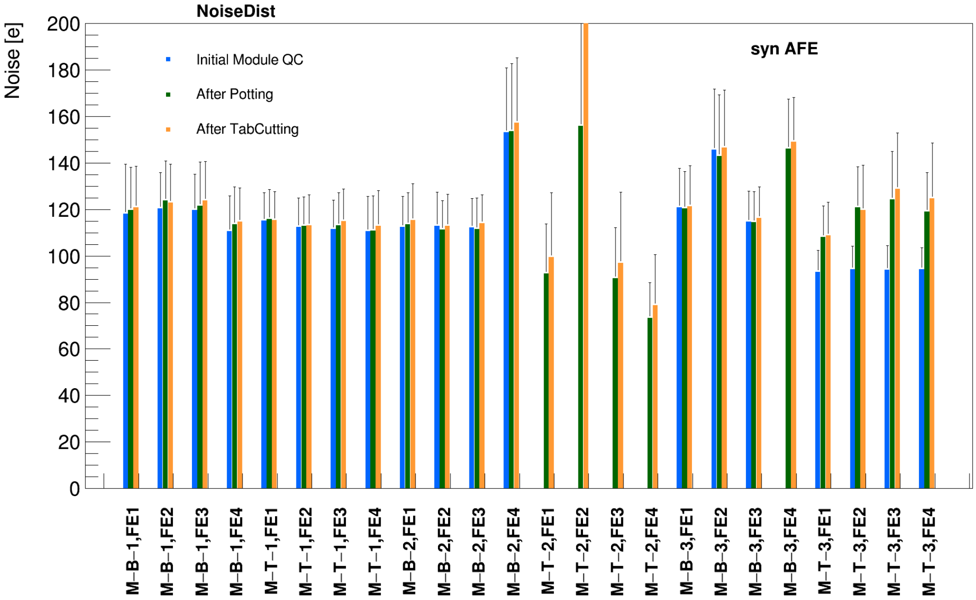

Figure B.1: Noise distribution of the synchronous FEs of the six modules.

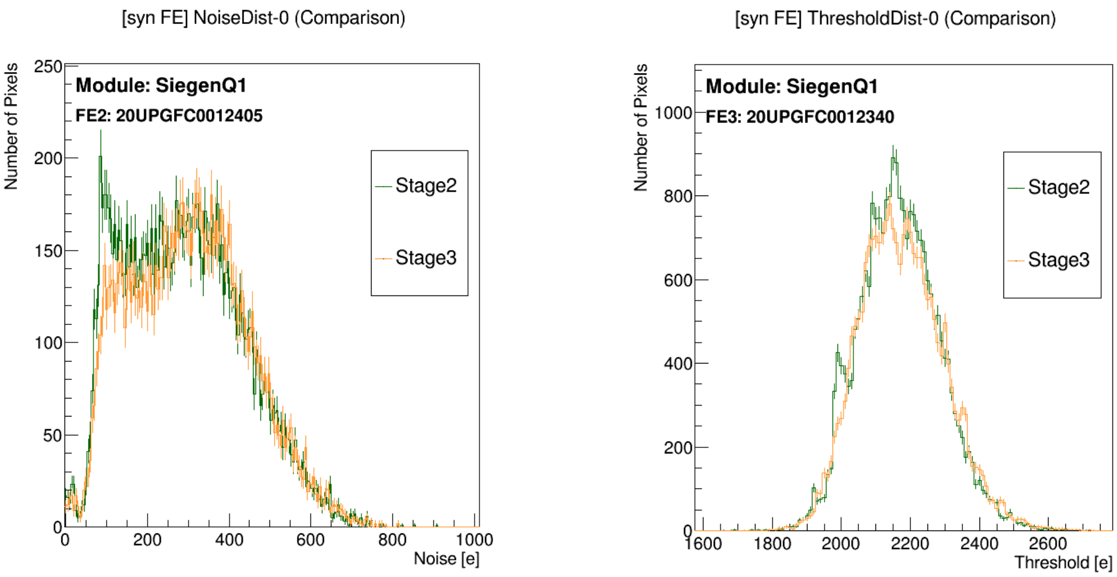

Figure B.2: The threshold and the noise distributions are shown for FE2, where it is visible that the threshold scan is run on a chip without or failed tuning. A tuned chip has $\mathcal{O}(2000)$ pixels at the peak threshold, whereas for this chip there are only $\mathcal{O}(800)$ pixels at the peak and large tails are visible.

initial module QC. In Figure B.2, the threshold and the noise distribution are shown for FE2, where it is visible that the threshold scan is run on a chip without or failed tuning. A tuned chip has $\mathcal{O}(2000)$ pixels at the peak threshold, whereas for this chip there are only $\mathcal{O}(800)$ pixels at the peak and large tails are visible.

For the other modules, the fitted noise distribution for the synchronous FEs are shown in Figure B.3. They as well have mainly very similar noise values around 120 e with some FEs broken, as shown in Figure 9.9. Only M8 and M9 have significantly higher noise values during module QC. As this is, however, only the case for the first measurement, it seems to be setup and not module related.

B.1.2. Linear FE

The fitted mean noise distributions for the linear FEs are shown in Figure B.4 and Figure B.5. The modules have very similar noise values around 70 e.

B.2. Source Scans

B.2.1. Synchronous FE

Figure B.6 displays the number of pixels without hits for the synchronous FEs in a source scan for the six modules. There are no additional pixels without hits beyond the already masked ones, hence all pixels are masked and dead, which means that they are disabled from the scans before. This is why only the plot for the disabled pixels is shown.

M-T-1 did not get a synchronous FE source scan, thus all of its pixels are masked, M-B-2

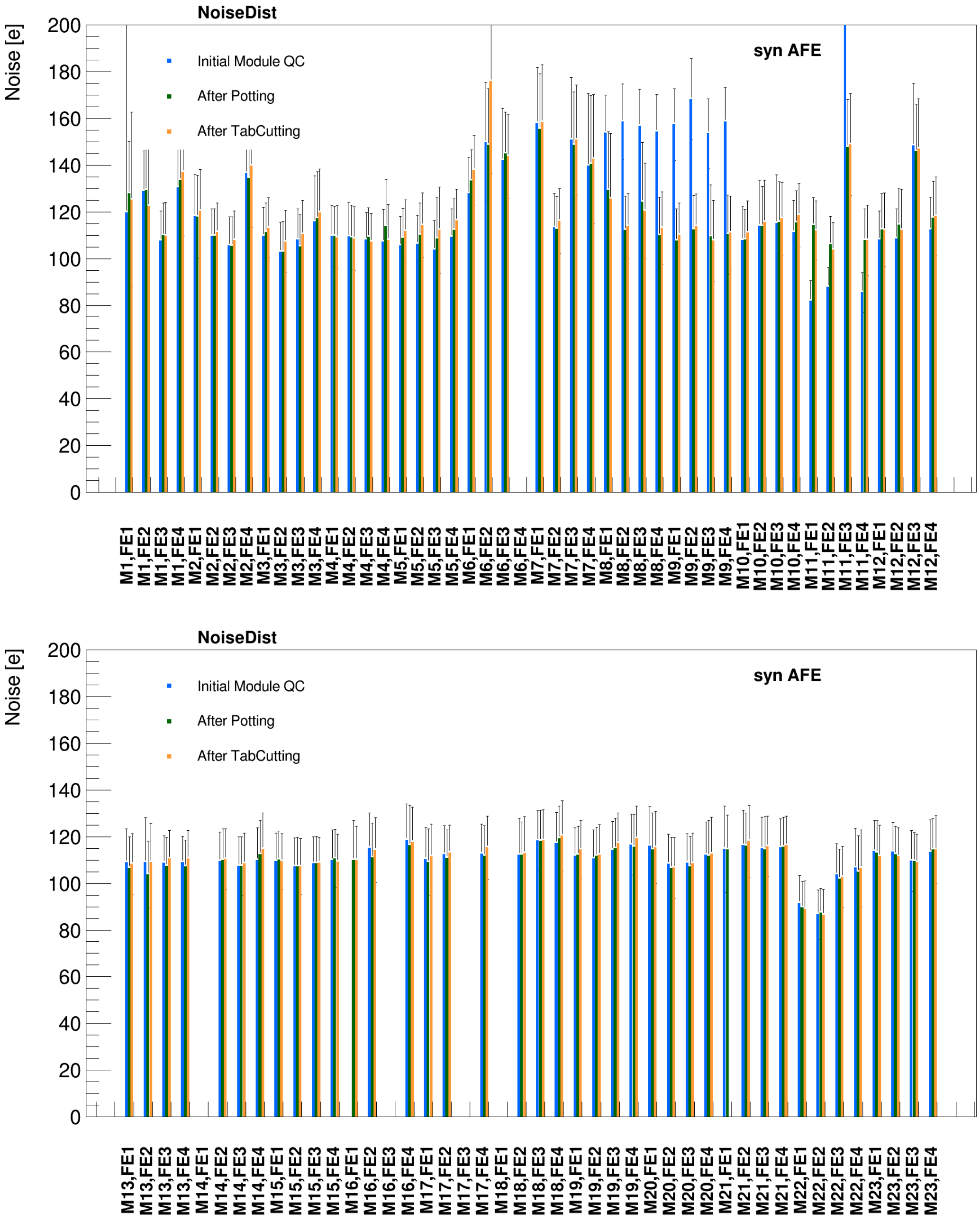

Figure B.3: Noise distributions for the synchronous FEs of the remaining modules.

has a low occupancy source scan in stage 1, as can be seen in Figure B.7. This also results in lots of masked and hence disabled pixels.

Figure B.8 shows the numbers of pixels with zero hits for the twelve modules in the source scan of the synchronous FE shown. All pixels with zero hits are masked, which means disabled.

M1 and M5 have no synchronous FE source scan in stage 1 so that all pixels are marked as masked pixels. This makes sense as there is no information about these pixels and thus the mask is set by the program to mask all pixels and disable them. M2, M3 and M4 have

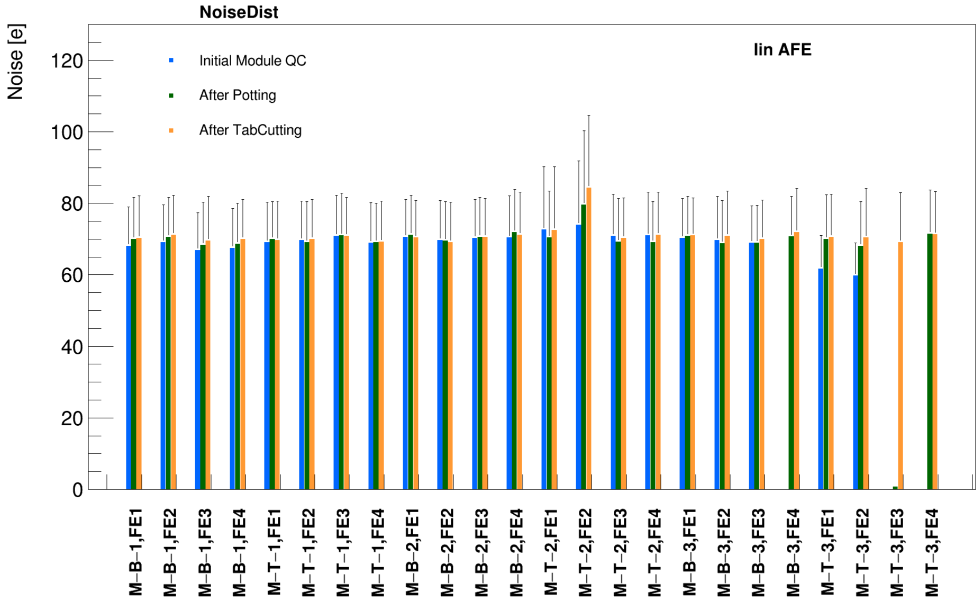

Figure B.4: Mean noise distributions for the linear FEs of the modules of the short SP-chain.

synchronous FE source scans with low occupancy in stage 1 and therefore disabled pixels. For all the other modules with a source scan in the initial stage there is no degradation after the second stage (potting) seen with respect to the previous stage.

Figure B.9 shows the analysis result of the low occupancy source scan for M2. This scan with low occupancy has disabled pixels, which is in principle not expected as digital- and analog scans are of good quality. One possible explanation, which can, however, not be verified, is that the source was still on during masking and thus resulting in masking pixels. An indication for this is the fact that the SMD components are shown as disabled. In a noise scan with a source still turned on, the sensor underneath the SMD components would get less hits, as the radiation is absorbed. Hence, in the real scan, where the pixels outside of the SMD component areas are masked as the irradiation was interpreted as noise before, a larger area under the SMD components would still be active and detect more.

In Figure B.10, the source scans for the synchronous FEs of the remaining eleven modules are displayed. For these modules some of the pixels with zero hits are dead.

M23 has a pattern in the synchronous FE source scan, as shown in Figure B.11, which is not necessarily a feature of the chip but most likely a general readout problem and hence results in dead pixels. M18 has several disabled pixels on the boarders of the FEs, also seen in Figure B.11 on the right. They have been marked as noisy in the noise scan.

B.2.2. Linear FE

In Figure B.12, the results for the source scans of the linear FEs of the six modules are displayed. The number of dead and disabled pixels for the linear FEs of M-B-3 and M-T-2 is remarkable. The first one has several bad analog pixels in the linear FE which are in stage 1 not yet masked and therefore counted as dead. A possible explanation for this is

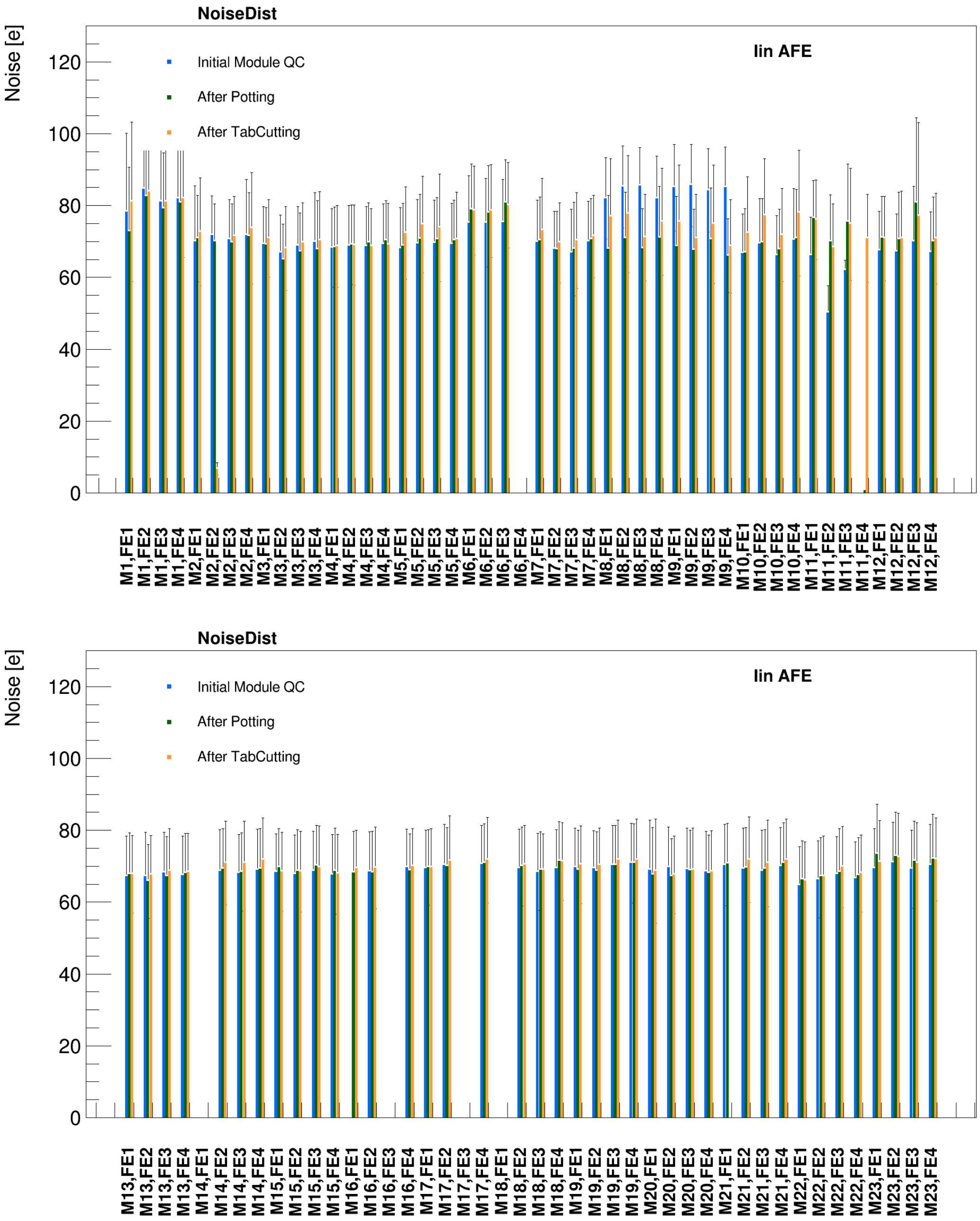

Figure B.5: Mean noise distributions for the linear FEs of the remaining modules.

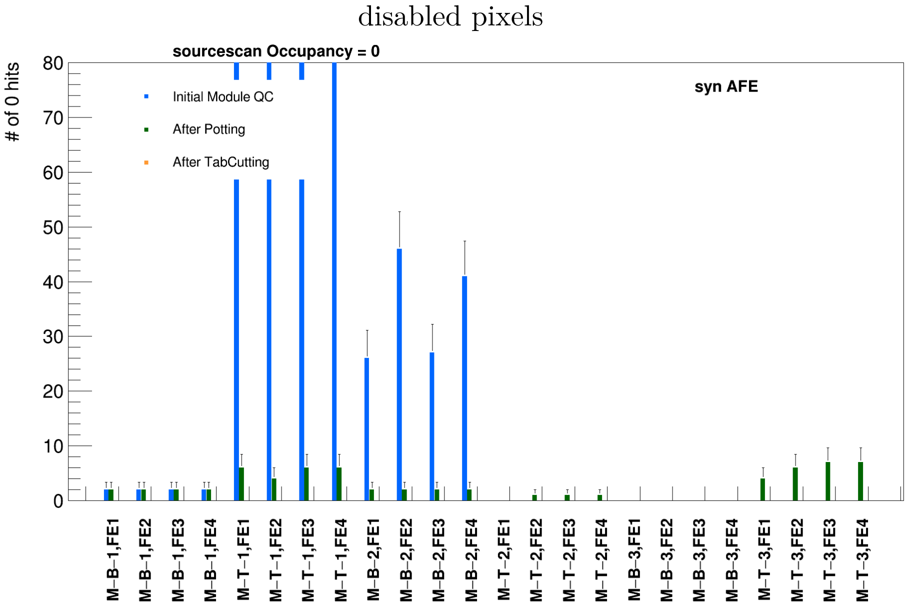

Figure B.6: The disabled pixels in the synchronous FEs are shown for the six modules for the demonstrator. There are no additional pixels without hits beyond the already masked ones.

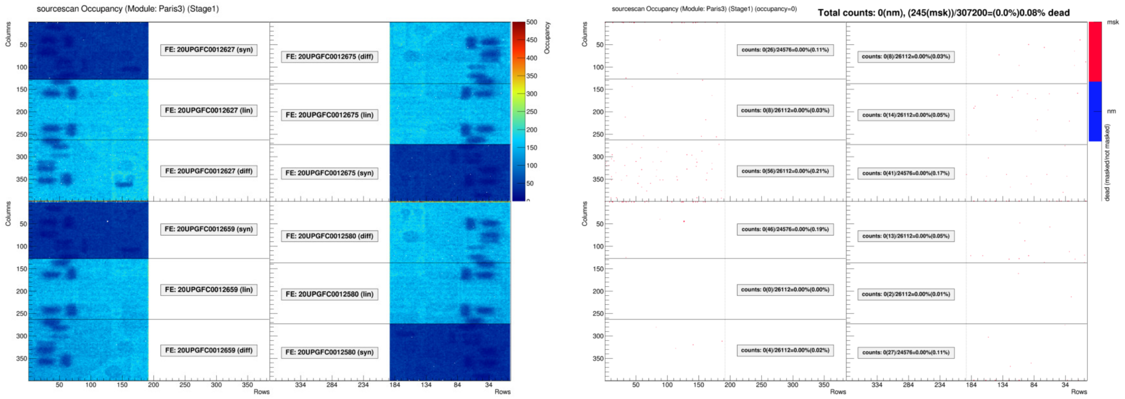

Figure B.7: The source scan in the initial stage has a very low occupancy as the source that was used is not very strong, hence requiring long integration times. The pixels marked as not masked "nm" (in blue) in the plot correspond to the dead pixels. The masked ("msk") pixels are disabled during the scan. There are no dead pixels, only disabled pixels.

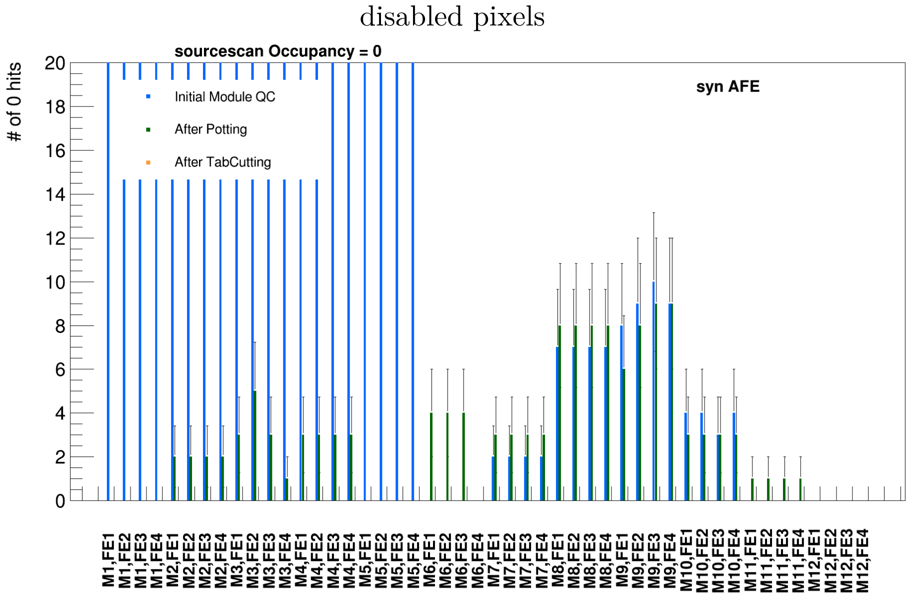

Figure B.8: Number of disabled pixels for the twelve modules in the source scans of the synchronous FEs.

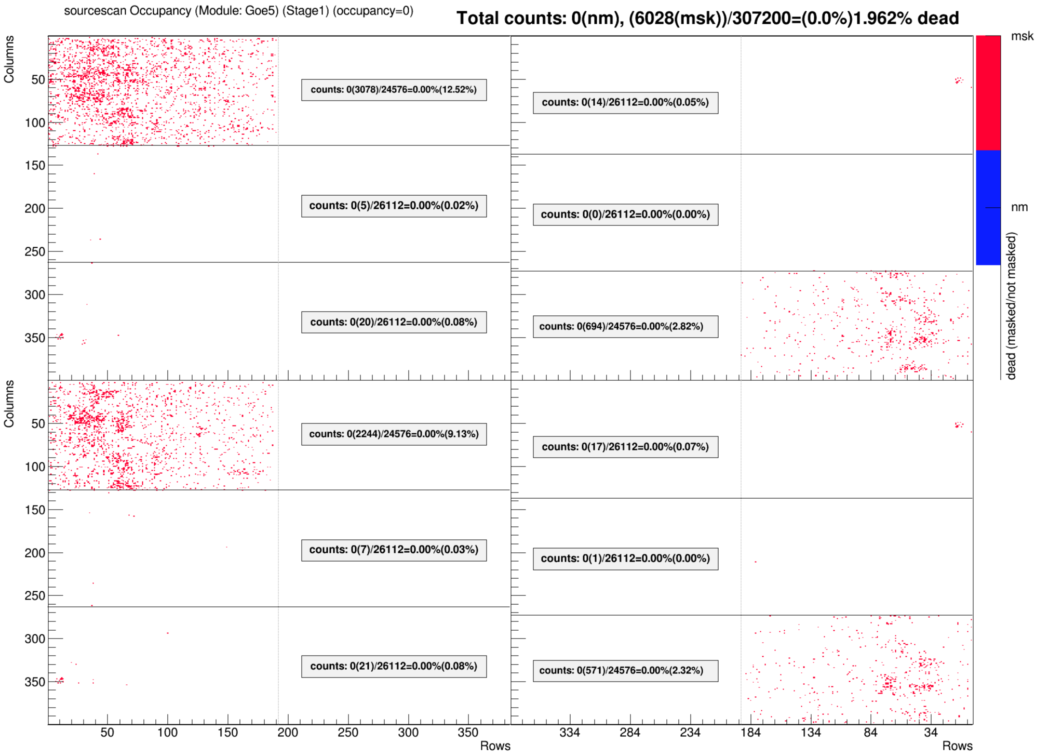

Figure B.9: M2 has 6028 pixels marked as masked from a low occupancy source scan. The pixels marked as not masked "nm" (in blue) in the plot correspond to the dead pixels. The masked ("msk") pixels are disabled during the scan.

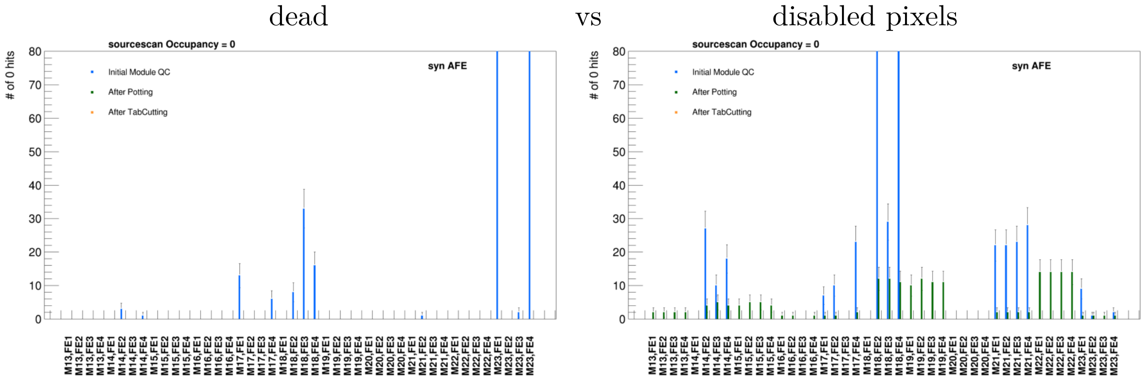
dead vs disabled pixels

Figure B.10: Dead and disabled pixels for the eleven modules in synchronous source scans.

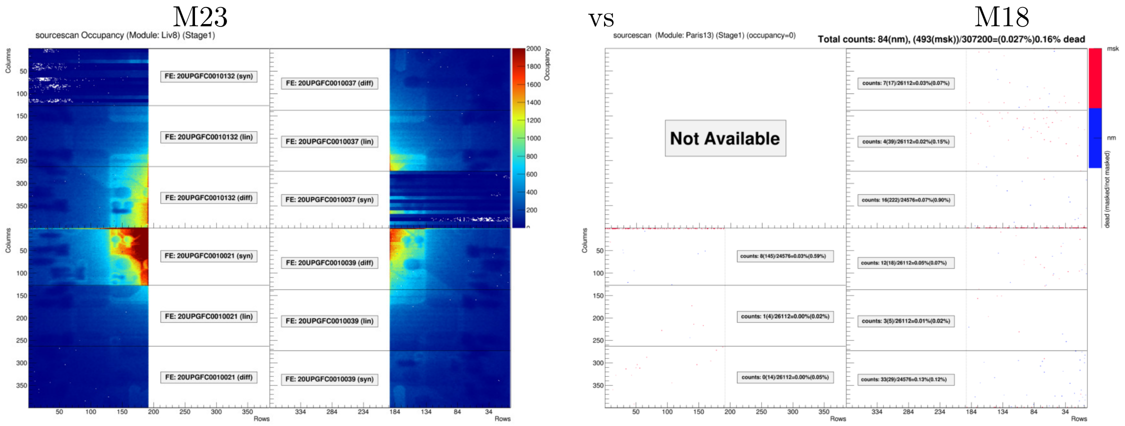
M23 vs M18

Figure B.11: For M23 a pattern is visible in the synchronous FE and M18 has more than 350 disabled pixels at the FE borders which were masked during the noise scan. The pixels marked as not masked "nm" (in blue) in the plot correspond to the dead pixels. The masked ("msk") pixels are disabled during the scan.

given in Section 9.2.4. M-T-2 has several analog pixel marked as bad, resulting in disabled pixels in the source scan.

Figure B.13 shows the same for the twelve modules. M3 has several dead pixels while M11 has a pattern of disabled pixels from the digital scan before, this has already been shown for the differential FE in Figure 9.17. In general, a pattern like this does not mean that the chip has broken parts but that there was a failure in the scan. Repeating of the scan usually solves the problem and should always be done to avoid these kinds of misleading results. It should be mentioned here again that only the analysis of the data is presented in this thesis and that the data sets come from many different origins, hence there is very little control over their content.

The remaining modules are shown in Figure B.14. M15 has disabled parts which originate from digital pixel parts being broken, as shown in Figure B.15. M19 and M22 have many disabled pixels from bad analog FEs.

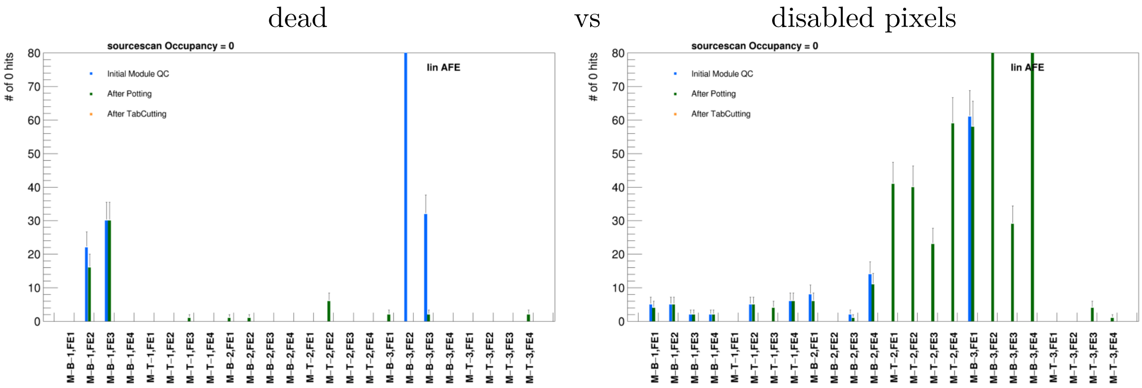

Figure B.12: Pixels with zero hits in the source scans of the linear FEs of the six modules.

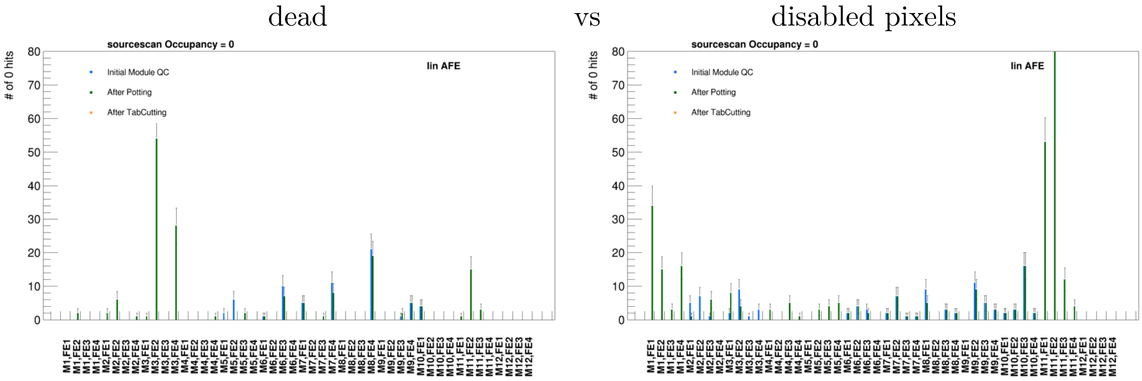

Figure B.13: Pixels with zero hits in the source scans of the linear FEs in the twelve modules.

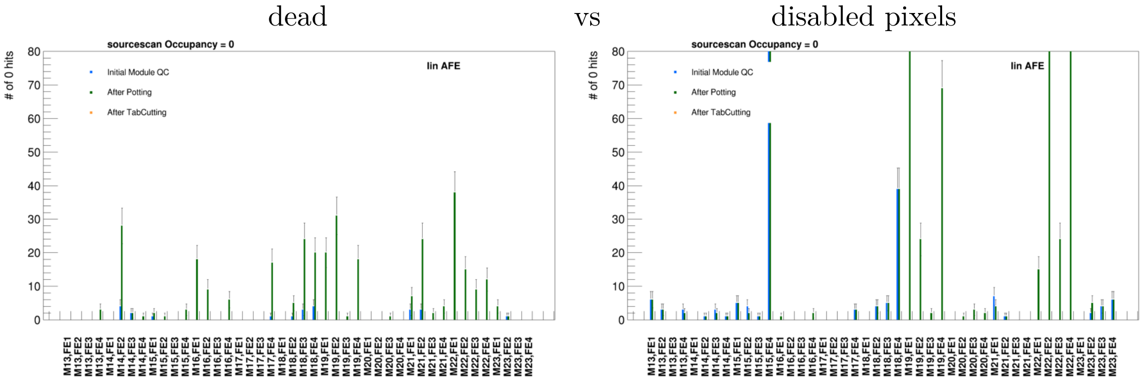

Figure B.14: The source scan results of the linear FEs of the remaining eleven modules.

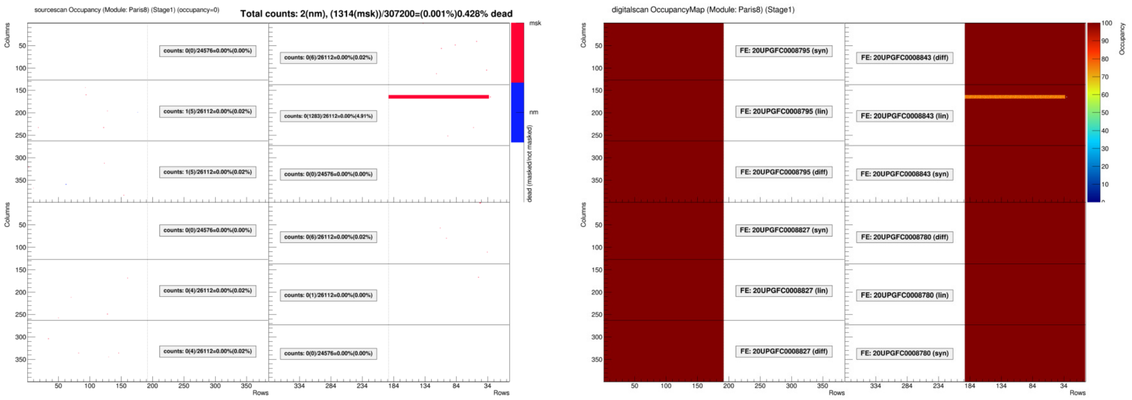

Figure B.15: Large broken area in digital FE part results in large disabled area in the linear FE of chip four of module M15. The pixels marked as not masked “nm” (in blue) in the plot correspond to the dead pixels. The masked (“msk”) pixels are disabled during the scan.

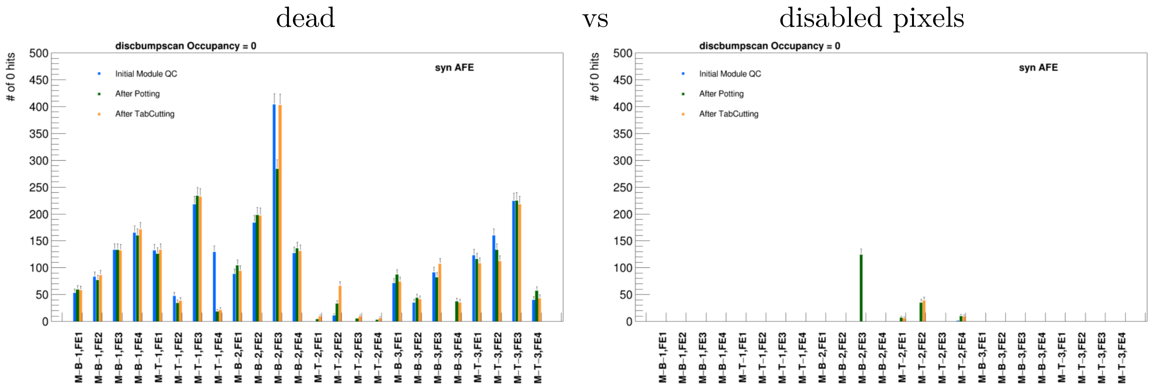

Figure B.16: Disconnected bump scans of the six modules for the synchronous FEs. There are many more dead than disabled pixels.

B.3. Disconnected Bump Scans

B.3.1. Synchronous FE

In Figure B.16, the disconnected bump scans for the synchronous FEs for the six modules are shown. It is evident that there are much more pixels marked with occupancy zero than in the source scans before.

The masking is calculated from the digital- and analog scan before the disconnected bump scan, as mentioned before for the source scan. M-B-2 has several masked pixels around the edge in stage 2 from a failed digital scan in FE3, which is shown in Figure B.17.

Figure B.18 displays the disconnected bump scan of the synchronous FEs of the twelve modules. M2 has in stage 3 a broken FE2, which led to masked and then disabled pixels. M4 has no digital scan for FE3 in stage 1, hence every single pixel with zero hits is masked.

In Figure B.19, the disconnected bump scans of the synchronous FEs of the eleven modules are depicted. M16 has no disconnected bump scans for the synchronous FEs, which results naturally in all pixels shown as masked.

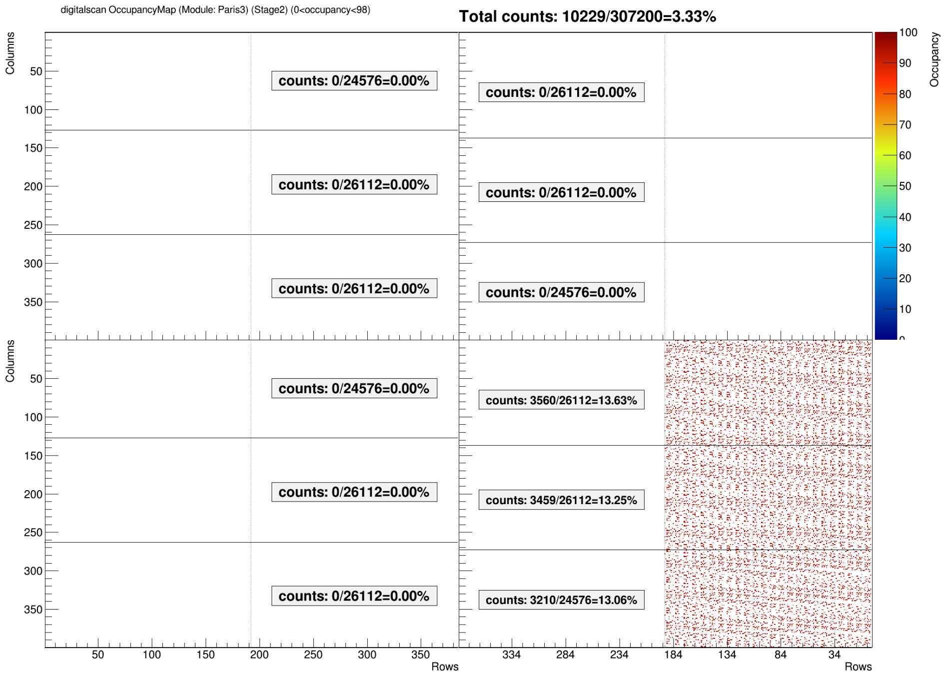

Figure B.17: Failed digital scan leading to masked pixels in later scans.

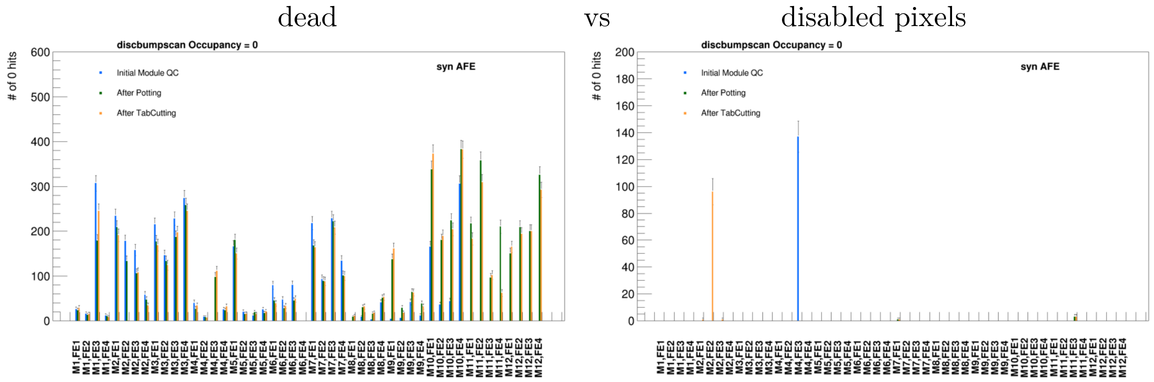

Figure B.18: Disconnected bump scans of the synchronous FEs of the twelve modules. There are many more dead than disabled pixels.

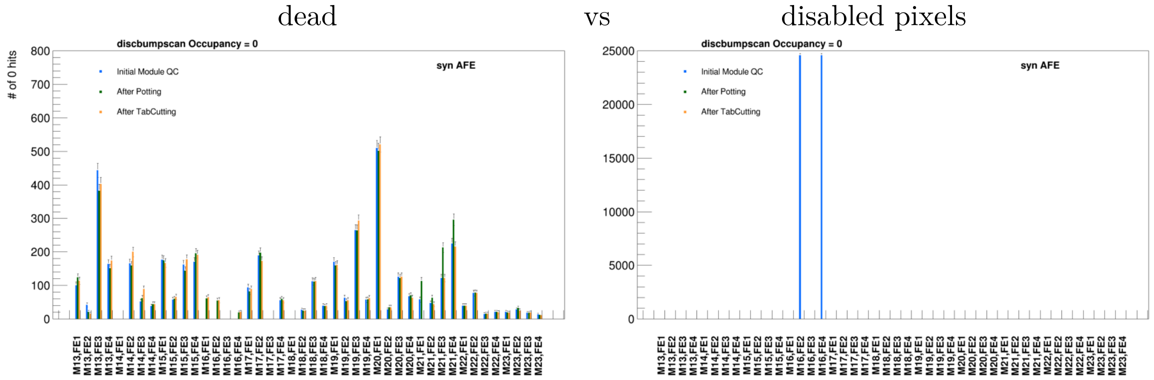

Figure B.19: Disconnected bump scans of the synchronous FEs of the eleven modules.

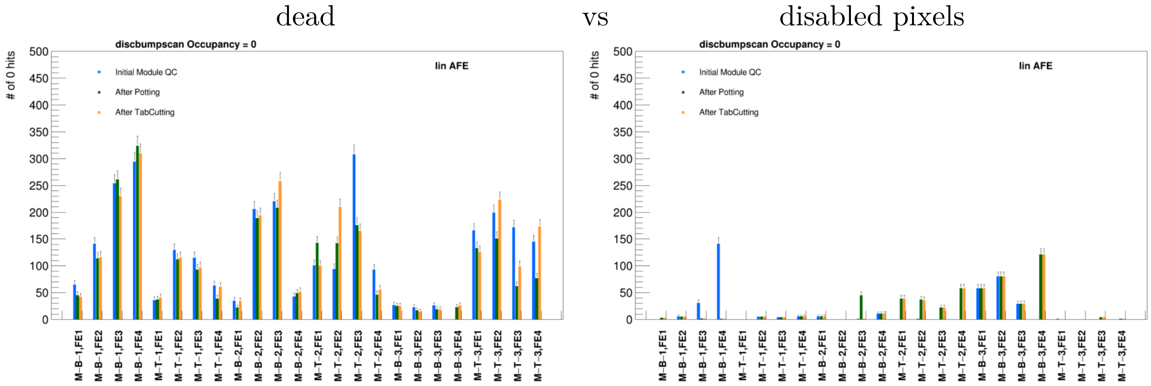

Figure B.20: Disconnected bump scans of the linear FEs of the six modules. M-B-1 and M-B-3 have lots of disabled pixels.

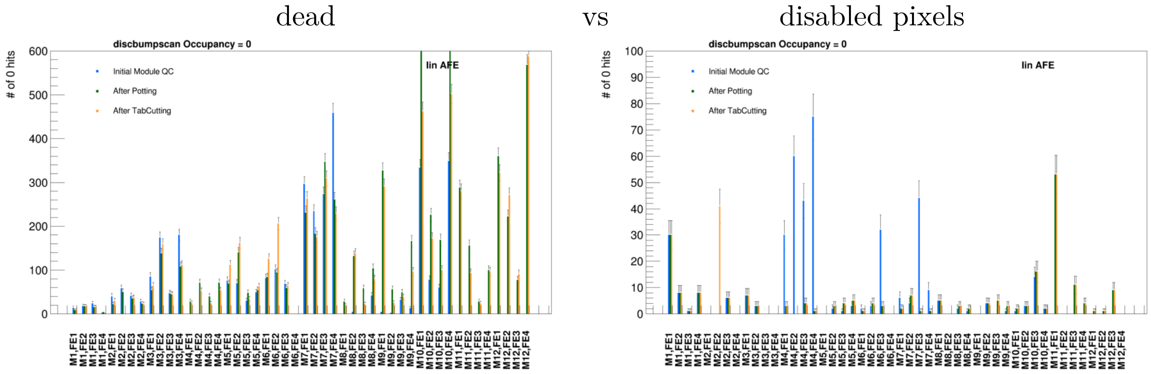

Figure B.21: Disconnected bump scans of the linear FEs of the twelve modules.

B.3.2. Linear FE

Figure B.20 shows the disconnected bump scans of the linear FEs of the six modules. M-B-1 has a bad quality analog scan for stage 1 and the linear FE hence lots of masked and disabled pixels. For M-B-3 the disabled pixels originate from dead pixels in the analog scan.

In Figure B.21, the disconnected bump scans of the linear FEs of the twelve modules are depicted. M2 has masked pixels in FE2 which result from the broken FE. M4 has masked pixels from the missing analog scan for the linear and the differential FE. Other masked pixels are mainly from bad analog pixels.

In Figure B.22, the disconnected bump scans of the linear FEs for the eleven modules are depicted. M15 has masked pixels from a bad digital pixel area as shown for the source scan in Figure B.15. M22 has a bad quality disconnected bump scan, which results in lots of dead pixels.

dead vs disabled pixels

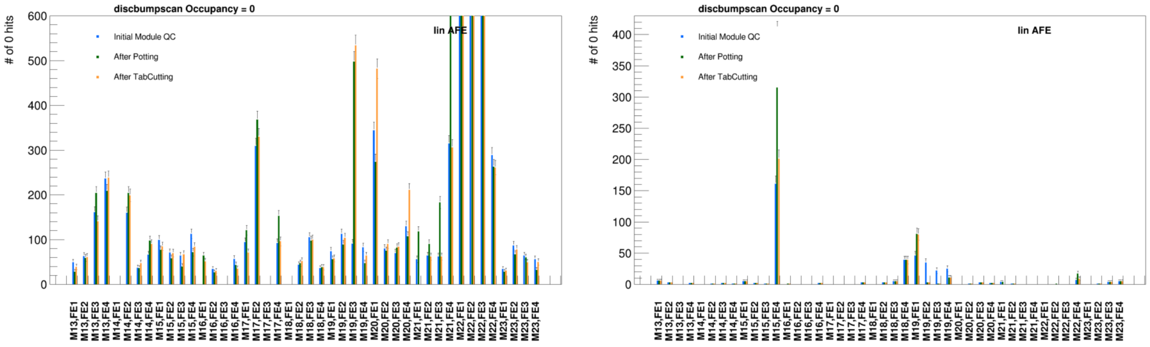

Figure B.22: Disconnected bump scans of the linear FEs shown for the eleven modules.